ATLANTIS PRESS

S. Shaswattam · Anil Kumar Das
Subrata Sarkar · Prahlad Halder
Editors

NTPC Transactions on Energy Research (NTER 2025)

A NETRA Initiative

OPEN ACCESS

एनटीपीसी NTPC
50 YEARS
OF POWERING GROWTH

NTPC Transactions on Energy Research
(NTER 2025)

S. Shaswattam · Anil Kumar Das ·
Subrata Sarkar · Prahlad Halder
Editors

NTPC Transactions on Energy Research (NTER 2025)

A NETRA Initiative

ATLANTIS PRESS

Editors
S. Shaswattam
NTPC Energy Technology Research Alliance
Greater Noida, Uttar Pradesh, India

Anil Kumar Das
NTPC Energy Technology Research Alliance
Greater Noida, Uttar Pradesh, India

Subrata Sarkar
NTPC Energy Technology Research Alliance
Greater Noida, Uttar Pradesh, India

Prahlad Halder
NTPC Energy Technology Research Alliance
Greater Noida, Uttar Pradesh, India

ISBN 978-94-6463-848-6 ISBN 978-94-6463-849-3 (eBook)
https://doi.org/10.2991/978-94-6463-849-3

This Atlantis Press imprint is published by the registered company Atlantis Press International B.V.,
part of Springer Nature
The registered company address is: Van Godewijckstraat 30 3311 GX Dordrecht Netherlands

Celebrating 50 Glorious Years of NTPC Ltd.

NTPC Energy Technology Research Alliance (NETRA)

The R&D Wing of NTPC

Preface

This open access volume titled **"NTPC Transactions on Energy Research (NTER 2025)"** is a curated collection of our in-house technical papers, covering a broad spectrum of energy topics from thermal power plants to renewable energy.

NTPC being the largest power utility of India and NETRA at its forefront for the applied R&D projects & technology, the articles in this volume provide valuable insights into current research and initiatives focused on renewables, sustainable power generation, high availability and reliability of the power plants and technological solutions for climate change mitigation. Managing the output side (flue gas, CO_2, coal ash) of power plant is becoming central for sustaining the fossil-fuel based power generation.

This volume covers diversified areas of critical topics, including methods for CO_2 capture and utilization to produce value-added products, the use of low-grade flue gas heat for water desalination, study on elemental mapping in fly ash, and innovative strategies for utilizing fly ash in resource generation. Acknowledging the growing importance of alternative energy sources, the volume also includes technical papers on solar thermal applications for space heating, advancements in hydrogen compression, and steam-enhanced gasification of municipal solid waste (MSW).

A central theme of this volume is the maintenance of power plant availability and reliability, with emphasis on condition assessment and failure analysis of various power plant components. This includes evaluation of SA213 T91 tube welds using the Magnetic Coercive Force (MCF) technique and failure analysis of boiler tubes & other power plant components. Additional contributions focus on the characterization of transformer oil and an innovative low level silica pretreatment for demineralization plant performance, mapping of chlorine distribution in Indian coal, and the use of artificial neural networks (ANN) for predictive maintenance in Distributed Control Systems (DCS) and Programmable Logic Controllers (PLC), reflecting the growing integration of AI in power plant monitoring and diagnostics.

This publication owes its success to the dedication of many individuals. We extend our sincere appreciation to all contributing authors and reviewers for their invaluable time, commitment and efforts in making this premier issue a success. We also acknowledge the contributions of the NETRA team members, with a special mention of NETRA Executives Dr. Aditya Ravindra Gokhale & Dr. Sameena Naaz Malik for their roles during the publication process.

We are confident that the insights shared herein will inspire future research, drive innovation, and advance our technological understanding within the energy sector.

Shaswattam
Executive Director-NTPC and
Head of NETRA

Introduction

NTPC is India's largest integrated power company with a vision to accelerate India's growth and energy transition. It has diversified into different areas of energy domain: power generation (thermal, hydro, solar, wind, biomass), coal-mining, power trading, etc. and aspires for sustainable business practices with emphasis on innovation & learning. As a leading player in the world energy sector, NTPC recognized the potential of cutting-edge technology in further improving its performance & efficiency and established NETRA (NTPC Energy Technology Research Alliance) in 2009 with its focus on technologies such as Carbon Capture, Utilisation and Storage (CCSU), Energy Storage, Green Hydrogen, Ash & Water Management. It also provides Cutting edge Advance Scientific Services to its stations and other Utilities in the fields of Metallurgy & Failure analysis, Non-Destructive Evaluations (NDE), Corrosion, Coal & Combustion, Electrical, Ash Utilisation, Water Chemistry and Tribology etc.

Various research projects have been taken and are underway, both at NTPC stations and NETRA premises, for validating the design & concepts for further upscaling them to a larger scale for sustainable operation of existing power stations, while accommodating the large-scale entry of renewables. Apart from in-house development of innovative technologies and solutions, NETRA has been at forefront in collaboration and networking with various prestigious national and international academic and research institutions to harness the specialized knowledge and expertise available with these institutes. NETRA is also instrumental as an important member in various committees on policy formulation for energy transition in India.

NETRA places great emphasis on knowledge dissemination through regular publications of technical papers, books, reports, and journal including presentations in various conferences, workshops, and national level committees. This open access volume "NTPC Transactions on Energy Research (NTER 2025)" is compilation of the in-house technical papers by NTPC researchers & scientific personnel on diverse important topics related to energy domain providing glimpses of efforts towards climate change mitigation and high-impact scientific services in Indian perspective.

Contents

Utilization of CO_2 for Methanol Synthesis from Coal- Fired Power Plant

Swapnil Patil*, Ankit Gupta , Sahil Chopra, Subrata Sarkar, S Shaswattam

Carbon Capture & Utilization Group, NTPC Energy Technology Research Alliance, NTPC Ltd., Greater Noida, Uttar Pradesh, India.

Corresponding author * : swapnilpatil@ntpc.co.in

Abstract. This paper describes a first-of-its-kind Flue Gas CO_2 to Methanol (FG-CTM) Demonstration Plant that has been developed to capture carbon dioxide from the flue gas of a fossil-fuel-based power plant and convert it into methanol through catalytic hydrogenation. The integrated system comprises three major process blocks: (i) CO_2 Capture, (ii) Hydrogen Generation via electrolysis, and (iii) Methanol Synthesis. This demonstration aims to establish the techno-economic feasibility of CO_2 capture and utilization (CCU) technologies in the context of coal-fired power generation. The methanol sample obtained from the stripper section and analyzed using gas chromatography technique showed 99.85% purity conforming to ASTM Grade A methanol.

Keywords: Carbon Capture and Utilization (CCU), Thermal Power, Methanol Synthesis, Proton exchange membrane (PEM) electrolyzer, CO_2 to Methanol.

1 Introduction

CO_2 emissions from fossil fuel use, are a major cause of global warming and a major part of fossil fuel is used for electricity generation. As per the report of Central Electrical Authority of India [1], the percentage share of electricity generation plant capacity by solar PV will increase from 16% in 2023 to 38% in 2030, and the percentage share of electricity generation plant capacity by coal and lignite will drop from 51% to 32%. In India, the installed capacity of electricity generation in 2023 is around 418 GW and it will become 777 GW in 2030. Although there is a decrease in the share of electricity generation plant capacity by coal and lignite, there will 19% increase in electricity generation plant capacity from 2023 to 2030, which will lead to an increase in the CO_2 emissions. To achieve net zero emissions, the first step is to reduce the CO_2 emissions per unit of power generation to the level of Combined Cycle Gas Turbine CO_2 emission which is around 490 g/kwh. The present CO_2 emission level of coal and lignite power plants is around 938 g/kwh [1].

S. Shaswattam et al. (eds.), *NTPC Transactions on Energy Research (NTER 2025)*,
https://doi.org/10.2991/978-94-6463-849-3_1

For long-lasting growth of industry energy security, energy affordability, and energy sustainability are important; to achieve these targets there are two methods. The first method is to blend green fuel in coal and the proportional amount of CO_2 emissions will be considered as a reduction in CO_2 emissions. The second method is CO_2 capture from flue gas. In the first method, 10% blending of biofuel pallets in coal-fired boiler is achieved and the feasibility of coal-fired boiler operation with 20% biofuel pallet blending is under investigation [2]. In second method, the captured CO_2 should be either stored or utilized in different products. If the CO_2 is converted to a valuable product, the cost of CO_2 capture and utilization may be recovered by the sale of the product. Hence the production cost of electricity can be the same in both cases.

For low carbon transition, the renewable power generation plant installed capacity is increasing rapidly. In future the renewable electricity generation will be high enough that excess electricity will be available in non-peak load conditions. This electricity can be utilized for green hydrogen generation. For base load, there will be requirement of power generation by fossil fuel and the CO_2 in flue gas will be captured. The potential avenues of CO_2 utilization for the product in demand are:

(i) Basic chemicals like Methanol, Ethanol, Dimethyl Ether, and Methane which can also be used as fuel for energy security.

(ii) Urea used as fertilizer for food security.

(iii) Carbon black of different morphologies which is utilized in different important product like in electrodes of rechargeable batteries, production high strength lightweight products, and Different organic chemicals.

The methanol can be used as:

(i) A fuel, blended with gasoline, or as a raw material to produce biodiesel (dimethyl ether, DME).
(ii) A raw material for various chemicals, like formaldehyde (mainly phenol, urea, melamine-formaldehyde, polyacetal resins, etc.), methyl tert-butyl ether (MTBE), ethylene and propylene.

The expected annual global methanol production will grow from 100 Mt to more than 120 Mt by end of 2025, and the rate of growth of methanol consumption will be more the 6% per year [3]. Due to this tremendous demand potential of methanol, it seems like a commercially viable option. The model of green methanol generation is based on interlinking 3-Green Pillars together i.e.

(i) Excess availability of renewable electricity,
(ii) Electrolysis of green hydrogen, and
(iii) Carbon capture from the flue gas and its utilization.

The current manuscript describes the 10 TPD capacity demonstration unit of green Methanol synthesis.

2 System Brief

There are three interconnected blocks in the Flue Gas CO_2 to Methanol synthesis (FG-CTM) demonstration plant:

(i) CO_2 Capture,
(ii) Hydrogen Generation with Electrolyzer, and
(iii) Methanol Synthesis by catalytic hydrogenation.

For CO_2 Capture, the flue gas is taken from Flue Gas Desulphurization (FGD) Plant. The Hydrogen Electrolyzer is a Proton Exchange Membrane (PEM) Electrolyzer.

2.1 Carbon Dioxide Capture

CO_2 in the flue gas can be captured in three scenarios:

(i) Pre-combustion: where the CO_2 is captured after partial oxidation of fuel.
(ii) Post-combustion: where the CO_2 is captured from the flue gas after complete oxidation.
(iii) Oxy combustion: where the CO_2 is captured from the flue gas after the complete (or partial) oxidation of fuel in presence of Oxygen instead of air.

A few separation technologies could be employed for CO_2 capture are [4]:

(i) Adsorption,
(ii) Physical absorption,
(iii) Chemical absorption,
(iv) Cryogenics separation,
(v) Membranes, and
(vi) Microalgae.

Most available adsorbents require high CO_2 concentration in flue gas and have low selectivity and detrimental effect of water on typical physisorbents, zeolites. Moreover, large-scale power plant requires large-scale flue gas treatment and present equipment configuration used for adsorption may not be suitable for large-scale applications [5].

Physical absorption of the CO_2 is based on Henry's law. Physical absorption requires high CO_2 partial pressures and gets separated by releasing the pressure. In this process, the main energy is required to pressurize the flue gas. Therefore, for economical CO_2 separation by physical absorption CO_2 partial pressures should be higher than 15 vol%. [6,7].

The CO_2 in the flue gas is liquified and separated from the in cryogenics separation. At atmospheric pressure, CO_2 condenses at −56.6 °C. Considering the costs of refrigeration, very high CO_2 concentration and preferably higher flue gas pressure is suitable. Typically, CO_2 is captured by this method after the oxyfuel process.

In membrane separation, the sorption of CO_2 from flue gas to liquid solvent is across the membrane. The membrane absorption devices are more compact than conventional packed absorption columns and are not susceptible to the difficulties in the conventional absorption process. However, to enable sorption of CO_2 across the membrane, the flue gas pressure must be equal to the liquid side pressure. In membrane absorption, the CO_2 separation efficiency depends on the CO_2 partial pressure in flue gas. As such, they are suitable for high flue gas pressure and high CO_2 concentration applications (well above 20 vol%) [8]. The captured CO_2 selectivity and the purity in the membrane separation process is low [6]. Therefore, multistage separation is necessary to improve the CO_2 purity, which requires extra capital and operating cost [6,7].

CO_2 capture efficiency by microalgae ranges between 40% and 93.7% [9]. However, the performance of microalgae in carbon emission reduction has not yet been fully understood and therefore requires more study. In chemical absorption, the solvent forms a weakly bonded CO_2 intermediate compound. Heating this intermediate compound gives the original solvent and a CO_2 stream. Even from gas with low concentration of CO_2, the selectivity is relatively high in chemical absorption, and separated CO_2 is also relatively pure. Therefore, chemical absorption is well suited for CO_2 capture for industrial flue gases.

Almost all thermal power plants in India have pulverized coal boilers, where the flue gas temperature is moderate, around 105-130 °C and CO_2 fraction in flue gas is around 11%-15%. To separate CO_2 from this flue gas, many chemisorption solvents are commercially available. The chemisorption process is exothermic, and the desorption process is endothermic. The temperature requirement for CO_2 desorption is also high (around 110 to 150 °C).

Primary and secondary alkanolamines react rapidly with CO_2 and form the thermally stable CO_2 carbamates with a high heat of absorption. Therefore, the solvent regeneration heat requirement and cost is also high. Moreover, the CO_2 loading capacity of alkanolamines is limited to 0.5 mol of CO_2 per mol of these amines [10]. The tertiary amine bicarbonate formation heat release is lower than that of carbamate formation, thus reducing solvent regeneration costs. Moreover, the CO_2 loading capacity of tertiary amines is 1 mol of CO_2 per mol of amine [10], but the rate of absorption is slow in tertiary amines.

Therefore, the blend of modified amines is used which optimize the rate of fast CO_2 absorption and low temperature & energy requirement for CO_2 desorption. APBS-CDR Max®, KM CDR Process™, BASF PuraTreart™ etc. are few CO_2 capture solvents

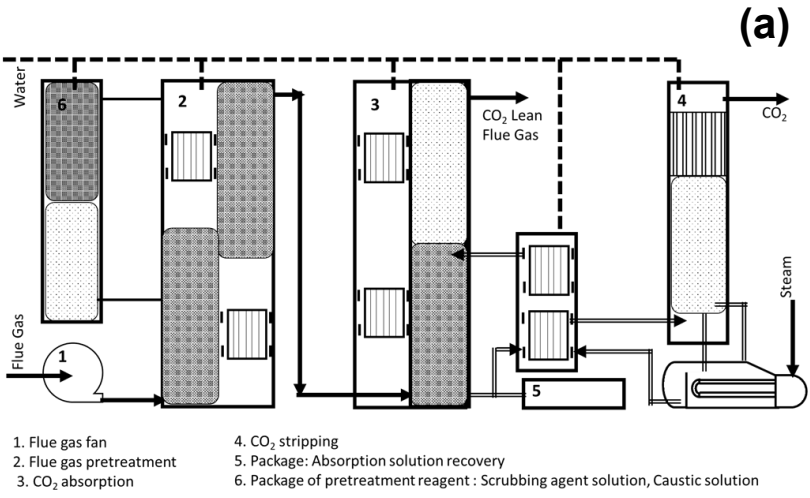

Fig. 1. (a) CO_2 Capture: Process flow diagram **(b)** Photograph of the CO_2 Capture pilot plant at NTPC Vindhyachal.

used in industry for capturing CO_2 from flue gases with CO_2 concentrations ranging from 2.5-25% by volume [4]. The main process in the carbon capture process is that CO_2 is absorbed from flue gas in amine solution, and this CO_2-rich amine solution is stripped by heating. The flue gas contains tiny amounts of particulate matter and sulfur dioxide, which are not removed by the Electrostatic Precipitator (ESP) and flue gas desulfurizer (FGD), respectively. The particulate matter and sulfur dioxide in the flue gas will poison the amine solution. Therefore, the first step before CO_2 absorption is to reduce the flue gas temperature and clean flue gas from particulate matter by water and reduce sulfur dioxide by sodium bicarbonate solution. There is a requirement to remove the heat during the absorption process. There is also a requirement to prevent the amine solution from escaping from the absorber (with CO_2-lean flue gas) and from the stripper (with captured CO_2) as shown in Figure 1(a). To further optimize heat requirements through heat integration, it's important to address impurities in the flue gas, such as sulfur dioxide, nitrogen oxides, and elevated oxygen levels, which can react with amine solvents to form heat-stable salts, leading to solvent degradation. To remove these salts, a portion of the stripper bottoms is directed to a reclaimer unit. In this unit, the solvent is evaporated, allowing non-volatile waste components to be separated. The reclaimed solvent is then returned to the absorber system for reuse. The plant capacity of CO_2 capture plant is 20 TPD and around 14 TPD CO_2 will be used for methanol synthesis. A visual representation of the demonstration plant is provided in Figure 1(b).

2.2 Hydrogen Electrolysis

Hydrogen is produced by breaking down water molecules into Hydrogen and Oxygen by passing them through the electrolyzer. Water is purified by removing traces of impurities/salts and fed into electrolyzer through the anode separator vessel. The following factors are used to compare alkaline and proton exchange membrane (PEM) electrolyzers, illustrating why PEM is often regarded as the superior choice in many applications.

Alkaline electrolyzers have a long operational history and cost-effectiveness. They typically operate at lower current densities (0.2–0.4 A/cm²), which can limit their responsiveness to dynamic power inputs. Since the alkaline electrolyzer has a large liquid electrolyte volume, it is less suitable for applications requiring rapid load changes. PEM electrolyzers employ a solid polymer electrolyte (e.g., Nafion) that conducts protons (H^+) from the anode to the cathode. PEM electrolyzers offer rapid start-up times and can quickly adjust to fluctuating power inputs, making them ideal for integration with renewable energy sources like wind and solar. Therefore, PEM electrolyzers are used for H_2 generation. [11,12]

To enhance operational flexibility, a PEM electrolyzer has been adopted, capable of functioning efficiently over a wide load range (10 –100%) and offering a rapid dynamic response. This makes it more suitable than conventional alkaline electrolyzers for managing variable process demands and aligning with the intermittent nature of renewable energy sources. The PEM allows only protons to pass through while blocking electrons.

Fig. 2. Photograph of the PEM electrolyzer installed at NTPC Vindhyachal.

During operation, the hydrogen atoms in water molecules migrate through the membrane and are released as hydrogen gas on the cathode side. Simultaneously, the remaining oxygen atoms exit from the anode side as oxygen gas along with water. The gas–liquid mixture exiting the anode is separated in the anode separator, while the hydrogen gas on the cathode side, containing trace amounts of water, is processed in the cathode separator.

After this stage, the hydrogen is directed to a dryer unit to achieve the desired purity level. The PEM electrolyzer in use has a hydrogen production capacity of 2 TPD (tons per day), with a discharge pressure of approximately 30 barg. The specific power consumption of the system ranges between 55–60 kWh per kilogram of hydrogen. A photograph of the plant setup is shown in Figure 2.

2.3 Methanol Synthesis Process

The catalytic hydrogenation of CO_2 to methanol presents a promising pathway for mitigating greenhouse gas emissions and producing valuable chemicals. This process typically involves the reaction of CO_2 with hydrogen (H_2) over a catalyst, yielding methanol (CH_3OH) as the primary product. Copper-based catalysts, such as $Cu/ZnO/Al_2O_3$, have been extensively studied due to their high selectivity and activity for methanol synthesis. Recent developments focus on enhancing these catalysts by doping with elements like ZrO_2, CeO_2, and Ga_2O_3 to improve stability and resistance to deactivation [13,14]. Studies have demonstrated that NiZn intermetallic catalysts, supported on

ZnO, can efficiently catalyze CO_2 hydrogenation to methanol under atmospheric pressure. These catalysts exhibit a high methanol production rate with excellent selectivity, making them promising candidates for solar-driven applications [15]. Photocatalytic reduction of CO_2 to methanol using sunlight has garnered significant attention. Materials such as carbon quantum dots, Bi-based compounds, g-C_3N_4, and metal-organic frameworks (MOFs) have been explored as photocatalysts. These systems aim to harness solar energy for sustainable methanol production [16]. An overview of the literature reviewed is shown in Table 1.

A demonstration plant with a production capacity of 10 TPD Methanol has been integrated with a 500 MW power unit at NTPC Vindhyachal, India, as illustrated in Figure 3. As shown in Figure 4, CO_2 and Hydrogen is compressed in the compression section, the compressed syngas is converted to crude methanol in the methanol synthesis section and the product methanol is purified in the distillation section.

Table 1. Key Studies on CO_2 to Methanol Conversion

Study	Catalytic System	Key Findings
Yusuf & Almomani (2023)	Cu/ZnO/Al_2O_3	Enhanced operating conditions for sustainable catalytic hydrogenation of CO_2 to methanol [13].
Han et al. (2024)	NiZn/ZnO	High-efficiency sunlight-driven CO_2 hydrogenation to methanol under atmospheric pressure [15].
Murthy et al. (2021)	Cu-based nanocatalysts	Overview of Cu-based nanocatalyst development for CO_2 hydrogenation to methanol [14].
Zhang et al. (2021)	Various photocatalysts	Advances in photocatalytic reduction of CO_2 to methanol using various materials [16].

Fig. 3. Photograph of the 10 TPD Methanol synthesis pilot plant installed at NTPC Vindhyachal.

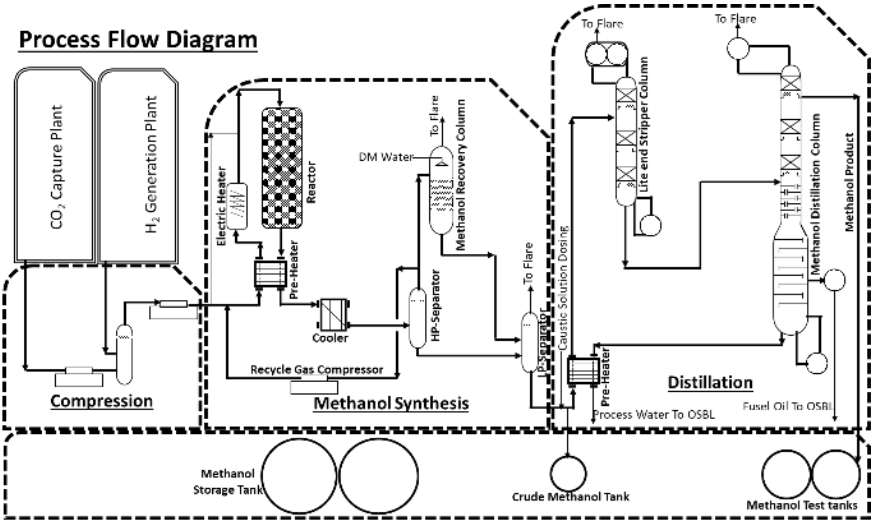

Fig. 4. Schematic of the Methanol synthesis process flow diagram.

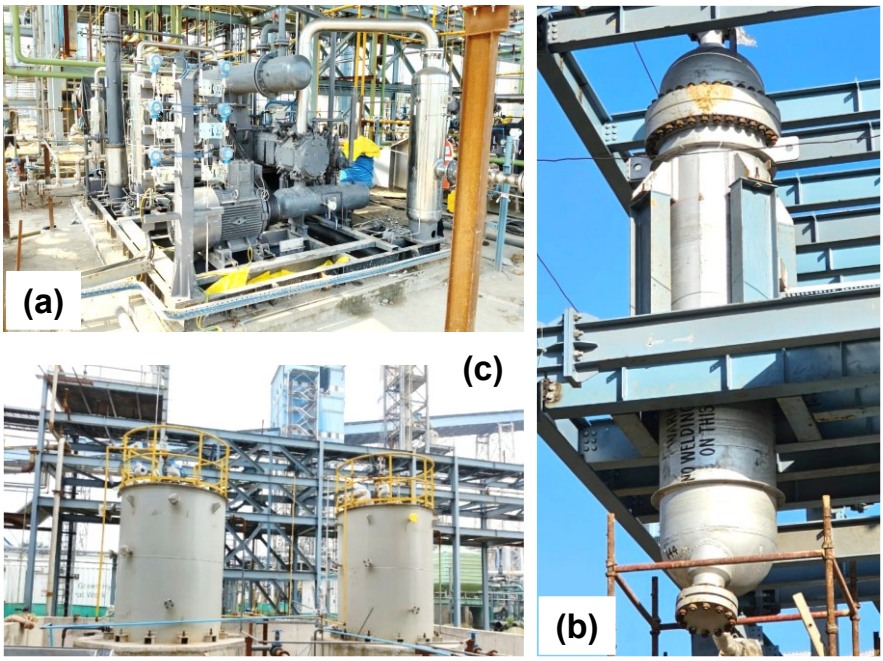

Fig. 5. Photographs of the key equipment installed in the pilot plant. **(a)** CO_2 Compressor, **(b)** Methanol Reactor, and **(c)** Product Methanol Storage Tanks

2.3.1 CO_2 and Syngas Compression

The CO_2 gas is initially compressed to 30.0 barg in a CO_2 compressor as shown in Figure 5(A). The H_2 gas is then mixed with the compressed CO_2, and now the mixture is called syn gas. The syngas, which is now at 30 barg is further compressed to 60 barg in the Synthesis Gas Compressor. The syngas temperature is raised to 235 °C -250 °C in the Electric heater.

2.3.2 Methanol Synthesis Reactor

Preheated syngas (Temperature around 235 °C - 250 °C) is now fed in the Methanol Reactor as shown in Figure 5(B). The Methanol Reactor contains a fixed bed of Cu catalyst to convert carbon dioxide and hydrogen to methanol and water.

$$CO_2 + 3H_2 \leftrightarrow CH_3OH + H_2O + \text{Heat} \quad (1)$$

The synthesis of methanol from CO_2 (Equation (1)) is less exothermic as compared to starting from CO in syngas, and it also involves a secondary reaction in the reverse water–gas shift (RWGS) (Equation (2))

$$CO_2 + H_2 \leftrightarrow CO + H_2O - Heat \quad (2)$$

The methanol synthesis process mostly uses $Cu/ZnO/Al_2O_3$ catalyst which can ensure appreciable performance at low temperatures. Some commercially available catalysts are MK-151 FENCE™ by TOPSOE, KATALCO™ 51-series by JOHNSON MATTHEY, MEGAMAX® 800 by CLARIANT, etc. The reactor outlet contains about 2.8 mol% methanol and the temperature is around 260 °C - 290 °C. The reactor outlet is first cooled in Synthesis Gas Heat Exchanger, which in turn preheats the feed of Methanol Reactor. To separate crude methanol, Methanol Reactor outlet is then further cooled to 40 °C and flashed in the HP Separator to separate out the unreacted gas and crude methanol liquid. Part of the unreacted gas from HP Separator is purged to maintain the inert gas level in the Methanol Reactor feed. Before purging the gas to flare, methanol is recovered in the Methanol Recovery Column. The remaining part of the unreacted gas from HP Separator is recycled and mixed with fresh make-up gas to preheat and to feed to the methanol reactor. There is an Electric Heater downstream of the preheater of the reactor. The Electric Heater is used for process start-up and for heating low-temperature reactor feed to maintain the temperature. To permit adequate control on higher reactor feed temperature, the feed syngas bypass is also provided around both exchangers.

2.3.3 HP Separator/ LP Separator/ Methanol Recovery Column

Crude Methanol collected in HP Separator and in Methanol Recovery Column is sent to LP Separator. The LP Separator separates the dissolved gases such as CO, H_2 and CO_2 from the crude methanol. The gases coming from LP Separator and Methanol Recovery Column go to flare. Crude Methanol collected in LP Separator is sent to the distillation section. There is also a provision to store crude methanol in Crude Methanol Tank along with the Product Methanol Test Tank and Product Methanol Storage Tank as shown in Figure 5(c).

2.3.4 Methanol Distillation

Crude methanol from the Methanol Synthesis Section is sent to the Distillation section for methanol purification. The distillation is carried out in two steps,

(i) Light End Stripper
(ii) Methanol Distillation column

Light End Stripper

Light End Stripper removes the dissolved gases like CO, H_2, CO_2, together with other light ends formed during the methanol synthesis reaction, such as dimethyl ether and

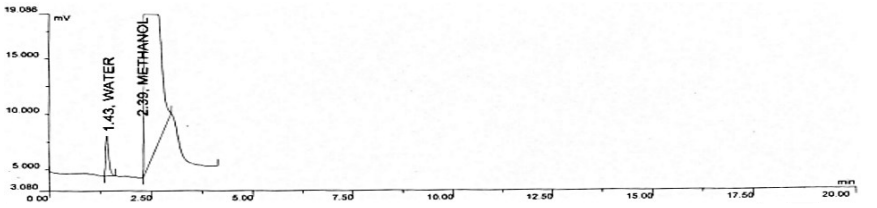

Fig 6. FID - GC plot showing the peak intensities obtained for the methanol sample obtained from the stripper reflux drum section.

methyl formate. The condensed methanol is fed back to the top of the light-end stripper column. The light end stripping column is operated at 0.4 barg pressure with a bottom temperature of 89 °C and a top temperature of 72 °C.

Methanol Distillation column

The purpose of Methanol Distillation column is to remove water and organic heavy ends and thus purify the methanol product. The heavy ends are predominantly alcohols such as iso-butanol and are known as fusel oil and water. The product methanol is withdrawn from top section of the column, cooled to 40°C, and sent to the Product Methanol Test Tank. Then, the product methanol is delivered to the Product Methanol Storage Tank. The Methanol distillation column is operated at 0.5 barg pressure with a bottom temperature of 125 °C and a top temperature of 75 °C. Fusel oil, is drawn off at an intermediate bed located in the stripping section of the column. The processed water collected from the bottom of the column is cooled through the Crude Methanol Heater. The methanol plant capacity is 10 TPD and utility consumption for all individual plants is given in Table 2.

The methanol sample was obtained through a sampling line at Stripper Reflux Drum. The methanol sample was analyzed for purity through gas chromatography (GC) technique equipped with a flame ionization detector. Figure 6 shows the FID - GC plot, it can be clearly seen that the methanol purity was 99.85% and the remaining was water; conforming to ASTM D – 1152 standard.

Table 2. Utility consumption in different blocks

No	Utility	Units	CO_2 Capture	H_2 Generation	Methanol Synthesis
1	Steam	kg /hr	1,600	-	982
2	DM water	kg /hr	120	1,000	1,500
3	Service water	kg /hr	600	-	13,000
4	Power	MW	0.2	5	1

3 Conclusion

The present manuscript has presented the conceptualization, design, and implementation of a carbon dioxide-to-methanol synthesis facility. The 10 TPD methanol demonstration plant represents a pivotal milestone in assessing the technical and economic viability of mitigating greenhouse gas emissions associated with coal-fired power generation. The facility is expected to yield critical operational data that will inform the techno-economic analysis necessary for scaling to a commercially viable, full-scale production system. The facility was able to produce 99.85% purity methanol which was confirmed through FID – GC technique.

This initiative aligns with the strategic objectives of NTPC Ltd., and the broader Indian power sector to substantially reduce carbon emissions in line with the CoP 26 agreements and commitments. It also contributes to the realization of India's Methanol Economy framework and the national Net Zero emissions target by 2070. By maintaining a systems-level integration across all stages of the process, the project enhances its translational relevance for industrial stakeholders and the scientific research community.

Acknowledgement: The authors express their sincere gratitude to Sh. Sujay Karmakar, CGM (NETRA), and Sh. Partha Mukherjee, AGM (NETRA), for their valuable guidance. We also extend our appreciation to the teams from NTPC Vindhyachal, M/s Jakson Ltd., and M/s TOYO for their continuous support in the successful implementation of this project.

References

1. A. Toppo, Report on Optimal Generation Capacity Mix for 2029 - 2030 (Version 2.0), Central Electricity Authority, Ministry of Power, Government of India, New Delhi, 2023.
2. Standard Operating Procedure for Biomass co-firing in FBC Boilers, National Mission on use of Biomass in Thermal Power Plants, https://samarth.powermin.gov.in/content/policies/80e5db53-014e-4dbf-ad85-a9d0ce9b654a.pdf
3. S. Kang, F. Boshell, A. Goeppert, P.G. Surya, I. Landälv, Innovation Outlook: Renewable Methanol, International Renewable Energy Agency and Methanol Institute, Abu Dhabi, 2021. ISBN 978-92-9260-320-5
4. M. Wang, A. Lawal, P. Stephenson, J. Sidders, C. Ramshaw, Post-combustion CO_2 capture with chemical absorption: A state-of-the-art review, Chemical Engineering Research and Design 89 (2011) 1609–1624.
5. L. Riboldi, O. Bolland, Overview on pressure swing adsorption (PSA) as CO_2 capture technology: stateof-the-art, limits and potentials, Energy Procedia 114 (2017) 2390–2400.
6. D. Gielen, J. Podkanski, Prospects for CO_2 Capture and Storage, International Energy Agency, 2024. ISBN 92-64-108-831
7. S. Chakravarti, A. Gupta, B. Hunek, Advanced technology for the capture of carbon dioxide from flue gases, First National Conference on Carbon Sequestration, Washington, DC, Citeseer, 2001: pp. 15–17.R.
8. Hou, C. Fong, B.D. Freeman, M.R. Hill, Z. Xie, Current status and advances in membrane technology for carbon capture, Sep Purif Technol 300 (2022) 121863.

9. Ighalo, J.O., et al., Progress in microalgae application for CO_2 sequestration, Cleaner Chem. Eng. 3 (2022) 100044.
10. P.D. Vaidya, E.Y. Kenig, CO_2 -alkanolamine reaction kinetics: a review of recent studies, Chemical Engineering & Technology: Industrial Chemistry-Plant Equipment-Process Engineering-Biotechnology 30 (2007) 1467–1474.
11. Carmo, M., Fritz, D. L., Mergel, J., & Stolten, D. (2013). A comprehensive review on PEM water electrolysis. International Journal of Hydrogen Energy, 38(12), 4901–4934. https://doi.org/10.1016/j.ijhydene.2013.01.151
12. Dincer, I., & Acar, C. (2015). Review and evaluation of hydrogen production methods for better sustainability. International Journal of Hydrogen Energy, 40(34), 11094–11111. https://doi.org/10.1016/j.ijhydene.2014.12.035
13. Yusuf, A. A., & Almomani, F. A. (2023). Enhanced operating conditions for sustainable catalytic hydrogenation of CO_2 to methanol using $Cu/ZnO/Al_2O_3$ catalyst. *Processes, 13*(2), 314. https://doi.org/10.3390/pr13020314
14. Murthy, R. N., & Kalevar, H. (2021). Copper-based nanocatalysts for methanol synthesis from CO_2: Recent advances and challenges. *ACS Energy Letters, 6*(3), 811–824. https://doi.org/10.1021/acsenergylett.3c00714
15. Han, L., Zhang, S., Liu, X., & Wang, Y. (2024). Highly efficient sunlight-driven CO_2 hydrogenation to methanol over a NiZn intermetallic catalyst. *arXiv preprint arXiv:2404.14085*. https://arxiv.org/abs/2404.14085
16. Zhang, Q., Li, K., & Wang, L. (2021). Advances in photocatalytic reduction of CO_2 to methanol: From fundamentals to practical applications. *EcoMat, 3*(2), e12078. https://doi.org/10.1002/eom2.12078

Experimental Investigation of CO_2 Sequestration in Fly Ash and Lime Composites via Mineral Carbonation: A Lab-Scale Study

Gaurav Richhariya*, Sunit Kumar Singh, Pranay Sharma, Aarti Sharma, G.D Vani, Ch. Srinivasu, Anil Kumar Das

Ash Utilization Group, NTPC Energy Technology Research Alliance, NTPC Ltd., Greater Noida, Uttar Pradesh, India.

*Corresponding author: grichhariya01@ntpc.co.in

Abstract. CO_2 emissions are widely acknowledged as the main factor behind the rapid increase in global temperatures, resulting in substantial changes to climate system. Emissions and waste from thermal power plants pose a serious environmental concern. This study aims to explore the cost-effective bulk utilization of fly ash for CO_2 sequestration. The fly ash and hydrated lime was mixed in varying proportions and tested for CO_2 sequestration, compressive strength, consistency, and free water content as a function of CO_2 mixing rate and injection pressure. Coal fly ash and hydrated lime composition with 4% (wt.) lime resulted in an impressive compression strength of 1.7 MPa and a CO_2 absorption of 5.4%.

Keywords: CO_2 sequestration, mineral carbonation, Fly ash & Concrete

1 Introduction

Anthropogenic carbon dioxide emissions are widely acknowledged as the primary catalyst for the accelerated rise in global temperatures during the past six decades, resulting in profound transformations of universal climate framework[1].Carbon capture and storage (CCS) may be substantially feasible as a strategy to abate the environmental impact of carbon dioxide emissions [2]. Mineral carbonation, Carbon dioxide capture through alkaline earth mineral reactions such as alkaline earth metal oxides or hydroxides, presents an attractive approach within the realm of CCS, potentially utilizing natural resources and industrial byproducts [3]. Silicate minerals enriched in calcium oxide or magnesium oxide, along with industrial waste products including steel slag, Coal Fly Ash (CFA), Coal Bottom Ash (CBA), bauxite residues, concrete waste, and municipal solid waste incineration residues, may be employed as raw materials for the mineral sequestration of carbon dioxide [4–7]. Despite having a relatively low content of free calcium oxide, CFA shows significant potential for mineral carbonation due to its large production volume [8]. Exceeding 800 million tons annually, CFA constitutes a substantial global byproduct. As Coal-fueled power station are major driver of global warming, contributing nearly 40% of greenhouse gas discharge, the on-site sequestration of CO_2 within these power plants using CFA can contribute to a substantial reduction in global CO_2 emissions [9]. Additionally, this

S. Shaswattam et al. (eds.), *NTPC Transactions on Energy Research (NTER 2025)*,
https://doi.org/10.2991/978-94-6463-849-3_2

approach has the potential to reduce both the expense and discharge associated with transporting CFA to landfills [10].

CFA possessing specific compositional characteristics finds broad application in the construction industry as an admixture [11,12]. Moreover, there exist methodologies for synthesizing materials such as zeolites and adsorbents from CFA, thereby expanding its potential utility for diverse purposes [13]. CFA isn't being used as much as it could be in practical situations around the world.

Massive quantities of coal fly ash are needlessly dumped in landfills and ash ponds, leading to severe environmental problems such groundwater contamination and degradation, spreading to natural areas, and deteriorating air quality [14]. Consequently, a significant increase in CFA utilization rates could provide a viable strategy for mitigating this environmental impact. The elevated CaO and MgO content in CFA can induce expansive reactions in construction materials, limiting its use in cement and concrete[15,16]. Sequestering CO_2 with CFA is a great way to reduce greenhouse gases and help manage the environmental problems caused by CFA. Utilizing CFA with lower CaO and MgO content can enhance its potential for application[17].The mineral carbonation process can be conducted in both moist and dry environments. However, the dry method, though simpler, faces challenges due to its sluggish reaction rate and limited CO_2 sequestration capacity, whereas wet carbonation demonstrates enhances CO_2 sequestration [18]. There are two approaches to wet carbonation: direct and indirect. The direct method transforms fly ash and carbonation products into solid, reusable material for construction or landfill disposal. In direct carbonation, fly ash reacts with CO_2 in an aqueous environment, forming carbonates through the reaction of carbonic acid with alkaline constituents [19]. Whereas in indirect carbonation, reactive components like calcium are first leached into a solution, and then react with CO_2 to form carbonates, offering better control over the final product. However, indirect carbonation is time and capital consuming. The direct method of carbonation offers the benefits of simplicity and reduced chemical use, making it the preferred technology for CO_2 mineralization using fly ash. The fundamental reaction in this process is the direct carbonation of fly ash with gaseous CO_2. Further, the limited calcium oxide (CaO) content in class F fly ash can hinder CO_2 sequestration. The interaction between fly ash, lime, and water under high pressure and temperature leads to hydration reactions, forming calcium silicate hydrates (CSH) and calcium aluminate hydrates (CAH). These compounds contribute to the development of high strength and durability. Hence, his research seeks to unlock the potential of CFA lime slurry for effective CO_2 capture by investigating the effects of temperature and pressure.

2 Materials & Method

2.1 Materials

The Coal Fly Ash-F (CFA-F) and Hydrated Lime (HL) were received from NTPC Ramagundam and Akshar chemical Mumbai with 90% purity, respectively. The CO_2 for the study was procured from Star Special Air with 99.99% purity. All the samples were prepared with normal water at ambient condition.

2.2 Methods

2.2.1 Particle Size Distributions

The particle size analysis was performed using Malvern Mastersizer HYDRO 2000MU. The fly ash sample was dried in oven at 105 °C for 24 hrs prior to analysis. The analysis was performed via wet analysis method, where sample was added to a dispersing medium (Deionized water) and ultra-sonicated for finer dispersion.

2.2.2 Elemental composition

Elemental analysis of CFA-F/HL was conducted using Energy-Dispersive X-ray Fluorescence (ED-XRF) spectroscopy (EX-6600 model, Xenemetrix). The sample was analyzed in its powder form. The spectrum was collected in the energy range 10 to 40 keV.

2.2.3 Slurry Preparation and CO_2 Purging

Table 1 outlines the various dosages of CFA-F, HL, and water that were mixed in different proportions to prepare the slurry. To sequester CO_2 within the slurry, CO_2 gas was purged during the stirring process as shown in Fig1. A 1 L PET (polyethylene terephthalate) trough was used to sequester CO_2 within the slurry. The trough was then sealed airtight, and the air was flushed out through an outlet port by CO_2 purging). Furthermore, the CO_2 injection pressure was controlled using a pressure regulator attached to the cylinder.

2.2.4 Effect of Solid- liquid ratio, stirring rate on CO_2 sequestration

CFA-F/HL slurries, prepared according to the specifications in Table 1, were exposed to varying CO_2 injection pressures ranging from 0.5 to 2 bar. The CFA-F/HL slurries were progressively agitated, achieving a fully homogeneous mix after 5 minutes of stirring. After 5-minute agitation, the slurries were allowed to dry at ambient conditions (atmospheric temperature ~25 °C, humidity ~20%, air pressure ~ 1 bar) for 24 hours. The dried samples were then crushed and analysed using STA to quantify CO_2 release. CO_2 sequestration by different CFA-F/HL slurries was measured at various range of injection pressure and rpm. Additionally, the influence of stirring rate on CO_2 sequestration was also investigated.

Table 1. Dosage of CFA-F, HL and Water

S. No	CFA-F	HL	Water	Sample
1	100%	0%	20%	S0
2	99%	1%	20%	S1
3	98%	2%	20%	S2
4	97%	3%	20%	S3
5	96%	4%	20%	S4
6	95%	5%	39%	S5
7	90%	10%	39%	S10

*CFA-F and HL together indicates 100% of solid material in all rows .water is added by weight of solid i.e flyash +lime.

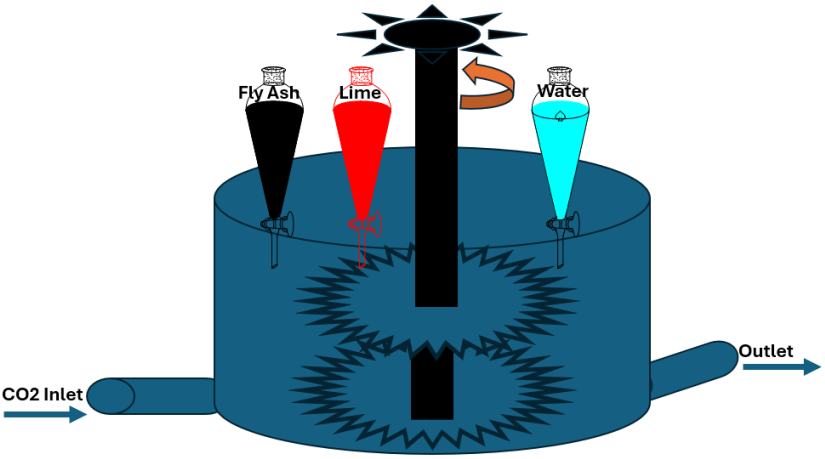

Fig. 1. Schematic for CO_2 purging setup

2.2.5 Measurement of CO_2 sequestration

The CO_2 sequestration in the CFA-F/HL slurry was evaluated through a Simultaneous Thermal Analyzer (STA 449 F1 JUPITER, NETZSCH), which integrates TGA and DSC techniques to analyse the thermal behaviour of materials and track mass changes, including CO_2 release during decomposition. After drying the CFA-F/HL slurry in a heated air oven at 40°C, the sample was crushed using a pulveriser. 10 milligrams of the crushed sample were then placed in the STA, where mass loss was recorded over time (Fig3). The STA was operated with temperature ramp rate of 30°C/min, form 40°C to 1000 °C with N_2 gas flow rate of 30 mL/min. The mass loss calculated from STA was plotted as a function of pressure and rpm.

2.2.6 Scanning Electron Microscope (SEM) Imaging for carbonate deposit

Scanning electron microscopy (SEM) (FEI Quanta 200, ThermoFisher Scientific, New Delhi, India) was employed to analyse the morphologies of CFA-F, HA, and the carbonate deposits formed due to CO_2 sequestration.

2.2.7 Consistency of Fly Ash Lime slurry

The Consistency of the slurry influences CO_2 diffusion within the mixture. If the slurry is too thick, gas penetration may be restricted, slowing carbonation. If too thin, CO_2 may escape before sufficient reaction with lime, reducing carbonate formation efficiency. The flow behaviour of the CFA-F/HL slurry, prepared as per Table 1, was studied using an atmospheric consistometer (Model 200, CTE, Tulsa, Oklahoma, USA). The various CFA-F/HL slurries were poured into the consistometer cup, which was equipped with a paddle and potentiometer. During the consistency test, the slurry cup maintained a constant rotation at 150 rpm, while the paddle gradually began rotating as the CFA-F/HL slurries hardened. As hardening progressed, the potentiometer coil twisted, generating torque. This torque, resulting from the slurry's hardening, was recorded as consistency and measured in Bearden units of consistency (Bc).

2.2.8 Cube Casting & Compressive Strength

The CFA-F/HL slurry, following CO_2 dosing, was poured into a cube mold measuring 70.5 × 70.5 × 70.5 mm^3. The cubes were allowed to dry in ambient conditions (atmospheric temperature ~25 °C, humidity ~20%, air pressure ~ 1 bar) for 24 hrs. Then, the cubes were subjected to compressive strength testing using Enkay 2000N compression testing machine as shown in Fig2.

Fig. 2. Cube Cast from S1 to S4 before and after CO_2 sequestration (a) and Enkay 2000N compression testing machine (a).

2.2.9 Assessment of free water in fly ash-lime slurry

Free water in cement and concrete is the excess water that isn't chemically bound to the cement particles. It significantly affects the strength, durability, and workability of concrete. The free water was determined using gravimetric method. To measure free water, a concrete cube was weighed (M1) before and after drying (M2) it in an oven at (105-110) ℃. The difference in weight % represents the amount of free water M.

$$\%\,\text{Free Water}\,M = \frac{(M_1 - M_2)}{M_1} \times 100 \tag{1}$$

3 Results and Discussion

3.1 Particle Size Analysis

The analysis of particle was done to measure the spread of CFA-F particles is presented as Fig3. Majority of the particles fall in the range of 100 µm, whereas approximately 30-40% particles are also observed in the range of 10 µm. Smaller particle size renders higher specific surface area which enhances the reactivity of particle with hydrated lime. This enhances reactivity further improves the durability of the fly ash lime composite. Additionally, smaller particles instigate micro porosity in the composite. This micro porosity improves absorption of CO_2 in to the composite.

3.2 Energy Dispersive X-ray Fluorescence (EDXRF)

The elemental composition of CFA-F and HL is presented in Table-2. Among the various oxides present in the CFA-F and HL. The EDXRF results of fly confirm the typical class F fly ash composition with low Ca and Mg content. The hydrated lime showed high amount of CaO of about 73.1%. Apart from Ca, other elements observed in the composition were of trivial level.

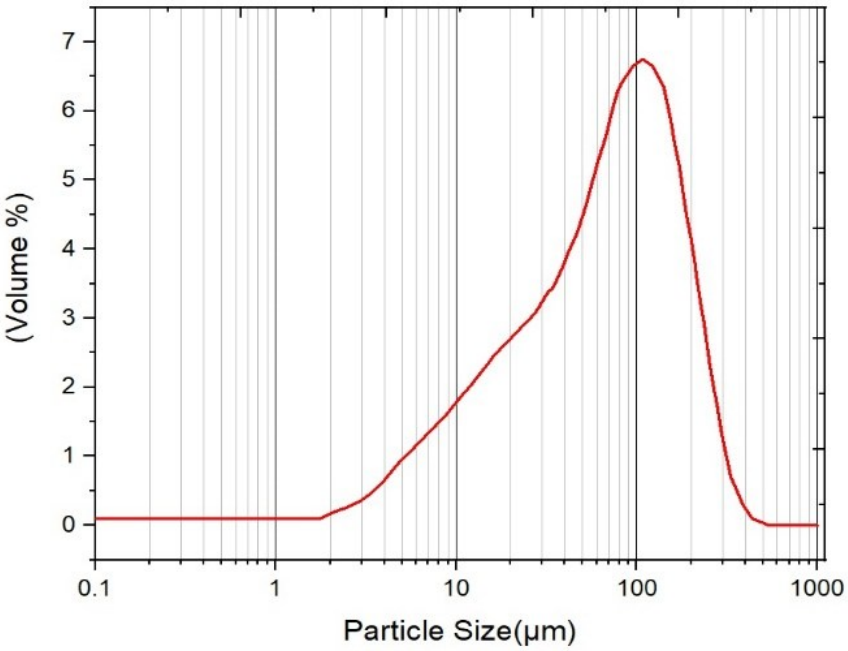

Fig. 3. Particle Size distribution of coal fly ash.

Table 2. Elemental Composition of Fly ash and Hydrate lime

Sample	CFA-F	HL
Na_2O	0.15	0.188
MgO	0.94	0.06
Al_2O_3	26.52	0.22
SiO_2	60.64	0.49
P_2O_5	0.18	0
SO_3	0.13	0.33
K_2O	1.51	0.14
CaO	1.19	73.16
TiO_2	2.02	0.02
MnO	0.032	0.01
Fe_2O_3	5.8	0.06

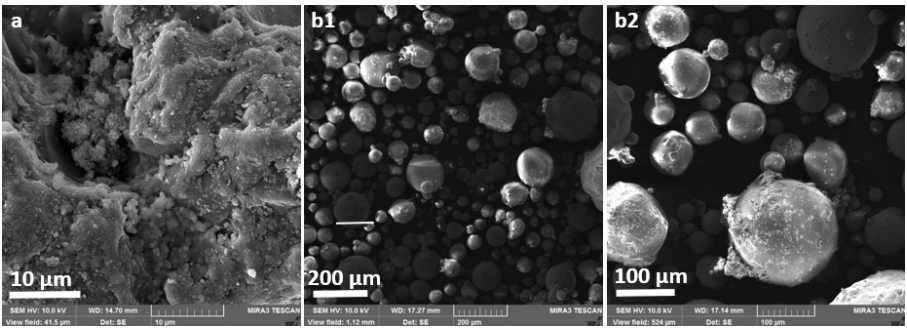

Fig. 4. SEM Images of (a) Hydrated Lime and (b1, b2) Coal Fly Ash.

3.3 SEM Analysis of CFA-F/HL slurry after carbonation

The SEM analysis Fig 4 (a) shows the irregular texture and morphology of calcium hydroxide flakes present in hydrated lime. In contrast, Fig 4(b1) displays the regular spherical geometry typical of CFA-F particles. Upon further magnification Fig 4(b2), the CFA-F particles exhibit a clear, rounded structure with particle size less than 200 µm. In an aqueous slurry phase, the spherical morphology of particles typically hinders gas diffusion. However, this slower diffusion rate can increase the contact time between CO_2 and lime particles, promoting carbonate formation in the slurry [20].

3.4 Effect of solid-liquid ratio, stirring rate on CO_2 sequestration

The resulting mass loss (due to $CaCO_3$ decomposition indicating CO_2 Sequestered) percentages were plotted against mixing rate at 1 bar in the Fig 5(a). The CO_2 sequestration percentage increases slightly up to 300 RPM. There was no significant increase in mass loss observed with further increase in mixing rate. However, the injection pressure significantly affected the mass loss observed. The CO_2 sequestration increases with increase in injection pressure up to 1.5 bar, as shown in Fig 5(b). There was no further mass loss observed beyond 1.5 bar. This is due to reason that CO_2 absorption is directly proportional to the lime content in the composite. CO_2 is trapped in the composited in the form carbonates of calcium. The mass loss is observed in Simultaneous Thermal Analyzer (STA) due to thermal decomposition of these carbonates at around 680 °C [20].

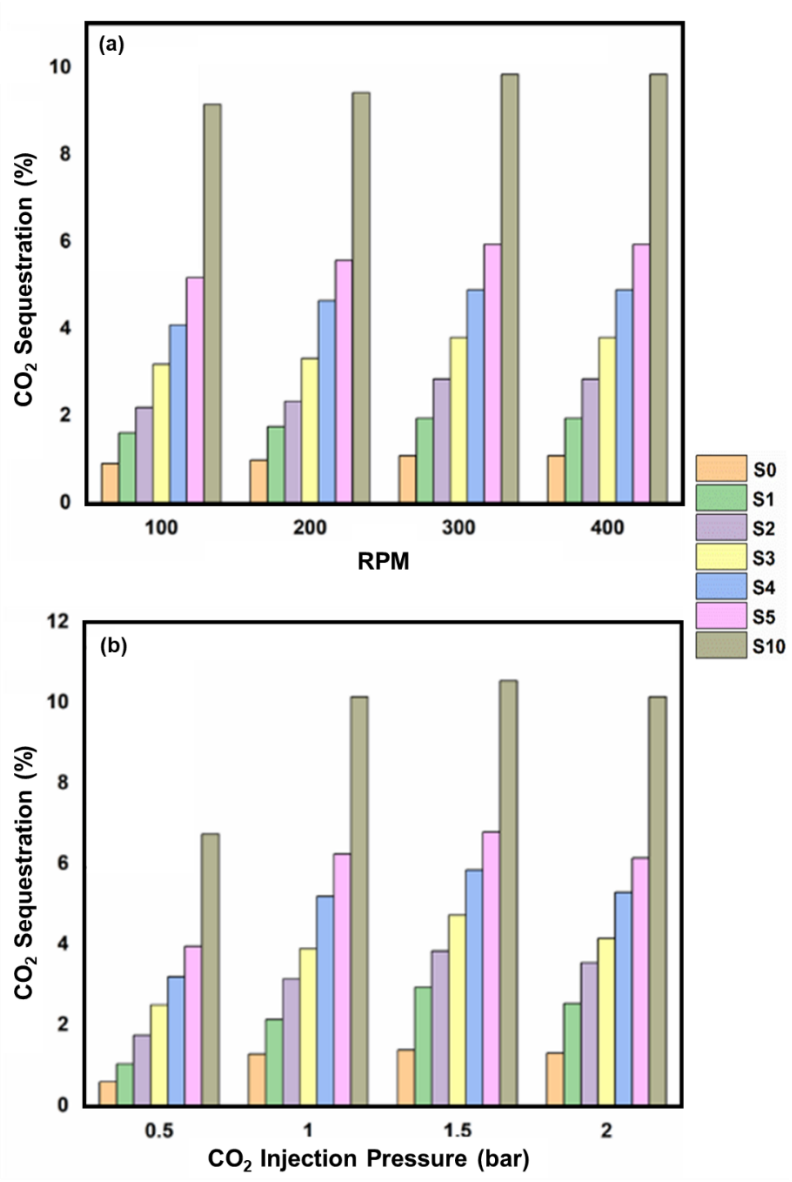

Fig. 5 Plots showing **(a)** CO_2 (%) uptake as a function of rpm at 1 bar pressure **(b)** % CO_2 (%) uptake as a function of injection pressure at 300 rpm.

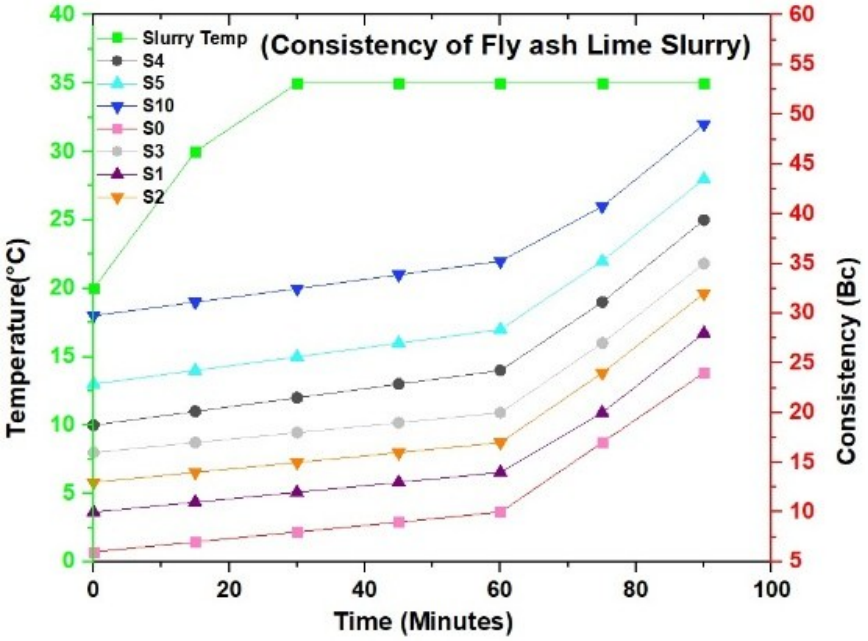

Fig. 6. Consistency studies of CFA-HL composites.

3.5 Consistency Test of Fly Ash Lime Slurry

The slurries were prepared according to the details in Table 1 and subjected to a consistency test performed as mentioned in section 2.2.7. All slurries were heated to 35 °C, and torque was measured over time. Slurries with higher water content exhibited a gradual thickening rate, as shown in Fig 6.

3.6 Free Water and Compressive Strength Assessment

Water is necessary for the hydration process of Fly ash lime composite block, where lime react with water to form a hardened matrix. If the free water content exceeds the amount required for hydration, it leads to the formation of voids as the excess water evaporates, reducing the block's strength. Fig 7(a) illustrates the free water content in various samples prepared according to Table 1. It was observed that the free water content decreased as the lime percentage increased from 0% to 4%, but no further reduction was noted with an increase to 5% and 10%. This could be attributed to the higher water content used during slurry preparation, which was 39% for the latter two samples, as indicated in Table 1. The compressive strength increased gradually with

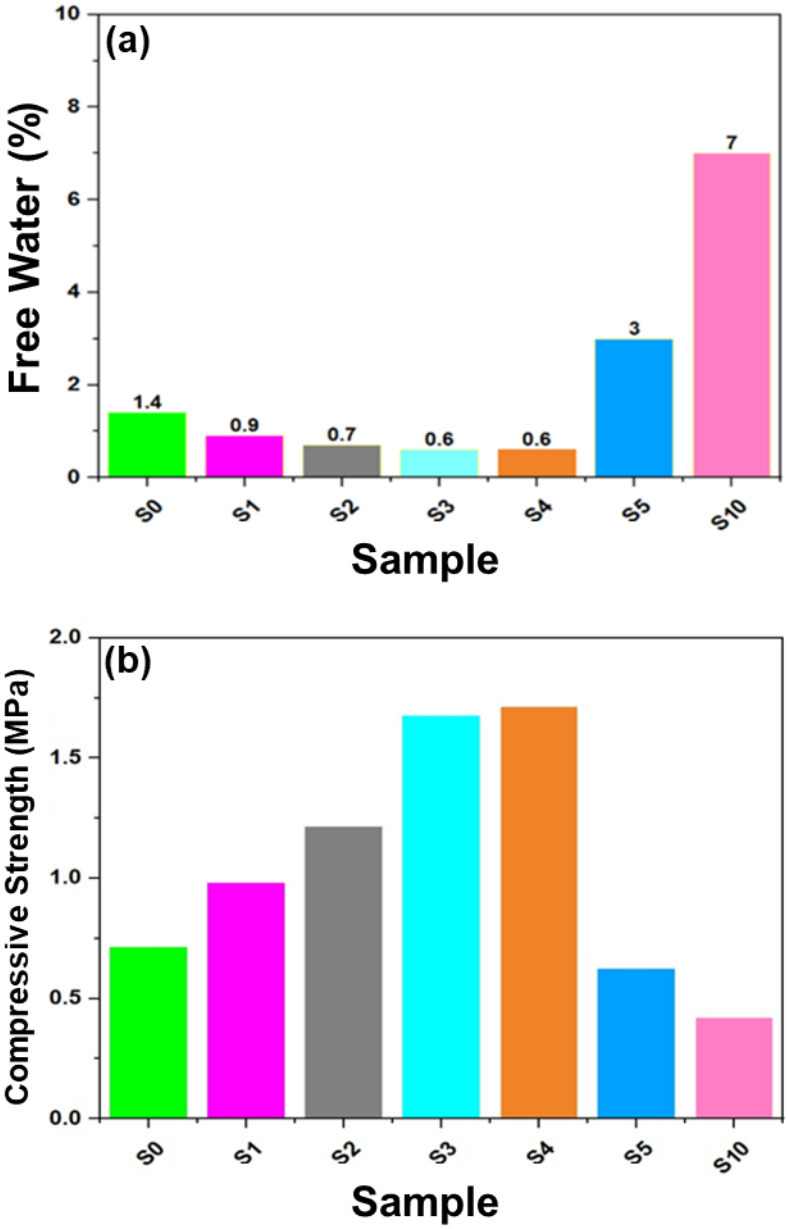

Fig. 7. Plots showing **(a)** Free water percentage **(b)** Compressive Strength of different samples.

increase in lime content up to 4% Fig 7(b). Thereafter, the compressive strength rapidly falls owing higher free water content.

4 Conclusion

This study highlights the effective utilization of Coal Fly Ash-F (CFA-F) from NTPC power station and hydrated lime (HL) for CO_2 sequestration through mineral carbonation, offering an eco-friendly solution to reduce CO_2 emissions while repurposing fly ash waste. The S4 composition, carbonated under specific pressures and agitation rates, achieved a peak compressive strength of approximately 1.7 MPa due to the synthesis of silicate hydrates and carbonates of calcium. Enhanced agitation and increased CO_2 injection pressure improved CO_2 sequestration (5.4%) and material strength, though no significant gains were observed beyond a pressure of 1.5 bar. This process provides a sustainable strategy for addressing CO_2 emissions and fly ash disposal challenges, offering a promising solution to environmental issues associated with thermal power plants.

Acknowledgments. The authors express their sincere gratitude to Executive Director (Mr.Shaswattam) NTPC Energy Technology & Research Alliance (NETRA) for providing the necessary facilities and support to carry out this research work. Special thanks are due to the laboratory and technical staff for their assistance in the experimental setup, CO_2 handling, and materials characterization. The authors also acknowledge the valuable discussions and guidance from colleagues in the field of carbon capture and utilization.

Disclosure of Interests. The authors declare that they have no competing interests relevant to the content of this article.

References:

[1] M.W. Jones, G.P. Peters, T. Gasser, R.M. Andrew, C. Schwingshackl, J. Gütschow, R.A. Houghton, P. Friedlingstein, J. Pongratz, C. Le Quéré, National contributions to climate change due to historical emissions of carbon dioxide, methane, and nitrous oxide since 1850, Sci. Data. 10 1–23(2023). https://doi.org/10.1038/s41597-023-02041-1.

[2] N. Singh, I. Farina, A. Petrillo, F. Colangelo, F. De Felice, Carbon capture, sequestration, and usage for clean and green environment: challenges and opportunities, Int. J. Sustain. Eng. 16 248–268(2023). https://doi.org/10.1080/19397038.2023.2256379.

[3] Neeraj, S. Yadav, Carbon storage by mineral carbonation and industrial applications of CO_2, Mater. Sci. Energy Technol. 3 494–500(2020. https://doi.org/10.1016/j.mset.2020.03.005.

[4] V.L.M. Molahid, F.M. Kusin, S.N.M.S. Hasan, N.A.A. Ramli, A.M. Abdullah, CO_2 Sequestration through Mineral Carbonation: Effect of Different Parameters on Carbonation of Fe-Rich Mine Waste Materials, Processes. 10 (2022). https://doi.org/10.3390/pr10020432.

[5] X. Yan, Y. Li, X. Ma, J. Zhao, Z. Wang, H. Liu, CO_2 capture by a novel CaO/MgO sorbent fabricated from industrial waste and dolomite under calcium looping conditions, New J. Chem. 43 5116–5125(2019). https://doi.org/10.1039/c8nj06257a.

[6] R. Liu, X. Wang, S. Gao, CO_2 capture and mineralization using carbide slag doped fly ash, Greenh. Gases Sci. Technol. 10 103–115(2020). https://doi.org/10.1002/ghg.1934.

[7] R. Roychand, J. Li, S. Kilmartin-Lynch, M. Saberian, J. Zhu, O. Youssf, T. Ngo, Carbon sequestration from waste and carbon dioxide mineralisation in concrete – A stronger, sustainable and eco-friendly solution to support circular economy, Constr. Build. Mater. 379 (2023). https://doi.org/10.1016/j.conbuildmat.2023.131221.

[8] L. pdf. Jiang, L. Cheng, Y. Zhang, G. Liu, J. Sun, A Review on CO_2 Sequestration via Mineralization of Coal Fly Ash, Energies. 16 (2023). https://doi.org/10.3390/en16176241.

[9] R. Shaw, S. Mukherjee, The development of carbon capture and storage (CCS) in India: A critical review, Carbon Capture Sci. Technol. 2 100036(2022). https://doi.org/10.1016/j.ccst.2022.100036.

[10] M.H. Fulekar, Disposal Of Fly Ash—An Environmental Problem, Int. J. Environ. Stud. 26 191–215(1986). https://doi.org/10.1080/00207238608710257.

[11] D.K. Nayak, P.P. Abhilash, R. Singh, R. Kumar, V. Kumar, Fly ash for sustainable construction: A review of fly ash concrete and its beneficial use case studies, Clean. Mater. 6 (2022). https://doi.org/10.1016/j.clema.2022.100143.

[12] W. Abbass, S.U. Mahmood, A. Ahmed, F. Aslam, A. Mohamed, Comparative analysis of enriched flyash based cement-sand compressed bricks under various curing regimes, Heliyon. 10 (2024) e26945. https://doi.org/10.1016/j.heliyon.2024.e26945.

[13] H. Liu, Conversion of Harmful Fly Ash Residue to Zeolites: Innovative Processes Focusing on Maximum Activation, Extraction, and Utilization of Aluminosilicate, ACS Omega. 7 20347–20356(2022).

https://doi.org/10.1021/acsomega.2c02388.

[14] C. Combustion, P. Management, Harvested Landfilled Fly Ash in Concrete : A Case Study, 2020 1–9(2021).

[15] G. Richhariya, D.T.K. Dora, N. Singhal, Synthesis of Ultralight Cement Using Solid Waste Fly Ash Cenosphere for Low-Fracture Gradient Formation with Reduced Shrinkage, J. Hazardous, Toxic, Radioact. Waste. (2021) 4021001. https://doi.org/10.1061/(asce)hz.2153-5515.0000587.

[16] G. Richhariya, T.K. Dora, P.P. Kundu, N. Singal, Y. Gupta, P. Singh, Impregnation of novel additives in cement for preventing fluid migration through the cement sheath in oil well, in: AIP Conf. Proc., 2019. https://doi.org/10.1063/1.5131611.

[17] A. Dindi, D.V. Quang, L.F. Vega, E. Nashef, M.R.M. Abu-Zahra, Applications of fly ash for CO_2 capture, utilization, and storage, J. CO_2 Util. 82–102(2019). https://doi.org/10.1016/j.jcou.2018.11.011.

[18] K.R. Senadeera, T.K. Jayasinghe, P.M. Jayasundara, G. Nanayakkara, M. Rathnayake, Investigation of CO_2Sequestration Possibility via Indirect Mineral Carbonation using Waste Coal Fly Ash, MERCon 2020 - 6th Int. Multidiscip. Moratuwa Eng. Res. Conf. Proc. 119–123(2020). https://doi.org/10.1109/MERCon50084.2020.9185202.

[19] Ji, L., & Yu, H. Carbon dioxide sequestration by direct mineralization of fly ash. In *Elsevier eBooks* (pp. 13–37) (2018). https://doi.org/10.1016/b978-0-08-102444-7.00002-2

[20] Ramachandran, P. A. Gas Absorption in Slurries Containing Fine Particles: Review of Models and Recent Advances. In Industrial & Engineering Chemistry Research (Vol. 46, Issue 10, pp. 3137–3152) (2007).

Failure Analysis of Spillway Gate of a Hydro Project - A Metallurgical Perspective

Deepak Kumar Gope, Anand D Varma, Anil Kumar Das, Prahlad Halder*

Advanced Materials Research Lab, NTPC Energy Technology Research Alliance, NTPC Ltd., Greater Noida, Uttar Pradesh, India.

*prahladhalder@ntpc.co.in

Abstract. The spillway gate plays a crucial role in ensuring the safety and structural integrity of a dam in any hydroelectric project, as it regulates the reservoir's water level to prevent it from exceeding its maximum capacity. Understanding the mechanism and causes of spillway gate failures is essential for enhancing their safety and improving reliability of the gate. The present case study investigates the analysis of a spillway gate failure of a hydropower plant in which the girder plate cracked in between the spindle support flanges. In-depth metallurgical analysis along with macro-study were carried out to identify the cause of failure and further preventive action plan was proposed. Microstructural analysis revealed that repair welding was carried out at the failed location which compromises the structural integrity of the component. The findings highlight the need to strengthen the quality assurance management and fabrication procedures for spillway gates to ensure their reliability and performance.

Keywords: Spillway gate, girder beam, microstructure, weld structure

1 Introduction

A spillway is a critical structure in a dam or reservoir designed to safely discharge excess water downstream during times of high inflow, such as during heavy rainfall or rapid snowmelt. The spillway ensures that the water level in the reservoir does not exceed its maximum capacity, thereby protecting the dam structure and preventing downstream flooding. A spillway gate is a mechanical structure installed on a spillway to control the flow of water released from a dam or reservoir [1–3]. It is a crucial structure on spillway for flood management, reservoir level control, and operational flexibility in hydropower and water management projects. It can be of different types depending on their construction and operation mode such as radial (Tainter) gate, vertical lift gate, flap gate, sliding gate, sector gate, rolling gate etc [4–6]. A flap gate on a spillway is a hinged gate designed to control the flow of water over a spillway crest. It is typically hinged at the bottom and operates by tilting backward or forward to regulate water discharge. Flap gates are commonly used in spillways where flexibility in flow control is required. They are particularly effective in low to medium head applications [6]. A key structural component of the flap gate is the girder beam, which plays a crucial role in bearing and distributing the substantial mechanical loads

S. Shaswattam et al. (eds.), *NTPC Transactions on Energy Research (NTER 2025)*,
https://doi.org/10.2991/978-94-6463-849-3_3

acting on the gate. It is a basically a primary horizontal support beam that spans over the entire length of the gate. To accommodate the spindle shaft, which facilitates the gate's movement, flanges were fabricated at both end of the front panel of the girder beam for support and alignment of the spindle shaft.

Failures of spillway gates have occurred worldwide due to various reasons. Failure of Folsom dam is a well-known example of spillway gate failure. The incident occurred in the year 1995 where the spillway gate failed due to fatigue cracking and corrosion [7–9]. Another incident occurred at Oroville dam at California in 2017. In this case the erosion of the main spillway takes place during high discharge [10]. Moreira et al. investigated the failure of piston rod in spillway floodgate. The piston was made up of AISI 410 steel which failed because of improper heat treatment leading to stress corrosion cracking [11]. In general, the common causes of spillway gate failure are material degradation, design inadequacies, operational error, inadequate maintenance and natural disasters [4,12,13]. In general, material degradation includes corrosion, fatigue or ageing of structural component whereas operational error includes delay in opening of gates or incorrect gate operation during emergencies. Inadequate maintenance indicates lack of regular inspection, repair of gate components, hinges, seals and hydraulic systems.

While these general failure modes are well-documented, however it was observed that there was limited literature available specifically addressing failures involving critical structural elements such as the girder beam particularly in flap gate designs. Notably, no published studies were found on the failure of the girder beam in flap gates. The present case study was taken from a hydropower project in which the girder beam plate between the spindle support flanges observed to be fractured. This fracture led to the failure of one of the spillway gates while other gates remained operational and did not result in any operational disruptions or casualties. This article presents a metallurgical failure analysis of the spillway gate of a hydropower project using visual observation, microstructural and mechanical analysis.

2 Methodology

2.1 Visual observation

Site visit was conducted to understand the failure, where it was observed that the failure had occurred on the spillway gate of a hydropower project. It has a chute type spillway consisting of six gates. The failure occurred in one of the spillway flap gates during operation. The flap gate suddenly fell down and became inoperative. Visual observation was carried out at failure site and on failed component and documented with several photographs which is shown in figure 1 and 2. The failure was observed in the girder plate between both the flange joint. The flange was taken from the site and cut using gas cutter into smaller parts for laboratory analysis which is shown in fig.2. One side of the girder plate has flange joint while the other side of the girder plate has shown weld spatters at the crack line.

2.2 Chemical composition

The chemical analysis was carried out using Optical Emission Spectrometry (OES) method (Make: M/s Thermofischer Scientific, ARL 3460). The analysis was performed at a flat location on the girder plate. Prior to the analysis, the sample surface was ground using emery paper to prepare a flat area with minimum dimensions of 12 × 12 mm².

2.3 Microstructural analysis and mechanical testing

For the microstructural study, small specimens were extracted from selected locations of the sample based on the area of interest using a precision abrasive cutting machine and proper precaution was taken to avoid heating of the sample as marked in Figure 2(f). All the selected specimens were then mounted ensuring proper edge retention for further metallography study purpose. The mounted specimens were subjected to multiple stages of grinding and polishing process to obtain a mirror-finish surface. The final stage of the polishing operation was carried out using a specific cloth suitable for 0.5–1 μm diamond paste. These metallographic specimens were examined under an optical microscope in both unetched and etched conditions to understand different microscopic features of the failed sample. Etching of the sample was performed using a 2% Nital solution. After the metallographic study, the molded samples were taken for microhardness measurement using a Vickers microhardness tester with a load of 0.5 kgf and a diamond indenter. The sample was prepared for tensile analysis from the region adjacent to the flange for mechanical tensile testing. The tensile specimen was prepared and tested as per the standard IS 1608:2005 [14].

3 Results and Discussion

3.1 Visual observation

During site visit it was observed that one of the spillway flap gates was fell down. Fig. 1(a) showed one of the operational spillway gates. It is to be noted that in the figure, it has two lifting spindles shaft (or lifting bracket) which support the girder beam of the gate. During flap gate operation, the flap gate suddenly fell down and went inoperative. The failed spillway gate was shown in fig 1(b). It showed the shearing of the front plate of girder beam in between lifting bracket shaft which is shown in fig. 1(c & d). At one end of the lifting bracket, the shaft was found detached, while at the other end, the front panel (or plate) of the girder beam was observed to be hanging. The thickness of the girder beam plate was 14 mm. The front panel of the beam failed in between flange area across the 400 mm width of the plate as can be seen from fig 2(a). The bottom part in between the flange was bend inward. The rear surface of the plate showed weld deposits on the fracture edge just below the top surface which was shown in fig 2(d). Keeping the crack part safe, the flange joints were cut using gas cutter for further analysis (fig. 2(c)). The samples for metallurgical sample were prepared as shown in the fig 2(f).

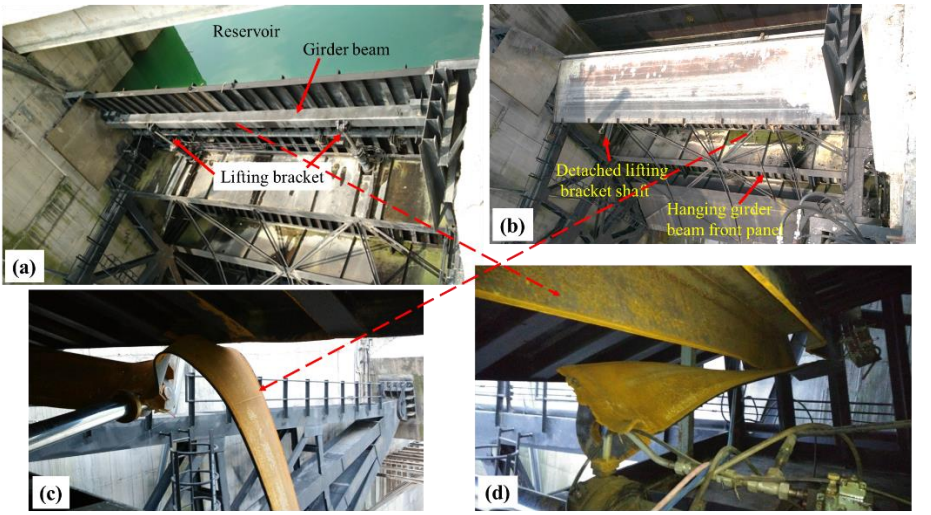

Fig. 1. (a) Image showed the operational spillway gate (spillway side view). It showed the normal condition of girder beam and lifting bracket with two spindles on both side of the gate; (b) Image showing the failed spillway gate. It showed detached lifting bracket shaft and hanging front panel of box beam (indicated by arrow); (c) Bending of front panel of girder beam at one side of the gate; (d) Other side of the gate showed failed flange part and tearing of front panel of girder beam.

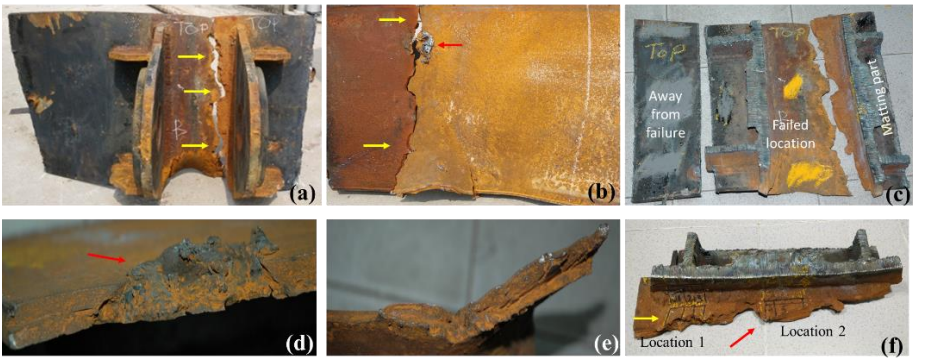

Fig. 2. (a) Image showed the crack in between the spindle support flange (marked in yellow arrow); (b) Rear side of the plate showed crack (marked in yellow arrow) and weld spatter (marked in red colour). It also showed bending at the bottom part; (c) The flange joint was cut for obtaining failure location: two matting parts of failure and one away from failure; (d) Fracture edge at mid-section showed blacking appearance weld material deposit; (e) Fracture edge at bottom side showed weld spatter; (f) Image showed the marking for metallurgical sample.

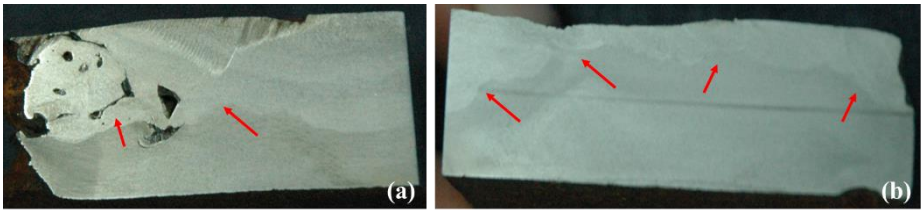

Fig. 3. (a) Cross-sectional view of polished surface at failed location shows metal deposit and weld porosity; (b) Cross-sectional view of the tube shows multiple welded structure.

3.2 Chemical composition

The chemical composition of the plate was carried out using Optical Emission Spectrometry (OES) method, was presented in table 1. The chemical composition of the plate conformed to be IS 2062 E410 (Fe540) Grade material. Here, CE in the table stands for carbon equivalent.

3.3 Microstructural analysis and Mechanical testing

Microstructural analysis was carried out at different locations as marked in fig. 2f. The macrostructure at fracture edge showed presence of weld porosity, multiple weld layers and inhomogeneity (fig 3a). Furthermore, a weld structure with varying layer thicknesses was observed on the surface of the plate. Weld build up was also observed in all the samples along the fracture edge as shown in fig. 3b. Thick oxide scale at the fracture edge was also observed.

Microstructure at fracture edge on flange side and rear side of girder plate showed welded structure (fig. 4 (a, b & d)) which indicated that a repair welding was carried out at that location. Repair welding is very critical part of operation and maintenance. If it is not done in proper way, it led to catastrophic failure of the component [15,16]. It also showed weld porosity with range varies from 0.8 mm to 1.25 mm. Magnified view (fig. 4c) showed the oxide scale penetration in to the material at fracture edge. Microstructure at mid thickness of the plate showed ferrite-pearlite structure. Microstructure at location 2 (fig. 5) showed sever inclusions in the material at fracture edge. Inclusion was also observed at the weld structure at flange side. The mid-section of the plate showed ferrite-pearlite structure.

Table 1. Details of the sample taken for case study

Steel grade	C	Si	Mn	S	P	CE
E410 (Fe 540) grade As per IS 2062:20	0.20 max	0.45 max	1.50 max	0.045 max	0.045 max	0.44 max
Analyzed (base metal)	0.17	0.31	1.45	0.043	0.027	0.41

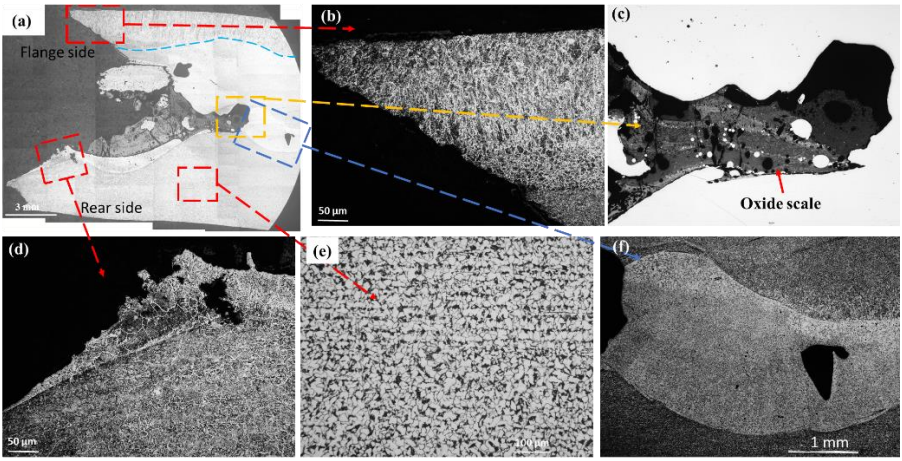

Fig. 4. (a) Microstructure showed weld structure and thick oxide scale; (b) Magnified view of the marked location indicated the weld structure (etched condition); (c) Magnified view at centre area showed oxide scale penetration (unetched condition); (d) Microstructure at rear side also showed weld structure with weld porosity (etched condition); (e) Microstructure at mid-section showed ferrite-pearlite structure (etched condition); (f) Microstructure at marked location showed weld porosity (etched condition).

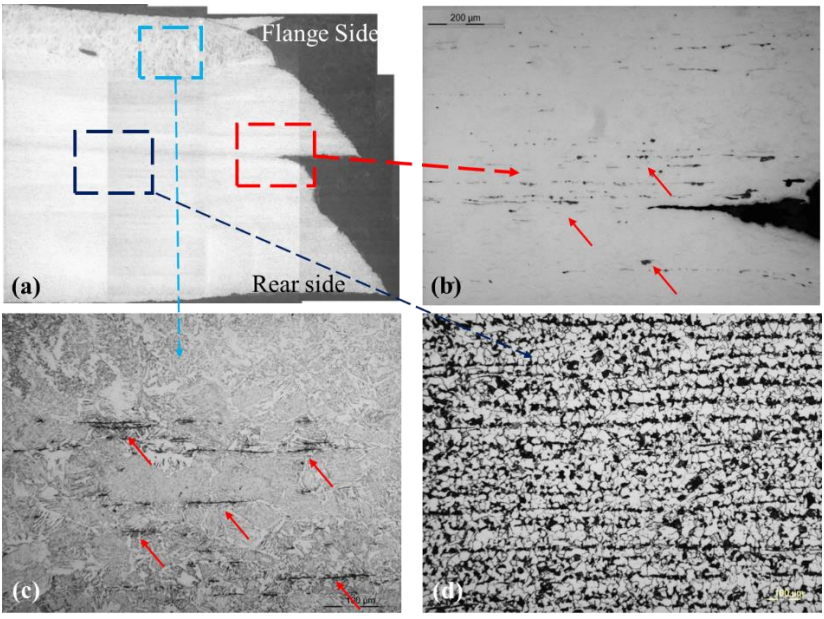

Fig. 5. (a) Microstructure at location 2 showed different structure at different location (unetched condition); (b) Microstructure in unetched condition showed inclusion at fracture edge; (c)

Microstructure at flange side showed weld structure and inclusion (etched condition); (d) Microstructure at mid-section of the plate in etched condition showed ferrite-pearlite structure.

The hardness of the sample at fracture edge having weld structure side was in the range of 269 – 280 HV0.5 while the hardness away from failure was in the range of 228 – 236 HV0.5 which is in accordance with the observed microstructure. The yield strength and ultimate tensile strength obtained from the tensile test are 468.2 MPa and 572 MPa respectively.

4 Conclusion

The failure analysis of the spillway flap gate sample was conducted through visual inspection, chemical analysis, microstructural examination, and mechanical testing. The conclusions drawn from the study are as follow:

- Chemical analysis showed that the material grade conformed to specified grade (E410 (Fe 540), IS 2062:20.
- Tensile analysis confirmed that the base material met the required strength as per the grade specifications.
- Microstructural study at the fracture edge showed evidence of weld deposits, inclusions, weld porosity, oxide scale, and multiple weld layers.
- These findings inferred that repair welding was carried out at the failure location and the quality of repair welding was not maintained properly. The weld repair procedure compromised the structural integrity of the component under operational load conditions.
- It is recommended to use new material as per the specification and avoid repair welding on structural members at load-bearing location to ensure reliability and safety of the components while operation.

Acknowledgments. Authors would like to express their gratitude to the Executive Director of NTPC NETRA for his motivation for writing this paper. Authors are also thankful to Dr. Y Ravi Kumar, Ex-AGM, NETRA for his guidance during the analysis. This work was not supported by any funding agency.

Disclosure of Interests. The authors declare that they have no conflicts of interest to disclose regarding the research presented in this manuscript.

References

[1] D.S. Bowles, J. Lewin, G. Ballard, Spillway gate reliability in the context of overall dam failure risk HEC lifesm model development View project, 2003. https://www.researchgate.net/publication/247622344.

[2] A. Nayak, A. Srivastav, M. Aggarwal, Ensuring Safe and Reliable Performance of Earth and Rock-Fill Dam of Koldam HEPP through Instrumentation, 2016. https://www.researchgate.net/publication/289344776.

[3] D.R. Przemyslaw, Risk Analysis in dam safety: The past, the present and the future, in: ICOLD Symposium on Sustainable Development of Dams and River Basins, 2021.

[4] G. Paxson, R. Indri, M. Landis, Addressing operational risks and uncertainties for gated spillways, 2015.

[5] BIC China, Working of Different Spillway Gates, (2005). https://www.bic-iwhr.com/news/how-do-different-spillway-gates-work.html (accessed January 21, 2025).

[6] Vortex Hydra, Custom Made Hydromechanical Equipment - Vortex Hydra Dams, (n.d.). https://www.vortexhydradams.com/vortex-hydra-dams-products/custom-made-hydromechanical-equipment/ (accessed January 24, 2025).

[7] K. Anami, N. Ishii, C.W. Knisely, T. Oku, Hydrodynamic pressure load on folsom dam tainter-gate at onset of failure due to flow-induced vibrations, Proceedings of the ASME 2005 Pressure Vessels and Piping Conference. Volume 4: Fluid Structure Interaction 4 (2008) 557–564. https://doi.org/https://doi.org/10.1115/PVP2005-71444.

[8] J. Salamon, USSD 2016 Annual Conference 1 Lessons learned from the spillway gate failure at Folsom dam, 2017.

[9] N. Ishii, K. Anami, C.W. Knisely, Retrospective consideration of a plausible vibration mechanism for the failure of the folsom dam tainter gate, 2014. www.ijmerr.com.

[10] A. Koskinas, A. Tegos, P. Tsira, P. Dimitriadis, T. Iliopoulou, P. Papanicolaou, D. Koutsoyiannis, T. Williamson, Insights into the Oroville dam 2017 Spillway incident, Geosciences (Switzerland) 9 (2019). https://doi.org/10.3390/geosciences9010037.

[11] D.C. Moreira, H.C. Furtado, J.S. Buarque, B.R. Cardoso, B. Merlin, D.D.C. Moreira, Failure analysis of AISI 410 stainless-steel piston rod in spillway floodgate, Eng Fail Anal 97 (2019) 506–517. https://doi.org/10.1016/j.engfailanal.2019.01.035.

[12] C. Xu, Z. Wang, H. Zhang, H. Li, D. Li, Investigation on mode-coupling parametric vibrations and instability of spillway radial gates under hydrodynamic excitation, Appl Math Model 106 (2022) 715–741. https://doi.org/https://doi.org/10.1016/j.apm.2022.02.013.

[13] J. Salamon, USSD 2016 Annual Conference 1 Lessons learned from the spillway gate failure at Folsom dam, 2017.

[14] Bureau of Indian Standards, IS 1608 (2005): Mechanical testing of metals - Tensile Testing, 2008.

[15] B.A. Miller, R.O. Taylor, P.D. Swartzentruber, B.P. Kelly, Failure of Steel Shafts Due to Improper Repair Welding, Journal of Failure Analysis and Prevention 23 (2023) 894–909. https://doi.org/10.1007/s11668-023-01629-4.

[16] D.J. Thomas, Weld Repair and the Importance of Analyzing Failure Mode, Journal of Failure Analysis and Prevention 16 (2016) 179–180. https://doi.org/10.1007/s11668-016-0086-1.

Failure Investigation of Boiler Tubes Failed Due to Thermal Fatigue and Corrosion Fatigue

Aditya Gokhale, Deepak Kumar Gope, Prahlad Halder, Anil Kumar Das, Anand D Varma*

Advanced Materials Research Lab, NTPC Energy Technology Research Alliance, NTPC Ltd., Greater Noida, Uttar Pradesh, India.
anandvarma@ntpc.co.in

Abstract. Flexible operations cause base load fluctuations in the power demand affecting the boiler operation. Failure due to thermal fatigue occurs for components subjected to cyclic load fluctuations. These fluctuations can be of mechanical or thermal nature. Corrosion fatigue is a special case of thermal fatigue wherein the damage is accentuated because of the action of corrosion occurring on the internal surface of the tube. In the present failure investigation, three different tubes were investigated viz., two water wall tubes and one economizer tube. The water wall tubes failed due to thermal fatigue, despite experiencing corrosive environment. Whereas, the economizer tube experienced corrosion fatigue environment. The investigation also points out that although, corrosion fatigue is a sub-set of thermal fatigue, it is necessarily not true that the tube should also experience overheating conditions.

Keywords: Thermal fatigue, corrosion fatigue, Ferrite, Pearlite.

1. Introduction

The coal fired power plant is the main backbone of India's power sector with an estimated share of close to 71% [1]. However, with recent emission norms and climatic challenges the renewable sector needs a big and immediate boost. The phasing out of old power plants, erratic supply nature of renewable power and the necessity to sustain the grid requirements puts pressure on all the available sources of power generation. Factors like wind, sunlight and climatic changes can cause erratic and unpredictable power generation from the renewables; this calls for flexible operation of power plants. The coal-fired boilers were designed for base-load operation with an operational timeline of close to 25 years. This results in selecting boiler materials which have better high-temperature creep performance capable of withstanding temperatures for longer time. However, flexible operation leads to thermal load fluctuations in boiler, which calls for materials that can withstand fluctuating loads and different temperatures. Although, fatigue and creep are design considerations, but these factors are considered

S. Shaswattam et al. (eds.), *NTPC Transactions on Energy Research (NTER 2025)*,
https://doi.org/10.2991/978-94-6463-849-3_4

for base load, general loads and unsteady temperature and pressure changes, boiler shut-downs and start-ups. However, due to the flexible operations, fatigue failure is also, now, becoming a harsh reality.

Boiler water walls are generally composed of SA-210 GrA/C and SA-213 T-22 grade materials [2,3]. These materials have high creep strength and high corrosion resistance. During operation the boiler is hot with the metal temperatures going as high as 700°C near the metal surface. Failure analysis by some authors have shown fatigue to be the primary cause. Failure analysis by Ahmad et.al.,[4] of a SA-210 A1 grade material showed that the wall side tubes failed due to a combination of thermal fatigue, corrosion fatigue and creep damage. Arora et.al., [5] investigated fatigue in carbon steel tubes under multiaxial loading. Azevedo et.al.,[6] investigated failure in a heat exchanger serpentine belonging to a vertical heat exchanger. The steel serpentine was made up of ASTM A 178 Grade A. The material failed just 2 years in service and the microstructure analysis showed wedge type cracks and de-carburization. Himarosa et.al., [7] conducted failure root cause analysis on platen-superheater and water confirmed that the crack propagation was under the influence of cyclic loading. Smith et.al., [8] conducted failure analysis for 0.5Cr-0.5Mo and 2.25Cr-1Mo boiler tubes. Circumferentially aligned cracks were observed which initiated due to sulfidation/thermal fatigue interactions. Crack tip corrosion assists crack growth.

Secondary reasons like stress concentration, incorrect material application and prior defects can also accelerate fatigue failure. Ghosh et.al., [9] investigated failure in a boiler water wall. It was found that unstable fluid flow in the water wall can lead to vibrational fatigue due to hammering effect. These fluctuations in load coupled be already present welding defect can cause fatigue failure.

The present manuscript investigates the failures in water wall and economiser tubes composed of SA210-GrA/C and SA213 T-22 grade of material. The SA210-GrA/C tube material was obtained from a 200 MW and 500 MW power plant and SA213 T-22 tube material was obtained from a 800 MW power plant. The investigation aims to bring out the various fatigue and corrosion fatigue damage mechanisms which caused failure.

2. Methodology

2.1 Chemical composition

Chemical composition was determined using an Optical Emission Spectrometer. An average of 5 sparks per sample is presented in Table 1.

2.2 Microstructural characterization

The failed tubes were first visually examined and then appropriate regions were selected for sectioning. Other regions of interest were also selected. Sectioned tube samples were mounted using a Buehler hot press mount with Bakelite moulding. This

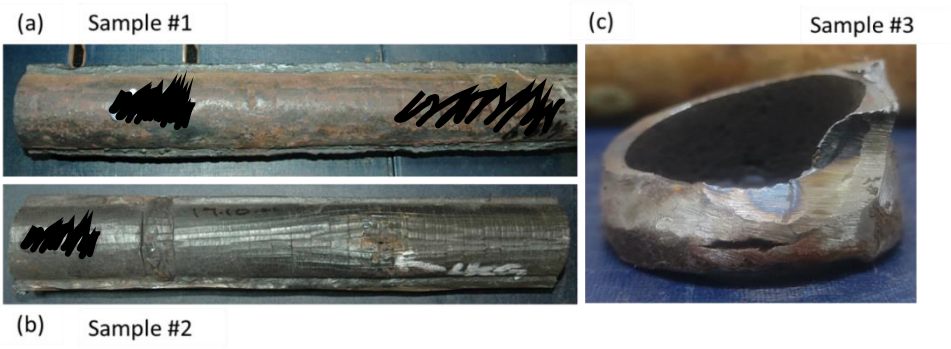

Fig. 1. Photograph of the as received failed tubes. (a) – (b) Water Wall tube (c) The stub of economiser tube connecting the header. Note: This belongs to the stub hence cutting was difficult.

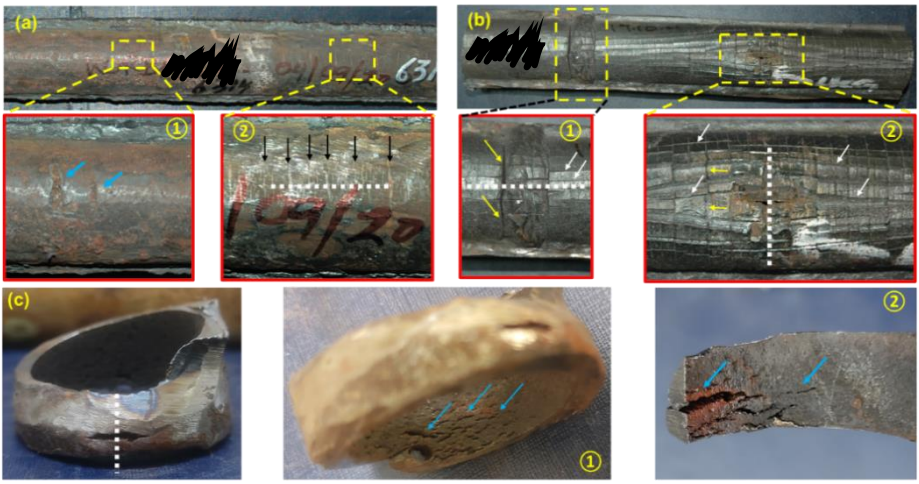

Fig. 2. Photographs of the as received failed tube showing different macro features (a) Sample#1: Water wall showing circumferentially aligned micro cracks, indicated by black arrows (b) Sample#2: Water Wall tube showing circumferentially longitudinally aligned cracks, indicated by yellow arrows and white arrows respectively. (c) Sample #3: The stub of economiser tube connecting the header. Internal surface showing numerous fissures, indicated by blue arrows. The white dotted line shows the sectioning plane for metallographic examination.

was followed by polishing on a diamond disc and SiC paper. Cloth polishing using 9 μm and 3 μm diamond slurries were employed. De-ionized water (DI) was used as a coolant and lubricant. A final polishing step using colloidal silica (particle size 0.01 μm) was employed to obtain a mirror finish. The mounted samples were cleaned in an ultrasonic cleaner with ethanol as cleaning medium. The samples were rinsed with

ethanol. The microstructure before and after etching was obtained using Leica DMi8 inverted microscope. To reveal the microconstituents, etching was performed in 2% Nital (2 ml HNO_3 in 98 ml ethanol). Hardness tests were carried using Tinius Olsen Vickers Hardness (500 gf - 12 seconds dwell time), using a diamond Vickers indenter.

2.3 Visual examination

Visual examination was carried using unaided eye. A Nikon D70S digital single – lens reflex camera was used to obtain photographs of the tubes.

3. Results

Photographs of the as received failed tubes is shown in Figure 1. The chemical composition of the three samples is presented in Table 1. Sample #1 and #2 are water wall tubes conforming to SA 210-GrA and SA 213 – T22. Sample #3 is an economiser tube conforming to SA210 – GrA. The tubes showed numerous damage features. Figure 2 shows the magnified view of the different features observed on the three samples through naked eyes. Sample #1 showed no failure however it showed a dent, shown in Figure 2 (a) ① and numerous circumferential lines or serrations, shown in Figure 2 (a) ②, on the external surface. Sample #2 showed a puncture type failure, shown in Figure 2 (b) ②. Sample #2 also showed longitudinal and circumferential cracks on the external surface. Sample #3 was the region near the stub weld and there was a problem accessing and cutting the sample for analysis; as a result, a ring was sent for analysis. Severe grinding marks can be seen in Figure 1 (c).

Metallographic examination revealed the damage mechanisms. Microstructural examination of Sample #1 showed sharp notches originating from the external surface, as shown in Figure 3. The notches had a very sharp tip with thickness ~0.04 mm. The external surface also showed de-carburization, with hardness ~147 HV0.5. Sample #2

	Elements (wt. %)						
Sample	**C%**	**Si%**	**Mn%**	**S%**	**P%**	**Cr%**	**Mo%**
Sample #1	0.29 ±0.003	0.27 ±0.0025	0.81 ±0.003	0.024 ± 0.001	0.016 ± 0.001	-	-
SA 210 – Gr A	0.35 Max	0.1 Min	0.29 – 1.06	0.035 Max	0.035 Max	-	-
Sample #2	0.0816 ±0.003	0.19 ±0.002	0.44 ±0.001	0.003 ± 0.0001	0.0012 ± 0.0001	2.43 ± 0.001	0.93 ± 0.002
SA213 T22	0.05 – 0.15	0.5 Max	0.3 –0.60	0.025 Max	0.025 Max	1.90 – 2.60	0.87 – 1.13
Sample #3	0.12 ± 0.002	0.20 ± 0.002	0.55 ±0.002	0.017 ±0.0002	0.014 ±0.0003	-	-
SA 210 – Gr A	0.35 Max	0.1 Min	0.29 – 1.06	0.035 Max	0.035 Max	-	-

showed both longitudinal and circumferential cracks, as seen in Figure 1 (b). Microstructural examination of Sample #2, near the puncture failed region, showed extensive thinning, as seen in Figure 4 (a). The failed edge showed numerous elongated voids (Figure 4 (b) & (c)). External surface showed marginal decarburized layer and small notches originating from the external surface. Closer examination of these notches revealed that oxidation progressed on the grain boundaries (shown in Figure 4 (f)). The microstructure showed extensive degradation with a considerable loss in the hardness wherein the hardness was 124 ±7 HV0.5. The circumferential cracks were observed originating from the external surface and travelling along the heat affected zone (HAZ) of the weld, as seen in Figure 5. Voids were also observed in the weld bead region (shown in Figure 5 ②). Hardness profile around the weld, base metal and HAZ showed a considerable drop in hardness. The hardness for this material is around 170 – 180 HV 0.5 [10]. However, in the present case the hardness has dropped to approximately 130 HV 0.5.

The economiser stub tube was received in a poor condition. The internal surface, shown in Figure 6, showed numerous fissures, indicated by magenta arrows. Some of the fissures have combined to form a large crack, indicated by red arrow. As opposed to the fatigue failure, the cracks in this sample originated from the internal surface, as shown in Figure 6 (b) – (d). Corrosion pits were evident and the corrosion also proceeded laterally (seen in Figure 6 (e)). It can be observed that the notches are originating from the internal surface and do not bear a sharp tip but rather a blunt bulbous head. This is a sign of prevailing corrosion activity. The hardness was in the range 147 – 150 HV0.5.

4. Discussion

The introduction of renewable power to tackle climate change has changed the energy production scenario. However, the dependence of renewables on sun, wind and water makes the dispatch of electricity erratic. This leads to erratic demands on coal fired power plants thereby calling a need for flexible operations which leads to erratic pressure and temperature fluctuations in the boiler [11]. A boiler is designed for baseload operations, some start-up and shut-down cycle along with special emphasis on long term properties such as creep. The effect of cyclic thermal stresses is similar to that induced by fluctuating or cyclic mechanical stresses. It may also occur in the regions where turbulent mixing of the fluids leads to rapid thermal transitions. All these factors are leading to fatigue failures in boiler tubes and headers. Besides temperatures there are other factors as well which contribute to the fatigue cracking. Some of the factors, and not limited to, are header expansion, piping loads, moment restraints and stub welds where header tubes are joined. Shibli et.al., [12] have discussed the plant and research experience in P-91 Martensitic Steel. The ability of low thickness components to reach thermal equilibrium is faster. Thus, higher strength steel grades like P-91, offers the potential to make thin-walled tubes. However, weld failures under

creep-fatigue interactions leading to Type-IV cracking was observed under simulated and service conditions. The $M_{23}C_6$ types of precipitates and Laves phase form faster in the fine grain HAZ region of 9Cr martensitic steels making them prone to cracking [11]. Azevedo et.al., [6] investigated the failure in an ASTM A 178 Grade A serpentine of a heat exchanger and concluded that cracking, leading to eventual failure, was due to thermal cycling. Cracks perpendicular to tube axis (i.e. transverse cracking) was observed on the external surface of the tube and same was observed in the microstructure. Figure 2 (a) and (b), shows the SA 210 - Gr.A and SA 213- T-22 water wall tubes wherein the transverse cracking is clearly evident. Microstructural examination also showed cracks originating from the external surface. Figure 3 shows the microstructure for Sample #1. It can be seen that the sharp notches originate from the external surface. Figure 3 (b) and (e) shows the sharp notches. One of the notches has almost consumed the entire thickness of the tube (Figure 3 (b)). The sharpness of the notch can be attributed to the frequency of fluctuation [13]; the higher the frequency of fluctuation the sharper the notch and a thinner base and vice-versa. The presence of de-carburization layer, shown in Figure 3 (c), is also evidence of the tube experiencing overheated conditions. Sample #2 showed a puncture type failure, transverse and longitudinal cracking, shown in Figure 2 (b). Longitudinal type cracking is a sign of short-term or long-term overheating failure; however, transverse type of cracking is a sign of thermal-fatigue failure [14]. Microstructural examination near the puncture failure showed presence of elongated creep voids; creep is a sign of long-term overheating. The presence of a decarburized layer, shown in Figure 4 (c), and the degraded microstructure, shown in Figure 4 (f), are signs of overheating. Fatigue crack propagation is from the external surface. Figure 4 (d) shows the cracking in the external surface and penetrating the tube metal. The near tip region of the crack tip, shown in Figure 4 (e), shows that the oxide filled crack propagation occurs on grain boundary (as indicated by black arrows in Figure 4 (e)). Vetriselvan et.al., [15] investigated thermal fatigue in T-91. They observed that in an unconstrained T91 tube crack initiation on the ID side of the tube was observed after 5000 cycles. Shibli et.al., [12] also pointed out, although debatable, that thicker components, under cycling duty, are more likely to fail than in base load plant.

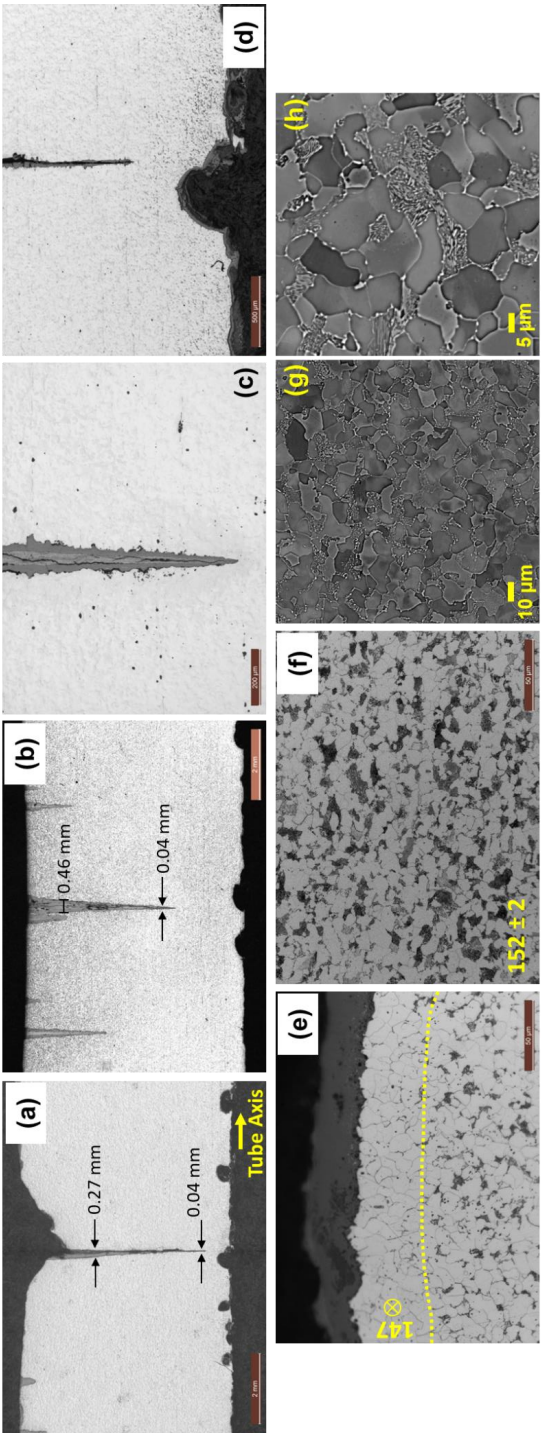

Fig. 3. Sample #1. (a) Longitudinal cross section **showing** the wedge type feature. (b) The wedge feature has almost consumed the entire thickness of the tube. (c) De-carburization can be observed on the external surface, demarcated by yellow dotted line. (d) Longitudinal cross section of the tube showing multiple wedge features. (e) The circumferentially aligned wedges are oxide filled with sharp tips. (f) Optical image showing the Ferrite-Pearlite microstructure. The numbers indicate the Vickers hardness at that particular location.

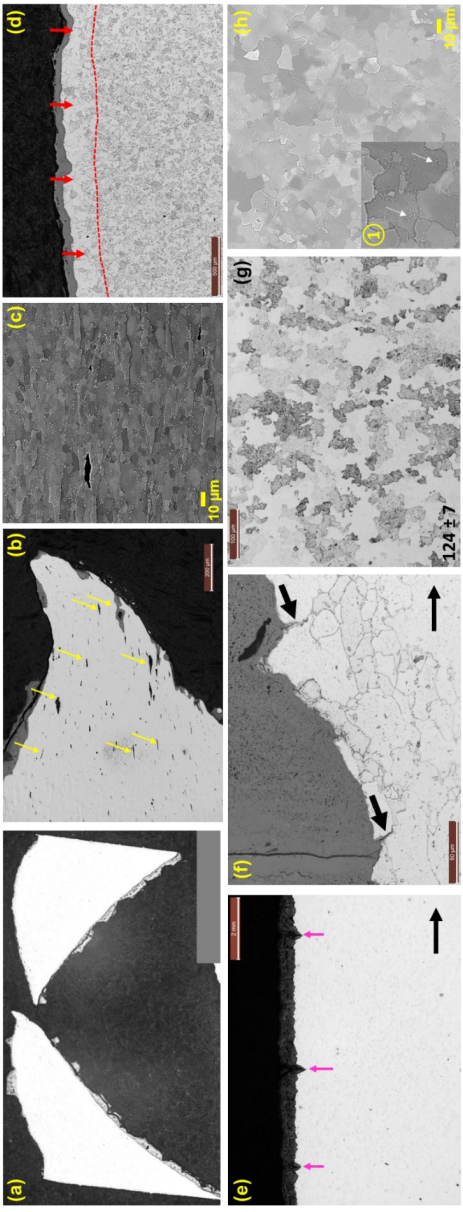

Fig. 4. Sample #2. (a) Circular cross section showing the failed edge. (b) Magnified image of the failed edge. The wedge feature has almost consumed the entire thickness of the tube. (c) De-carburization can be observed on the external surface, demarcated by yellow dotted line. (d) Longitudinal cross section of the tube showing multiple wedge features. (e) The circumferentially aligned wedges are oxide filled with sharp tips. (f) Optical image showing the Ferrite-Pearlite microstructure.

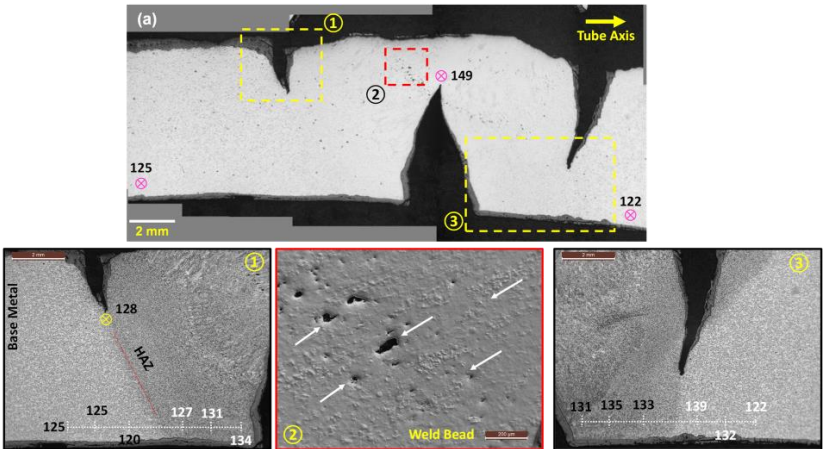

Fig. 5. Sample #2. (a) Microstructure of the welded region showing the cracks. Note that these cracks are wider than the ones observed in sample #1. ① and ③ shows the cracks initiating from the external surface along the HAZ. ② Shows the weld bead region with numerous creep voids in the weld bead region. The numbers indicate the hardness.

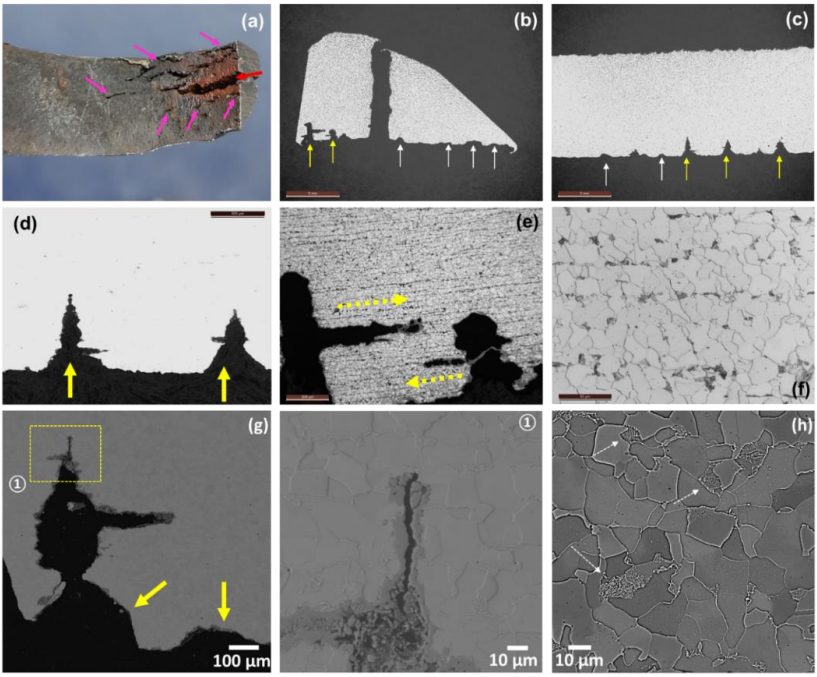

Fig. 6. Sample #3. (a) Photograph of the internal surface of the weld stub region showing numerous fissures, indicated by magenta arrows, and the large crack, indicated by red arrow. (b) – (d) Microstructure of the failed region showing the corrosion pits, indicated by white arrows, and the corrosion fatigue cracks, indicated by yellow arrows. (e) Microstructure near the corrosion fatigue crack showing the lateral corrosion attack. (d) Microstructure showing healthy Ferrite-Pearlite.

Corrosion fatigue is fatigue in corrosive environment. The fatigue cracks originate from the internal surface as pitting due to corrosion makes these site vulnerable for crack initiation. Ahmad et.al., investigated failure in SA 210-A1 grade tube. It was observed that the internal surface showed evidence of corrosion on the internal side of the tube. Transgranular cracks were found to originate from the internal surface of the tube with the origins tracing back to the base of the corrosion pit. Ahmad et.al., [16] concluded that one of the tubes failed due to corrosion fatigue and also interplay of thermal fatigue and creep-fatigue interaction. Corrosion fatigue is usually catastrophic and calls for an immediate shutdown due to failure. Generally, corrosion fatigue initiates from the internal side in water wall tubes and appears as multiple fissures on the internal side, which are visible through naked eyes; these fissures combine to form a larger crack [17][18]. In the present case the internal surface of the failed tube showed extensive fissures and cracking, shown in Figure 6 (a). Metallographic examination revealed that the internal surface showed corrosion pits, shown in Figure 6 (b) and (c). Notches originating from the internal surface were also observed, as shown in Figure 6 (d) and (e). The optical image, shown in Figure 6 (f), shows a Ferrite-Pearlite microstructure. The cracks are originating from the internal surface of the tube. Unlike the thermal fatigue cracks, as shown in Figure 3, these cracks have a wider base and circular or bulbous head unlike sharp tips of their thermal fatigue cracks counterparts. Furthermore, the evidence of corrosion is clear wherein it not only progresses inwards but also sideways (as seen in Figure 6 (e)).

5. Conclusion

The present failure investigation encompasses and brings out the differences between thermal fatigue and corrosion fatigue in boiler tubes.

i. In thermal fatigue, the presence of sharp oxide filled notches originating from the external surface is a clear indication of the tube experiencing the thermal fatigue conditions.
ii. Notches from internal surface are also indicators of thermal fatigue but they differ from the ones observed in corrosion fatigue.
iii. In corrosion fatigue notches from the internal surface bear bulbous tip with no/negligible loss in tube metal hardness.
iv. Evidence of metal loss from the internal (fluid) side along with sharp notches and combination of both is a good indicator of corrosion fatigue.
v. Due to thermal fluctuations, there is a degradation of microstructure in the case of thermal fatigue, but in corrosion fatigue the degradation is not that evident.

Acknowledgement

The authors are thankful to Sh. Arun Sharma for assisting in sample preparation. The authors are also thankful to Sh. Shaswattam for his words of encouragement. Overall infrastructure support by NTPC Ltd., is also acknowledged.

Disclosure of Interests. The authors declare that they have no conflicts of interest to disclose regarding the research presented in this manuscript.

References

[1] Govt. of India, Ministry of Coal, Generation of Thermal Power from Raw Coal, (n.d.).

[2] ASTM, Standard Specification for Seamless Medium-Carbon Steel Boiler and Superheater Tubes, in: ASTM A210/A210M-19, 2019: p. 03.

[3] ASTM, Standard Specification for Seamless Ferritic and Austenitic Alloy-Steel Boiler, Superheater, and Heat-Exchanger Tubes, in: ASTM A213/A213M-22a, 2023: pp. 15–30.

[4] S.R. Ahmed, L.A. Agarwal, B.S.S. Daniel, Effect of Different Post Weld Heat Treatments on the Mechanical properties of Cr-Mo Boiler Steel Welded with SMAW Process, Mater Today Proc 2 (2015) 1059–1066. https://doi.org/10.1016/j.matpr.2015.07.002.

[5] P. Arora, S.K. Gupta, R.K. Singh, S. Sivaprasad, FATIGUE STUDIES ON CARBON STEEL TUBES UNDER MULTIAXIAL LOADING, 2015. https://www.researchgate.net/publication/281372112.

[6] C.R.F. Azevedo, G.S. Alves, Failure analysis of a heat-exchanger serpentine, Eng Fail Anal 12 (2005) 193–200. https://doi.org/10.1016/j.engfailanal.2004.07.001.

[7] R. Adi Himarosa, S. Dini Hariyanto, W. Hozaifa Hasan, M. Akhsin Muflikhun, Failure analysis of platen superheater tube, water wall tube, and sealpot plate: A case study from electricity power plant in indonesia, Eng Fail Anal 135 (2022). https://doi.org/10.1016/j.engfailanal.2022.106108.

[8] B.J. Smith, A.R. Marder, A Metallurgical Mechanism for Corrosion-Fatigue (Circumferential) Crack Initiation and Propagation in Cr-Mo Boiler Tube Steels, n.d.

[9] D. Ghosh, H. Roy, C. Subramanian, Metallurgical Failure Investigation of Premature Failed Platen Water Wall Tube in a Thermal Power Plant Boiler, Journal of Failure Analysis and Prevention 21 (2021) 733–737. https://doi.org/10.1007/s11668-021-01137-3.

[10] A.S. for T. and Materials, A213/A213M-18: Standard Specification for Seamless Ferritic and Austenitic Alloy-Steel Boiler, Superheater , and Heat-Exchanger Tubes, ASTM International i (2018).

[11] J. Heo, M. Park, J.M. Kim, D.W. Jang, J.H. Han, Effect of Flexible Operation on Residual Life of High-Temperature Components of Power Plants, Processes 11 (2023). https://doi.org/10.3390/pr11061679.

[12] A. Shibli, F. Starr, Some aspects of plant and research experience in the use of new high strength martensitic steel P91, International Journal of Pressure Vessels and Piping 84 (2007) 114–122. https://doi.org/10.1016/j.ijpvp.2006.11.002.

[13] James J Dillon, Paul B Desch, Tammy S Lai, The Nalco Guided to Boiler Failure Analysis, second edition, 2011.

[14] J. Dillon, P. Desch, T. Lai, D. Flynn, The Nalco Guide to Boiler Failure Analysis, Second Edition, The McGraw-Hill Companies, 2011.

[15] R. Vetriselvan, P. Sathiya, G. Ravichandran, Experimental and numerical investigation on thermal fatigue behaviour of 9Cr 1Mo steel tubes, Eng Fail Anal 84 (2018) 139–150. https://doi.org/10.1016/j.engfailanal.2017.11.005.

[16] J. Ahmad, J. Purbolaksono, L.C. Beng, Thermal fatigue and corrosion fatigue in heat recovery area wall side tubes, Eng Fail Anal 17 (2010) 334–343. https://doi.org/10.1016/j.engfailanal.2009.06.014.

[17] Testex, Corrosion Fatigue Cracking Paper, (n.d.).

[18] Materials R-Tech, EpicFail – Corrosion Fatigue, (n.d.).

Visual Appearance of Waterwall Tube Failures Due to Hydrogen Damage Mechanism in Coal Fired Power Plants

Deepak Kumar Gope, Anil Kumar Das, Prahlad Halder*

Advanced Materials Research Lab, NTPC Energy Technology Research Alliance, NTPC Ltd., Greater Noida, Uttar Pradesh, India.

*prahladhalder@ntpc.co.in

Abstract

Failures of boiler tubes in coal fired power plant are due to unforeseen reasons are a major concern to power engineers. Out of different failure mechanisms, hydrogen damage is one of the corrosion related mechanisms assisted by high temperature that occurs predominantly in water wall tubes of the subcritical boiler. The general physical appearance of a water wall tube failure on account of Hydrogen Damage is "Window Opening". This paper highlights two other distinct failure appearances associated with hydrogen damage, and their appearance exhibits as "Slit Type" and "Puncture type" opening. It is also observed that hydrogen damage may occur both in relatively new units with only a few years of services and in older plants. Micro-fissures observation in optical microscopy is one of its key assertive features. The study also showed that the failure was intergranular in nature. Based on the evidences, it was observed that the failure was high temperature hydrogen induced under deposit corrosion in nature.

Keywords: Hydrogen damage, water wall tube, micro-fissures, under deposit corrosion

1 Introduction

Coal-fired power plants play a vital role in the energy sector due to their ability to provide reliable and large-scale power generation. Despite the growing emphasis on renewable energy sources, thermal power plants remain essential for meeting global energy demands [1]. The main components of a thermal power plant include the boiler, turbine, generator, condenser, and cooling system. Among them boiler is considered to be the heart of a coal-fired power plant. The primary function of a boiler is to produce steam at the desired pressure and temperature by converting the chemical energy stored in the fuel (primarily coal) into heat energy [2]. This steam acts as the working fluid for the power cycle and is essential for the turbine's operation. Power plant boilers are generally categorized into major four types – (a) Subcritical, (b) Supercritical, (c) Ultra-supercritical, and (d) Advanced ultra-supercritical boiler, based on operating pressure and temperature. A subcritical boiler operates at 17.2 MPa pressures which is below

S. Shaswattam et al. (eds.), *NTPC Transactions on Energy Research (NTER 2025)*,
https://doi.org/10.2991/978-94-6463-849-3_5

the critical point of water (22.1 MPa) [3]. A boiler is basically a large pressure vessel consisting of large number of tubes and pipes. All the four sides of boiler are fabricated by panels of hundreds of tubes. Boiler tubes mainly consist of water walls, economiser, reheater and superheater tubes depending on the different heat zones of the boiler. The water wall tube in a boiler is a series of closely spaced tubes (usually made of carbon steel or low alloy steel) that form part of the boiler's furnace walls. In subcritical boilers, water and steam exist in separate phases, and steam is produced through the phase change of water into steam in the evaporator section which mainly consists of water wall tubes. Boiler tubes are among the most failure-prone components due to exposure to extreme heat and pressure. General boiler tube failure damage mechanisms are overheating, creep, erosion, hydrogen damage, stress corrosion cracking, pitting, flow accelerated corrosion, fatigue failure, thermal fatigue and welding related failures.

In general, failures of the water wall tubes are on account of different factors such as ash accumulation, corrosion and overheating etc. Hydrogen damage is one of the corrosion-related phenomena. It is basically an under-deposit corrosion mechanism at elevated temperature in which metals become susceptible to embrittlement due to the absorption of hydrogen atoms [4]. Hydrogen damage is a broader term which includes different mechanism leading to the failure of the components. It includes low temperature hydrogen embrittlement, high temperature hydrogen attack, hydrogen induced blistering, hydrogen induced cracking and hydride formation [5]. Low temperature hydrogen embrittlement refers to the loss of ductility and/or the formation of cracks in metals or alloys due to the presence of atomic hydrogen, typically at low temperatures. It can occur in various forms, depending on the material properties, manufacturing processes, and environmental conditions. It includes both irreversible embrittlement and cracking that may occur during manufacturing, before the component is put into service, as well as damage that develops during actual service. High-Temperature Hydrogen Attack (HTHA) is a permanent and irreversible degradation of a metal’s mechanical properties due to exposure to hydrogen at elevated temperatures. Unlike corrosion or erosion, HTHA is an internal damage mechanism. It does not cause visible wall thinning or large-scale deformation, making it harder to detect without detailed inspection techniques [5, 6]. Hydrogen damage occurs when hydrogen atoms diffuse into the metal lattice, often during high-temperature operations or exposure to corrosive environments, leading to a significant reduction in the material's ductility and strength [7]. The atomic hydrogen when combined with carbon in steel at elevated temperatures and pressures, results in the formation of methane gas along the ferrite grain boundaries [8–11].

The locations of the hydrogen damage failure are confined to the water wall tubes in power plant components. This phenomenon can occur in wide spectrum of material grade like carbon steel, austenitic stainless steel, Aluminium, magnesium etc. depending on the working environment [6].

In majority of the existing literatures, hydrogen damage failures are predominantly characterized by a classical window-type opening appearance [4,9,12]. In this paper three case studies were taken from three different subcritical boilers with different ages of thermal power plants. This paper discusses about the visual appearance of hydrogen damage mechanism in boiler components. It includes slit type opening and puncture

type opening apart from window type opening. Through three distinct case studies, authors provide a comprehensive illustration of these varied failure appearances of hydrogen damage which is rarely available in the existing literature. It also provides some preventive measures of hydrogen damage.

2 Methodology

The present study analyzed three failed samples collected from boilers of varying capacities and service durations. The detail of the sample is presented in table 1. In all the cases, failures occurred in the water wall section which is in the high heat flux zone of the boiler. From table 1, it can be observed that the power rating of the thermal power plant is from 110 MW to 500 MW and all the plants have subcritical boiler. The 110 MW power plant operates at ~13-15 MPa pressure and ~ 537-543°C temperature. The 250 MW boiler operates at a pressure of ~15-17MPa and 537-543°C temperature while the 500 MW boiler operates at a pressure of ~17-19 MPa and 537-543°C temperature.

2.1 Visual observation

Visual observation of the samples was carried out by unaided eye and stereo microscope (make M/s Leica). Images were captured using Nikon D70S camera. Figure 1 showed the images of the as received samples. Fig 1 (a & b) represents sample number 1 which is a window type opening failure. This sample was taken from 110 MW power plant. Fig 1 (c & d) shows sample no. 2 which is a puncture type opening and taken from a 250 MW power plant. Fig 1 (e, f & g) illustrate the images of sample no. 3 which was failed from a 500 MW boiler.

Table 1. Details of the samples taken for case study

Sample No.	Plant Capacity (MW)	Plant Age (Years)	Dimension of sample (OD X T) in mm Away from Failure	Visual appearance
1	110	24	63.5 X 6.3	Window type opening (WTO)
2	250	8	63.2 X 7.6	Puncture type opening (PTO)
3	500	31	57.5 X 7	Slit type opening (STO)

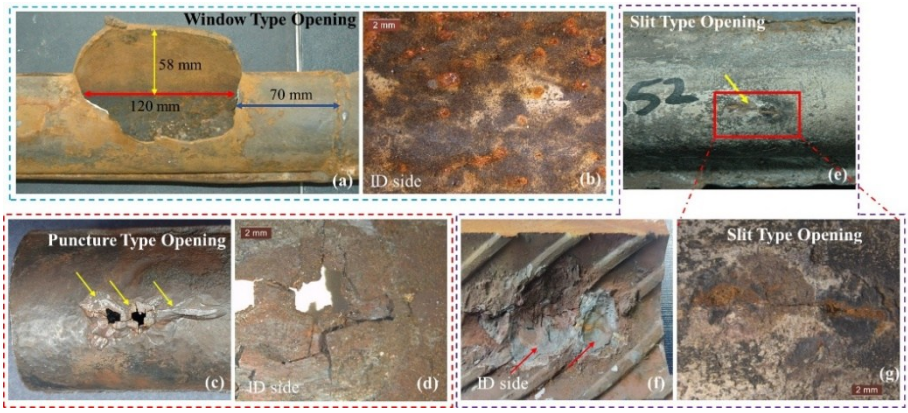

Fig. 1. (a) As received tube showed window type opening failure near to the weld joint; (b) ID side of the tube showed pitting and corrosion; (c) As received tube showed puncture type opening with two punctures and sever erosion marks around it; (d) ID side of the tube after sectioning showed oxide layer and its spallation around the crack; (e) The sample tube showed slit type opening at OD (Outside Diameter) side of the tube; (f) ID side of the tube showed under deposit corrosion in localised region with crater of iron oxide; (g) Magnified view of the tube at marked location showed short and intact crack having length ~25 mm.

2.2 Chemical composition

The chemical analysis of all the samples was carried using Optical Emission Spectrometer (OES) method (Make: M/s Thermofischer scientific, ARL 3460). Before chemical analysis, the samples were grinded to obtained a flat and smooth area of minimum dimension of 12 x 12 mm^2.

2.3 Microstructure and hardness analysis

For microstructural study purpose, small specimens from selected locations of all the samples were taken using precision abrasive cutting machine (to avoid heating) and mounted for suitable edge retention. All the mounted specimens were subjected to multiple stages of grinding & polishing to obtain a mirror finish surface. The last stage of polishing operation is carried out using specific cloth suitable for 0.5 – 1 µm diamond paste. These metallographic specimens were studied under optical microscope (Make: M/s Leica microsystem, DMi8) with un-etched and etched conditions. Etching of the samples were done using 2% Nital solution. After metallographic study, the mould samples are taken for micro hardness analysis using Vickers micro hardness tester (Make: M/s Tinius Olsen) with a load of 0.5 kgf using a diamond indenter.

3 Results

3.1 Sample no. 1

The sample tube was failed as window type opening. The failure was at a distance of 70 mm from the circumferential welding as indicated in fig 1 (a). The opening was ~58 mm wide and 120 mm in length. The thickness of the tube at fracture edge was ~4 mm. The side of the tube opposite to the failure did not show any damage. However, the inner wall of the tube opposite to failure showed corrosion and pitting which is shown in fig. 1(b).

Microstructure showed multiple cracks originating from internal surface. The length of these cracks varies from 0.22 mm to 1.17 mm. Magnified view (fig. 2b) of indicated location showed numerous intergranular micro fissures and degraded structure. Fracture edge also showed numerous micro-fissures as can be observed in fig 2c. Microhardness at failed location was in the range of 124 – 137 HV0.5.

3.2 Sample no. 2

The as received tube sample showed two punctures having circular appearance (approx. dia 3 mm). Sever thinning and erosion marks were observed around the failed location. The dip erosion mark was ~26 mm in length along the longitudinal direction of the tube. Magnified view of external surface of the failed location showed multiple cracks around the punctures. The sample was sectioned to open the tube for study of its internal surface. The internal surface at failed location showed under deposits corrosion & spallation of oxide layer. The side opposite to failed location showed no failure.

Microstructure at failed location showed thick oxide layer of thickness ~1.76 mm at ID side of the tube. It also showed sever thinning at fracture edge. Tube thickness at failed location was ~1 mm. The magnified view at fracture edge showed numerous micro fissures. Microhardness at failure location was in the range of 172 – 175 HV 0.5.

3.3 Sample no. 3

The water wall tube showed tightly intact crack. The crack was ~25 mm in length. The tube was sectioned to observe the internal surface at failed location. The inner surface showed under deposit corrosion with crater of iron oxide. Thinning of the tube at failed location was also observed. Thickness of tube at failure was ~3.3 mm while the thickness of the tube away from the failure was 7 mm.

Microstructure at failed location shows through crack of width 330 μm with thick oxide layer of thickness ~1.4 mm at ID side of the tube. It showed numerous micro fissures around the cracks. Microstructure showed ferritic & pearlite structure with intergranular micro-fissures. Microhardness values at failed location were in the range of 147 – 150 HV0.5.

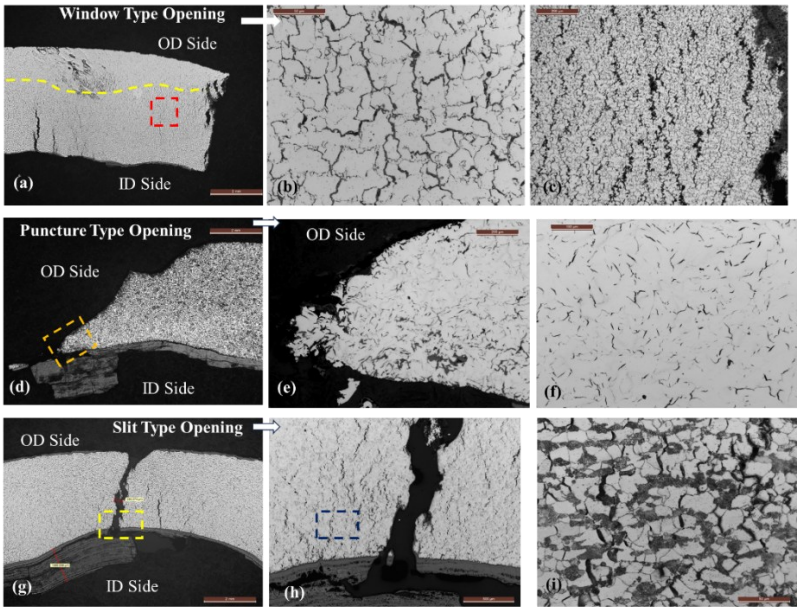

Fig 2. (a) Microstructure for sample no. 1 showed multiple cracks originating from internal surface. The crack length varies from 0.22 mm to 1.17 mm. The yellow dotted line showed the extend of micro fissures from ID side (Unetched condition) (feature at top left side is polishing error); (b) Magnified view at fracture edge (marked by red dotted box in fig a) showed numerous micro-fissures. (Unetched condition); (c) Microstructure at fracture edge, showed numerous intergranular micro fissures. (Etched condition) and decarburization; (d) Microstructure for Sample no. 2 showed thick oxide layer at ID side of the tube (etched condition); (e) At fracture edge, micro-fissures and oxide filled cracks observed (Unetched condition) (Magnification: 50X marked by orange dotted box); (f) At fracture edge (unetched condition) microstructure showed micro-fissures, (Magnification: 200X); (g) Microstructure for sample no. 3 showed thick oxide layer and through crack; (h) Microstructure showed numerous micro fissures on both side of the crack; (i) Microstructure showed numerous intergranular micro fissures.

Table 2. Chemical composition and other details of the samples.

Steel grade (%)	C	Si	Mn	S	P
SA210 Gr. C[13]	0.35 Max	0.10 Min	0.29 –1.06	0.035 Max	0.035 Max
Sample no. 1 (110MW)	0.24	0.18	0.54	0.005	0.013
Sample no. 2 (250 MW)	0.24	0.21	0.74	0.005	0.011
Sample no. 3 (500 MW)	0.29	0.20	0.91	0.0036	0.019

3.4 Chemical Analysis

The Chemical composition of all the tube samples obtained through OES analysis are shown in table 2.

4 Discussion

Hydrogen damage is a broad term associated with material degradation due to interaction of hydrogen with material. In this degradation, the material loses its ductility and strength. Waterwall tubes in coalfired power plant carries water and/or steam. When there is a deviation in water chemistry, it may lead to under deposit corrosion. The deposit creates a barrier between the water and the metal surface, causing localized heat retention and reduced heat transfer. Beneath the deposits, water decomposition at high temperatures initiates corrosion reactions that generate atomic hydrogen (H). This atomic hydrogen diffuses into the metal, reacting with Fe_3C (iron carbide) at the grain boundaries to form CH_4 (methane) which have high volume fraction of methane [6,14] results in micro fissures.

The location of water wall tube is in the high heat flux zone of the boiler. In sample no. 2 (250 MW boiler) the failure occurred in a period of 8 years' time as mentioned in table 1. Contrast to this, the third case (500 MW boiler) which was in service for more than 30 years. Thus, hydrogen damage failure is independent of year of service. Whenever, the water chemistry was compromised it results in corrosion which may subsequently leads to hydrogen damage.

The samples were sectioned from the failure location and prepared for metallurgical analysis as discussed in methodology part. When the polished samples were examined under an optical microscope, numerous micro-fissures were observed. These fissures were clearly visible in unetched condition which is one of the key microstructural features of hydrogen damage.

The slit type opening is very localized as compared to WTO and PTO type failure appearance. The affected area in the form of micro-fissures is most prominent in the WTO mode and extends to nearly 81% of the tube thickness at the fracture edge. Complete decarburization of pearlite was observed in WTO mode. Also, there is no significant reduction in thickness of tube material at fracture edge as compared to sample no. 3 (STO). The possible reason for thickness reduction in sample no. 3 is the extent of under deposit corrosion. The thickness of under deposit oxide layer at failure in this sample was ~1.4 mm. No comparison regarding thickness reduction can be made for PTO sample, as external steam erosion on the OD side of the tube has influenced the measurement. Therefore, the overall assessment of failure modes should consider multiple contributing factors, including: (a) affected areas, (b) area of under deposit corrosion, (c) thickness reduction due to under deposit corrosion, (d) temperature

influence at the heat flux region, (e) dimension of the component and operating temperature and pressure.

Higher hydrogen concentrations significantly increased the tendency for intergranular (IG) cracking while the transgranular mode of cracking was evident at lower hydrogen pressure [15]. A brittle fracture is typically associated with IG-type failure[16]. However, it may be inferred that micro fissures regions are the indication of amount of hydrogen absorption. In all the three samples, the rupture of tubes was due to the formation and linkage of micro-fissures which is a typical signature of hydrogen damage mechanism. Intergranular mode of failure was predominant in all the three samples.

Remedial Mechanism for Hydrogen Damage. Once water wall tube failure was detected due to hydrogen damage, suitable corrective action should be taken to minimize loss of power generation which includes (a) thickness survey across the affected region, (b) Replace all the affected tubes, (c) Assessment of deposit analysis and corrective measures as per OEM guidelines, (d) Corrosion mapping and (e) NDT technique like UT (Ultrasonic Testing) and Eddy current. This is important because, even though localized, the failures would be found in most of the adjacent tubes. The preventive measures that the power plant should follow in order to avoid loss of power generation due to hydrogen damage are as follow:

- Boiler water chemistry parameters recommended by OEM/Plant should be maintained to avoid internal deposition
- During overhauling or maintenance location prone for deposition to be assessed to avoid any significant under deposit corrosion.
- Periodic assessments to be carried out for deposit analysis as per standard guidelines & accordingly suitable action to be taken.

5 Conclusion

Based on the analysis of all the three case studies of different capacity of subcritical boilers following conclusion can be drawn:

i. The failure appearance of hydrogen damage can also be manifested as “Puncture-type opening” or “Slit-type opening” apart from “Window-type openings.

ii. Hydrogen damage phenomenon is localised in nature as observed in the boiler tubes and it may happen within very short span of time to years old service if water chemistry is not maintained properly.

iii. The failure of the water wall tubes was attributed to under-deposit corrosion phenomenon, which creates an environment for ionization of hydrogen and its diffusion into the base metal under high temperature and pressure. Therefore, the nature of failure of all the three tubes was high temperature hydrogen induced under deposit corrosion.

iv. A key microstructural feature was the presence of micro-fissures which is intergranular in nature.

v. The possible reasons for different appearance of failure were affected areas with micro fissures, thickness reduction, extent of under deposit corrosion, temperature, pressure and geometry of the components.
vi. Based on this study, it may be inferred that the reason for WTO was that the affected areas on account of micro-fissures were very high as compared to STO & PTO type.
vii. It might be inferred that metallographic technique is very reliable & confirmative method for failure of tube due to hydrogen damage.

Acknowledgments. Authors would like to express their gratitude to the Executive Director of NTPC NETRA for strong motivation for writing this paper. This work was not supported by any funding agency.

Disclosure of Interests. The authors declare that they have no conflicts of interest to disclose regarding the research presented in this manuscript.

References

[1] V.K. Yadav, M. Fulekar, M.H. Fulekar, The current scenario of thermal power plants and fly ash: production and utilization with a focus in India, International Journal of Advance Engineering and Research Development 5 (2018). https://www.researchgate.net/publication/329942803.

[2] I. Dincer, Y. Bicer, Fundamentals of energy systems, Integrated Energy Systems for Multigeneration (2020) 33–83. https://doi.org/10.1016/B978-0-12-809943-8.00002-9.

[3] A.A. Nuraini, S. Salmi, H.A. Aziz, Efficiency and Boiler Parameters Effects in Sub-critical Boiler with Different Types of Sub-bituminous Coal, Iranian Journal of Science and Technology - Transactions of Mechanical Engineering 44 (2020) 247–256. https://doi.org/10.1007/s40997-018-0249-7.

[4] James J Dillon, Paul B Desch, Tammy S Lai, The Nalco Guided to Boiler Failure Analysis, second edition, 2011.

[5] K. Poorhaydari, A Comprehensive Examination of High-Temperature Hydrogen Attack—A Review of over a Century of Investigations, J Mater Eng Perform 30 (2021) 7875–7908. https://doi.org/10.1007/s11665-021-06045-z.

[6] X. Li, X. Ma, J. Zhang, E. Akiyama, Y. Wang, X. Song, Review of Hydrogen Embrittlement in Metals: Hydrogen Diffusion, Hydrogen Characterization, Hydrogen Embrittlement Mechanism and Prevention, Acta Metallurgica Sinica (English Letters) 33 (2020) 759–773. https://doi.org/10.1007/s40195-020-01039-7.

[7] M. Moshtaghi, B. Loder, M. Safyari, T. Willidal, T. Hojo, G. Mori, Hydrogen trapping and desorption affected by ferrite grain boundary types in shielded metal and flux-cored arc weldments with Ni addition, Int J Hydrogen Energy 47 (2022) 20676–20683. https://doi.org/10.1016/J.IJHYDENE.2022.04.260.

[8] M. Djukic, G. Bakic, M. Djukic, V. Sijacki Zeravcic, G. Bakic, D. Milanovic, B. Andjelic, Model of Influencing Factors for Hydrogen Damages of Boiler Evaporator Tubes, n.d. https://www.researchgate.net/publication/236612261.

[9] M.B. Djukic, V. Sijacki Zeravcic, G.M. Bakic, A. Sedmak, B. Rajicic, Hydrogen damage of steels: A case study and hydrogen embrittlement model, Eng Fail Anal 58 (2015) 485–498. https://doi.org/10.1016/j.engfailanal.2015.05.017.

[10] R.A. Oriani, The diffusion and trapping of hydrogen in steel, Acta Metallurgica 18 (1970) 147–157. https://doi.org/10.1016/0001-6160(70)90078-7.

[11] Y.S. Chen, C. Huang, P.Y. Liu, H.W. Yen, R. Niu, P. Burr, K.L. Moore, E. Martínez-Pañeda, A. Atrens, J.M. Cairney, Hydrogen trapping and embrittlement in metals – A review, Int J Hydrogen Energy (2024). https://doi.org/10.1016/j.ijhydene.2024.04.076.

[12] Y.S. Kim, W.C. Kim, J. Jain, E.W. Huang, S.Y. Lee, Hydrogen Embrittlement of a Boiler Water Wall Tube in a District Heating System, Metals (Basel) 12 (2022). https://doi.org/10.3390/met12081276.

[13] ASTM, Standard Specification for Seamless Medium-Carbon Steel Boiler and Superheater Tubes, in: ASTM A210/A210M-19, 2019: p. 03.

[14] S. Lynch, Discussion of some recent literature on hydrogen-embrittlement mechanisms: addressing common misunderstandings, Corrosion Reviews 37 (2019) 377–395. https://doi.org/10.1515/corrrev-2019-0017.

[15] Y. Ogawa, D. Birenis, H. Matsunaga, O. Takakuwa, J. Yamabe, Ø. Prytz, A. Thøgersen, The role of intergranular fracture on hydrogen-assisted fatigue crack propagation in pure iron at a low stress intensity range, Materials Science and Engineering: A 733 (2018) 316–328. https://doi.org/10.1016/j.msea.2018.07.014.

[16] E.D. Merson, P.N. Myagkikh, V.A. Poluyanov, D.L. Merson, A. Vinogradov, Features of the Hydrogen-Assisted Cracking Mechanism in the Low-Carbon Steel at Ex- and In-situ Hydrogen Charging, in: Procedia Structural Integrity, Elsevier B.V., 2018: pp. 1141–1147. https://doi.org/10.1016/j.prostr.2018.12.238.

Coercivity Measurement as a Tool for Assessing the Quality of Post Weld Heat Treatment of T91 Boiler Tubes

Avijit Mondal*, Anil Kumar Das, Satish Chand, Sandeep Kumar, Chandra Bhushan Kesari
NDE, Imaging and Life Management Lab, NTPC Energy Technology Research Alliance, NTPC Ltd., Greater Noida, Uttar Pradesh, India.
*Corresponding author E-mail: avijitmondal@ntpc.co.in

Abstract. Modified 9Cr-1Mo steel (T91) is widely used in power generation due to its superior high-temperature strength, extended creep rupture life, excellent oxidation and corrosion resistance, and good weldability. However, weld joints in T91 components are often the most failure-prone regions, making it essential to assess their behaviour for long-term reliability. Post-weld heat treatment (PWHT) plays a critical role by relieving residual stresses and tempering the martensitic structure in the fusion zone, thereby minimizing strength gradients across the weld. In field applications, verifying the effectiveness of PWHT requires dependable non-destructive evaluation (NDE) methods. While portable hardness testing is commonly employed, it often yields inconsistent results and may not reliably reflect the overall condition of the material.

An alternative approach involves measuring Magnetic Coercive Force (MCF), which correlates with magnetic hardness in ferromagnetic materials. This study aimed to investigate the influence of different PWHT conditions on the MCF of T91 welds. The experiments examined how MCF varied under a range of PWHT cycles, with soaking temperatures up to 790°C and durations up to 120 minutes. Results indicated that higher soaking temperatures and longer durations led to a decrease in MCF values within the weld metal. This reduction aligned with lower hardness levels and increased carbide precipitation in the microstructure. Based on these results, a threshold for acceptable MCF values has been established. Exceeding this threshold can signal the need for corrective actions, enabling proactive maintenance and reducing the risk of premature failures or unexpected shutdowns in thermal power plants.

Keywords: Coercivity; Post Weld Heat Treatment; T91 Steels; Microstructures; Hardness.

1. Introduction

Modified 9Cr-1Mo (T91) steel belongs to a class of ferritic steel known for their exceptional creep resistance, making them well-suited for high-temperature environments. These steels are widely used in critical components such as main steam piping, superheaters, reheaters, and headers in fossil fuel-fired power plants, as well as in nuclear steam generators for fast breeder reactors. Their

S. Shaswattam et al. (eds.), *NTPC Transactions on Energy Research (NTER 2025)*,
https://doi.org/10.2991/978-94-6463-849-3_6

expanding range of applications underscores their significance in contemporary power plant operations [1]. Growing interest is being directed toward investigating the welding characteristics of T91 steel due to its critical role in high-temperature applications. Studies have shown that a significant proportion of failures in steam generator components occur specifically at the weld joints [2]. The fusion zone of as-welded T91 steel contains newly formed martensite, a hard and brittle phase that heightens the risk of premature failure. Variations in strength across the weld axis arise due to differences in phase composition and grain size across the fusion zone, heat-affected zone (HAZ), and base metal. These issues are further intensified by residual stress generated during welding. To address these challenges, PWHT is employed to relieve residual stress and temper the martensitic phase, thereby minimizing strength gradients [3]. According to the ASME Boiler and Pressure Vessel Code - Section VIII, Division 1 [4], PWHT for T91 steel should involve soaking at temperatures between 730°C and 775°C. Without adequate PWHT, the martensitic phase remains un-tempered, resulting in elevated hardness levels that can compromise performance and increase the likelihood of failures. Multiple case studies [5-7] have documented failures in T91 steel components due to insufficient heat treatment, highlighting the critical importance of proper PWHT. To ensure the quality of PWHT, NDE methods are crucial, particularly in on-site conditions. Among these, portable hardness testing is the most employed technique to assess the effectiveness of PWHT. According to J. Parker [8], a maximum hardness value of 280 HB-measured using a portable hardness tester is the acceptance criterion for PWHT quality in modified T91 welds performed in the field. Despite its widespread use, this method has certain limitations. Numerous variables, such as the type of equipment and testing procedures, can significantly influence the results of field hardness tests. Achieving accurate hardness reading typically depends on meticulous surface preparation, including grinding and polishing, as well as the careful and consistent application of testing techniques by the operator [8].

Ferromagnetic steels like modified T91 exhibit magnetic properties that are highly responsive to variations in microstructure, stress levels, and corrosion. The coercive force /MCF, also known as coercivity; quantifies a material's resistance to demagnetization when subjected to an external magnetic field. Microstructural factors, including grain coarsening, precipitation, and defects like voids, dislocations, and inclusions, significantly influence MCF [1, 9-13]. These factors impede the movement of magnetic domain walls, resulting in an increased MCF. Variations in MCF can offer valuable insights into the microstructural condition of the material.

A review of multiple studies [1, 9-13] indicates that the magnitude of the MCF in ferromagnetic materials reflects their magnetic hardness. The ferromagnetic nature of modified T91 steel allows the use of micro-magnetic techniques-such as magnetic coercivity measurements-which are highly sensitive to microstructural and stress variations, to assess the effects of heat treatment on weld joints. Recent research has investigated how welding and PWHT influence

the MCF of both modified T91 and T22 steels [1, 9-13]. In particular, Sudharshanam et al. [1] and Mondal et al. [9-10] evaluated the quality of PWHT in modified T91 steel welds through MCF measurement. Similarly, Sambamurthy et al. [12] studied the PWHT behaviour of modified 9Cr-1Mo weldments using Magnetic Barkhausen Emission techniques. More recently, Roy et al. [13] examined the behaviour of post-weld heat-treated T22 steel joints using electromagnetic NDE parameters. The present study builds upon the findings of Sudharshanam et al. [1] and Mondal et al. [9-10]. However, a review of the literature reveals a notable gap: limited research specifically addresses the impact of welding and PWHT on the MCF of T91 boiler tubes. Of particular interest, Das et al. [14] recently demonstrated a novel application of MCF measurement for the in-situ detection and quantification of oxide scale exfoliation in stainless steel boiler tubes.

This study focused on examining the effects of various PWHT conditions on the MCF as well as on the hardness of T91 welds. The experiments tested soaking temperatures of up to 790°C and durations extending to 120 minutes. The primary objective is to establish MCF measurement as a dependable evaluation criterion, replacing hardness testing, to assess the quality of PWHT in T91 steel weldments.

2. Method of Investigation

T91 boiler tubes of thermal power plant, featuring an outer diameter of 44.5 mm and a wall thickness of 6 mm, were joined using the TIG welding technique. This process employed AWS E 9015 B9 low hydrogen electrodes with a diameter of 2.4 mm, in accordance with the Welding Procedure Specification (WPS) for T91 tubes. Throughout the welding process, a consistent root gap of 3 mm and an included groove angle of 60° were maintained. The preheating temperature was set at 220°C, and the inter-pass temperature was controlled and limited to 350°C. The various phases of the welding process for the modified T91 tubes are depicted in Figure 1. Following the welding procedure, the components were cooled to 90°C at a controlled rate of 150°C/h before commencing the PWHT cycle. Soaking temperatures were tested at five different levels: 700°C, 730°C, 750°C, 770°C, and 790°C. For each temperature, three soaking durations were applied: 30 minutes, 60 minutes, and 120 minutes, culminating in a total of fifteen PWHT cycles. The purpose of this experimental setup was to examine the relationship between the weld's hardness and its MCF values under different soaking temperatures and time durations. The minimum soaking temperature of 700°C was selected to simulate potential suboptimal PWHT conditions that might arise in field applications, while the maximum was capped at 790°C to prevent both the weld and base metal from surpassing the AC1 temperature of 830°C. Throughout all fifteen PWHT cycles, heating and cooling rates were consistently maintained at 150°C/h. To validate any potential relationship between hardness and MCF in as-welded conditions, two samples of welded tubes without PWHT were preserved. Metallographic specimens were prepared using standard grinding and polishing methods. For etching, Villela's reagent; consisting of 95 ml of

ethanol, 5 ml of hydrochloric acid (HCl), and 1 gm of picric acid-was applied to reveal the microstructure.

The hardness (Vickers hardness with a load of 5 kg) of the transverse cross-section samples taken from the weld tubes (Figure 4) was measured within the weld zone for all seventeen specimens. The hardness profiles for the base metal, heat-affected zone (HAZ), and weld zone across all seventeen samples are illustrated in Figure 5, with each sample undergoing a total of 22 measurements. Hardness measurements were conducted at a depth of 1 mm with a spacing of 1 mm between consecutive measurement points. The ten highest hardness values from the weld zone (Figure 4) were selected for analysis for each sample.

The MCF value for each PWHT sample was measured alongside that of the as-welded condition for comparison. Measurements were taken using a "Magnetic Structurescope," an instrument equipped with magnetizing pole tips and a digital display, as illustrated in Figure 2. This device functions based on the principle of magnetic hysteresis. It applies current pulses to magnetize the material beneath the pole tips, followed by rapid demagnetization through current reversal. The reverse magnetizing force adjusts the magnetic retentivity, allowing the instrument's internal circuitry to accurately compute the MCF. The measurement range of the device spans from 0.4 to 40 A cm^{-1}. The test setup used for evaluating MCF in welds is also depicted in Figure 2.

Fig 1. Photographs showing different stages of Welding of T91 Boiler Tubes. **(a)** Cut to Length, **(b)** Face or Bevel, **(c)** Cleaning, **(d)** Alignment, **(e)** Root Pass, **(f)** Hot Pass, **(g)** Heating Cycle in PWHT, **(h)** Soaking and Cooling Cycle and **(i)** Final Welded Tube

Table 1: Chemical Composition (wt %) of T91 As-received Tube

C	Si	Mn	P	S	Cr	Mo	Ni	Nb	V	Fe
0.135	**0.275**	**0.46**	**0.012**	**0.004**	**8.4**	**0.90**	**0.13**	**0.09**	**0.2**	**rest**

Fig 2. Photograph of MCF Measurement Test Setup Utilizing a Magnetic Structurescope.

3. Results and Discussion

3.1 Material Composition

The composition of the as – received tube is shown in Table 1. The tube conforms to SA 213 – T91 grade of material.

3.2 Micro Structural Analysis of As - received as well As-welded Structures of T91 Tubes

The ideal microstructure for Grade 91 components consists of tempered martensite, distinguished by a well-developed network of $M_{23}C_6$ carbides and MX-type carbo-nitrides. These precipitates generally form along lath boundaries and at defect sites within the substructure [11, 15]. Photomicrographs of properly heat-treated T91 steel typically reveal this characteristic tempered martensitic structure. However, the critical precipitate network responsible for the material's creep strength cannot be fully evaluated through optical microscopy alone. To achieve a detailed and accurate microstructural analysis, advanced characterization methods such as transmission electron microscopy (TEM) are required. Earlier studies [10-11] have shown that TEM analyses of as-received P91 pipes reveal a tempered martensitic matrix characterized by a high dislocation density and the presence of various precipitate types. Excessive tempering can adversely affect the martensitic structure, potentially leading to its complete degradation. While the cooling rate ultimately determines the final microstructure, factors such as the peak temperature and hold time during normalizing treatments significantly influence the size of the austenite grains. This grain size can be controlled by either adjusting the temperature or modifying the hold duration during the normalizing process. Pre-conditioning treatments, including normalizing and tempering, yield a tempered martensitic microstructure

featuring acicular prior austenite grains in the base metal. Studies have demonstrated that a large number of precipitates-predominantly $M_{23}C_6$ carbides, where the metallic element M can include Cr, Fe, Mo, Mn, or their combinations-are commonly found along lath boundaries and prior austenite grain boundaries. When subjected to post-weld heat treatment (PWHT) at 770°C, the microstructures within both the heat-affected zone (HAZ) and the weld zone undergo significant transformations, as illustrated in Figure 3. Analysis of the weld zone at various depths indicates substantial reductions in the volume fraction of precipitates following annealing at this temperature. In the fusion zone, prior austenite grains transform into newly formed martensite, while tempered martensite coarsens as heat treatment temperatures rise. Studies have documented precipitation behavior in weld microstructures subjected to PWHT at 700°C for 60 minutes. At this soaking temperature, precipitates in the base metal zone align along lath boundaries. Increasing the soaking temperature to 770°C for the same duration leads to a significant increase in alloy carbide precipitation within the weld microstructure. Further elevation to 790°C results in additional coarsening of the tempered martensite, as noted in previous research [10].

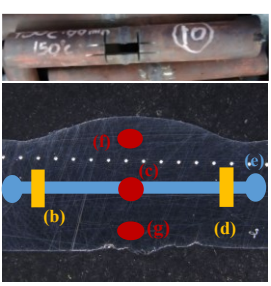

Schematic Illustration of the Sampling Locations Selected for Microstructural Analysis

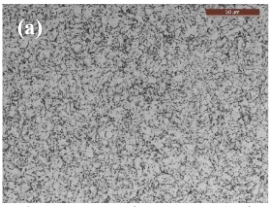

Microstructure of Base Metal (Left)

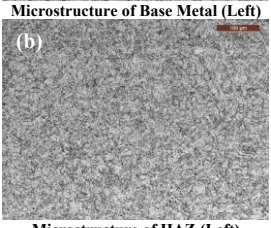

Microstructure of HAZ (Left)

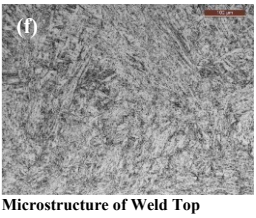

Microstructure of Weld Top

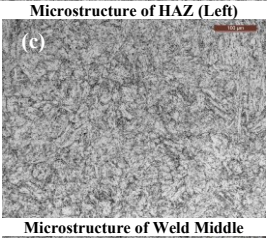

Microstructure of Weld Middle

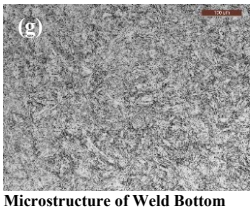

Microstructure of Weld Bottom

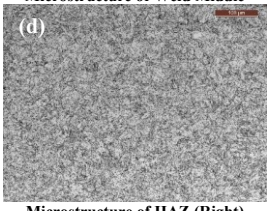

Microstructure of HAZ (Right)

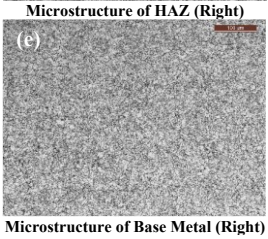

Microstructure of Base Metal (Right)

Fig 3. Microstructure of (a, e) Parent, (b, d) HAZ and (c, f, g) Weld Region after PWHT at 770°C, & 60 min of T-91 Weld Tubes.

Fig 4. Photograph of Welded Tubes and Hardness Measurement Location

3.3 Hardness and Microstructural Influence of As welded and Post Weld Heat Treated Samples

Hardness measurements were performed along the transverse cross-section of the weld joints, with the results plotted as a function of distance from the weld centre (refer to Figure 5). These hardness values are closely linked to the underlying microstructure of the material. In the as-welded condition, the fusion zone exhibits a hardness of approximately 410 HV5, primarily due to the formation of fresh martensite. After PWHT, this hardness gradually declines as the martensitic structure undergoes tempering. The reduction in hardness within the fusion zone is further influenced by the coarsening of lath martensite and the transformation of retained austenite into softer alpha ferrite at elevated PWHT temperatures. In the as-welded state, the highest hardness-around 430 HV5 -is recorded in the coarse-grain heat-affected zone (CGHAZ), followed by a sharp decrease to about 330 HV5 in the inter-critical heat-affected zone (ICHAZ). This downward trend continues after PWHT, reflecting the thermal gradients experienced during the welding process. In the CGHAZ, temperatures can reach up to 1500°C, leading to carbide dissolution and an increase in hardness due to solid solution strengthening. In contrast, the ICHAZ-located further from the fusion line-experiences lower peak temperatures that are insufficient to dissolve carbides, resulting in reduced hardness in that region [16, 17]. Moving from the ICHAZ toward the base metal, a slight rise in hardness is observed for both as welded and PWHT samples. This increase is attributed to the limited impact of the welding thermal cycle on the base metal and the presence of a finer grain structure compared to the CGHAZ. Figure 6 illustrates a consistent decline in the hardness of the welds following PWHT cycles 1 to 15. This decrease in hardness is primarily due to the gradual reduction in dislocation density within the weld during these cycles. As the weld experiences progressive tempering throughout PWHT cycles 1 to 15, a steady decline in hardness is observed.

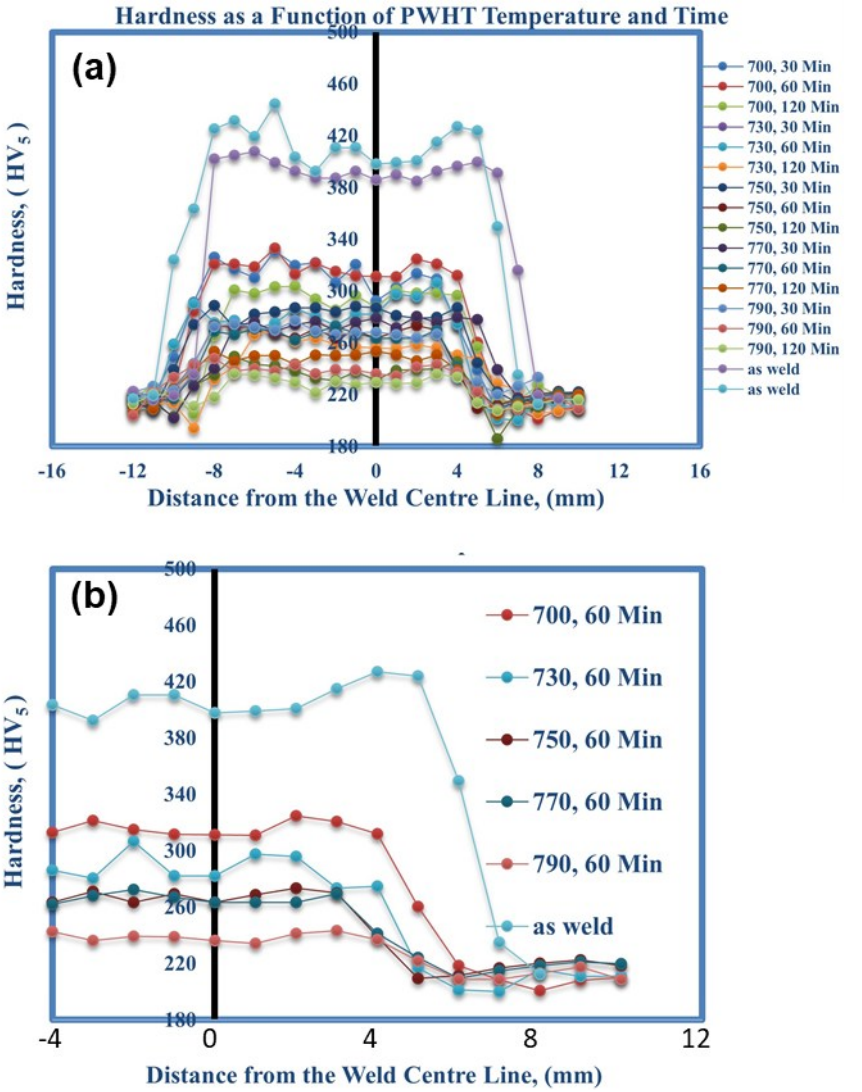

Fig 5. Hardness Variation with Distance from Weld Center for (a) All Samples and (b) Samples Soaked for 60 Minutes, Including the As - welded Sample.

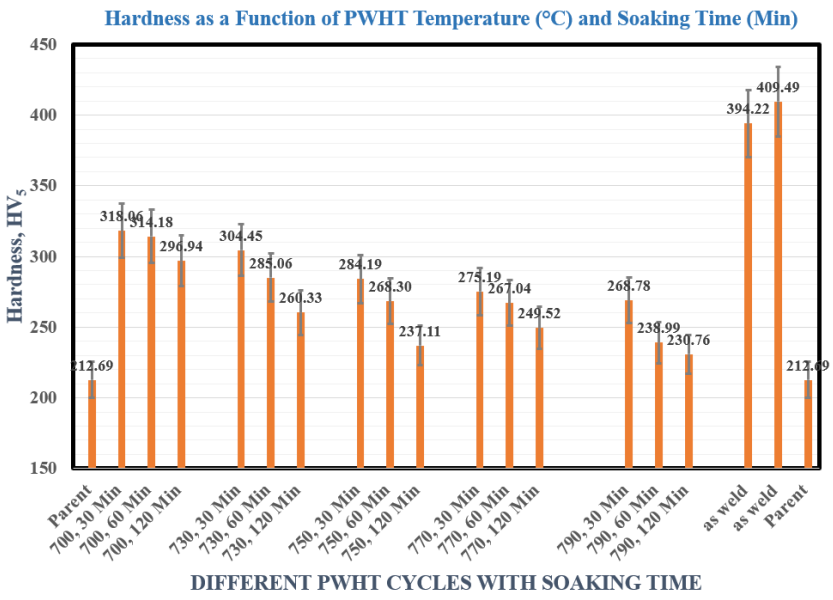

Fig 6. Hardness Variation Based on PWHT Temperature and Soaking Duration

3.4 Coercive Force in As welded and PWHT Samples

The MCF of the weld in its as-welded state ranges from 19.65 to 20.47 A cm^{-1}, exhibiting a gradual decrease as both soaking temperature and time increase during PWHT, as depicted in Figure 7. In the as-welded condition, the weld metal of T91 steel predominantly consists of martensite laths [17-20]. The elevated MCF observed in this state is primarily due to the presence of fine, newly formed martensite, which demonstrates greater magnetic hardness, along with residual stresses generated during the welding process. Martensite laths create a pinning effect that hinders dislocation movement, thereby increasing resistance to magnetic domain wall motion during magnetization. This restricted domain wall mobility explains the elevated coercivity observed in the as-welded condition. Following PWHT, the martensite laths in the weld metal begin to decompose, resulting in a lower dislocation density and a subsequent decrease in resistance to domain wall motion compared to the as-welded state. With fewer obstacles present, magnetization becomes easier, resulting in a consistent decline in coercivity throughout PWHT cycles 1 to 15, as illustrated in Figure 7. Recent studies [11] have shown that the filler material used in welding possesses lower coercivity than the base metal, making it magnetically softer. This disparity in magnetic coercivity is influenced by phase transformations that occur under varying PWHT conditions, as reflected in Figure 7. As PWHT temperatures increase, the number of pinning sites-such as dislocations, carbides, and grain boundaries-decreases, which facilitates easier movement of domain walls and contributes to lower MCF values. Figure 7 further illustrates that at a soaking

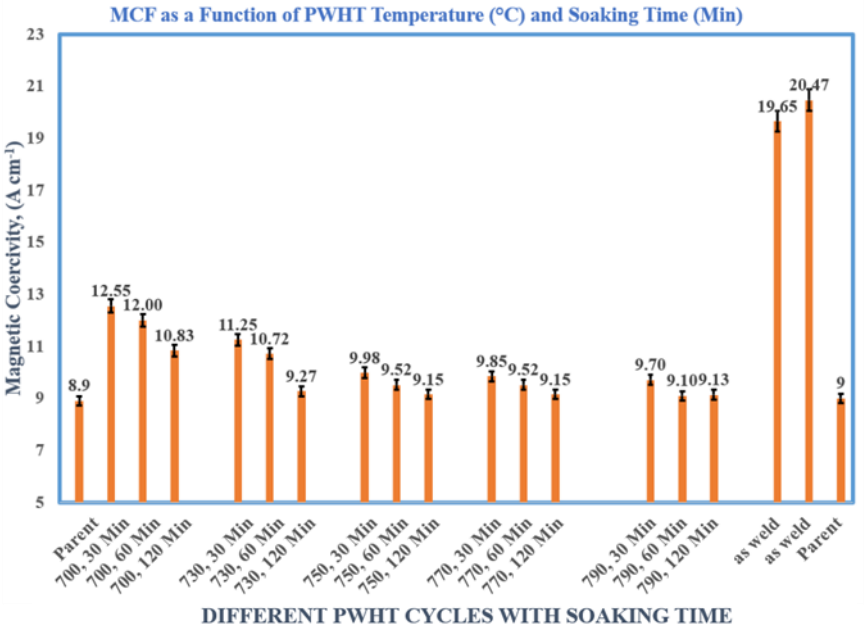

Fig 7. Coercive Force as a Function of PWHT Temperature and Holding Time

temperature of 700°C, increasing the soaking duration from 30 to 120 minutes leads to a more pronounced reduction in MCF. A similar trend is observed at soaking temperatures of 730°C, 750°C, 770°C, and 790°C. The most substantial reduction in MCF (55.39%) occurs at the highest soaking temperature (790°C) with the longest soaking time (120 minutes) among all fifteen PWHT cycles. This trend can be attributed to the increased activation energies available at elevated temperatures, which promote dislocation movement and lead to a notable reduction in dislocation density. The gradual decrease in MCF observed after PWHT cycles 1 through 15 can be attributed to the increased mobility of magnetic domain walls. This behavior in the base metal regions is consistent with findings reported in earlier studies [1, 9-11].

4. Establishment of a Criterion for Assessing the Quality of PWHT in T91 Welds.

Coercivity of the weld clearly reflects the extent of tempering achieved through PWHT, as discussed previously. Therefore, coercivity can serve as a qualitative measure for assessing the quality of PWHT in T91 welds. Additionally, Figure 8 illustrates that the percentage reduction in coercive force resulting from PWHT cycles 1 to 15 is directly proportional to the percentage reduction in weld hardness. To quantify this relationship, a regression equation was developed to mathematically represent the correlation between the percentage reduction in

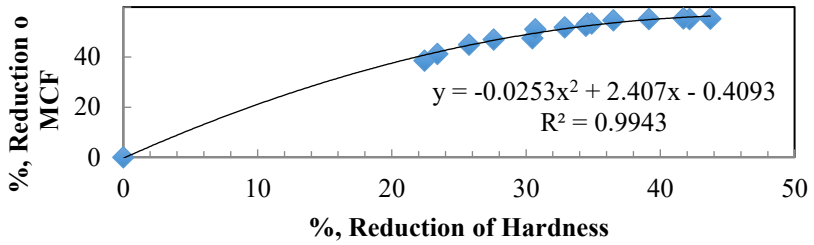

Fig 8. Correlation between %, Reduction in MCF and Hardness of T91 Weld Metal Following PWHT Cycles 1-15.

MCF and the percentage reduction in weld hardness, as shown below:

$$\mathbf{y} = -0.0253x^2 + 2.407x - 0.4093, R^2 = 0.99433 \ldots (1)$$

In this equation, 'y' denotes the %, reduction in MCF, while 'x' represents the %, reduction in hardness. The coefficient of correlation (R^2) for this equation is calculated to be 0.99433(close to unity), indicating a very high degree of correlation. Additionally, according to EPRI document [8], the maximum permissible hardness for T91 steel welds that have undergone satisfactory PWHT should not exceed 280 HB, which is roughly equivalent to 294 HV.

Using this criterion, the equivalent condition for the coercive force of weld is established. In this study, the average hardness of the weld in its as-welded state is measured at 410 HV5 (Figure 5). With a target post-PWHT hardness set at 294 HV5, the necessary average reduction in hardness for acceptable PWHT quality is calculated to be 28.29%. According to Equation (1), this corresponds to an average reduction in MCF of 47.48%. Given an as-welded MCF value of 20.47 A cm^{-1}, it follows that a minimum reduction of 47.48% in MCF (equivalent to a 28.29% reduction in hardness) is required for the PWHT to be deemed acceptable. This results in a maximum allowable MCF value of 10.75 A cm^{-1} for the weld following PWHT. The MCF values for the weld after PWHT cycles 1-4 exceed this acceptable limit of 10.75 A cm^{-1}. Furthermore, the lowest hardness recorded after these cycles is 296 HV5, which remains above the acceptable threshold of 294 HV5. Consequently, the quality of PWHT for welds from cycles 1-4 is considered unacceptable, as both MCF and hardness surpass the established limits. In contrast, PWHT cycles 5-15 yield weld hardness and MCF values fall below the specified limits, indicating acceptable PWHT quality. Thus, a criterion for acceptable PWHT quality in T91 welds has been established: "The MCF of the weld must not exceed 10.75 A cm^{-1} after PWHT." This finding offers a new and transferable framework for identifying T91 welds that have undergone inadequate PWHT. By employing this method, substandard welds can be readily identified, allowing for timely corrective actions to prevent premature service failures and unexpected plant outages.

Fig 9. In-Situ Evaluation of PWHT Effectiveness for T91 Boiler Tubes Through MCF Measurement.

5. Field Implementation: Evaluation of the Effectiveness of PWHT on T91 Tubes Through In-Situ Coercive Force Measurement

Following successful laboratory demonstrations, an MCF-based assessment of PWHT was carried out at a 660 MW NTPC plant as shown in Figure 9. This assessment involved measurements on 694 T91 tube welds, which included samples from the superheater header, outlet header, HRH, and superheater hanger tubes, as well as 156 T91 reheater inlet and outlet header tubes. A similar measurement technique had previously been utilized by the original equipment manufacturer (OEM) for T22 water wall tube welds at another NTPC facility. The field measurements revealed several advantages of using MCF-based assessments, including:

a) High efficiency and speed of the process.
b) Minimal surface preparation requirements compared to traditional hardness testing.
c) Consistent and reliable results.

This measurement technique offers a rapid and dependable method for evaluating the effectiveness of PWHT on T91 welds, facilitating the quick identification of welds that require proper heat treatment or rewelding.

6. Conclusion

The research examined the MCF, microstructure, and hardness of T91 tube welds subjected to different PWHT conditions, which included control adjustments in soaking temperature and duration. The main findings are summarized as follows:

i. **Base Metal Microstructure**: The base metal exhibited tempered martensite and acicular prior austenite grains, with numerous precipitates located along the boundaries of lath martensite and prior austenite. In contrast, the fusion zone displayed columnar grain structures lacking secondary particles.
ii. **Hardness Distribution:** In the as-welded condition, the hardness increased from 410 HV5 in the fusion zone to 430 HV5 in the coarse-grained heat-affected zone (CGHAZ) due to the presence of dissolved and undissolved carbides. A sharp decrease to 330 HV5 was noted in the inter-critical heat-affected zone (ICHAZ).
iii. **Effect of PWHT on MCF:** MCF values showed a consistent decline with increasing PWHT soaking temperatures, reaching up to 790°C, and longer soaking durations of up to 120 minutes.
iv. **MCF as a Heat Treatment Indicator:** MCF measurements were effective in assessing the quality of PWHT in T91 welds.
v. **Correlation Between MCF and Hardness:** A strong correlation was observed between the reduction in MCF and the decrease in weld hardness following PWHT.
vi. **Quality Criterion:** A benchmark was established, suggesting that the MCF of the weld should not exceed 10.75 $A \cdot cm^{-1}$ after PWHT to ensure the weld's acceptable quality.

These findings provide valuable insights for evaluating the effectiveness of PWHT in T91 welds, particularly under practical field conditions.

Acknowledgments

The authors wish to extend their heartfelt gratitude to ED (NETRA) for his invaluable advice, suggestions, support, guidance, and encouragement in implementing these techniques at NTPC stations. They also thank the management of NTPC Talcher Kaniha and the coordinating departments for their cooperation and support during the welding experiments. Special thanks are due to Dr. V. Sudharsanam from WRI, BHEL, Trichy, for his significant assistance and contributions during the initial phases of the project. Additionally, appreciation is expressed to the NETRA Metallurgy Lab for their support in hardness measurement and microstructural characterization.

References

[1] V. Sudharsanam, V. Senthilkumar, N. Raju, R. Vetriselvan, "Evaluation of Post Weld Heat Treatment Quality of Modified 9Cr-1Mo (P91) Steel Weld by Magnetic Coercive Force Measurements," Archives of Civil and Mechanical Engineering 15 (2015), 847-853.
[2] I. A. Shibli, "Engineering Issues in Turbine Machinery, Power Plant and Renewables," In: Proc. 6th Int. Charles Parsons Turbine Conf. on Dublin: Maney Publishers; 2003, 261-79.
[3] P. D. Smet, H. V. Wortel, "Controlling Heat Treatment of Welded P91 Hardness Testing Proves to be a Powerful Tool for Checking the Condition of P91," Welding 2006, 42-4.
[4] American Society of Mechanical Engineers (ASME), ASME Boiler and Pressure Vessel Code – VIII, Rules for Construction of Pressure Vessels, Division 1, 2013 ed., The American Society of Mechanical Engineers, New York, 2013.
[5] M.Z. Hamzah, M.L. Ibrahim, Q.H. Chye, B. Ahmad, J.I.I. Hussain, J. Purbolaksono, "Evaluation on the Hardness and Microstructures of T91 Reheater Tubes after Post-Weld Heat Treatment," Engineering Failure Analysis 26 (2012), 349–354.
[6] D. Buzza, "P91 Piping Fabrication Guidelines, in: American Electric Power Combined Cycle User's Conference, USA, 2013, Available from: http://ccusers.org/wpcontent/uploads/2012/04/111031_CCUG_P91_Fabrication_Guidelines_Dave_Buzza-1. pdf (accessed: 05 May).
[7] R.L. Klueh, J.P. Shingledecker, Investigation of a Modified 9Cr– 1Mo (P91) Pipe Failure, ORNL/TM-2006/1, Oak Ridge National Laboratory, Tennessee, 2006.
[8] J. Parker, "The Use of Portable Hardness Testing in Field Applications for Grade 91 Steel," The Electric Power Research Institute (EPRI) Report No: 1024695, June 2012.
[9] A. Mondal, A.K. Das, S. Chand, "Application of Advanced NDE Tools for Health and Life Assessment of Critical Power Plant Components During the Flexible Operation Regime," In: Ghose, B., Manoharan, V., Mulaveesala, R. (eds) (2024). Advances in Non-Destructive Evaluation (NDE). NDE 2021. Lecture Notes in Mechanical Engineering. Springer, Singapore. https://doi.org/10.1007/978-981-97-1036-2_17
[10] A. Mondal, A.K. Das, "Internal AUSC Project Titled "Non-destructive Evaluation of Post Weld Heat Treatment Quality of Ferromagnetic Steel (P91) Weld by Magnetic Coercive Force (MCF) Measurement", Project No: AUSC-N-NTR-NDEL-006, Report Submission (July 2019).
[11] R. K. Roy, A. K. Das, A. K. Metya, A. Mondal, A. K. Panda, M. Ghosh, S. Chand, S. P. Sagar, S. K. Das, A. Chhabra, S. Jaganathan, A. Mitra, "Microstructure Atlas of P91 Steel", Springer Singapore, Published: 27 April 2023, https://link.springer.com/book/10.1007/978-981-19-9562-0
[12] E. Sambamurthy, S. Dutta, A. K. Panda, A. Mitra, R. K. Roy, "Evaluation of Post-Weld Heat Treatment Behavior in Modified 9Cr-1Mo Steel Weldment by Magnetic Barkhausen Emission," International Journal of Pressure Vessels and Piping 123-124 (2014) 86-91.
[13] R. K. Roy, P. Murugaiyan and A. K. Panda, "Evaluation of Post-Weld Heat-Treated 2.25Cr-1Mo Steel Joint Behaviors by Electromagnetic NDE Parameters," Journal of Superconductivity and Novel Magnetism, Research, Volume 3, (July 2024), Pages 1677–1687.
[14] A.K Das, A. Mondal, S. Chand, A. Chhabra "In-situ Detection and Quantification of Oxide Scale Exfoliation in Stainless Steel Boiler Tubes by Magnetic Coercive Force (MCF) Measurement., In: Mandayam S, Sagar SP (eds) Advances in non-destructive

evaluation. lecture notes in mechanical engineering. Springer, Singapore. https://doi.org/10.1007/978-981-16-9093-8_14.
[15] J. Shingledecker, "Evaluation of Grade 91 Microstructure and Creep Rupture Strength as a Result of Heat Treatment Around the Intercritical Zone," The Electric Power Research Institute (EPRI) Report No: 1015818, March 2009
[16] J. Siefert, "Creep Strength-Enhanced Ferritic (CSEF) Steel Welding Guide," The Electric Power Research Institute (EPRI) Report No: 1026584, August 2013
[17] M. Sireesha, S.K. Albert, S. Sundaresan, "Microstructure and Mechanical Properties 0f Weld Fusion Zones in Modified 9Cr– 1Mo Steel," Journal of Materials Engineering and Performance 10 (3) (2001) 320–329.
[18] G. Guntz, M. Julien, G. Kottmann, F. Pellicani, A. Pouilly, J. C. Vaillant, The T91 Book: Ferrtic Steel Tube and Pipe for High Temperature Use in Boilers. France: Vallourec Industries; 1990.
[19] J. Parker, "The Effect of Variables on the Results of Field Hardness Testing of Grade 91 Steel," The Electric Power Research Institute (EPRI) Report No:1024694, November 2011
[20] L. Cipolla, P. Folgarait, J. Parker "Advanced Metallurgical Characterization of Grade 91 Steel Samples," The Electric Power Research Institute (EPRI) Report No: 1024721, January 2012

Industrial RO Membrane Based Demineralization Plant Performance Optimization - An Innovative Low Level Silica Pretreatment Approach

Narendra K Soni, TN Seetharaman, M M Dastagir, B Srinivas
Advanced Instrumentation Lab, Chemistry Department, NTPC R & T, Ramagundam, Telangana, India

narendraksoni@ntpc.co.in

Abstract. India is a water-stressed country, having only 4% of the world's water resources available for 18% of the world's population. Multi-stage Reverse osmosis (RO) in combination with wastewater RO(WW-RO) is in practice now for the Industrial demineralization process actualizing the zero liquid discharge concept. The design of the de-mineralization plant depends upon the quality of the water source. Natural water holds a considerable amount of silica (SiO_2) up to 100 mg/L. The factors affecting RO membrane performance were studied, of which, silica fouling in combination with minerals and organics is found to be the main factor among other factors. The silica is hence complex in nature and silica fouling is generally not easy to control, thereby, resulting in performance failure of RO membranes. The present study discusses the effect of dolomite treatment, soluble magnesium compounds and sparingly soluble magnesium compounds on silica removal in boiler-feed water. It is found that the dolomite treatment in the pre-treatment step is ineffective for silica removal. The effective silica removal with soluble magnesium compounds increases the conductivity in the treated waters, and with sparingly soluble magnesium compounds is found only 40% effective; for increased effectiveness up to 86% pre-acidification was the condition which caused conductivity increase. In the present study, 90% of silica removal is achieved without pre-acidification along with the co-benefit of conductivity re-duction of feed water to the RO system. Therefore, the developed solution is efficient, cost-effective and environmentally friendly, which has not reported so far and is unclear in the literature available.

Keywords: MgO, Silica removal, Pre-treatment, Reverse osmosis Membranes.

1. Introduction

Globally, India ranks fifth in terms of electricity generation and sixth largest energy consumer with a growing energy demand of 3.6% per year due to economic development. The total electricity demand is projected to cross 950 GW by 2030[1]. India per capita water availability is declining rapidly due to factors like population growth, urbanization, industrialization, and climate change [2]. The National water consumption is expected to grow from 1.4% in 2025 to 9% by 2050 in power generation and this figure is likely to vary quite significantly from region to region[3]. In India, as per the business business-as-usual scenario, it is projected that the Industrial sector's Gross domestic product(GDP) contribution will be around 40% of the total GDP and

S. Shaswattam et al. (eds.), *NTPC Transactions on Energy Research (NTER 2025)*,
https://doi.org/10.2991/978-94-6463-849-3_7

the Industrial water demand is expected to increase by 102 m^3/person/year by 2050. The scarcity of water is already being faced by thermal power plants due to the non-availability of fresh water and this problem is expected to be further aggravated. Thus, there will be an urgent need to minimize water consumption requirements for thermal power plants.

Multi-stage Reverse Osmosis in combination with wastewater RO (WW-RO) presently is in practice for environment friendly industrial demineralization in line with the zero liquid discharge practices. Its design and efficiency depend upon the source water quality. Natural water sources hold silica (SiO_2) 1-40 mg/L and in some geographic areas, about 100 mg/L [4-7]. Due to silica's complex nature, silica fouling control is quite difficult, which often causes failure in RO system performance. The silica removal using soluble magnesium compounds was found effective, but they increased the conductivity in the treated waters. Therefore, the use of sparingly soluble magnesium compounds was found to be a promising alternative but only 40% silica removal was obtained, for higher Silica removal of 80-86% pre-acidification was needed [8]. In the present study, effectiveness of silica removal is found 90% without pre-acidification with the additional benefit of reduced feed conductivity to RO as suggested elsewhere[9]. Commercial use of powerful cleaning chemicals like hydrofluoric acid (HF) and ammonium bifluoride (NH_4HF_2) generally in practice to control silica fouling, but can cause equipment, membrane damage and environmental concerns [10]. Due to fouling, the recovery rate reduces and demands high feed water and more reject generation for the equal water treatment volume. This may further cause inefficient running and sometimes cause complete failure of the RO system. Since the raw water source available is hard water of a high pH around 8.5, the calcium-induced silica fouling is also one of the possible reasons for failure in the performance of RO membranes in line with earlier findings, Severe colloidal silica fouling was also observed during the trial using hardwater, evident by more rapid flux decline, more colloidal silica on scaled membrane in autopsy and an increased amount of silica from dissolving scaling species on scaled membranes surfaces[11]. The mineral scaling issue is also seen in RO membrane, found responsible for low water recovery rates and deteriorated system performance, Gypsum scaling causes pore wetting by crystallization mechanism silica scaling forms highly adhesive, irreversible layers, by polymerization mechanism [12]. The relationship between membrane surface properties and silica fouling in RO is also proven where the strong relationship of silica scaling with the membrane surface charge was seen [13]. Demineralization plays a crucial role in preventing silica entry to the boiler for steam generation, the elevated silica concentrations in steam can lead to silica deposition in the low-pressure turbine. Also, a thin layer of silica scale in the boiler can cause boiler tube failure and result in huge economic loss to the power plant.

The higher water treatment cost of is affordable in comparison to efficiency loss due to scale deposition in water wall tubes resulting in low heat transfer, and high fuel consumption which may further lead to boiler tube failures and hence forced shutdown of power plant unit. The boiler tube with iron and silica scale is shown in Fig.1 and the composition of the scale is shown in Table 1.

Fig.1. The picture showing boiler tube blockage with predominantly iron and silica rich deposit.

Table-1 Chemical Analysis of the boiler tube blockage material

Sample Name	% Fe as Fe_2O_3	% Cu as CuO	% Ca as CaO	% Na as Na_2O	% Mg As MgO	% K As K_2O	% Si As SiO_2
Deposit sample	65.4	1.49	0.13	0.46	0.15	0	25.2

Even small-scale boiler of 500hp can have 2% energy loss with calcium and magnesium scale of 0.8mm and same thickness scale of iron and silica the energy loss is multiple times i.e. 7%[14].

1.1 Background

Agricultural development has exponentially increased in recent times near the power plant study area, resulting in increased organic loading in source water[Table 2]. The presence of organics in water along with silica can accelerate the silica fouling in RO membranes. Silica fouling against organic content loaded in feed water was an added research challenge[15]. The same has been seen elsewhere in autopsy results of high Loss on Ignition (LOI) value along with the presence of silica and other metals. The foulant composition had organic matter and inorganic matter, viz., iron, calcium, magnesium, acid insoluble matter, silica, sulphate, molybdenum, boron, potassium,

sodium, hydrocarbons, total phosphate, organo-phosphate, ortho-phosphate. Simultaneously, minor contaminants like soluble organic fouling, chromium, aluminum, manganese, sulphite, cobalt, copper, nickel, zinc, and fluoride have shown their adequate presence. The introduction of sodium hypochlorite (hypo) dosing in combination with ClO_2 in clarifier helped us in controlling organics.

After pretreatment, the demineralization plant includes the ultrafiltration-reverse osmosis-mixed bed (UF-RO-MB) system. In the RO systems, two key parameters of permeate (silica and conductivity) were showing signs of deterioration over time and indicative of several factors that could be impacting the overall efficiency and lifespan of the membranes[Fig-2&3]. The RO permeate conductivity and silica were found to be touching 80 µS/cm and 8500 µg/L against design estimates of 32.47 µS/cm and 286 µg/L respectively. The parameters are found to show an increasing trend from the start of the RO plant operation. Since the commissioning, the design raw water reactive silica was 20 to 23 mg/L as SiO_2 and the silica in the clarifier outlet of the pre-treatment plant was maintained 18-19 mg/L against the design value of 10 mg/L[Table-3]. At the ultrafiltration (UF) outlet, the SDI values were touching five against the design value of maximum 3 where SDI parameter T1 was found around 50 seconds against the recommended value of 20 seconds, indicating issues in the pre-treatment step and resulted in forced shut down of UF-RO-MB demineralization plant.

Table-2: Total Organic Carbon (TOC) measurement data**.**

Sample Name	TOC (mg/L)
Raw Water	6.974
Aerator O/L	6.527
Clarifier O/L	5.984
Filter bed O/L	5.744
UF I/L	5.850
UF O/L	4.643
RO Permeate	0.113
RO Reject	107.9

Table-3: Reactive silica Value variation in DM Process.

Sample Name	Reactive silica(mg/L)
Raw water	20-23
Clarifier outlet	18-19
RO inlet	16-18
RO permeate	0.9-8.5
RO reject	102-58
MB outlet	0.007-0.012

Investigation and root cause analysis were performed, and several process modifications were made like at Pretreatment, the dosing points were shifted to near aerator to have enough opportunity for mixing and reaction time from earlier dosing point at clarifier, scrapper drive of DM clarifier under continuous operation, the design oxidation-reduction potential(ORP) was revised from 100 to 200 and recommended to keep below 200, optimized dosing of ClO_2 along with sodium hypochlorite, maintaining the UF & RO cartridge pre-filter dP below 0.5 kg/cm2 and the chemical enhanced backwash frequency of UF has been doubled given fouling, however, integrity of UF membrane was found ok, but improvement in SDI was observed for shorter duration only.

It was noticed that UF was having periodical differential pressure(dP) high for which backwash frequency has been doubled, the rise of dP from about 0.5 kg/cm2 to 0.9 kg/cm2 was unusual. The main cause for this was supposed to be iron, turbidity and organic fouling, The raw water TOC is seen to be more than 7 mg/L. It was found that UF is not at all preventing the passage of colloidal silica which it was expected to do. Some membranes were extracted earlier for autopsy analysis at another plant with a history of RO efficiency deterioration, the analysis revealed the type of foulants that have clogged the membranes, thus easing root cause analysis and prevention in the future. As per the report, the main foulants were silica, colloidal silica, phosphate, and iron. The sample elements were taken from the front and rear ends of RO stage 1. The visual observation showed the fouling, the front one was more fouled showing iron and colloidal fouling were predominant factors. This also con-firmed the initial assumptions. The probe test and its analysis revealed many of the membranes were irreparably damaged. Also, there was a problem of flow balancing, among membranes. The use of silica-based anti-scalant for high reactive silica at the RO inlet was started, however, no improvement in permeate parameters was observed.

The UF & RO membrane's performance so deteriorated that it was not economical to use them further for water de-mineralization. Therefore, the replacement of both UF & RO membranes was done. Even after the replacement of the new UF & RO membrane, the SDI was maintained just below the manufacturer's SDI limit of five but not below three and the initial time(T1) parameter of SDI was also found more than the recommended value of 20 seconds. The RO permeate silica was found to be multiple times (more than 1 mg/L) than the design (0.3 mg/L) due to high input silica (>10 mg/L) in the RO feed with the existing dolomite treatment. The high silica in RO permeates further reduces the output of MB and results in high chemical consumption and, short operational life of resin and equipment. Hence, improvement of the pre-treatment process along with silica reduction below ten mg/L is the key factor of performance improvement of the DM plant.

Mitigating silica scaling in subsequent RO systems, the silica concentration reduction in the feed water during the pre-treatment step and the remaining particle removal in UF can be a simple but effective step. In this section, experiments were done to mitigate the silica issue of the pretreatment-demineralization (PT-DM) system. In the present case, the conventional dolomite treatment was seen to be ineffective for silica removal and contributed as a primary factor in the performance deterioration of RO membranes. The effective silica removal with soluble magnesium compounds increases the conductivity in the treated waters while a promising alternative of using sparingly

soluble magnesium compounds can achieve only 40% silica removal; for higher Silica removal of 80-86%, pre-acidification was needed. In the present study, 90% of Silica removal is achieved without pre-acidification along with the co-benefit of conductivity reduction of feed water. [16]. The result obtained with sparingly soluble magnesium compound was not only effective for silica removal but also decreased the conductivity of pre-treated water significantly, Therefore, the developed low-level silica reduction along with conductivity reduction in pretreatment step of RO-based Demineralized water treatment plant is efficient, cost-effective and environment friendly, which is not covered so far and unclear in the literature available [17-18]

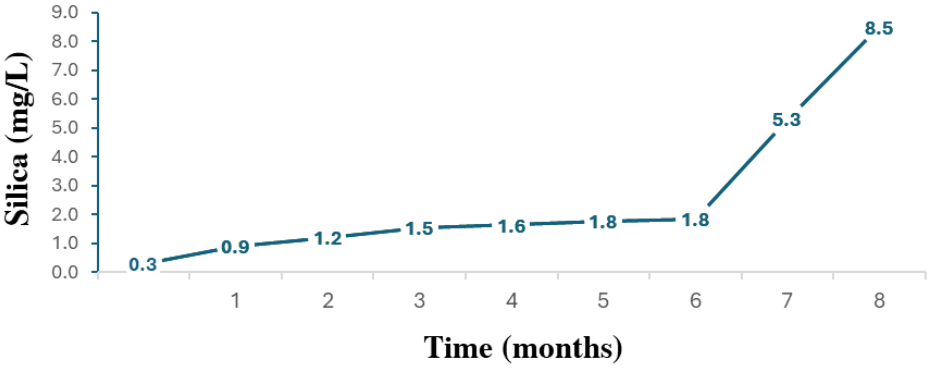

Fig.2. The performance deterioration of RO with respect to permeates silica.

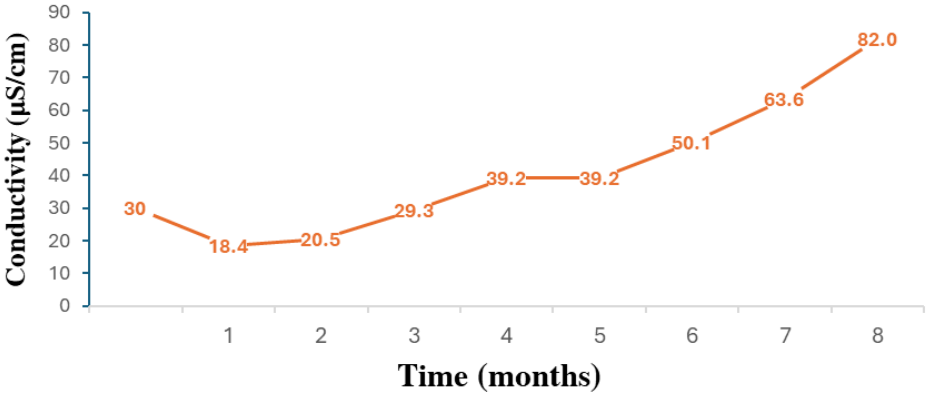

Fig.3. The performance deterioration of RO versus permeates conductivity.

1.2 Chemistry of Silica

The chemistry of silica (SiO_2) is complex, silica has four covalent bonding sites like carbon. The silica nucleus is bigger as compared to the nucleus of carbon, double

or triple bond formation is not common in silica, also more than six silica atoms long chain compounds are not common. silica exists in different crystalline as well as amorphous forms. In water, the solubility of crystalline silica is exceptionally low in the order of six mg/L SiO_2. Amorphous silica solubility of 100-140 mg/L has a much higher SiO_2. When silica is dissolved in water, it forms Mono silicic acid ($Si(OH)_4$) which monomeric will remain in the state if its concentration stays less than about 2 mM [19]. In comparison to carbonic acid Silicic acid is a weak acid with a smaller Ka than carbonic acid. Silicic acid K1 = $2x10^{-10}$, silicate ions can be found only a few µg/L at neutral pH, but the presence of alkalinity encourages the formation of silicate ions, increasing the solubility of "silica"[Eq.(1)].

$$Si(OH)4 + OH^- \rightarrow [SiO(OH)3]^- + \mathrm{H2O} \quad (1)$$

With the increase in pH, silica solubility increases and at pH around ten, silica is found in the form of silicate ions and is soluble, which is found in the present study too. In the absence of alkalinity or other stabilizing ions, Silicic acid molecules polymerize easily as $(H2SiO_3)n$. Silica is one of the most common scales on RO membranes during desalination processes. The silica exists in three forms firstly Monomer silicic acid ($Si(OH)_4$), which is also known as dissolved or reactive silica, secondly colloidal or polymer silicic acid, and thirdly particulate silica as clay, silt, and sand. Colloidal silica does not react with ammonium molybdate and is referred to as non-reactive silica [20-21].

Table-4 Different type of Silica with Size [23]

Silica form	Size(microns)
Filterable	>0.45
Colloidal	0.01-0.45
Polymeric	<0.01
Monomeric	<0.0001

The particles below 0.1 microns are likely to exist in dissolved form. The colloidal silica can appear after digestion like in a power plant boiler drum at high pressure and temperature. The filterable silica, less than 0.45 microns can be evaluated using a 0.45- micron filter to find the silt density index (SDI) ahead of RO systems [Table 4]. Silica solubility is of important concern as it gets concentrated in the reject stream of the membrane. RO systems cannot achieve complete removal of reactive silica-like ion exchange but are far better in removing non-reactive silica like colloidal as well as particulate silica

1.3 Chemistry of Magnesium oxide & Silica

Magnesium is the eighth most abundant element in the Earth's crust (about 2.3% by weight) and the third most abundant element in seawater solution (about 1300 mg/L), present naturally as dolomite, magnesite, and silicate in rocks. The market volume of magnesium oxide (MgO) is estimated to be around 22.6 million metric tons by 2030[22]. The light burnt or calcined MgO has high reactivity and a large specific surface area. The large surface area and proximity to silica molecules allow MgO to be

much more effective as found in the present case. The advantage of calcined MgO is that it adds almost no dissolved solids to the water. pH and temperature are also key factors in silica reduction by precipitation. The precipitation increases with increasing temperature and completes at elevated temperatures. pH kept high enough i.e., Higher than ten to result in precipitation of magnesium but controlled in such a way that not to go so high i.e., more than eleven which can make the precipitant resoluble.

$$MgO + SiO2 \xrightarrow{pH\sim10} (MgO)x\,(SiO2)x\,.\,(H2O)x\ (x = \text{variable}) \qquad (2)$$

Silica removal by magnesium hydroxide is not clear and may be simple adsorption onto the surface of $Mg(OH)_2$ and removed to a certain extent with concurrent precipitation with $Mg(OH)_2$ or Magnesium silicate may be formed [e.g., Mg_2SiO_4 (Forsterite)]. However, Magnesium-based compounds along with Coagulants and Flocculants are found quite effective in promoting the aggregation of small particles into larger flocs and therefore lead to clear water at the outlet of the clarifier[Eq.(2)]. The clarity of the water at the upper side of the precipitated flocs was monitored and compared with the different test jars. The jar having the clearest water shows the most successful treatment conditions [23-25].

2. Experimental

2.1 Materials and methods

The Indian standard 3025-50 (2001): methods of sampling and tests (Physical and Chemical) for water and wastewater, part 50: Jar Test (Coagulation Test) was used to determine the optimum dosage of coagulant, coagulant aids and the optimum pH of coagulation for removal of turbidity and color caused by colloidal and non-settleable particles followed by sedimentation under quiescent condition.

The instrument used for this study consists of a semi-automatic jar test apparatus Scientech make, model SE-157 supplied by ISO 9001 certified M/s Scientech, India,

The jar test apparatus used has an LED digital display, a touch-sensitive keypad, six jars, and six stainless steel stirring paddles with a 10-300 rpm speed range along with a speed regulator and timer that supports a determination of the exact amount of input needed to trigger flocculation.

Standard methods for the examination of water and wastewater, APHA 24th edition, 4500-H^+ pH, 2510-conductivity, 2130-turbidity, 4500-SiO_2 silica, method 3111D were used to determine the parameters including reactive as well as colloidal silica.

The material used during the jar test experiment is optimized as calcined MgO, hydrated lime, ferric chloride and anionic polyelectrolyte(PE) (Table 5).

Table-5 Material used for jar test study

Material	Grade	CAS No.
$FeCl_3$	IS 711:1970(2006)	7705-08-0
Hydrated Lime	IS 1540:1990(2003)	1305-62-0
Dolomite	IS 1760-3 (1992)	16389-88-1
PE	Industrial grade	9003-05-8
Calcined MgO(light)	Industrial grade	1309-48-4

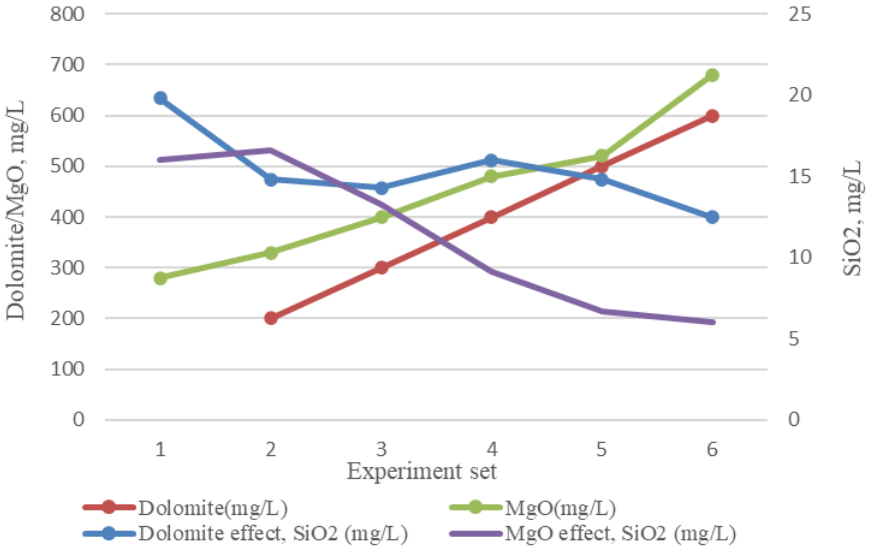

Fig.4. Dosing optimization of dolomite and MgO for silica reduction

Various experiments were performed to establish the optimum combination of Dolomite as well as MgO, but even after using up to 600 mg/L dolomite silica reduction could not achieve the design requirement of less than 10 mg/L silica at the feed of RO, however, it could be achieved with only 480 mg/L MgO [Fig.4].

Jar tests with various combination has been performed which simulate the similar conditions of mixing and settling present in clarifiers of pre-treatment plants with the proper control of stirring speed[Table-5]. The 480mg/L has been found the optimized dose of MgO for required silica reduction of less than 10mg/L, while with dolomite, it could not be achieved

Table-5 The comparison of jar test results obtained versus raw water quality

Parameters/Set	Set-1	Set-2	Set-3	Set-4	Set-5	Set-6
Dolomite(mg/L)	200	300	400	500	600	700
MgO(mg/L)	280	330	400	480	520	680
SiO_2 (mg/L), Dolomite effect	14.8	14.3	16	14.8	12.5	17.4
SiO_2 (mg/L), MgO effect	16	16.6	13.3	9.1	6.7	6

3. Result & discussion

The pre-treatment of river water is an essential integral step to producing quality DM water. The design input silica requirement for RO based DM plant was 10 mg/L, the existing dolomite-based treatment combination of dolomite, FeCl3, lime and poly-electrolyte (PE) was found to be ineffective and not able to reduce the silica level at the desired design level whereas the newly developed treatment methodology MgO, $FeCl_3$, lime and PE can address the silica issue and found to be promising silica treatment option for RO based DM plant. The co-benefit of the developed method is not only found promising in the removal of reactive silica, but the more problematic colloidal silica is also reduced quite significantly. The other advantage of the method is a reduction in Conductivity which further reduces the ionic load on RO membranes and hence enhances life and performance of the RO-DM system.

The Jar test results has been compared for both dolomite as well as MgO under similar conditions of mixing and settling present in clarifiers of pre-treatment plants with the proper control of stirring speed[Table-6]. The material used during the jar test experiment is optimized as MgO 480 mg/L, Lime 120 mg/L, $FeCl_3$ 30 mg/L and PE 2 mg/L.

Table-6 The comparison of jar test results obtained versus raw water quality.

Parameters	Raw water	Design Dolomite treatment	Newly developed treatment
pH at 25°C	8.8	10.14	10.04
Sp. Cond(µS/cm)	451	358	357
Turbidity (NTU)	1.60	0.2	0.1
Total SiO_2 (mg/L)	32.1	14.2	3.20
Colloidal SiO_2 (mg/L)	12.0	1.3	1.0
Reactive SiO_2 (mg/L)	20.1	12.9	2.2
Silica reduction (%)		56%	90%

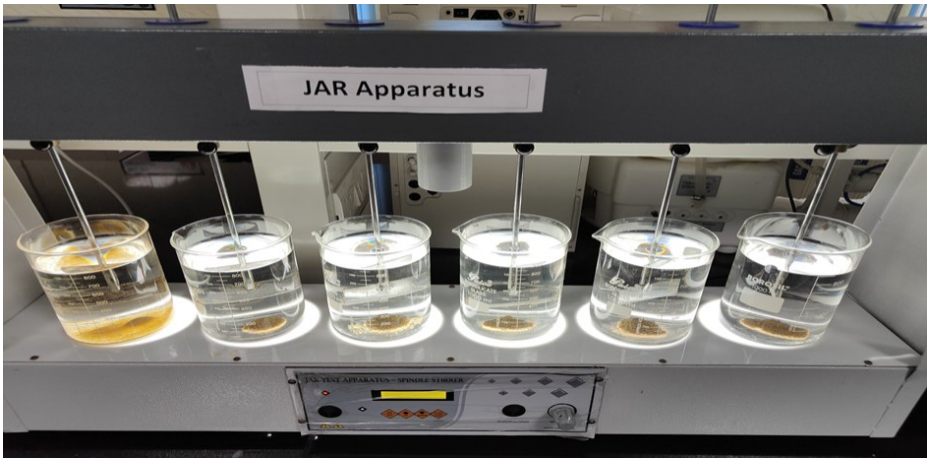

Fig.5. Test setup shows clear water after test completion. (most clear water in right most jar of optimized Mg based treatment)

It can be seen in the above results that the dolomite for silica treatment in combination with other OEM recommended pre-treatment plant (PTP) chemicals are found to be only 56% while Mg-based compound with the same other OEM recommended PTP chemicals were found to be most effective in treating reactive as well as colloidal silica. Lab simulation efforts were started to find primary factors, interrelation of constructive interaction among factors, if any, and to discover any other controlling factors that might exist to make pretreatment at WTP more effective. The design of the experiment (DOE) initially constituted two factors with dolomite, $FeCl_3$, PE and lime as originally designed by specification[Fig.5]. When this did not reach the desired result, another substitute for dolomite chemical was found and a three-factor with three-level experiment was planned. In total, more than twenty experiments were performed at the lab. Finally, the best formulation of substitute chemicals was found to produce acceptable results as per the goals set out in the planning stage. The most noteworthy was the finding that simply replacing dolomite with another suitable substitute keeping all other dosing chemicals constant, could reduce both iron, TOC, and colloidal best through a three-factor constructive interaction. The proposed pre-treatment is effective in reducing both forms of silica, i.e., reactive, and colloidal silica.

The developed solution is a key step toward mitigating the challenges associated with the pre-treatment of silica in the DM-RO plant.

1. Realistic assessment of designed dolomite treatment
2. Ascertained the factors towards UF-RO deterioration.
3. Effectively running the Clarifier with optimized chemical dosing.
4. Ascertained the reasons behind design silica carryover in the pre-treatment step.
5. Developed a method for obtaining the Silica level below the design value for the RO inlet.

4. Conclusion and Recommendations

The factors affecting RO membrane performance were studied, the mineral and organics-induced silica fouling is found to be the main factors among other factors. The silica is complex, and its fouling is not easy to control, which results in the performance failure of RO membranes. Mitigating silica scaling in subsequent RO systems, the silica concentration reduction in the feed water during the pretreatment step and the remaining particle removal in UF can be a simple but effective step. In the present study, various Jar test experiments were performed to establish the optimum combination of dolomite as well as MgO, but even after using up to 600 mg/L dolomite silica reduction could not achieve the design requirement of less than 10 mg/L silica at the feed of RO, however, it could be achieved with only 480 mg/L MgO. The key finding of the proposed pre-treatment is that it is effective in reducing both forms of silica, i.e., reactive, and colloidal silica and 90% silica removal is achieved along with the co-benefit of conductivity reduction without the pre-acidification requirement as suggested elsewhere. Therefore, the developed solution is efficient, cost-effective and environmentally friendly, which has not been reported so far and is unclear in the literature available. In NTPC, the treatment is its first of a kind and can be replicated in the PT-UF-RO-MB demineralization plants operational at many of its thermal power plants for further efficiency improvement.

Acknowledgments. The authors are grateful to Sh. Shaswattam, ED(NETRA), Sh. C K Samanta, HOP(R&T), Sh. Prasenjit Pal, Project Director (MBRAPP), Sh. A K Tripathi, GM(O&M) Ramagundam, Sh. A R Dash, GM(O&M) Telangana, Sh. V. Chandrasekharan, GM(CC-OS), Sh. Santosh Tiwari, GM(C&T) Telangana, Sh. A.K. Das, GM (NETRA), Sh. L K Nayak, AGM(PE Mech-WS) for their valuable guidance, support & encouragement to carry out the study useful for operating stations to address silica chemistry-induced failures at RO-based de-mineralization plants. The authors are also thankful to Sh. T Radhakrishna, Sh. Prag Sood, Ms. Priya L, Sh. Prahlad Haldar, Sh. Anand Verma, Sh. Vignesh T, Sh. Ankit Verma, Sh. Pranay, Sh. Abhijit S, Sh. R K Tripathi, Sh. H K Joshi and Sh. Aditya R Gokhale for extending valuable support during the study. The authors are also thankful to team R&T Chemistry, OS-Chemistry and NETRA for their regular support during the study

Disclosure of Interests. The authors have no competing interests to declare that are relevant to the content of this article.

References

1. Study of assessment of water footprints of India's long term energy scenarios New Delhi, The Energy and Resources Institute, Niti Aayog, Project Report No. 2015WM07, (2017)
2. Evaluation of centrally sponsored schemes in water resources, environment and forest sector, approach & methodology, report 2020/UCSS09/1 (2020)
3. Al-Rehaili AM., Comparative chemical clarification for silica removal from RO groundwater feed. Desalination. 159:21–31 (2003)
4. Gorzalski AS, Coronell O., Fouling of nanofiltration membranes in full-and bench-scale systems treating groundwater containing silica, J Membr Sci.,468, 349–359 (2014)

5. Sheikholeslami R, Bright J., Silica and metals removal by pretreatment to prevent fouling of reverse osmosis membranes. Desalination, 143, 255–267. (2002)
6. Neofotistou E, Demadis KD., Use of anti-scalants for mitigation of silica (SiO_2) fouling and deposition: fundamentals and applications in desalination systems, Desalination, 67, 257–272 (2004)
7. Ning RY, Discussion of silica speciation, fouling, control, and maximum reduction, Desalination, 151, 67–73 (2003)
8. Isabel Latour et al., Silica removal with sparingly soluble magnesium compounds, Separation and Purification Technology, vol.138, pp. 210-218. (2014)
9. E. Sarabian et al., Synergistic effect of calcium and magnesium on silica polymerization and colloidal silica fouling in bench-scale reverse osmosis filtration, Desalination and Water Treatment, 3081–17 (2023)
10. K.-G. Lu, M. Li, H. Huang, Silica scaling of reverse osmosis membranes preconditioned by natural organic matter, Sci. Total Environ., 746, 141178, (2020).
11. Jiapeng Li et al, Study of the fouling behavior of typical inorganic-organic foulant in silicates-bearing mine wastewater on reverse osmosis membrane, Journal of Environmental Chemical Engineering, vol 12(3), 113117, (2024)
12. Tiezheng Tong et al, A tale of two minerals: contrasting behaviors and mitigation strategies of gypsum scaling and silica scaling in membrane desalination, Frontiers of Environmental Science & Engineering, vol 19, 3, (2025)
13. Tiezheng Tong et al., Relating Silica Scaling in Reverse Osmosis to Membrane Surface Properties, Environmental Science & Technology. vol 51(8), (2017)
14. Robert G massey, Energy conservation program guide for industry and commerce(EPIC), NBS handbook 115, supplement 1, 3-26, (1975)
15. Quay AN, Tong T, Hashmi SM, Zhou Y, Zhao S, Elimelech M. combined organic fouling, and inorganic scaling in reverse osmosis: role of protein–silica interactions. Environ Sci Technol. 52, 9145–9153, (2018)
16. Isabel Latour et al, Silica removal with sparingly soluble magnesium compounds, Separation and Purification Technology, vol 138, pp 210-218, (2014)
17. Ivonne García et al, Continuous electrocoagulation-flocculation-sedimentation process to remove arsenic, fluoride, and hydrated silica from drinking water, Journal of Water Process Engineering, vol 69, 106571, (2025)
18. Park, D et al, Combined impacts of aluminum and silica ions on RO membrane fouling in full-scale ultrapure water production facilities, Desalination, vol. 577, 117380, (2024)
19. Peter Meyers, Behavior of silica in ion-exchange and other systems, international water conference, Pittsburgh, PA, (1999)
20. E.G. Darton, M. Fazell, A statistical review of 150 membrane autopsies, 62nd Annual International Water Conference, Pittsburgh, pp. 157–163 (2001)
21. Ralph K. Iler, The chemistry of silica: solubility, polymerization, colloid and surface properties and biochemistry of silica, pp. 896 (1979)
22. Global magnesium oxide market, Statista Research Department, vol. 2015-2030 (2024)
23. Indian Standard of Sampling and Tests (Physical and Chemical) for Water and Wastewater, Methods IS:3025, P-50 (2001)
24. Ralph K. Iler, The chemistry of silica: solubility, polymerization, colloid and surface properties, and biochemistry of silica. John Wiley & sons, pp. 896, (1979)

S.D. Faust, O.M. Aly, Chemistry of water treatment, Butterworths publishers, (1983

A Comparative Electrical and Physicochemical Parameter Study for Fault Analysis and Health Assessment of Transformers through Insulating Oil

Sujit Kumar Guchhait, Shyam Khatana, Rajendra Kumar Saini*, Anil Kumar Das
Transformer Oil Lab, NTPC Energy Technology Research Alliance, NTPC Ltd.,
Greater Noida, Uttar Pradesh, India.
*rajendrakumarsaini@ntpc.co.in

Abstract. Power plant transformer health evaluation plays a significant role for efficiency and continuous performance in electric power generation and transmission. When a power transformer is in service, it faces numerous stresses such as electrical stress, thermal stress etc. leading to the release of various C1-C3 hydrocarbon gases (i.e., methane, ethane, acetylene, ethylene, etc.) from the transformer oil and other gases such as CO_2, CO, hydrogen from paper insulation etc. along with various electrical & physicochemical properties such as specific resistivity, Tan Delta, and breakdown voltage (BDV), among others, are altered. In this context, health assessment and continuous monitoring of transformers and failure analysis are crucial to the reliability of a thermal power plant. In this work, we have considered 10 different transformers and comparatively studied these transformers via dissolved gas analysis and various electrical & physicochemical parameters via transformer oil analysis to interpret types of failure and monitor health of a transformer. From this study it has been found that OS6 sample shows the highest amount of hydrogen (2267 PPM) which suggests partial discharge taking place in the transformer. On the other hand, OS2 and OS6 samples show a high amount of acetylene which indicates arcing occurring in the transformer. BDV of OS6 is also less in compared to recommended value. This may be due to the high amount of moisture present in the sample.

Keywords: Power plant transformer, Insulating oil, Aging, Dissolved gas analysis.

1 Introduction

The requirement for the enhancement of electrical power grid infrastructure is of paramount importance, particularly due to the rising distribution of thermal power units to facilitate the current transition to smart grids. Transformers are one of the significant and costly elements of an electricity network, regardless of whether it is utilized for generating, transmitting, or distributing electricity [1]. Any failure in the transformer produces an abrupt disruption in power supply, raises the cost of repair, and affects the efficiency of the power system. As a result, preventing transformer failure and maintaining continuous operation is vital to the entire system's resiliency. The insulation component of an electrical transformer plays a role for its long-term dependability and safety [2]. Cellulose and insulating oil insulation are critical components of oil-immersed transformer insulation design due to their high dielectric strength, which allows them to resist elevated voltages and avoid an arc discharging. It may also monitor the transformer's electrical and chemical conditions and improve heat dissipation in the core and windings that heated up throughout operation due to various power losses [3]. Transformer oil can be categorized into two types: (a) mineral oil and (b) synthetic oil. Mineral oil is also categorized into two parts i.e. naphthenic type mineral oil and paraffinic type mineral oil whereas ester-based and silicone-based oils

S. Shaswattam et al. (eds.), *NTPC Transactions on Energy Research (NTER 2025)*,
https://doi.org/10.2991/978-94-6463-849-3_8

are examples of synthetic oils [4]. A power transformer experiences electrical and thermal stress during operation which leads to various incipient faults. These faults subsequently generate a variety of gases which are partially dissolved in the transformer oil. Thermal breakdown and electrical disruptions are the two main reasons why gas forms within a running transformer. At standard working temperatures, all transformers produce some amount of gas. Transformers oil is a complex chain of hydrocarbon molecules that decompose in thermal or electrical faults. Carbon-carbon and carbon-hydrogen bonds are broken in the primary chemical processes. Hydrocarbon molecules and active atomic hydrogen are formed via this reaction. These components may react with one another to generate the following gases: hydrogen (H_2), methane (CH_4), acetylene (C_2H_2), ethylene (C_2H_4), and ethane (C_2H_6). Moreover, when insulation composed of cellulose is present, thermal breakdown or electric failures produce hydrogen (H_2), carbon monoxide (CO), methane (CH_4), and carbon dioxide (CO_2) [5-6]. Acetylene is mostly associated with arcing, where temperatures can rise to a thousand degrees; ethylene is associated with hot patches ranging from 150 °C to 1000 °C and hydrogen is produced because of partial discharge (PD) [6-8]. Dissolved gas analysis (DGA) is the most important and effective technique for assessing these gases in the condition of oil-filled electrical transformers [6, 8]. Based on the DGA results one can screen the transformer's health condition and implement the suitable preventative maintenance programmed to minimize unforeseen outages. Several ways to analyze transformer failures through DGA have been established, which can be classified into two types: conventional methods and computational methods [8- 12]. However, interpretation of dissolved gases results is often complex and should always be done with care. Roger's methods, Key gas, Doernenburg Ratios, Duval's Triangles and Pentagons are the most used in gas-in-oil diagnostics in addition to IEC 60599 [9, 13]. Rogers' approaches comprise three gas ratios: C_2H_2/C_2H_4, C_2H_4/C_2H_6, and CH_4/H_2, which are used for interpreting gases produced in mineral in accordance with IEEE guidelines [14]. The Rogers Ratios gives a lot of information on dissolved gas analysis (DGA) however it suffers from certain drawbacks. Transformer faults are also categorized using the Duval's Triangle Technique, which is based on the ratios of ethylene, methane and acetylene. It is to be noted that acetylene (C_2H_2) is associated with extremely high temperature/arcing faults, ethylene (C_2H_4) with high temperature faults, and methane (CH_4) with low energy/temperature faults. A diagram illustrating the proportions for each of these gases is positioned on both sides of the triangle. This procedure may be used to find out the six fundamental fault categories. The Duval Triangle approach's fault area limits are depicted in Figure 1 as % CH_4, % C_2H_4 and % C_2H_2. Fault zones are classified as follows in Figure 1: (i) partial discharges (PD) corona type; (ii) D1: discharge of lower energy; (iii) D2: discharge of high energy discharges; (iv) There are three types of thermal faults: T1 (temperature < 300 ºC), T2 (temperature < 300 ºC), and T3 (temperature > 700 ºC). Ahmed Maher et al. explored the dissipation parameters and DGA of minerals oil-based fluids after electrical and thermal failures [15]. Sherif S.M. Ghoneim et al established a new methodology to analyze dissolve as compared with the Duval Triangle, IEC, and Rogers' methods correspondingly [16]. Joseph J. Kelly has suggested that DGA is an important tool for fault and failure analysis of a transformer and recommended that dissolved-gas analysis may be done on a semi-annual or even a quarterly basis [17].

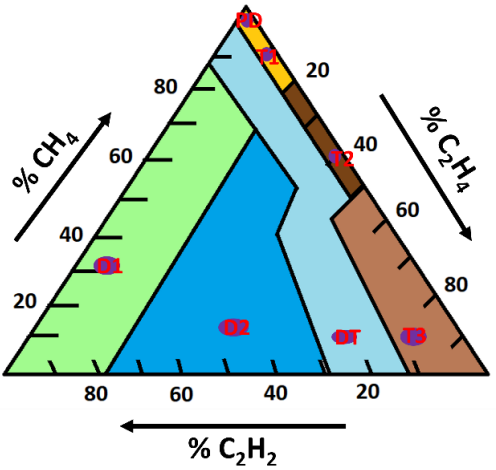

Fig. 1. General Duval Triangle Plot (not in scale) [12]

On the other hand, breakdown voltage (BDV), dissipation factor measurement (Tan δ), moisture analysis, acidity etc are the essential test parameters which can give more insights on the fault analysis [18-20]. The dielectric strength of an insulating material depends on the nature of voltage that is applied, electrode configuration, temperatures, and moisture. By using the outcome of the breakdown strength investigation of transformer oil, appropriate dielectric materials for the associated higher-voltage appliances could be investigated. Based on the previous literature survey, it has been found that there is very few research work are available which deals with failure and health assessment of power plant transformer through insulating oil analysis. This present work will give a broader in-depth concept and interoperation about the transformer oil analysis for failure and heath assessment of a transformer.

2 Experimental

Material and Method: Ten oil samples from different NTPC power plant transformers have been collected. The investigated oils are of mineral type and characterized as received, no further treatment has been done. In this present work oil samples (OS) have been designated as OS1, OS2, OS3, OS4, OS5, OS6, OS7, OS8, OS9 and OS10.

Dissolved gas in the transformer oil has been analyzed through transformer oil gas analyzer (TOGA) which consists of headspace GC of model no 7890B. The test oil samples are carefully transferred into the headspace viz. vial. The gases are removed starting the oil via means of the headspace auto-sampler and injected onto a 8890B GC with two detectors. The head space line temperature is 150 °C. The Thermal Conductivity Detector (TCD) was used for the analysis of hydrogen (H_2), oxygen (O_2), and nitrogen (N_2). The Flame Ionized Detector (FID) with methanizer was used for the analysis of methane (CH_4), carbon mono-oxide (CO), carbon di-oxide (CO_2), ethane (C_2H_6), ethylene (C_2H_4), and acetylene (C_2H_2). The fraction containing H_2, O_2, and N_2, CH_4, and CO is examined by molecular sieve-5 Å column. H_2, O_2, and N_2 are detected by the TCD. The TCD parameters are as follows: heater temperature is 150°C, reference flow is 25 ml/min and makeup flow gas are 5 ml/min. After passing through

the methanizer, CO and methane are detected by the FID. CO_2 and the C-2 product (such as C_2H_4, C_2H_6, etc.) have been separated and extracted from the PLOT-Q column when the molecular sieve column is bypassed. After passing through the methanizer, these are detected by the flame-ionization detector (FID). Argon is employed as a carrier gas to transport the chemicals in the injection loop from the stationary phase to the detectors. The flow rate of argon was 12 ml per minute and has maintained. Argon, air, nitrogen and hydrogen gases are 99.999 % pure. The test method at which 8890B GC-8697A HSS is operating as per ASTM D 3612-C. A brief GC program with ramped temperature is demonstrated in table 1. Moisture content has been measured using coulometric Karl fisher titration method using Mettler Toledo C-30 instrument. The test has been carried out according to ASTM D 6304 to measure water content present in transformer oil.

Breakdown Voltage (BDV) of insulating oil has been determined using Megger™ make an automatic breakdown voltage tester. This approach involves subjecting the oil to a constantly rising alternating voltage until it breaks down. The test has been carried out according to ASTM D877 to measure BDV of insulating transformer oil samples. Tan Delta & resistivity measurement of transformer oil has been carried out by automatic ADTR-2K Plus instrument. To determine the Tan δ, the sample of insulating oil is filled into a test cell. The electrical losses of the cell are then directly compared to those of the low loss standard capacitor after it has been connected to the circuit of an appropriate AC bridge. DC resistivity is determined by measuring the current that flows between the electrodes when a certain voltage is applied to the oil. Dielectric Dissipation Factor (DDF, Tan δ) and specific resistance measurement have been carried out according to ASTM D924 and ASTM D1169 methods respectively.

Total acidity in transformer oil sample has been determined as per ASTM D 974 test method. In this method oil sample is shaken well for uniform distribution of sludge in a glass bottle and agitate until all sediment becomes homogenously suspended in the oil. In a 100 ml plastic cup, introduce a weighed quantity of sample (10-15 gm) & add 60 ml of solvent used for titration (solvent mixture of Toluene: Isopropyl alcohol: water ratio = 500:495:5]. Swirl until the sample entirely gets dissolved in the solvent mixture. Titrate immediately at room temperature till the end point is reached through incremental addition of KOH solution and swirl to disperse the KOH as necessary. The total acidity has been calculated by the subsequent equation (1).

$$\text{Total Acid Number} = \frac{\{(\text{A} - \text{B}) \times \text{N} \times 56.1\}}{W} \text{ mg KOH per gm of oil} \quad (1)$$

Here "A" = amount of KOH (in ml) necessary for the titration, "B" = the KOH (in ml) required for blank test; "N" = normality of KOH solution used, and "W" = weight of the oil sample used. The measurements (water content, tan δ, and resistivity, and breakdown voltage) are carried out at room temperature and ambient pressure.

3 Results and Discussions

Generally, oil has been utilized in transformers for cooling and insulating purposes. Internal condition of a transformer can be diagnosed by carrying out various analyses such as dissolved gas analysis (DGA), moisture analysis, BDV test, Tan delta and

acidity test etc. Abnormal electrical or thermal activity can be uncovered by these diagnostic tests.

3.1 Comparative Dissolved Gas Analysis

The most popular diagnostic tool for identifying and assessing transformer defects is DGA analysis. Gases that remain dissolved in the transformer oil can be produced as a result of electrical or thermal transformer faults. When put under potential fault circumstances, the transformer oil and the insulating materials decompose into distinctive byproducts. These suggestive gases, which are produced in the transformer, can be used to identify the failure kind. Hydrocarbons including CH_4, C_2H_2, C_2H_4, and C_2H_6 are also produced as transformer gases, along with H_2, CO, and CO_2. The identification and measurement of these gases can give an early indication of issues emerging with the transformer. This can help with preventive maintenance. and measurement of these gases can offer an early indication of potential issues with electrical equipment. In this present investigation, the detailed DGA analysis has been illustrated in figure 2. From these oil samples, it is found that OS6 gives the highest amount of hydrogen (2267 PPM) which may be due to partial discharge (PD) taking place in the transformer. It is to be noted that according to IEEE guideline, a transformer oil sample should not exceed hydrogen value not more than 100 PPM. On the other hand, OS2 and OS6 show high amount of acetylene which suggests arcing. For fault analysis, there are various methods such as the Dornenburg ratio method, key method, Rogers' ratio method, nomograph method, Duval triangle method, IEC ratio method, and CIGRE method are available. However, in this present study, we will discuss the fault analysis using the most popular Rogers' ratio method and Duval triangle method.

Table 1. GC program parameters

Head Space	Oven Temperature (°C)	70
	Loop Temperature (°C)	150
	Transfer Line Temperature (°C)	150
Oven	Set Value	230
	Rate (°C/min)	24
	Hold time (min)	6
Front Detector (FID)	Heater Temperature (°C)	250
TCD	Heater Temperature (°C)	250

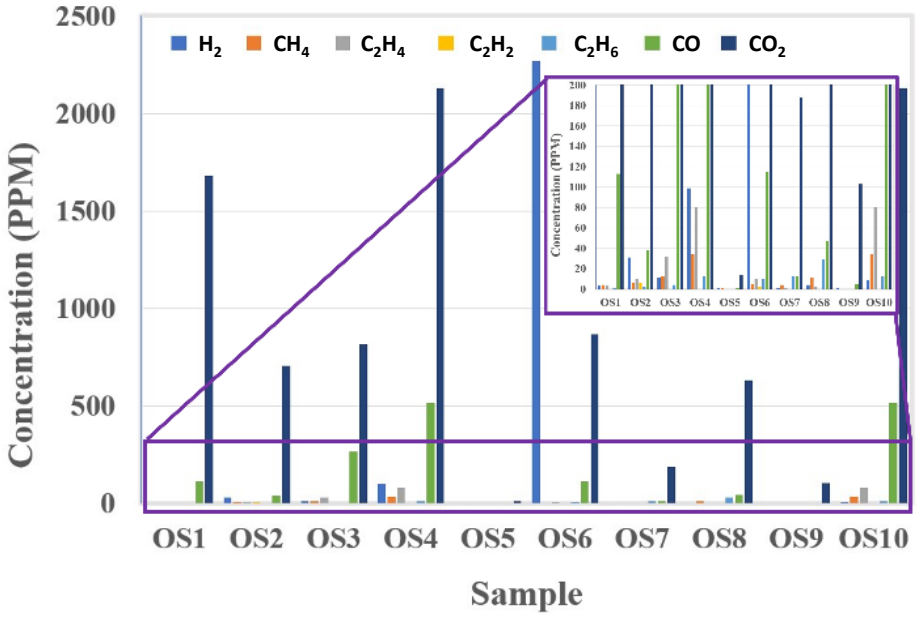

Fig. 2. Dissolved gas concentration in transformer oil samples

3.2 Comparative Fault and Failure analysis through Rogers Method

The most used gas ratio technique for transformer fault investigation is Rogers, which distinguishes numerous thermal fault categories. The gas mixtures ratio of CH_4/H_2, C_2H_4/C_2H_6, and C_2H_2/C_2H_4 are all analyzed using the Rogers technique. Faults are diagnosed using a simple identification technique based on ratio ranges. Employing gas ratios, the Rogers ratio offers a fundamental technique for finding defects. Normal aging, partial discharges regardless of monitoring, and thermal/electrical failure of severity are the situations that can be identified in an oil-insulated transformer.
Table 2 shows the Rogers gas ratio and their fault remarks. From this Rogers ratio table, it can be interpreted that OS5 transformer oil sample does not experience any fault however other transformer oil samples experiences thermal fault (OS1, OS3, OS4, OS10), partial discharge-corona with tracking (OS6) overheating (OS7, OS8) and arcing (OS2). This approach is successful because it links each case's gas examination to the findings of many failure investigations.

3.3 Comparative Fault and Failure analysis through Duval Triangle Method

The Duval Triangle methodology employs the relative position of three different Gases of CH_4, C_2H_4, and C_2H_2 on a triangular diagram together with their values. The triangle is plotted by converting gases through triangular measurements. Partial discharges (PD), low and elevated energy arcing electrical faults and thermal faults (hot areas of varying range of temperatures) are the evident flaws. To diagnose an error, the total amounts of gases (CH_4, C_2H_2 and C_2H_4) are calculated. The fraction of every gas in the

whole is then determined by dividing the amount of individual gas by the overall amount. The percentages of the total can be plotted on the triangle to ascertain the diagnosis. Table 3 gives the Duval Triangle Ratio of the dissolved gases and corresponding plot has been depicted in figure 3. From table 3 and figure 3, it can be summarized that OS7, OS8 transformer oil sample experience T1 fault zone, OS1, OS6 transformer oil sample experiences T2 fault zone, OS4, OS10 transformer oil sample experiences T3 fault zone, OS2 transformer oil sample experiences DT fault zone and OS5 transformer oil sample experiences PD fault zone.

Table 2. Rogers Ratios calculation from DGA analysis

Oil Sample	Fault Gas Ratio			Remarks/Fault analysis
	C_2H_2/C_2H_4	CH_4/H_2	C_2H_4/C_2H_6	
OS1	0	1.33	3	Thermal < 700 ºC
OS2	0.6	0.19	5	Arcing-high energy discharge
OS3	0	1.18	3	Thermal < 700 ºC
OS4	0	0.38	1	Low temperature thermal fault
OS5	0	1	0	No fault
OS6	0.2	0.02	1	Partial discharge-Corona with tracking
OS7	0	4	0.083	Slight overheating up to 150ºC
OS8	0	2.75	0.068	Overheating to 150 - 200ºC
OS9	0	0	0	Not identified
OS10	0	3.77	6.67	Thermal > 700ºC

Table 3. Duval Triangle Calculation from DGA analysis

Oil Sample	% of CH_4	% of C_2H_4	% of C_2H_2	Fault Zone
OS1	57	42.9	0	T2
OS2	27.3	45.5	27.3	DT
OS3	52	48	0	T2
OS4	29.8	70.2	0	T3
OS5	100	0	0	PD
OS6	80.6	16.1	3.2	T2
OS7	80	20	0	T1
OS8	84.6	15.4	0	T1
OS9	0	0	0	-
OS10	29.8	70.2	0	T3

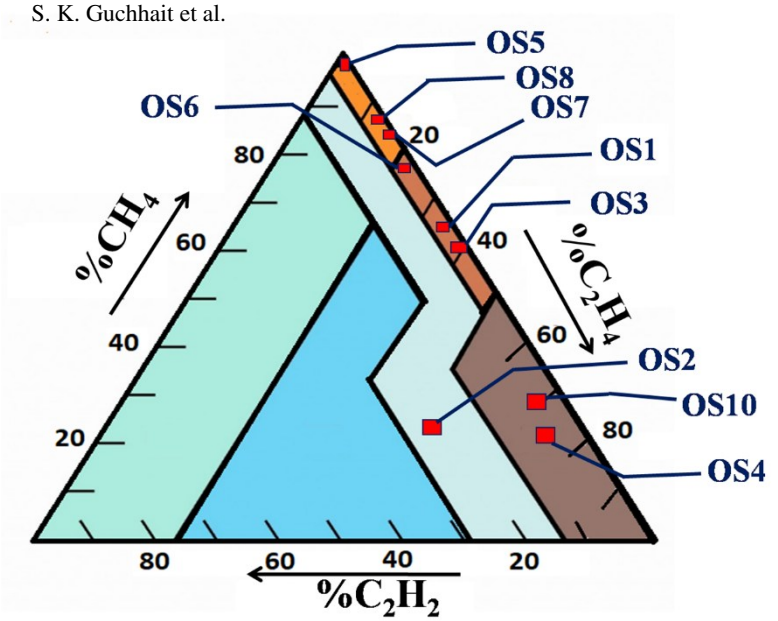

Fig. 3. Duval Triangle Analysis Plot of the Transformer Oil samples

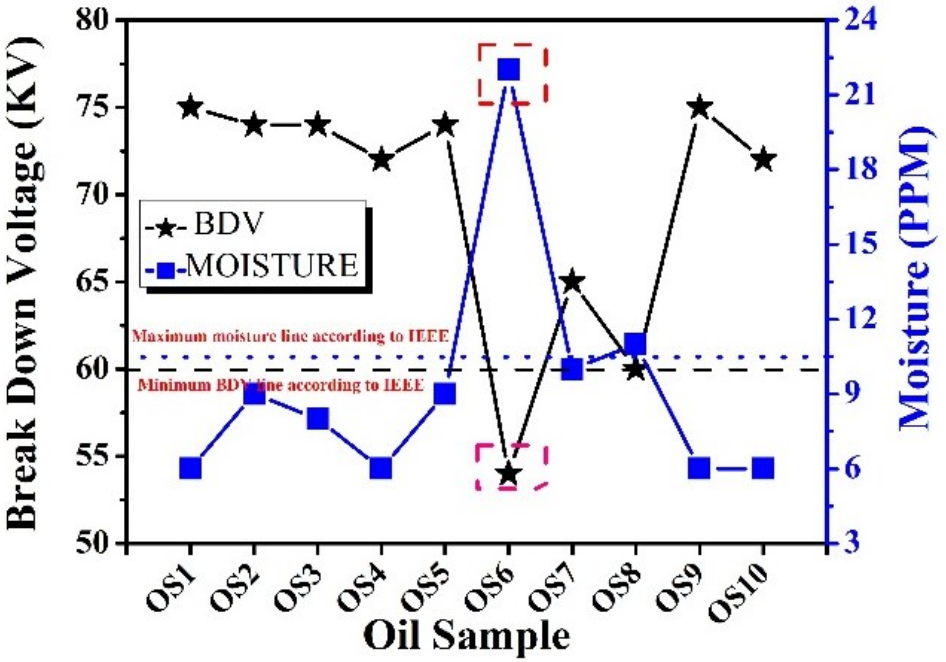

Fig. 4. A comparative relationship between moisture and breakdown voltage

3.4 Moisture and Breakdown Voltage Analysis

Moisture in transformer oil is especially undesirable since it degrades the oil's dielectric characteristics. The amount of moisture in the oil influences the paper protection of a transformer's windings and core. BDV of transformer oil is also known for its dielectric strength. Breakdown voltage is measured by sparking connections among two electrodes drenched in oil and separated by a certain gap. Figure 4 represents a comparative relation between moisture and breakdown voltage of the studied transformer oil samples.

A low BDV value indicates that the oil contains conductive materials and moisture (see figure 4). However, as moisture in transformer oil desorbs, the oil's localized gas concentration increases, which makes bubble formation more likely. The effectiveness of an electrical transformer will be impacted if the insulating oil contains more water than 10 ppm according to IEEE guidelines [21, 22]. In this present investigation, OS6 and OS8 samples show the highest amount of moisture contained in the samples whose BDV value is much less as compared to others (see Table 4).

3.5 Tan delta and Specific Resistivity Analysis

Tan Delta analysis is an important tool for determining the quality of a transformer's insulating system. Tan Delta, commonly referred to as the loss of angle tangent, is a measure of active current to reactive current in insulating substances, which reflects the insulation's dielectric loss [23]. Active Current is the power consumed for heating, also known as the in-phase component, whereas reactive current, known as out-of-phase component. Smaller tan δ values result in lesser dielectric loss and improved insulation effectiveness. Specific resistivity is another significant characteristic of transformer oil. It is measured in ohm-cm at a certain temperature [24]. Oil's resistivity diminishes dramatically as the temperature rises. The inside temperature of e oil will be at ambient temperature immediately after charging a transformer after a long shut down, however the temperature will be quite important and at overload it will reach up to 90°C. As a result, the insulating oil's resistivity should be high at ambient conditions while also being appropriate at high temperatures. There are clear links between Tan-δ and insulating oil resistance. The tan-delta rises while the insulating oil's resistivity decreases, and inversely [25]. From table 4, it has been found that the resistivity and the Tan-δ of different oil samples are different as the oil samples exposed in different conditions as discussed earlier. From table 4, it can be inferred that OS1, OS3, OS4, OS10 transformer oil samples have the smaller Tan delta value with compares to other sample. This indicates that samples have lesser dielectric loss and improved insulation effectiveness. On the other hand, OS1, OS3, OS4, OS10 shows higher specific resistivity value.

3.6 Acidity Analysis

One crucial characteristic of transformer oil is its acidity. The acidity of oil accelerates the oxidation reaction and deteriorates the insulating qualities of paper and coil insulation [26]. It may also lead to sludge formation in the oil in extreme case. The insulating property of oil reduces as the acid value increases [27]. However, in this present study acidity of transformer is within in limit as per standard (see table 4).

Table 4. Various physio-chemical parameters

Oil Sample	BDV (KV)	Moisture Content (PPM)	Tan Delta	Specific Resistivity (GΩ-cm)	Acidity (mg KOH/gm of oil)
OS1	75	6	0.001	32.4	0.05
OS2	74	9	0.003	28.19	0.05
OS3	74	8	0.001	67.35	0.03
OS4	72	6	0.001	61.48	0.05
OS5	74	9	0.01	3.8	0.02
OS6	54	22	0.02	0.48	0.05
OS7	65	10	0.016	2.39	0.05
OS8	60	11	0.019	1.21	0.05
OS9	75	6	0.01	3.9	0.05
OS10	72	6	0.001	61.48	0.05
IEEE recommended Value	60 (Minimum)	10 (Maximum)	0.01 (Maximum)	0.1 (Minimum)	0.3 (Maximum)

4 Conclusion

Analysis of dissolved fault gases and other electrical and other physicochemical parameters such as specific resistivity, Tan-δ, and breakdown voltage (BDV), acidity, moisture, is a feasible and efficient approach for detecting incipient fault and determining their extent. In this study it has been found that OS6 sample shows the highest amount of hydrogen (2267 PPM) which suggests partial discharge (PD) taking place in the transformer. On the other hand, OS2 and OS6 samples show a high amount of acetylene which indicated arcing is occurring in the transformer. It is proven that fault gases in transformer oil deteriorate its electrical insulating properties in huge economic loss. BDV of OS6 is also less in compared to recommended value. This may be due to the high amount of moisture present in the sample. Like this its Tan-δ also reached its maximum value. However, in this present study acidity of all transformers is within the limit as per standard. In accordance with the study, regular inspection of the liquid dielectric medium within the transformer which provides a wealth of information about the oil and overall health of the transformer can help prevent transformer failure.

References

1. Sun, H.C., Huang, Y.C. and Huang, C.M.: A review of dissolved gas analysis in power transformers. Energy Procedia 14,1220-1225 (2012)
2. Arshad, M.I.S.M. and Islam, S.M.: Power transformer critical diagnostics for reliability and life extension. In Canadian Conference on Electrical and Computer Engineering 2004 (IEEE Cat. No. 04CH37513) 625-628. IEEE, Canada (2004)

3. Chandran, L.R., Babu, G.A., Nair, M.G. and Ilango, K.: A review on status monitoring techniques of transformer and a case study on loss of life calculation of distribution transformers. Materials Today: Proceedings 46, 4659-4666 (2021)
4. Wang, X., Tang, C., Huang, B., Hao, J. and Chen, G.: Review of research progress on the electrical properties and modification of mineral insulating oils used in power transformers. Energies 11(3), 487 (2018)
5. Wang, M.V.A.J., Vandermaar, A.J. and Srivastava, K.D.: Review of condition assessment of power transformers in service. IEEE Electrical insulation magazine 18(6), 12-25 (2002)
6. Hamrick, L.: Dissolved gas analysis for transformers. Neta World 01-04 (2009).
7. Singh, S. and Bandyopadhyay, M.N.: Dissolved gas analysis technique for incipient fault diagnosis in power transformers: A bibliographic survey. IEEE Electrical insulation magazine 26(6), 41-46 (2010)
8. Jalbert, J. and Gilbert, R.: Decomposition of transformer oils: a new approach for the determination of dissolved gases. IEEE transactions on power delivery 12(2), 754-760 (1997)
9. Ali, M.S., Omar, A., Jaafar, A.S.A. and Mohamed, S.H.: Conventional methods of dissolved gas analysis using oil-immersed power transformer for fault diagnosis: A review. Electric Power Systems Research 216, 109064 (2023)
10. Mahmoudi, N., Samimi, M.H. and Mohseni, H.: Experiences with transformer diagnosis by DGA: case studies. IET Generation, Transmission & Distribution 13(23), 5431-5439 (2019)
11. Zhang, Y., Tang, Y., Liu, Y. and Liang, Z.: Fault diagnosis of transformer using artificial intelligence: A review. Frontiers in Energy Research 10, 1006474 (2022)
12. Faiz, J. and Soleimani, M.: Dissolved gas analysis evaluation in electric power transformers using conventional methods a review. IEEE Transactions on Dielectrics and Electrical Insulation 24(2), 1239-1248 (2017)
13. Irungu, G.K., Akumu, A.O. and Munda, J.L.: Fault diagnostics in oil filled electrical equipment: Review of duval triangle and possibility of alternatives. In 2016 IEEE Electrical Insulation Conference (EIC), pp. 174-177. IEEE, Canada (2016)
14. Soni, R., Joshi, S., Lakhiani, V. and Jhala, A.: Condition Monitoring of Power Transformer Using Dissolved Gas Analysis of Mineral Oil: A Review. International Journal of Advance Engineering and Research Development 3, 2348-4470 (2015)
15. Maher, A., Mansour, D.E.A., Helal, K. and Abd El Aal, R.A.: Dissolved gas analysis and dissipation factor measurement of mineral oil-based nanofluids under thermal and electrical faults. High Voltage 8(3), 455-465 (2023)
16. Ghoneim, S.S. and Taha, I.B.: A new approach of DGA interpretation technique for transformer fault diagnosis. International Journal of Electrical Power & Energy Systems 81, 265-274 (2016)
17. Kelly, J.J.: Transformer fault diagnosis by dissolved-gas analysis. IEEE Transactions on Industry Applications 6, 777-782 (1980)
18. Rao, U.M., Fofana, I. and Sarathi, R.: Alternative liquid dielectrics for high voltage transformer insulation systems: performance analysis and applications. John Wiley & Sons. New Jersey (2022)
19. Soni, R. and Mehta, B.: A review on transformer condition monitoring with critical investigation of mineral oil and alternate dielectric fluids. Electric Power Systems Research 214, 108954 (2023)
20. Ghani, S.A., Muhamad, N.A., Chairul, I.S. and Jamri, N.: A study of moisture effects on the breakdown voltage and spectral characteristics of mineral and palm oil-based insulation oils. ARPN Journal of Engineering and Applied Sciences 11(8), 5012-5020 (2016)
21. Rao, U.M., Fofana, I. and N'cho, J.S.: On some imperative IEEE standards for usage of natural ester liquids in transformers. IEEE Access 8, 145446-145456 (2020)
22. Nunn, T.: A comparison of liquid-filled and dry-type transformer technologies. In 2000 IEEE-IAS/PCA Cement Industry Technical Conference. Conference Record (Cat. No. 00CH37047), pp. 105-112. IEEE, USA (2000)
23. Chu, D. and Lux, A.: On-line monitoring of power transformers and components: a review of key parameters. In Proceedings: Electrical insulation conference and electrical

manufacturing and coil winding conference (Cat. No. 99CH37035), pp. 669-675 IEEE, USA (1999)
24. Stannett, A.W.: The conductivity of hydrocarbon transformer oil containing water and solid conducting particles. British Journal of Applied Physics 2(4), 110 (1951)
25. Suhaimi, N.S., Ishak, M.T., Rahman, A.R., Muhammad, F., Abidin, M.Z. and Khairi, A.K..: A review on palm oil-based nanofluids as a future resource for green transformer insulation system. IEEE Access 10, 103563-103586 (2022)
26. Tanteh, D.N. and Al-Liddawi, S.Y.: Properties of transformer oil that affect efficiency 48, (2014)
27. Liao, R., Hao, J., Chen, G., Ma, Z. and Yang, L.: A comparative study of physicochemical, dielectric and thermal properties of pressboard insulation impregnated with natural ester and mineral oil. IEEE Transactions on dielectrics and electrical insulation, 18(5), 1626-1637 (2011)

Solar Thermal-Based Desalination Using Non-Imaging Evacuated Tube Collectors with Compound Parabolic Concentrator

Ankit Gupta *, Swapnil Patil

Solar Thermal Group, NTPC Energy Technology Research Alliance, NTPC Ltd., Greater Noida, Uttar Pradesh, India.

Corresponding author * ankitgupta02@ntpc.co.in

Abstract. Water scarcity is a major issue in coastal areas which is addressed by converting sea water to potable water through reverse osmosis known as Seawater reverse-osmosis (SWRO). This process requires heat which is often achieved through electrical energy. In the first-of-its-kind facility in India, a 120 tons per day solar thermal based sea water desalination was developed, and deployed at NTECL Vallur, which utilizes Non-Imaging Evacuated Tube Collectors (ETCs) integrated with Compound Parabolic Concentrators (CPCs) enclosed in toughened glass covers to harness Global Horizontal Irradiance (GHI). This system eliminates the need for solar tracking. The system produces hot water at an average temperature of 68°C, with an 11°C temperature differential across the solar field under an average GHI of 557 W/m². The heated water is supplied to a six-effect Multiple Effect Distillation (MED) unit for desalination. Over a six-hour operating window, the plant achieved a distillate production rate of 5.5 tons per hour, with a product water conductivity of approximately 4.3 µS/cm, TDS of 40 mg/L, and pH of 7.2.

Keywords: Solar Thermal, Evacuated Tube Collectors, Compound Parabolic Concentrator

Abbreviations:

TPD	Tons per day
NETRA	NTPC Energy Technology Research Alliance
NTECL	NTPC Tamil Nadu Energy Company Limited
GHI	Global Horizontal Irradiance
DNI	Direct Normal Irradiation
NIC	Non-imaging Concentrator
EPC	Evacuated Tube Collectors with Compound Parabolic
CPC	Concentrator
MED	Multi-Effect Distillation
MSF	Multi-Stage Flash Evaporation
SWRO	Seawater reverse-osmosis

S. Shaswattam et al. (eds.), *NTPC Transactions on Energy Research (NTER 2025)*,
https://doi.org/10.2991/978-94-6463-849-3_9

1 Introduction

The global scarcity of drinking water is intensifying rapidly, driven by population growth, industrialization, and climate variability. The widening gap between water demand and available freshwater resources presents a critical challenge, particularly in coastal and arid regions. Conventionally, freshwater is sourced from lakes, rivers, and reservoirs, followed by treatment to meet potable water standards. However, with growing stress on these conventional sources, saline water—particularly seawater—has emerged as a viable alternative for freshwater generation through desalination technologies [1].

Among desalination methods, seawater reverse osmosis (SWRO) has been widely adopted in countries with access to coastal waters due to its lower specific energy consumption and cost for large-scale plants [2]. Nonetheless, SWRO systems require a stable power supply and skilled operation, which limits their deployment in remote or underdeveloped areas. In such regions, where water demand is typically modest, the use of small-scale thermal desalination systems becomes attractive due to their operational simplicity and reduced reliance on high-pressure components [3].

Thermal desalination technologies, such as Multi-Stage Flash (MSF) and Multi-Effect Distillation (MED), rely heavily on heat energy, which constitutes a significant portion of their operating costs [4]. However, when these systems are integrated with waste heat from power plants or renewable sources like solar thermal energy, the overall cost of water production can be substantially reduced, improving economic viability [5]. Loewy et al. [6] recommended hybrid desalination systems combining power and desalination in the Gaza Strip to enhance resource efficiency and energy recovery.

In this context, solar thermal-based desalination offers a promising, environment-friendly solution. Particularly in coastal regions, where seawater is abundant and solar insolation is high, solar-assisted thermal desalination can provide a decentralized, off-grid method for freshwater generation. Recent developments in compound parabolic concentrators (CPCs) and non-imaging evacuated tube collectors (ETCs) have enabled efficient harvesting of Global Horizontal Irradiance (GHI) without the need for mechanical solar tracking, thus improving system reliability and reducing operational complexity [7].

The present work describes the design, development, and performance evaluation of a 120 TPD solar thermal desalination pilot plant, installed by NTPC Energy Technology Research Alliance (NETRA) at the NTECL Vallur site in Chennai. The system utilizes CPC-integrated non-imaging ETCs to supply hot water to a six-effect MED unit. This study demonstrates a sustainable and modular desalination solution tailored for remote and resource-constrained coastal environments.

2 Selection of Technology

2.1 Thermal Desalination Technology Methods:

There are mainly two types of distillation systems used in thermal desalination: multi-stage flash evaporation (MSF) and multi-effect distillation (MED) units [8]. Among these, MED systems are generally more energy-efficient, as they reuse the latent heat of vapor from one effect to drive evaporation in the next, thereby increasing freshwater yield per unit of thermal input [9]. In cases where severe scaling issues are encountered, multi-effect flash evaporation is preferred due to its better handling of high-salinity and scaling-prone feedwater [10]. To further enhance efficiency, mechanical vapor compression (MVC) can be employed, wherein vapor from the last stage of the MED unit is compressed and reused in the first stage, significantly improving the gain output ratio (GOR).

In support of such design approaches, Viswanathan et al. [11] shared key insights from the RAMDAS project on solar desalination, which highlighted the importance of deploying low-maintenance, robust systems tailored for rural and remote settings where skilled technical manpower is limited. The study underscored the effectiveness of integrating solar thermal energy sources with simple MED configurations and emphasized the need for modular, user-friendly designs that can operate reliably in decentralized infrastructure without heavy operational oversight.

2.2 Solar Thermal Collectors:

Solar radiation reaching the Earth's surface can be categorized into two main components, and solar thermal collectors are typically designed to operate based on either of these [12]. Direct Normal Irradiation (DNI) refers to solar radiation that arrives in a straight line from the sun, with minimal scattering or absorption, and is measured on a surface oriented perpendicular to the sun's rays. GHI represents the total solar energy received on a horizontal surface, including both direct and diffuse components.

While photovoltaic (PV) systems primarily operate within the visible portion of the electromagnetic spectrum and rely on GHI, solar thermal collectors - especially those used in concentrating systems, are typically designed to harness DNI. These collectors absorb a broader range of the solar spectrum, including infrared radiation, and generally require sun-tracking mechanisms to maintain optimal alignment with the sun throughout the day [13].

2.2.1 DNI Type Solar Collectors:

Solar Thermal collectors operating on DNI are Parabolic Trough, Linear Fresnel, Dish, and Tower Dish, Tower, Parabolic Trough, and Linear Fresnel. The collectors are shown in the Fig. 1. However, for efficient operation of these systems, the efficiency of the solar tracker must be considered as the heat energy generated from these solar thermal technologies utilizes DNI component of the solar radiation.

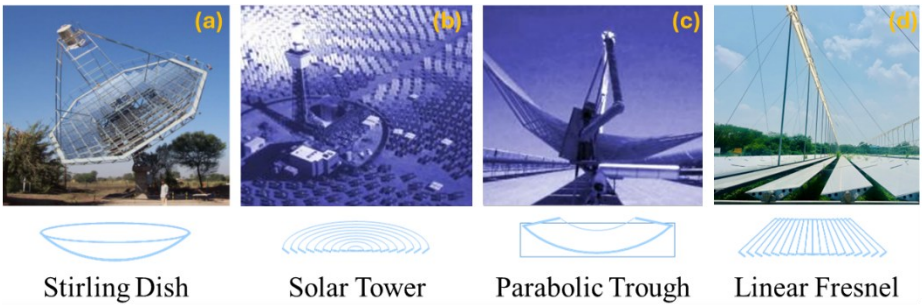

Fig. 1. Different types of solar thermal collectors based on Direct Normal Irradiation (DNI) (a) Stirling Dish (b) Solar Tower (c) Parabolic Trough (d) Linear Fresnel.

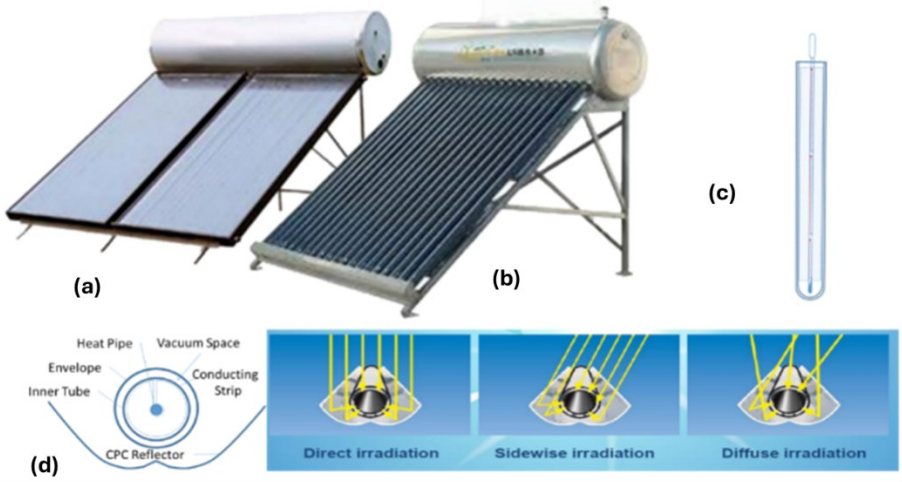

Fig. 2. Collectors for Global Horizontal Irradiation (GHI) (a) Flat Plate Collector (b) Evacuated Tube Collector (c) Heat Pipe (d) CPC reflector

The solar tracker requires control system, rotating parts and electricity for motors which in turn increase capital cost and operating cost.

2.2.2 GHI Type Solar Collectors:

As shown in the Fig. 2, flat plate collectors and evacuated tube collectors are GHI-type collectors. In GHI type of collectors, evacuated tube collectors are the most efficient type of hot water solar collectors. These collectors have evacuated glass, allowing them to operate well in colder climates. Inside this evacuated type of collector, there can be either a U-tube or a heat pipe for circulating the process fluid that absorbs heat within the evacuated tube. In the heat pipe configuration, the tube is partially filled with a working fluid under evacuated conditions. When exposed to solar radiation, the fluid evaporates and rises, transferring heat to the process liquid through a condenser interface. Upon condensation, the liquid returns to the bottom of the pipe via gravity, enabling a passive, continuous heat transfer cycle [13]. The performance, durability, and quality of these collectors were validated according to the EN 12975 standard, which specifies the general requirements and testing methods for solar thermal collectors, including evacuated tube systems [14]. The arrangement of the heat-pipe in the evacuated tube is shown in Fig 3 (c).

Souliotis et al. [15] demonstrated that the integration of CPCs with evacuated tube collectors significantly enhances solar collection efficiency. CPCs operate on GHI and do not require sun-tracking systems, making them especially effective for passive, low-maintenance designs. These reflectors have been shown to improve thermal performance by increasing water temperature and enhancing heat retention, as illustrated in Fig. 3 (d). Solar thermal desalination systems, particularly those based on MED, can operate efficiently at moderate temperatures below 100 ºC [16], making them compatible with CPC-based solar collectors. Mortazavi et al. [17] further confirmed the cost-effectiveness, thermal efficiency, and suitability of CPCs for low-temperature applications in solar desalination, especially in off-grid or semi-urban environments.

Fig. 3. Single collector ETC-CPC, with Toughened Glass Cover and Multi Effect Distillation over the structure.

Transmittance is an important property, especially in applications like solar panels, optical devices, and displays, as it affects the amount of light or radiation that can be transmitted through the material. To facilitate easy cleaning, the ETC-CPC-24 collector was designed and developed within a housing box equipped with toughened cover glass, which has a transmittance ≥ 91% and CPC having reflectivity ≥ 86%. The quality of the toughened cover glass was validated in accordance with ISO 9001 standards. The setup is shown in Fig. 3. General standards and considerations for cover glass are:

1. Material Composition

- **Glass Type**: Typically, soda-lime or low-iron glass is used in solar applications to achieve high solar transmittance due to its lower iron content and higher clarity [18].
- **Coatings**: Anti-reflective (AR) coatings are commonly applied to reduce reflection losses and further enhance light transmission through the glass [19].

2. Thickness of the Glass

The thickness of the glass significantly influences its transmittance. Thinner glass typically permits more light to pass through, though optical performance is also affected by coating type and base material selection [20].

3. Surface Quality

High-quality cover glass should have a smooth, clear surface with minimal imperfections. Scratches, dust, or any contaminants can reduce effective transmittance.

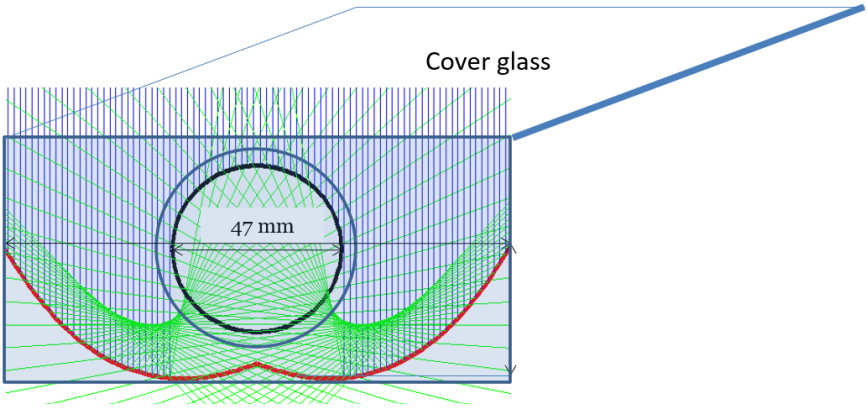

Fig. 4. Raytracing on a Single Evacuated Tube with CPC and Glass Cover.

- **Optical Clarity:** The glass should be free from defects, such as bubbles or inclusions, that could scatter or absorb light.

The evaluation of optical performance of ETC-CPC with cover glass was carried out using the Ray-tracing Method in MATLAB as shown in Fig. 4. Ray-tracing techniques are appropriate for evaluating line-axis systems. Considering all the above merits / demerits, a best combination of non-imaging type CPC along with multi-effect distillation was configured for an efficient desalination system near coastal regions.

3 Results and Discussion

3.1 Process Description

The present solar thermal desalination system was installed at NTECL Vallur. The desalination plant is divided into two parts. First is the LP steam Generator Block and the other is the Desalination block. In the present set up the solar thermal collector working on GHI were deployed. Instead of a U-tube, a heat pipe which is dry plug system was used inside the evacuated tube to carry thermal energy in this project. Based on our experience, in heat-pipe not only there is any requirement to isolate the damaged evacuated tube, but the replacement of the evacuated tube is also easy. To minimize both capital and operating cost, GHI type collectors were used. A block diagram of the system is shown in Fig. 5.

3.2 LP steam Generation Block

This block is mainly designed to produce hot water via solar thermal technology only. This technology consists of a CPC for generating of hot water. The generated hot water is flashed in a flash chamber which is maintained under partial vacuum to generate low pressure steam. This steam is then utilized as a motive steam in next block.

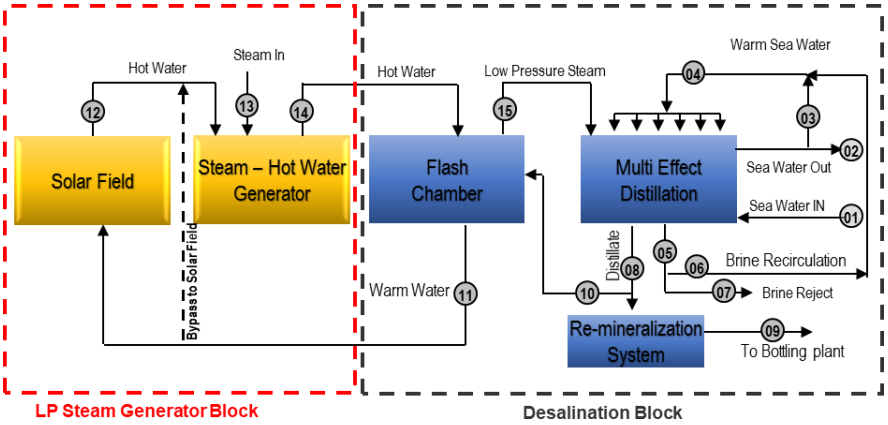

Fig. 5. Block diagram of solar thermal desalination system

3.3 Desalination Block

The MED is operated under partial vacuum. The hot water coming from the solar block is sprayed in flash chamber. In the flash chamber, which is maintained under vacuum, the hot water is flashed to produce low-pressure (LP) steam. The reduced pressure in the chamber lowers the boiling point of water, causing a portion of it to evaporate using the sensible heat of the water. The remaining warm water in the flash chamber is then returned to the solar field to generate additional hot water during the daytime. The produced flash steam serves as motive steam for the first effect of the MED system, also maintained under vacuum. In this chamber, seawater is sprayed over the LP steam piping. The combination of the high skin temperature of the piping and the vacuum environment causes part of the sprayed seawater to evaporate. This vapor is then directed to the subsequent distillation chamber, where it acts as working steam, repeating this process through eight effects with a gain output ratio (GOR) of approximately six (6). To maximize thermal energy efficiency within a desalination system, effects are used. The desalinated vapours produced in last effect is condensed in a condenser, and the resulting distilled water in each effect and condenser is sent to a remineralization system to ensure high-quality potable drinking water. The design details are given in Table 1 and the installed plant is shown in Fig. 6. Liu et al., [21] developed mathematical and economic models for thermal and economic performance on solar desalination system with evacuated tube collectors and low-temperature multi-effect distillation. They analyzed two independent parameters heating steam temperature of the first effect and number of effects. With the increasing number of effects, the freshwater cost decreases gradually.

Thermal inertia refers to the ability of a system to resist changes in temperature, meaning it can absorb or release heat with minimal immediate fluctuation in its thermal state [22]. In distillation and other thermally-driven processes, maintaining adequate thermal inertia is critical to ensure temperature stability, which helps prevent performance drops, product quality degradation, and equipment stress due to abrupt thermal shifts. The process requires a stable, consistent heat source to maintain steady distillation operations. Sudden variations in temperature can lead to inefficiency, lower product quality, or even equipment stress. To achieve consistent distillate production of 120 TPD (tons per day) and maintain thermal inertia, an alternate source of heat, such as low-pressure steam, can be supplied from a power plant. Low-pressure steam is an efficient and cost-effective heat source in many industrial processes, particularly in systems that require consistent, moderate heating over extended periods. Power plants often have excess steam that can be used for processes like distillation. Supplying low-pressure steam from a power plant helps in ensuring that the required thermal energy for distillation is available continuously without interruptions.

The differential average temperature maintained between the output and input of the solar field was 11°C. The solar field generated hot water at an average temperature of 68°C, with an average GHI of 557 W/m². The performance of the Solar Thermal Desalination Plant is plotted in Graph 1. Over a six-hour period, the average distillate water production rate was 5.5 tons per hour, with an average conductivity of approximately 4.3 µS/cm. The reliance on sophisticated mechanical rotating components like solar trackers has been significantly reduced by using NIC in solar thermal desalination, leading to increased system reliability and decreased electricity consumption. Various solar thermal and desalination technologies were examined to identify the most economical option suitable for installation and operation in remote coastal areas, requiring minimal electricity and manpower. Nevertheless, the author is of the view that due to rising costs of energy, desalination costs may not decrease in the future despite technological advancement in existing technology, raw materials and future operating costs.

Table 1. Design details of Solar thermal seawater desalination pilot plant.

Multi Effect Distillation (MED)	Solar Field
• Integrated Design with Flash Chamber & MED	• Number of Bay: 5 Nos
• Number of Effects in MED: 8 Nos	• Modules in each Bay: 110 Nos (22x 5)
• Gain Output Ratio: 6	• Collectors in each Module: 24 Nos
• Capacity= 120 TPD	• Total number of Modules: 550 Nos
• Output distilled water quality: TDS ≤ 5 ppm	• Total Collector Area: 2,420 m^2

Fig. 6. Site photograph of the Solar Thermal (ETC-CPC) field of 2,420 m^2

4 Benefits of the present system

a) Sustainable and Environment-Friendly Green Energy: Utilizes renewable solar energy, significantly reducing dependence on fossil fuels and lowering greenhouse gas emissions.

b) Minimal Chemical Consumption: The Multi-Effect Distillation (MED) process operates at a design temperature of 65ºC, which is below the solubility limits of scaling compounds such as: Carbonates (70ºC), Sulfates (67ºC). This minimizes scaling and reduces the need for antiscalant chemicals.

c) Continuous Operation: Unlike intermittent systems, solar thermal desalination can support continuous operation when coupled with thermal energy storage. This ensures: (1) High water yield, (2) Increased plant availability and reliability.

d) Modular and Scalable Design: The system architecture allows for: (1) Easy expansion based on water demand, (2) Flexible integration with existing infrastructure.

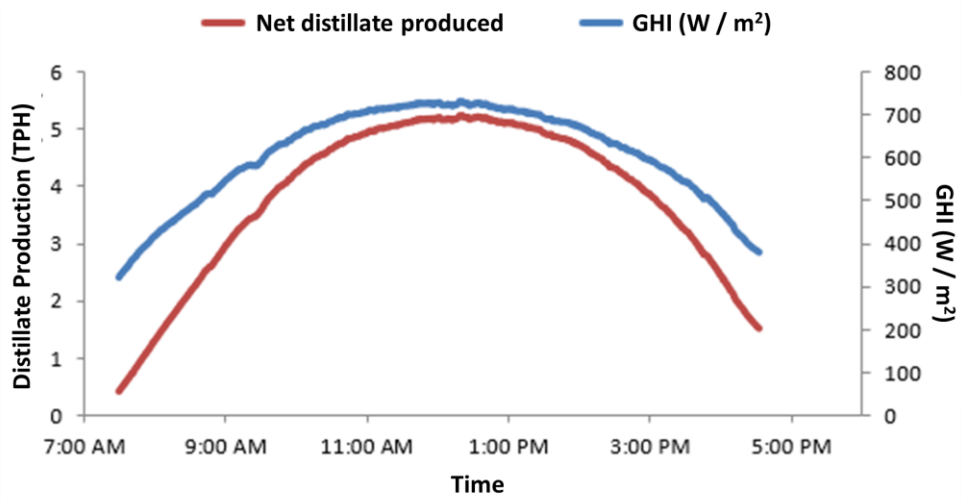

Fig 7. Plot showing the production of Distillate and time of the day along with corresponding

5 Applications of ETC-CPC

In addition to Cost-effective seawater desalination, these collectors are used for pre-heating fluids in various applications, including solar thermal cooking, milk pasteurization, and solar thermal air conditioning. The distilled water produced through solar thermal desalination can also be utilized in electrolyzers for hydrogen generation. This approach can help reduce the reliance on freshwater for hydrogen production, particularly in coastal regions.

6 Conclusions

i. The present project has deployed Solar Thermal based Desalination using Non-Imaging Evacuated Tube Collectors with Compound Parabolic Concentrator at NTECL Vallur and is successfully running. Though covered glass is used, it does not have considerable effect on the production of hot water in the system.

ii. The plant is producing 120 TPD of drinking water conforming to IS 10500 standards. The water achieved the TDS of 40 mg/l and pH 7.2, which makes it slightly alkaline. Potassium carbonate and Magnesium chloride levels were 20 ppm each.

iii. The levelized cost of water production comes around INR 0.31 per litre, assuming the plant life of 25 years.

iv. The mean emissions calculated for solar thermal-based desalination are 3.88 kg CO2 eq./m³. When comparing this to Reverse Osmosis (RO) systems, using solar thermal desalination to produce 5,833 m³ of distilled water annually results in a total reduction of 18,206 kg of CO2 emissions per year.

v. Among the cost constitution of ETC solar desalination system, the proportion of the cost of evacuated tube collector is the largest (31%), then the cost of civil installation and auxiliary equipment and the cost of manpower is second (15%).

Acknowledgement: Authors are grateful to Sh. Shaswattam ED (NETRA) for his guidance. Sincere thanks to team NTECL Vallur & M/S KGISL for their constant support to implement the project successfully.

References

[1] Gude, V.G.: Desalination and water reuse to address global water scarcity. Rev. Environ. Sci. Bio/Technol. 15, 583–606 (2016)

[2] Greenlee, L.F., Lawler, D.F., Freeman, B.D., Marrot, B., Moulin, P.: Reverse osmosis desalination: Water sources, technology, and challenges. Water Res. 43(9), 2317–2334 (2009)

[3] Elimelech, M., Phillip, W.A.: The future of seawater desalination: Energy, technology, and the environment. Science 333(6043), 712–717 (2011)

[4] Qtaishat, M., Banat, F.: Desalination using renewable energy: A viable solution for the Arab region. Renew. Sustain. Energy Rev. 43, 460–476 (2013)

[5] Ghaffour, N., Bundschuh, J., Mahmoudi, H., Goosen, M.F.A.: Renewable energy-driven innovative energy-efficient desalination technologies. Appl. Energy 136, 1155–1165 (2014)

[6] Loewy, T.: The case for seawater desalination to solve the water shortage in the Gaza Strip. Desalination 99(2–3), 459–481 (1994)

[7] Mortazavi, S.M., Maleki, A.: A review of solar compound parabolic collectors in water desalination systems. Int. J. Modelling and Simulation. https://doi.org/10.1080/02286203.2019.1626539 (2019)

[8] El-Dessouky, H.T., Ettouney, H.M.: Fundamentals of Salt Water Desalination. Elsevier, Amsterdam (2002)

[9] Quteishat, K., Abu-Arabi, M.K.: Desalination processes and multistage flash distillation and multi-effect distillation processes. Desalination and Water Treatment 15(1–3), 69–81 (2010)

[10] Al-Karaghouli, A., Kazmerski, L.L.: Energy consumption and water production cost of conventional and renewable-energy-powered desalination processes. Renew. Sustain. Energy Rev. 24, 343–356 (2013)

[11]Viswanathan, S.P., Abraham, R., Saini, V., Bajpai, S.: Public Private Partnership on Water - Lessons from RAMDAS project on Solar Desalination. In: International Conference on Innovative Technologies and Management for Water Security, pp. 1–2. Chennai, India (2014)

[12]Duffie, J.A., Beckman, W.A.: Solar Engineering of Thermal Processes. 4th edn. Wiley, Hoboken (2013)

[13]Kalogirou, S.A.: Solar Energy Engineering: Processes and Systems. 2nd edn. Academic Press, Oxford (2009)

[14]Kalogirou, S.A.: Solar Energy Engineering: Processes and Systems. 2nd edn. Academic Press, Oxford (2009)

[14]European Committee for Standardization (CEN): EN 12975-1: Thermal Solar Systems and Components — Solar Collectors — Part 1: General Requirements. CEN, Brussels (2006)

[15]Souliotis, M., Tripanagnostopoulos, Y.: Study of the distribution of the absorbed solar radiation on the performance of a CPC-type ICS water heater. Renew. Energy 33, 846–858 (2008)

[16]Kalogirou, S.A.: Seawater desalination using renewable energy sources. Prog. Energy Combust. Sci. 31(3), 242–281 (2005)

[17]Mortazavi, S.M., Maleki, A.: A review of solar compound parabolic collectors in water desalination systems. Int. J. Modelling and Simulation. https://doi.org/10.1080/02286203.2019.1626539 (2019)

[18]Han, J., Luo, Z., Zhao, X., Karuturi, S.K.: Optical modeling and analysis of low-iron glass for photovoltaic module applications. Sol. Energy Mater. Sol. Cells 130, 161–168 (2014)

[19]Yamada, N., Fujimoto, K., Saitoh, T.: Development of anti-reflection coatings for glass used in solar modules. J. Non-Cryst. Solids 356(11–17), 737–741 (2010)

[20]Jelle, B.P., Hynd, A., Gustavsen, A.: Building integrated photovoltaic products: A state-of-the-art review and future research opportunities. Sol. Energy Mater. Sol. Cells 100, 69–96 (2012)

[21]Liu, X., Chen, W., Gu, M., Shen, S., Cao, G.: Thermal and economic analyses of solar desalination system with evacuated tube collectors. Sol. Energy 93, 144–150 (2013)

[22]Cabeza, L.F., Castell, A., Medrano, M., Leppers, R., Zalba, B.: Use of thermal energy storage (TES) with phase change materials (PCM) in buildings: A review. Renew. Sustain. Energy Rev. 11(6), 1145–1181 (2007)

Design and Development of 10 kWh Solar Thermal Space Heating with Thermal Energy Storage

Ankit Gupta *, Neeraj Goswami, Subrata Sarkar, S Shaswattam

Solar Thermal Group, NTPC Energy Technology Research Alliance, NTPC Ltd., Greater Noida, Uttar Pradesh, India

Corresponding author * ankitgupta02@ntpc.co.in

Abstract. Solar space heating presents a sustainable solution for maintaining indoor thermal comfort by utilizing solar thermal energy. This technology is broadly categorized into active systems, which use fluid-based solar collectors and distribution mechanisms, and passive systems, which rely on architectural features to naturally capture and retain solar heat. The present study focuses on an active solar space heating system that integrates heat pipe-based evacuated tube collectors (ETCs) with a paraffin-based thermal energy storage (TES) unit to enable nighttime space heating in remote, cold regions. The system architecture comprises three key components: the solar collector unit, thermal energy storage unit, and space heater. Field implementation demonstrated an energy storage capacity of approximately 16 kWh under an average Global Horizontal Irradiance (GHI) of 2.4 kWh/m², effectively maintaining consistent indoor temperatures throughout the night. The simplicity of installation, minimal maintenance requirements, and reliable performance under low solar input conditions underscore the system's suitability for off-grid applications in regions such as Leh. The results affirm the viability of this integrated solar thermal system as an efficient, cost-effective solution for domestic space heating in sun-rich, high-altitude cold climates.

Keywords: Solar Thermal Heating, Solar Collectors, Thermal Energy Storage, Paraffin wax

Abbreviations:

Thermal Energy Required = Q_{th}
Melting Temperature of PCM = T_1
Water Inlet Temperature = T_{w1}
Water Outlet Temperature = T_{w2}
Inner Diameter of Tube = D_{in}
Outer Diameter of Tube = D_o
Change in temperature of Thermic Fluid = $\triangle T_{TF}$
Heat Required from Thermic Fluid / hr = Q_{TF}
Heat Transfer Coefficient of TF = HTC_{TF}
Logarithmic mean temperature difference = LMTD
Heat Transfer / length= Q
Phase Change Material = PCM
Thermic Fluid = TF
Enthalpy of PCM = H_{PCM}
Density of PCM = ρ_{PCM}
Density of TF = ρ_{TF}
Viscosity of TF = μ_{TF}
Velocity of TF = V_{TF}
Specific Heat capacity of TF = Cp_{TF}
Reynolds number = Re
Prandtl number = Pr
Thermal Energy Storage = TES

S. Shaswattam et al. (eds.), *NTPC Transactions on Energy Research (NTER 2025)*,
https://doi.org/10.2991/978-94-6463-849-3_10

1 Introduction

Solar space heating is one of the more intuitive use of solar thermal energy by using the sun's heat to subsequently heat spaces within buildings, drying of agricultural products etc. Technology within space heating can be separated into two distinct categories: passive and active [1]. Active space heating captures energy from sunlight, either as heat or electricity, to augment heating systems, while passive space heating captures heat from the sun as it comes into home through windows, roofs and walls to heat objects in the room. Active space heating uses large flat-plate or evacuated tube collectors on a rooftop or ground mounted to absorb the thermal energy and redistribute it to the fluid. Solar thermal space heating systems, when integrated with TES, offer a sustainable solution to address the intermittent nature of solar energy, particularly in regions with significant diurnal temperature variations. A broad range of technologies and systems are currently available for capturing solar energy. These systems are generally categorized into direct and indirect methods, both of which are continually advancing in terms of efficiency, cost-effectiveness, and versatility of use [2]. Latent Heat Storage utilizes phase change materials (PCMs) that absorb or release heat during phase transitions, such as from solid to liquid. Numerous experimental and simulation studies have assessed the thermal performance of phase change materials. Results have shown that incorporating PCMs into wall systems can lead to energy savings of up to 30%, while also reducing peak indoor temperatures by 3–5°C in hot climates [3,4]. Combining PCMs with insulation materials has demonstrated synergistic improvements in energy efficiency [5]. These outcomes highlight the effectiveness of PCM integration, particularly in regions with significant diurnal temperature fluctuations. There is also a growing focus on PCM retrofitting methods and dynamic thermal modeling to further enhance energy savings [6].

PCMs offer higher energy densities compared to Sensible Heat Storage and maintain a constant temperature during the phase change process [7]. However, challenges include issues related to material stability, heat transfer rates, and cost. The combination of solar collectors and TES enables the storage of excess thermal energy generated during the day for use during nighttime or cloudy periods, thereby enhancing the reliability and efficiency of space heating applications.

Passive space heating uses organic PCMs that store thermal energy during melting and release it during solidification. This latent heat storage helps buffer indoor temperature fluctuations. When integrated into building components such as walls, roofs, ceilings, or floors, PCMs can delay heat transfer, reduce HVAC loads, and stabilize indoor temperatures. Organic PCMs are more commonly used in building applications due to their reliability and compatibility with construction materials [8].

The present manuscript discusses the process and method for design and development of an active mode of space heating system utilizing a PCM

material, keeping in mind a volume of 100 ft^3, and harnessing solar heat with a daily average GHI of 2.4 kWh/m^2.

1.1 System Brief:

An innovative active solar space heating system is customized to meet the requirement of 10 kWh of thermal energy for heating a space volume of 10 X 10 X 10 cubic feet during non-sunshine hours. Highly efficient heat pipe based solar energy collector arrangement of 6.25 m^2, was deployed to harvest the solar energy. To deliver the heat energy for space heating during non-sunshine hours, an efficient and cost-effective paraffin-based thermal storage system was envisaged [2]. Collector support structure was designed and fabricated to suit the geo location of colder region to realize maximum annual yield. The system was designed to transfer heat using water & ethylene glycol [9]. All the components in the system are designed keeping in mind of easy installation and maintenance.

1.2 Process Description:

The solar thermal heating system utilized in this study comprises ETCs integrated with heat pipes for efficient solar energy absorption and transfer. Each heat pipe is sealed and partially filled with a working fluid, housed within a vacuum-sealed glass tube to minimize thermal losses. The condenser end of the heat pipe is embedded into a top manifold header, through which a water-based heat transfer fluid is circulated. During solar irradiation hours, a circulation pump actively drives water into the hot header of the collector array. As the heat pipes absorb incident solar energy, the internal working fluid vaporizes and conveys heat to the manifold through condensation. This thermal exchange raises the water temperature to approximately 70 °C [1,2].

The heated water is subsequently directed to TES. The TES unit incorporates paraffin wax as PCM, selected for its favorable thermal stability, cost-effectiveness, and melting point suitable for low-temperature applications [2,7]. Upon contact with the 70 °C water, the paraffin wax undergoes a solid-to-liquid phase transition, storing latent heat. During this heat exchange process, the water cools to around 60 °C before being recirculated to the solar collector system for reheating, thus forming a closed-loop thermal cycle. This setup allows for continuous and reliable energy storage during peak solar hours and ensures thermal availability during non-sunshine periods, improving the overall efficiency of the space heating system. A schematic representation of this thermal process is illustrated in Figure 1(a).

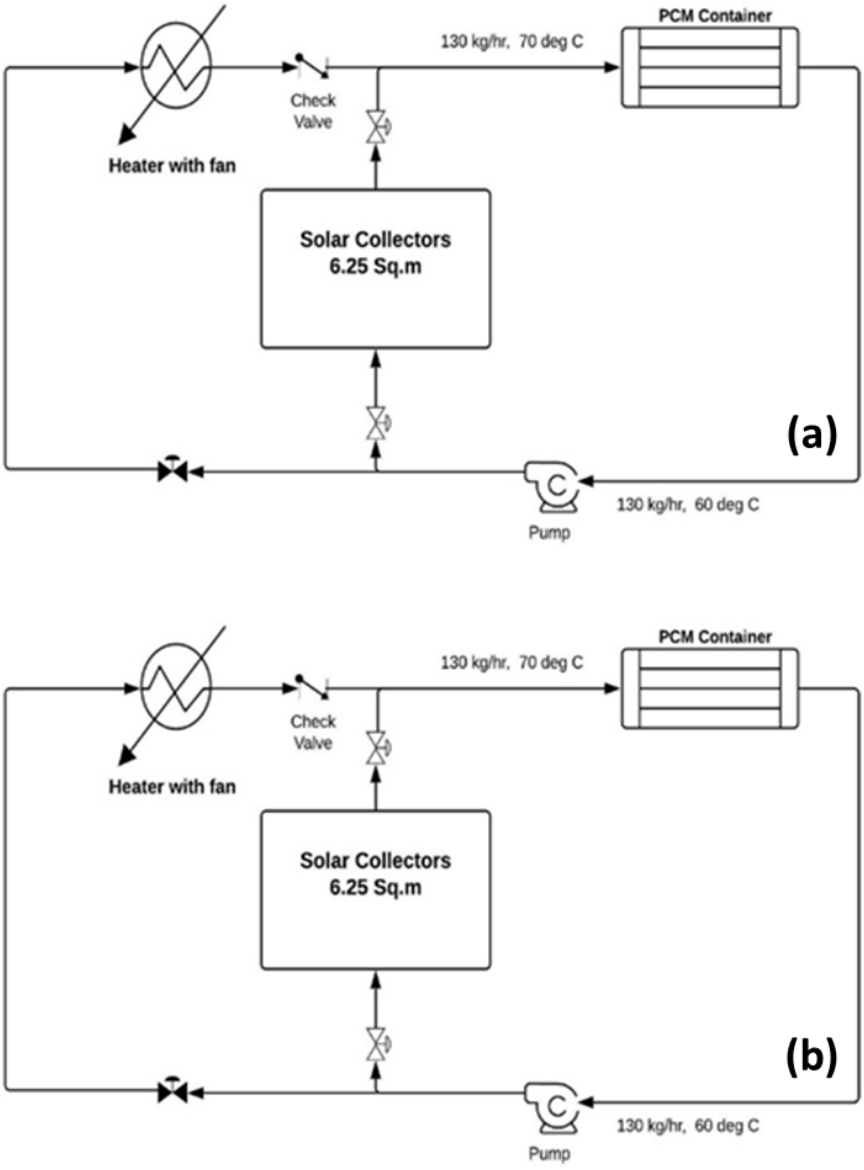

Fig. 1. (a) Process flow at 4 kWh/m^2/ day GHI during daytime. (b) Process flow during night-hours for 10kWh Thermal energy.

During nighttime or low solar radiation periods, the water in the circulation loop cools down to approximately 40 °C. As it enters the TES unit, it is reheated to around 50 °C by drawing on the latent heat stored in the molten paraffin wax from the daytime charging phase. This thermally upgraded water is then directed to a heat dissipator unit, where it transfers thermal energy to the surrounding air via a heat exchanger, effectively providing space heating.

Following heat exchange, the water temperature decreases back to 40 °C, completing the thermal cycle. It is then recirculated into the TES unit for reheating, thereby maintaining a continuous closed-loop operation. This process ensures thermal buffering and indoor temperature regulation during non-sunshine hours. A schematic of the nighttime heat delivery cycle is illustrated in Figure 1(b).

1.3 Description of the system:

The major components of the space heating system are Evacuated tube collectors, PCM heat exchanger and radiator.

1.3.1 Solar Thermal Collector:

The solar thermal heating system operates on the principle of GHI and comprises of ETC integrated with a heat pipe configuration, designed to meet a thermal load of 1 kW for 10 hours per day, equivalent to 10 kWh of energy. The solar collector field is dimensioned to supply this thermal requirement based on an average GHI of 4 kWh/m²/day, as recorded at NETRA, Greater Noida.

Each evacuated tube measures 1.8 m in length and 0.047 m in diameter and is coupled to a heat pipe that facilitates efficient thermal transfer from the absorber to the working fluid. A single header connects 20 evacuated tubes, and the system comprises a total of four (4) such headers, as shown schematically in Figure 2(a).

The headers are fabricated using rectangular cross-section tubing with dimensions 50 mm × 25 mm, into which the condenser sections of the heat pipes are inserted. This configuration enhances the effective heat transfer area, promoting efficient conduction from the heat pipes to the circulating fluid.

Table 1. Specifications of the system

1.	Heat required in the room	1 kW
2.	Hours of Operation	10 hours
3.	Total Energy to heat the room	10 kWh
4.	Average Solar Radiation	4 kWh/m^2/ day
5.	Solar collector optical to thermal energy conversion Efficiency	40%
6.	Solar Thermal Collector Area	6.25 m^2

Water flows through the headers at a velocity of 0.15 m/s, ensuring uniform heat pickup and minimal thermal stratification. The heat pipe-to-header assembly is illustrated in Figure 2(b).

This ETC based heat pipe configuration offers modular scalability, high thermal efficiency, and reliable performance across a range of climatic conditions. By operating on GHI, the system can effectively capture diffuse and scattered solar radiation, eliminating the need for sun-tracking mechanisms. This makes it particularly suitable for regions with variable or fluctuating solar availability. Furthermore, the integration of CPCs enhances the thermal collection efficiency of ETCs under non-ideal radiation conditions [10], making them an excellent choice for low- to medium-temperature thermal applications [1,11].

1.3.2 Thermal Energy Storage System:

The PCM employed in the TES unit is paraffin wax, selected for its low melting point, high latent heat capacity, chemical stability, and wide availability [2,7]. The paraffin wax used in this system has a melting temperature of 57 °C and a latent heat of fusion of 176 kJ/kg, making it highly suitable for low- to medium-temperature thermal applications [2].

During solar charging hours, water heated to 70 °C circulates through copper tubes embedded in the TES module. As the hot water flows through these tubes, it transfers thermal energy to the surrounding paraffin wax, causing it to melt and store energy in the form of latent heat. This stored heat is subsequently utilized during night hours to raise the temperature of return water from 40 °C to 50 °C, thereby maintaining consistent thermal output.

The heat exchanger system is designed to transfer a total of 10 kWh of thermal energy. To achieve this, a total heat transfer area of 17 m² was calculated and realized using copper tubing with an outer diameter of 15.87 mm. The paraffin wax layer is assumed to have a thickness of 21 mm per meter of tube length. Accordingly, a total of 93 meters of copper tubing was coiled and immersed within the liquid PCM, optimizing the surface area for heat transfer. The modular heat exchanger assembly is housed within a storage tank with dimensions of 710 mm × 550 mm × 950 mm, as depicted in Figure 2 (c) and Figure 2 (d). This design ensures effective thermal charging and discharging while maintaining system compactness and efficiency, critical for residential or off-grid thermal management applications [7, 12].

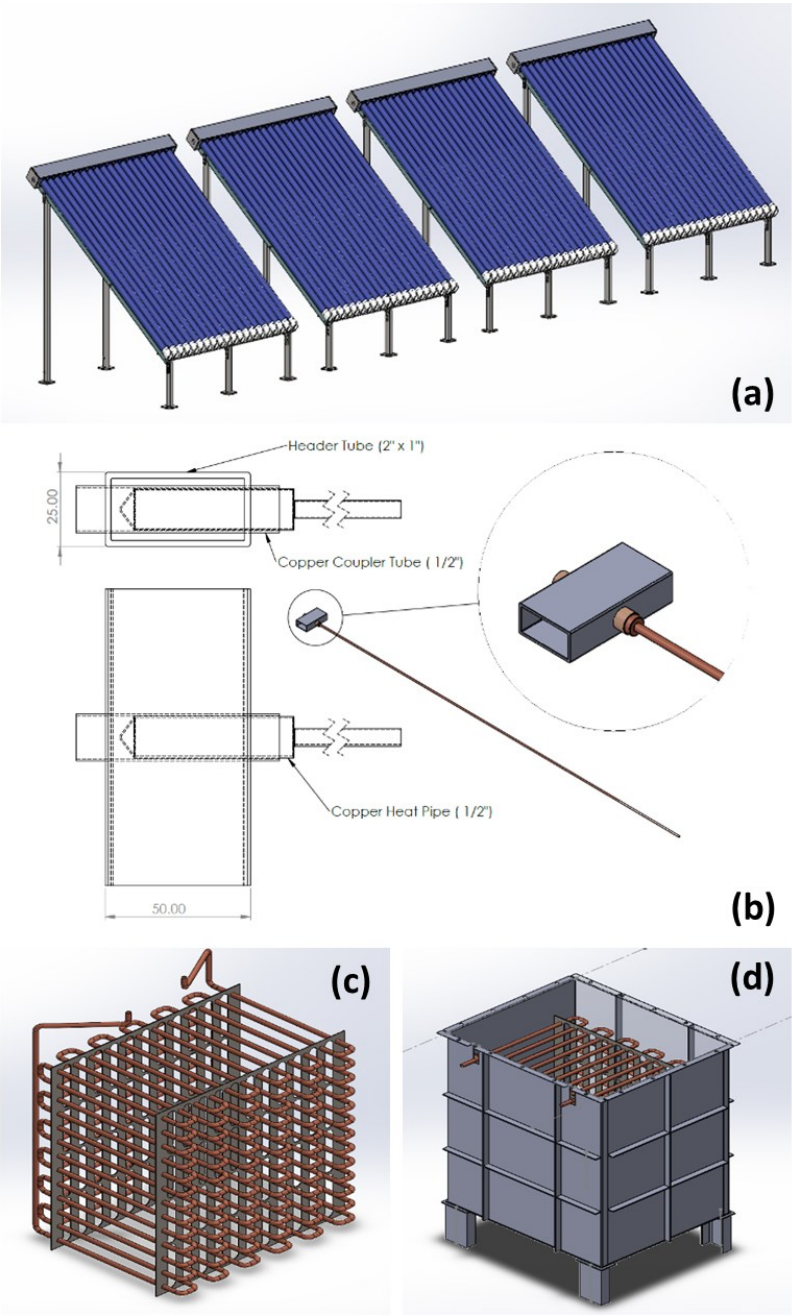

Fig. 2. (a) Evacuated Tube collectors with heat pipe configuration. (b) Heat Pipe Assembly with Header Tube. (c) Heat Exchanger Unit of TES (d) Covered PCM Heat Exchanger

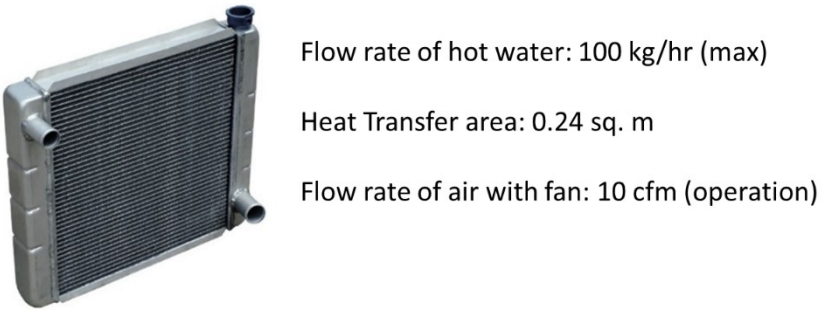

Fig. 3. Photograph of the Room Heater

1.3.3 Water Circulation System:

The water circulation system comprises a pump and solenoid valves to selectively route flow between the solar collectors and PCM module, alongside hand-operated valves for system isolation. Monitoring of critical fluid parameters is achieved via pressure gauges and flow meters [13]. All components are neatly organized within a plumbing panel, arranged as per the P&ID layout. Flexible hoses connect the solar collectors, PCM unit, and room heater to the panel, providing modular flexibility and ease of maintenance [14,15].

Operated as a closed-loop at a nominal 1.5 bar, the system incorporates a 24-liter bladder-style expansion tank to accommodate thermally induced volume variations and stabilize pressure [16]. Such tanks are widely used in solar thermal and hydronic systems to prevent overpressure and extend component life [13].

Daytime operation channels the working fluid between the PCM module and solar collectors, charging thermal energy into the PCM [14,15]. During nighttime, circulation switches between the PCM module and space heater, enabling heat release for ambient heating. This day/night switching is controlled by solenoid valves activated via time or temperature signals [17].

1.3.4 Room Heater:

A forced convection mode of heat transfer is employed to transfer thermal energy from hot water to room air. In this system, hot water flows through a finned-tube heat exchanger, which increases the effective surface area for heat transfer. A fan forces air across the heat exchanger fins, significantly enhancing convective heat transfer efficiency [18,19]. The use of extended surfaces (fins) facilitates efficient energy exchange even at relatively low fluid temperatures [20]. Such water-to-air heating modules are compact, reliable, and suitable for

applications involving solar thermal or PCM-based energy storage systems [12, 21]. The schematic of the heating module is shown in Figure 3.

2 Design Methodology for PCM-Based TES Systems

The appropriate selection of PCM is a critical factor in enhancing the efficiency and performance of any TES system. In this project, paraffin wax was selected due to its moderate melting temperature, high latent heat capacity, chemical stability, and non-corrosive nature, making it highly suitable for nighttime heat delivery in low-temperature space heating applications [2, 7].

The design and thermal modelling of the PCM-based heat exchanger system involve determining the thermal load required for the maximum water mass flow rate, from which the required heat transfer area and PCM thickness are derived. These parameters are calculated considering the standard tube diameters available for fabrication. The resulting heat transfer coefficient is then used to estimate the total tube length and number of tubes required, which in turn guides the selection of the optimal tank geometry and module configuration.

In the thermal design process, the following assumptions were made:

1. Only conduction occurs between the molten PCM and the tube surface, representing the worst-case scenario for heat transfer [12].
2. Water is always present inside the tubes and serves as the heat transfer fluid, consistently transferring energy to the PCM surface.

The volume of paraffin wax required is computed based on the total thermal energy demand of the TES system. A summary of the key design parameters for the TES unit employing paraffin wax is presented in Table 2.

$$\text{Volume of PCM}=\frac{Q_{th}}{H_{PCM}}\times\frac{1}{\rho_{PCM}} \tag{1}$$

Using energy balance, the maximum mass flow rate inside the tubes is calculated.

$$Volume\ of\ TF=\frac{Q_{TF}}{Cp_{TF}\times(T_{w2}-T_{w1})}\times\frac{1}{\rho_{TF}} \tag{2}$$

$$Velocity\ of\ TF=\frac{Volume\ of\ TF}{\frac{\pi}{4}(D_{in})^2} \tag{3}$$

Table 2. Design parameters for required PCM

1.	Enthalpy of Paraffin Wax	176 kJ / kg
2.	Mass of PCM required	204.55 kg
3.	Density of Paraffin wax	820 kg / m^3
4.	Volume of PCM required	0.25 m^3
5.	Maximum water flow	0.0239 kg /s

2.1 Charging of TES

During daytime charging, the melting point of paraffin wax was considered to be 57 °C, a value that aligns well with its typical thermal operating range in low-temperature latent heat thermal energy storage (LHTES) systems [12]. The inlet and outlet temperatures of the circulating water were observed to be 40 °C and 50 °C, respectively. Using these values, the LMTD, a key parameter for assessing heat exchanger performance was calculated to be 11.27 °C. This value provides a basis for the heat transfer rate estimation between the heat transfer fluid and the PCM. The use of paraffin wax in such applications is supported by its relatively narrow melting range, chemical stability, and high latent heat capacity, which contribute to effective energy storage and retrieval [2, 22].

$$\mathrm{LMTD} = \frac{\triangle \mathrm{Ta} - \triangle \mathrm{Tb}}{ln\triangle \mathrm{Ta} - ln\triangle \mathrm{Tb}} \tag{4}$$

$$(\triangle T_a = T_1 - T_{w1},\ \triangle T_b = T_1 - T_{w2}) \tag{5}$$

2.2 Discharging of TES

In the discharging phase of the TES system, heat stored in the paraffin wax during the charging cycle is released to raise the temperature of circulating water. Assuming a worst-case thermal condition, the temperature difference (ΔT) used in the heat transfer calculation is 11.27 °C, which corresponds to the LMTD determined during system operation.

To evaluate the heat transfer rate between the PCM and the circulating water, the thermal resistance model is applied. The overall thermal resistance is the sum of three individual resistances encountered during the process:

- Case 1: Convective resistance due to water flow inside the copper tubes (internal surface)
- Case 2: Conduction resistance across the tube wall (copper material)
- Case 3: Conductive resistance through the paraffin wax (PCM module) surrounding the tubes

The total thermal resistance, as detailed in Table 3, forms the basis for computing the overall heat transfer coefficient (U-value) of the TES module. This U-value is critical for determining the thermal discharge capacity and response time of the system under varying loads and ambient conditions [12,23].

This resistance-based approach is commonly employed in the thermal modeling of PCM heat exchangers, particularly in worst-case (pure conduction) scenarios where natural convection in the PCM is negligible or absent [24].

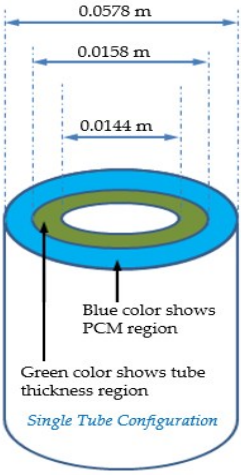

Fig. 4. The dimensions of the tube are based on salt thickness.

Fig. 5. Photograph of the Installed system.

$$PCM\ Outer\ Diameter = (2\ X\ Thickness\ of\ PCM) + D_o \tag{5}$$

$$\mathrm{Re} = \frac{\rho_{TF} \times V_{\mathrm{TF}} \times D_{in}}{\mu_{TF}} \tag{6}$$

$$(HTC_{TF}) = \frac{k \times 0.023 \times R_e^{0.8} \times P_r^{0.4}}{D_{in}} \tag{7}$$

$$Total\ Resistance = Resistance\ by\ PCM + Resistance\ by\ Tube + Resistance\ by\ TF \tag{8}$$

$$\mathrm{Q} = \frac{LMTD}{Total\ Resistance} \tag{9}$$

$$Length\ of\ Tube\ = \frac{Total\ Heat\ Required}{Q} \tag{20}$$

3 Result & Discussion

The system was installed and tested at NTPC NETRA, Greater Noida, during the month of December, when the daily average GHI was 2.4 kWh/m² shown in Figure 5.

The charging-discharging cycle of the system was thoroughly evaluated. During the day, solar thermal energy was collected using heat pipe-based evacuated tube collectors and stored in a paraffin-based TES unit. The TES charging period spanned from 10:00 AM to 5:00 PM. On average, approximately 16 kWh of thermal energy was stored in the TES, which was later utilized during nighttime to maintain a consistent indoor temperature. This highlights the system's improved efficiency and strong potential for practical application. Figure 6 (a) illustrates the average energy stored during the TES charging period.

Table 3. Design parameters for heat transfer

1.	Melting point temp. of Paraffin Wax	57°C
2.	Inlet temperature of Water	65 °C
3.	Outlet temperature of Water	75 °C
4.	Delta T (LMTD)	12.33 °C
5.	Tube Outlet Diameter (Standard size available, Figure 4)	0.0158 m
6.	Tube Inlet Diameter (Based on pipe schedule)	0.0144 m
7.	Reynolds number for water	2647.8
8.	Conductivity of water	0.5 W/mK
9.	Heat transfer	914.6 W/m^2K
10.	Convective heat transfer resistance (per unit length)	0.0242 mK/W
11.	Thermal conductivity of tube	398 W / mK
12.	Tube resistance (per unit length)	$3.76x10^{-5}$mK/W
13.	Paraffin wax thickness (based on weld gap required)	0.021 m
14.	Diameter with PCM thickness	0.0578 m
15.	Thermal conductivity of Paraffin Wax	0.2 W/mK
16.	Paraffin wax resistance	1.0323 mK/W
17.	Total resistance	1.0566 mK/W
18.	Outer diameter (based on PCM thickness)	0.0578 m
19.	Heat Transfer rate, Q	10.666 W/m
20.	Length of tube for 1 kW heat transfer	93.5 m

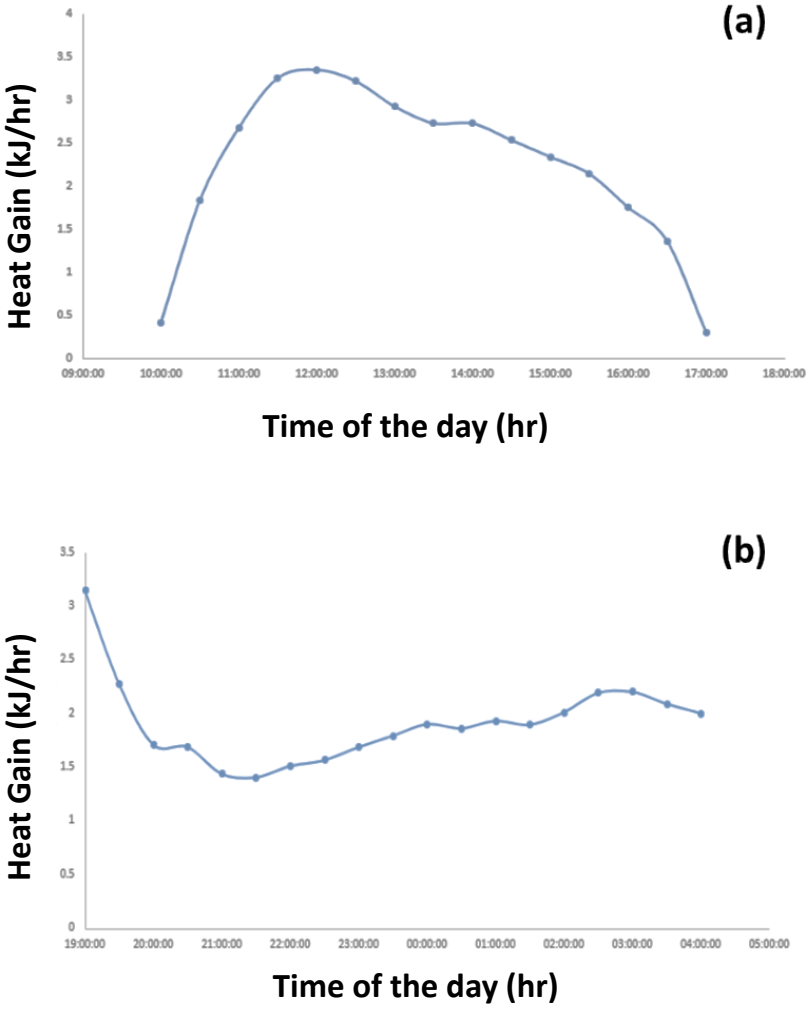

Fig. 6. (a) Plot during Charging of the system (Heat Gain v/s Time) (b) Plot during Discharging of the system (Heat Loss v/s Time).

TES heat was utilized for heating a space of 10 X 10 X 10 cubic feet during the nighttime i.e from 7:00 pm to 4:00 am to maintain the room temperature of 15 °C. Figure 6b shows the average energy released during the discharging process. Considering the charging and discharging cycle of the system, it is concluded that system would be very beneficial for the remote locations where an abundance of sunlight is available during daytime e.g., Leh etc. and nights are very cold. The system is very easy to install and maintain, which makes it feasible for domestic use in such regions. TES-enhanced solar thermal systems can play a significant role in reducing energy consumption and greenhouse gas emissions in buildings.

The successful demonstration of the prototype system, extending this system as a broader adoption of heat pump-based cooling and heating technologies across its townships to substantially reduce overall electricity consumption is under consideration. As an initial strategic move in this direction, developing and demonstrating a 140 TR solar thermal and thermal energy storage-based 24x7 air conditioning system for a hospital is being envisaged. The system will comprise of a CPC, positioned beneath the ETC to improve thermal energy capture efficiency. The new project aims to establish a sustainable and energy-efficient HVAC solution that utilizes solar energy and advanced thermal storage to provide continuous operation both day and night.

4 Conclusion

i.Solar space heating presents a sustainable solution for maintaining indoor thermal comfort by utilizing the solar thermal energy.
ii. The present study has demonstrated a cost effective active solar space heating system that integrates heat pipe base evacuated tube collectors and uses paraffin wax as working fluid. The system has successfully demonstrated night time space heating.
iii. Field implementation demonstrated an energy storage capacity of approximately 16 kWh under an average Global Horizontal Irradiance (GHI) of 2.4 kWh/m², effectively maintaining consistent indoor temperatures throughout the night.

References

[1] Kalogirou, S.A.: Solar thermal collectors and applications. Progress in Energy and Combustion Science 30(3), 231–295 (2004)

[2] Sharma, A., Tyagi, V.V., Chen, C.R., Buddhi, D.: Review on thermal energy storage with phase change materials and applications. Renewable and Sustainable Energy Reviews 13(2), 318–345 (2009)

[3] Tyagi, V.V., Kaushik, S.C., Tyagi, S.K., Akiyama, T.: Development of phase change materials based microencapsulated technology for building applications: A review. Renewable and Sustainable Energy Reviews 15(2), 1373–1391 (2011)

[4] Kuznik, F., David, D., Johannes, K., Roux, J.J.: A review on phase change materials integrated in building walls. Renewable and Sustainable Energy Reviews 15(1), 379–391 (2011)

[5] Zhang, Y., Zhou, G., Lin, K., Zhang, Q., Di, H.: Application of latent heat thermal energy storage in buildings: State-of-the-art and outlook. Building and Environment 42(6), 2197–2209 (2007)

[6] Soares, N., Costa, J.J., Gaspar, A.R., Santos, P.: Review of passive PCM latent heat thermal energy storage systems towards buildings' energy efficiency. Energy and Buildings 59, 82–103 (2013)

[7] Farid, M.M., Khudhair, A.M., Razack, S.A.K., Al-Hallaj, S.: A review on phase change energy storage: materials and applications. Energy Conversion and Management 45(9–10), 1597–1615 (2004)

[8] Kenisarin, M.M., Mahkamov, K.: Solar energy storage using phase change materials. Renewable and Sustainable Energy Reviews 11(9), 1913–1965 (2007)

[9] You, S., Hu, X., Tang, Z.: Experimental investigation on thermal performance of a flat plate solar collector using water and water-ethylene glycol mixture. Energy Conversion and Management 76, 893–901 (2013)

[10] Souliotis, M., Tripanagnostopoulos, Y., Nousia, T.: Performance of CPC type solar collectors. Renewable Energy 34(6), 1575–1583 (2009)

[11] Zambolin, E., Del Col, D.: Experimental analysis of thermal performance of flat plate and evacuated tube solar collectors in stationary standard and daily conditions. Solar Energy 84(8), 1382–1396 (2010)

[12] Agyenim, F., Hewitt, N., Eames, P., Smyth, M.: A review of materials, heat transfer and phase change problem formulation for latent heat thermal energy storage systems (LHTESS). Renewable and Sustainable Energy Reviews 14(2), 615–628 (2010)

[13] Duda Energy: Blue 24 L Vertical Potable Water Expansion Tank. https://www.dudadiesel.com/choose_item.php?id=ExpTank-024V-PW (n.d.)

[14] Lv, Z., Wang, Y., Wang, L., Liu, W., Wu, S.: Experimental research on a solar energy phase change heat storage heating system applied in the rural area. Sustainability 15(3), 2575 (2023)

[15] Niu, F., Yu, N., Zhang, L., Wang, S.: Experimental study of phase change materials coupled with solar thermal energy for building heating in winter. Renewable Energy 138, 192–202 (2019)

[16] Watts: Series ETX, ETSX Pressurized Expansion Tanks for Potable Hot Water. https://www.watts.com/dfsmedia/0533dbba17714b1ab581ab07a4cbb521/24277-source/pg-thermexpansion-pdf (n.d.)

[17] Lu, Y., Wu, D., Yang, S., Wang, H.: Experimental study on double pipe PCM floor heating system. Renewable Energy 149, 1432–1444 (2020)

[18] Kakac, S., Liu, H.: Heat Exchangers: Selection, Rating, and Thermal Design. 2nd edn. CRC Press, Boca Raton (2002)

[19] Incropera, F.P., DeWitt, D.P., Bergman, T.L., Lavine, A.S.: Fundamentals of Heat and Mass Transfer. 6th edn. Wiley, New York (2007)

[20] Holman, J.P.: Heat Transfer. 10th edn. McGraw-Hill, New York (2010)

[21] Shaikh, P.H., Nor, N.B.M., Nallagownden, P., Elamvazuthi, I., Ibrahim, T.: A review on optimized control systems for building energy and comfort management of smart sustainable buildings. Renewable and Sustainable Energy Reviews 34, 409–429 (2014)

[22] Zalba, B., Marín, J.M., Cabeza, L.F., Mehling, H.: Review on thermal energy storage with phase change: materials, heat transfer analysis and applications. Applied Thermal Engineering 23(3), 251–283 (2003)

[23] Ismail, K.A.R., Henriquez, J.R.: Numerical and experimental study of cylindrical and rectangular latent heat storage units. Applied Thermal Engineering 21(18), 1735–1749 (2001)

[24] Mehling, H., Cabeza, L.F.: Heat and Cold Storage with PCM: An Up-to-Date Introduction into Basics and Applications. Springer, Berlin (2008)

Metal Hydride-Based Hydrogen Compressor for Hydrogen Microgrid

Shanta Kumar*, Vinod Kumar, Ajay Kuntal, Yashwant Kumar Saini,

Prabhat Ranjan, Manish Sonker

Hydrogen, Biomass & Waste to Energy Group, NTPC Energy Technology Research Alliance, NTPC Ltd., Greater Noida, Uttar Pradesh, India.
*shantakumar@ntpc.co.in

Abstract. Developing a static metal hydride-based hydrogen compression system with minimal thermal energy requirements and low maintenance is key to building a robust and efficient hydrogen microgrid, where compression plays a critical role. A hydrogen microgrid constitutes a viable approach for the sustainable supply and storage of energy across industrial, institutional, and remote community sectors. The green hydrogen microgrid encompasses renewable energy sources (RES) for electricity generation, in conjunction with integrated systems for hydrogen production, compression, storage, and fuel cell-based energy conversion. To address the challenge of hydrogen compression for high-pressure storage in hydrogen microgrids, a three-stage metal hydride hydrogen compressor (MHHC) was developed. This system overcomes the typical delivery pressure limitation (<100 bar) by compressing hydrogen to pressures exceeding 150 bar. The three-stage MHHC was successfully commissioned and tested, achieving a delivery pressure of 160 bar with heat transfer fluid (HTF) circulated at approximately 45 °C. This approach demonstrates techno-commercial viability, particularly when the MHHC is operated utilizing waste heat or renewable thermal energy sources. Overall, the findings underscore thermochemical hydrogen compression as a robust and energy-efficient approach for hydrogen microgrid applications, effectively meeting the escalating energy demands in remote and hard-to-access regions.

Keywords: Hydrogen Microgrid, Metal Hydride, Hydrogen compressor

1 Introduction

Hydrogen microgrids provide a reliable and sustainable solution for energy supply and storage in industrial, institutional, and remote settings. Designed for stand-alone operation, these systems support the advancement of the hydrogen economy. Solar-powered hydrogen microgrids offer a practical approach for rural electrification and improve system resilience against outages caused by extreme weather events [1]. The global focus on mitigating climate change has prioritized carbon emission reduction in energy policy, accelerating the transition toward hydrogen-based infrastructure [2]. At the

S. Shaswattam et al. (eds.), *NTPC Transactions on Energy Research (NTER 2025)*,
https://doi.org/10.2991/978-94-6463-849-3_11

same time, there is a growing need for eco-friendly ways to produce hydrogen and create green hydrogen supply chains to help reduce carbon emissions from energy systems that rely on fossil fuels.

A microgrid is a localized energy system that integrates distributed energy resources (DERs), such as photovoltaic (PV) panels, waste-to-energy units, and other generators with energy storage systems (e.g., batteries and hydrogen storage) and connected electrical or thermal loads. Equipped with intelligent control systems, a microgrid can operate either in parallel with the main utility grid or independently in island mode [3]. Microgrids are typically classified according to various criteria, including operational mode (grid-connected or stand-alone), supervisory control architecture (centralized or decentralized), electrical configuration (single-phase or three-phase), power type (AC or DC), and the nature of integrated components such as power generation sources, storage systems, and demand-side loads [3].

In a hydrogen-based microgrid, hydrogen is typically produced through water electrolysis powered by renewable energy sources (RES), such as solar energy. At present, green hydrogen production technologies typically operate at pressures of approximately 30 bar [2]. The produced hydrogen is then compressed and stored at high pressure for later use. To meet the water requirements for electrolysis, treated wastewater may be utilized through technologies such as electrodialysis reversal (EDR). For electricity generation, the stored hydrogen is supplied to a fuel cell, which converts it into electrical energy, enabling a clean and reliable power supply.

Because of the low volumetric energy density of hydrogen, it is required to store hydrogen at significantly elevated pressures to ensure its practical applications [4]. This requirement has underscored the importance of developing efficient hydrogen compression systems that are cost-effective, demand low operational energy, and require minimal maintenance to ensure sustainable performance. Conventional mechanical compressors, though widely used, are bulky. Moreover, they generate substantial noise due to moving components and consume considerable electrical energy. Overall, they are facing operational inefficiencies [5].

In contrast, MHHCs offer a promising alternative, utilising thermal energy for hydrogen absorption and desorption. These systems operate silently, as they do not have moving parts. They also require comparatively lower energy input, and hence they are more efficient [5]. Besides having application in hydrogen compression, metal hydrides find extensive utility in hydrogen storage, transportation, purification, and thermal energy storage owing to their unique chemical and thermodynamic properties [5, 6-9]. Notably, MHHCs are capable of supplying hydrogen gas to refueling stations and other storage facilities [10].

It has been projected that the adoption of MHHCs could reduce compression costs by approximately 15-20% relative to conventional methods. Metal hydride-based hydrogen compressors are thermally driven systems capable of compressing hydrogen to higher pressures in either single or multiple stages [11-13].

The working principle of MHHC involves a reversible reaction where a metal (M) with desired characteristics reacts exothermally with hydrogens, producing MH compounds (absorption) and releasing heat (Q) [14]. The reverse reaction, that is, endothermic desorption, occurs at high temperature, whereas compressed hydrogen releases

from the MH bed [13]. The reversible absorption/desorption reactions are represented as shown in Eq. 1, whereas equilibrium of the reaction depends on hydrogen pressure (p), hydrogen concentration in the MH bed (C), and MH bed temperature (T) [14].

$$M(s) + \frac{x}{2}H_2 \rightleftharpoons MH_x(s) + Q \quad (1)$$

Pressurized hydrogen finds various applications in coal-based thermal power plants. At NTPC Energy Technology and Research Alliance (NETRA), demonstration facilities for a hydrogen microgrid powered by solar energy have been established, comprising hydrogen production, compression, storage, and fuel cell-based energy conversion. The compressed hydrogen storage system stores hydrogen up to 200 bar. Currently, mechanical compressors are deployed, resulting in complex, multistage compression systems with high operational and maintenance costs due to their reliance on moving components.

As per the collaborative project on MHHC, an alternate compression system, it has been envisaged to fabricate hydrogen storage reactors of 10000 L of hydrogen storage capacity with hydrogen compression up to 300 bar operating at a temperature (between 80 °C and 300 °C) and a hydrogen supply pressure (between 5 bar and 25 bar).

Metal hydride alloys $La_{0.8}Ce_{0.2}Ni_5$, $La_{0.5}Ce_{0.5}Ni_4Fe$, and $Ti_{0.8}Zr_{0.2}CrMn_{0.3}Fe_{0.6}Ni_{0.1}$ were utilized in the first, second, and third stage reactors, respectively. Following fabrication, each reactor was individually activated. Subsequently, the stages were coupled to form a complete three-stage metal hydride-based hydrogen compressor (MHHC), which was experimentally demonstrated to compress hydrogen to pressures exceeding 150 bar. The detailed design, development, construction, and performance evaluation of the MHHC system are presented in the authors' previous publication [4]. The present study highlights the continuous hydrogen filling into a high-pressure storage cylinder and its integration with a hydrogen microgrid, specifically targeting industrial application scenarios.

For future deployment in hydrogen refueling stations, particularly in the transport sector, where hydrogen needs to be compressed to 700–800 bar, further design and development may be undertaken, whereas the number of compression stages may be increased, thermal design may be improved, and advanced hydride-forming alloys with higher plateau pressures and faster kinetics may be selected. Plateau pressure is the pressure of the plateau region of PCT isotherm plots representing the relationship between pressure, concentration, and temperature for a metal hydride material, where hydrogen concentration changes while pressure remains almost constant.

The demand for hydrogen will increase manifold with the scaling of carbon capture and utilization (CCU) projects in thermal power plants. Carbon dioxide, captured from flue gas, will be utilized to produce methanol, ethanol, urea, sustainable aviation fuel, etc., using hydrogen to achieve the goals of energy transition. Presently, NTPC has designed an innovative green hydrogen-based microgrid system to supply 200 kW of power round-the-clock, replacing the existing diesel gensets at off-grid Army locations where temperatures drop to -30 °C at an altitude of 4,400 metres, reducing carbon emissions by 1500 tonnes annually [15]. Low-cost options for the hydrogen compressors with fewer maintenance requirements will facilitate achieving the goal of the storage

of hydrogen at high pressure. Under this scenario, the MHHC technology holds strong potential as a scalable, safe, and energy-efficient solution for high-pressure hydrogen delivery in the green hydrogen economy.

2 Materials and Methods

The hydrogen microgrid demonstration setup comprises six main components as shown in Fig. 1: (i) a solar photovoltaic power supply system, (ii) a wastewater treatment unit, (iii) hydrogen generation systems, (iv) compressed hydrogen storage systems, (v) a fuel cell-based power generation unit, and (vi) a power delivery system. The schematic consisting of the above systems is shown in Fig. 2.

2.1 Solar Photovoltaic (PV) Power Supply System

The electrical energy required for both the electrolysis of water for green hydrogen production and the operation of the electrodialysis reversal (EDR) system for wastewater treatment is supplied by a solar photovoltaic plant with an installed capacity of 4 MWp. The details of the solar plant capacity are mentioned in Table 1.

2.2 Wastewater Treatment Unit.

To address the requirement of the pure water for the electrolysis process (about 12 kg of water for 1 kg of hydrogen generation) under a water-stressed ecosystem, water reuse, the electrodialysis reversal (EDR) process is employed to treat wastewater for electrolysis. In the hydrogen microgrid setup, wastewater is sourced from the Sewage Treatment Plant (STP) operated by the local municipal corporation, and it is treated on-site using the EDR system. Schematic of EDR system is shown in Fig. 3.

The electrodialysis reversal (EDR) system is a membrane-based separation technology that utilizes alternating anion exchange membranes (AEMs) and cation exchange membranes (CEMs) [16, 17]. AEMs contain positively charged groups that allow anion passage while blocking cations; CEMs have negatively charged groups that allow cations and restrict anions [18]. These membranes create concentrated, diluted, and electrode wash compartments.

When an electric field is applied, anions migrate toward the anode and cations toward the cathode. The electrodes, made of titanium coated with mixed metal oxides (Pt, Ru, Rh), facilitate ion transport [19]. To prevent membrane fouling from charged particulates, the polarity of the voltage is reversed every 30–60 minutes, a process known as electrodialysis reversal (EDR), which effectively cleans the membranes by reversing ion flow.

At 75% water recovery and 25 °C, EDR energy consumption ranges from 0.49 kWh/m³ (for 1000 mg/L TDS) to 1.75 kWh/m³ (for 5000 mg/L TDS). The EDR system at NETRA can purify up to one tonne of sewage treatment plant (STP) water per day for use in hydrogen electrolysis. The details of the EDR system are provided in Table 2.

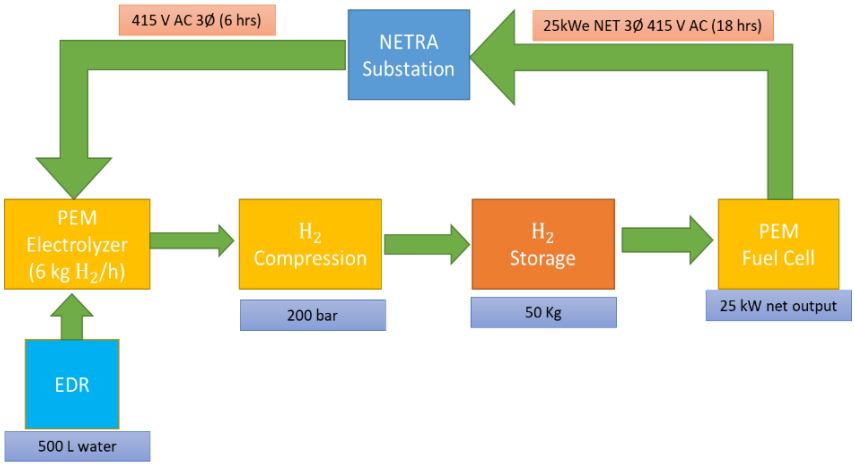

Fig. 1. Schematic diagram of Hydrogen Microgrid.

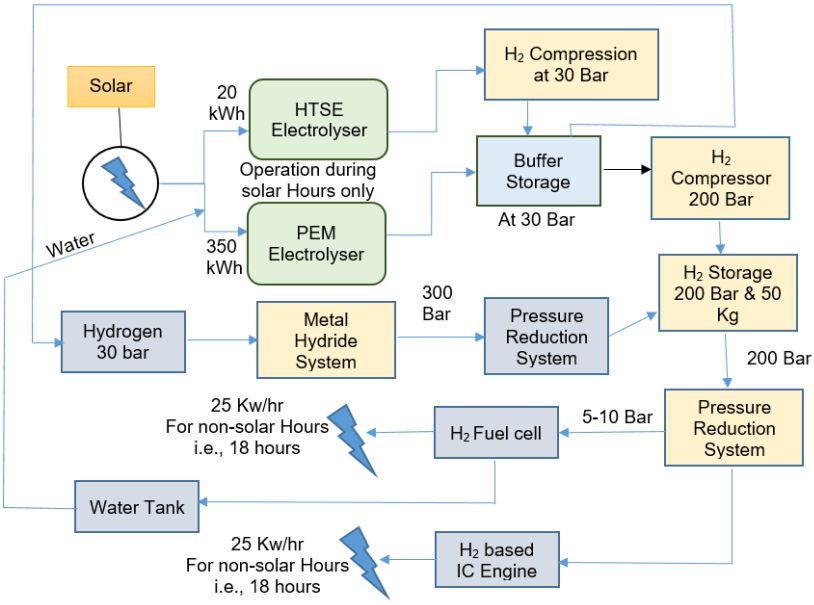

Fig. 2. Constituents of Green Hydrogen Grid (net 25 kWh 24x7).

Table 1. Details of Solar Plant at NETRA

Item	Capacity
Solar Module Rating (Wp)	545
Inverter Rating (kW)	3300
Total Modules in Plant	7410
Plant DC Capacity (kWp)	4038

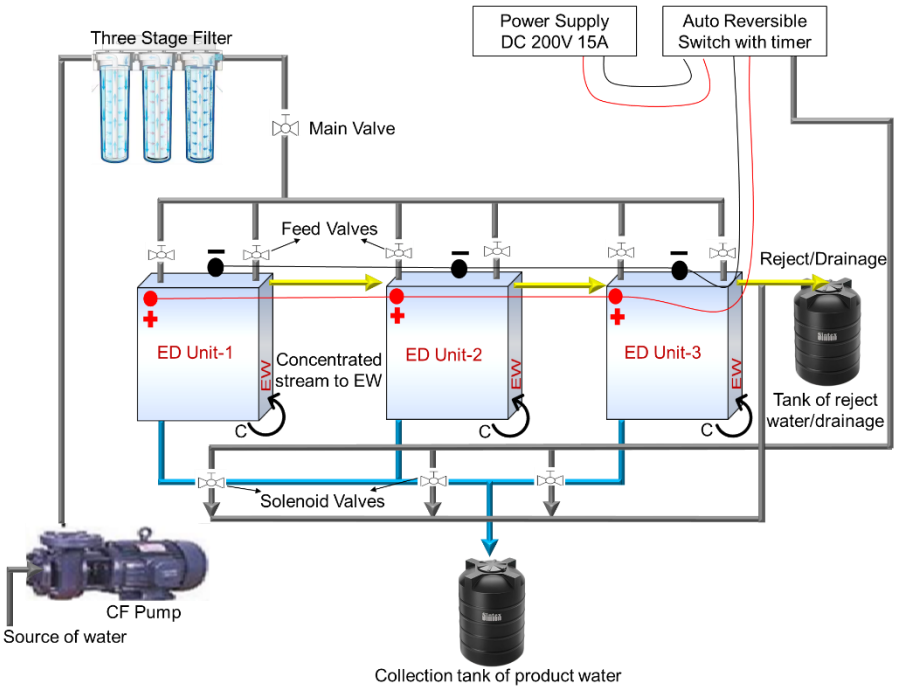

Fig. 3. Schematic drawing of EDR system

Table 2. Details of the EDR system at NETRA

Parameters	Value
Capacity of the plant	1000-1100 L/h
TDS of Feed water	1500-2500 mg/L
Size of the unit/no. of unit	80 cm * 40 cm / 3
Number of cell pair of membranes in each unit	120
Running time	8h then 15 minutes reversal
EDR Inlet/Outlet (using APHA test method)	pH: 8.6 / 7.7 Conductivity (µs/cm): 1760 / 905.7 TDS (ppm): 1056/541.4 Turbidity (NTU): 0.48/0.38 Chloride [Cl^-] (ppm): 259.5/100.7 Ca Hardness (ppm): 130/40 Mg Hardness (ppm): 122/50 Total Hardness (ppm): 252 P-Alkalinity (ppm): 28/- M-Alkalinity (ppm): 404/246

2.3 Green Hydrogen Generation

A polymer electrolyte membrane (PEM)-based electrolyser system has been installed at NETRA to produce 6 kg/h of hydrogen with the designed power input of approximately 350 kW. Alternately, a solid oxide electrolytic cell (SOEC) has also been installed to electrolyse high-temperature steam with temperatures around 800–850 °C, producing approximately 0.5 kg/h of hydrogen. Notably, the high-temperature steam electrolyser (HTSE) consumes around 20% less electricity compared to the PEM-based system, owing to improved thermodynamic efficiency at elevated temperatures.

PEM-based electrolyser. In a PEM electrolyzer, when water is introduced at the anode and a direct current (DC) is applied across the electrodes, the platinum-coated anode catalyzes the electrolysis reaction, splitting water into oxygen gas, protons (H^+), and electrons. The DC potential drives the electrons through an external circuit toward the cathode, while the polymer electrolyte membrane selectively conducts the protons from the anode to the cathode. At the cathode, these protons combine with the incoming electrons to form hydrogen gas (H_2). The membrane permits only the transport of positive ions, thereby ensuring the spatial separation of hydrogen and oxygen gases, which can then be collected and stored independently. The membrane, serving as the electrolyte, is typically made of perfluorosulfonic acid (PFSA) or perfluorocarboxylic acid (PFCA) polymers, valued for their high proton conductivity and stability [20]. The schematic of PEM electrolyser has been shown in Fig. 4 and details are listed in Table 3. The power requirement is sourced from solar plant as shown in Fig. 5.

$$Anode \quad 2H_2O \rightarrow O_2 + 4H^+ + 4e^- \tag{2}$$

$$Cathode \quad 4H^+ + 4e^- \rightarrow 2H_2 \tag{3}$$

HTSE based electrolyser. As shown in Fig. 6, the Solid Oxide Electrolytic Cell (SOEC)-based High-Temperature Steam Electrolyser (HTSE) enables the electrolysis of steam at elevated temperatures (~850 °C), offering significantly higher efficiencies compared to conventional alkaline or polymer electrolyte membrane (PEM) electrolysers. HTSE cells are composed of oxygen ion-conducting ceramic membrane electrolytes. A dense ceramic electrolyte is sandwiched between two porous, electronically conductive electrodes that possess high catalytic activity. In this system, ultrapure steam is preheated to the required operating temperature and introduced into the cathode side of the HTSE unit, where reactions occur (Eq. 4) [21].

$$Cathode\ Reaction \quad 2H_2O + 4e^- \rightarrow H_2 + 4O^{2-} \tag{4}$$

The resulting oxygen ions (O^{2-}) migrate through the solid electrolyte under the influence of the electric field and are oxidized at the anode, releasing oxygen gas via the reaction (Eq. 5) [22]:

$$Anode \quad O^{2-} \rightarrow \frac{1}{2}O_2 + 2e^- \tag{5}$$

The main subsystem of the SOE system has been enlisted in Table 4.

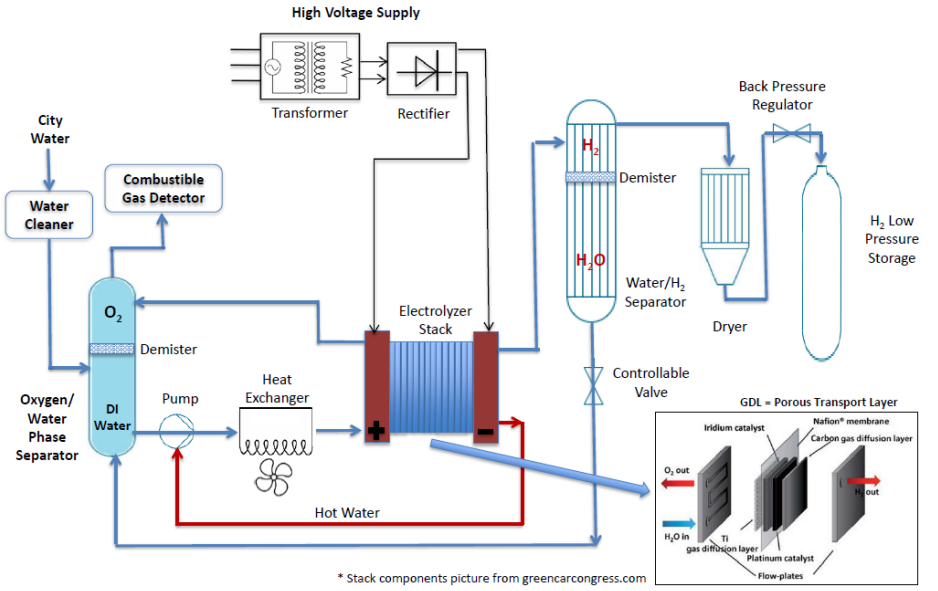

Fig. 4. Schematic of Polymer electrolyte membrane (PEM) electrolysis

Table 3. Detail of PEM Electrolyser

Item	Description
Model of Electrolyser	Mark 1
Technology	PEM
Hydrogen Production Rate	6 kg/h
Stack operating temperature	Max. of 85 degree C
Power rating (DC)	300 kW
Inlet Water (Normal)	2.7 L/min
Inlet water pressure	30 psi (2.1 bar)
Rejected water	1.3 L/min
Material of construction (H2 pressure reduction system)	Valve body: SS304, Internal: SS316, piping & fitting SS304 % SS316
AC Power consumption	5.5 kWh/Nm3 H2 or 55 kWh/kg H2
Start-up time (from off state)	10 min
Ramp-up time (minimum to full load)	5 s
DI water consumption	1.4 L/min (quality of water with less than 2 micro-siemens/cm)
Coolant	Liquid cooled (glycol-water mixture)
Interface connection	H2 product port -.75 in O2 and H2 vent port – diluted in plenum. Inlet water line diameter- 1in Drain port (rejected water) - .5 in
Cost	Rs. 1.31 Cr

Fig. 5. Site photograph of the hydrogen microgrid.

Fig. 6. Site photograph of the TSE System showing various components.

Table 4. Main Sub-system of SOE system

Physical Devices	Control Devices	System Wide Setting
Solid Oxide electrolysis cell (SOEC) stacks and Hotbox assembly	Classical feedback Controllers	System components
Heat exchangers (HXs),	Feedforward controllers	
Molten salt bath,	Temperature control valves (TCVs)	
H2-O2 steam generator (combustor)	Control bus	
Electric Topping Heaters (ETHs)	**Other Equipment**	
Hydrogen/Steam Mixer	H2 Leak Detector	
Hydrogen recycle loop	Gas Purity Analyzer	
Flash drum	HVAC	
Switchyard	Chiller Unit	
Mass flow controllers		
Electrical Panel		

2.4 Power Production System

The compressed hydrogen is used for electricity generation through either a fuel cell system with a 25-kW capacity or a hydrogen-fuelled internal combustion engine. According to the design of the hydrogen microgrid at NETRA, approximately 2 kg of the stored hydrogen per hour is fed into the fuel cell to generate electricity, supplying 25 kWe into the microgrid during non-solar hours (18 hours). The details of the fuel cell have been listed in Table 5. The typical fuel cell at NETRA is shown in Fig. 7.

Polymer Electrolyte Membrane (PEM) fuel cells are high-efficiency (50–60%) electrochemical systems that convert hydrogen into electricity and heat. They consist of platinum-catalyzed anode and cathode electrodes separated by a proton-conducting, water-based acidic polymer membrane [22]. At the anode, hydrogen is split into protons and electrons; the electrons generate electricity via an external circuit, while the protons travel through the membrane to the cathode, where they react with oxygen to form water and release heat. Bipolar plates provide structural integrity, enable electron conduction, distribute gases, and manage thermal output. A single PEM cell generates 0.5–0.7 V under standard operating conditions.

2.5 Compressed Hydrogen Storage Systems

Hydrogen produced from the PEM electrolyser at ~10 bar and from the SOEC system at ~0.5 bar is compressed to ~30 bar using diaphragm compressors and fed into a common buffer tank. Then, hydrogen is further compressed up to ~200 bar using a two-stage diaphragm compressor as shown in Fig. 8 and stored in a high-pressure storage system. The details of the diaphragm compressor are listed in Table 6. As shown in Fig. 9, the storage unit consists of 20 cylinders arranged in five stacked layers on a steel frame, enclosed with safety provisions in compliance with PESO regulations.

Table 5. Details of fuel cell.

Technical Data	Description
Main system parameters	The system is based on the FC stack platform. Output power is 40 kW, maximum current is 334 A, system output voltage is 125-250 V, load modulation is 30-100 %, and operation modes are idle, stand-by, run mode, and emergency
Anode (Hydrogen) Line	Swagelok standard fittings, hydrogen pressure required is between 8 and 12 barg, hydrogen quality should be as per ISO 14687
Cathode (air) Line	It includes an integrated compressor and 3-phase inverter, fresh air supply for the cathode sub-system, depleted air extraction, and drainage of condensed water.
Cooling Line	Liquid cooled, Tin- 65-70 OC, Tout-75-80 OC, coolant is a mixture of De-ionized water and Glycol, liquid to air heat exchanger, connection ports/tubes
Communication Means	Based on the CAN interface (CAN 2.0B Extended frame)
Dimension of Metal enclosure (L X W X H)	920 X 920 X 920 mm

Fig. 7. Photograph of the Fuel Cell.

Fig. 8. Site photograph of the Diaphragm Compressor

Fig. 9. Site photograph of the Hydrogen Storage.

Table 6. Details of the Diaphragm Compressor

Parameter	Value
Compressor Model/Type	D1-70/100, Metal diaphragm type, electrically driven, water cooled, two stages
Suction Pressure (Temperature)	27 barg (Ambient)
Maximum discharge pressure	200 barg,
Operating media/Flow rate	Hydrogen gas, 85 SCMH
H2 purity at compressor inlet/outlet	99.99%/99.99%
Construction Material	Process Head: 300 series stainless steel. Check Valves: 316 SS, 17-4 PH, Vespel peak, Process seal-Viton, Oil Seal – Buna, Diaphragm (Gas/Middle/Oil) -301 SS, Leak detection -316 SS, Brass
Cost	Rs. 1.75 Cr.

2.6 MHHC

Metal hydride-based thermochemical hydrogen compression works on the characteristic absorption-desorption cycle at different sets of temperature and pressure conditions. The process of development of multi-stage MHHC has been shown in Fig. 10.

Design and Development of MHHC. The 3-stage MHHC has been designed and developed to meet the estimates of parameters listed in Table 7. Design consideration for the MH reactors are taken to optimize the hydrogen compression capacity, compression ratio, thermal efficiency, and mass of the reactors, while maximizing mechanical and

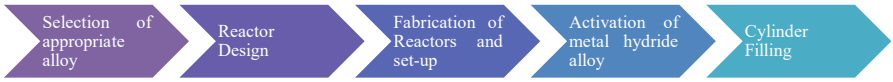

Fig. 10. Process of development of multi-stage MHHC

structural strength to withstand high pressures within the MH bed [23, 24, 25]. The design guidelines in Division 2 of Section VIII of the American Society of Mechanical Engineers (ASME) Boiler and Pressure Vessel Code were followed [26, 27]. Based on the above design considerations, 19 tubes were used in each reactor of the MHHC. The outer diameter of 33.4 mm, with a wall thickness of 4.55 mm for all the reactors. The length of all 19 tubes for Stage 1 and Stage 2 is 1000 mm. For the Stage 3 reactor, all 19 tubes have a length of 1200 mm. Tubes are arranged on concentric circles: one tube is kept in the centre, 6 tubes are arranged in the middle circle with a radius of 43.44 mm, and 12 tubes are arranged in the outer circle with a radius of 86.8 mm, equally distributed. The tube sheet has a diameter of 232.5 mm and a thickness of 14.8 mm.

To prevent the escape of metal hydride powder along with hydrogen during desorption, one end of each tube was capped by welding tubular sintered porous filters. The pore size of the filters was 0.5 µm, and the external diameter was 13 mm. SS316 material was used for manufacturing these filters. Another end had provision for using thermocouples as well as alloy filling into the reactors. The details of the developed 3-stage metal hydride-based compressor have been delineated in Table 8.

The absorption time and the reacted fraction are two important parameters for hydrogen filling of a cylinder using the MHHC. Absorption time is the duration of hydrogen absorption indicated by the rise in temperature until the temperature reaches the initial HTF temperature and reacted fraction is the ratio of the amount of hydrogen absorbed (m_{abs,H_2}) in the MH bed to the maximum storage capacity of the alloy in the MH bed.

Table 7. Design considerations for the selection of metal alloys.

Parameters	**Value (available)**
Maximum source temperature	120-130°C
Available hydrogen pressure at source (PEM based electrolyzer at NETRA generating hydrogen at 10-12 bar)	10-20 bar
Desired delivery pressure (hydrogen is stored at 200 bar at NETRA)	200-300 bar
Storage capacity for compressed hydrogen	6000 L of H_2
Stages of MHHC	Three stages
Absorption temperature (chosen)	5-20°C
Desorption set point (chosen)	80-90°C

Table 8. The details of the developed 3-stage metal hydride-based compressor.

Parameters	Details
Alloy for the first-stage reactor	$La_{0.8}Ce_{0.2}Ni_5$ (AB_5 type), (suitable for supply pressure 3 bar, output pressure 200 bar [28])
Alloy for the second-stage reactor	$La_{0.5}Ce_{0.5}Ni_4Fe$ (AB_5 type), can compress hydrogen up to 32 bar at ~60 °C, doped Fe enhances interaction with the hydrogen atom [29]
Alloy for the third-stage reactor	$Ti_{0.8}Zr_{0.2}CrMn_{0.3}Fe_{0.6}Ni_{0.1}$ (AB_2 type)
Benefits of alloying	Regulates the hydrogen plateau pressure and improves the reaction kinetics [30]
Procurement of alloy	5-10 mm alloy granules were procured from a China-based agency, M/s Zhongke Scientific & Technical Co. Ltd.
The quantity of alloys filled in the reactors	25-30 kg of powdered alloys (as 5-10 mm granules using planetary ball mills)
Storage capacity (wt.%), absorption pressures, and desorption pressures of alloys	The storage capacity (wt.%) of La.0.8Ce0.2Ni5, La0.5Ce0.5Ni4Fe, and Ti0.8Zr0.2CrMn0.3Fe0.6Ni0.1 are 1.42, 1.3 and 1.3 respectively, absorption pressures at 5°C are ~3.68, ~11.3, and ~55.3 bars respectively, and desorption pressures at 60°C are ~10.28, ~31.54, and ~145.7 bars respectively.
Densities of chosen MH alloys	The density (ρ_{MH}) of AB_5-type alloys (used in stages 1 and 2) is ~8400 kg/m³ (approximated), and that of AB_2-type alloys is ~6000 kg/m³ (approximated).

3 Results and Discussion

The temperature, the hydrogen mass flow rate and the HTF flow rate are the important parameters, which determine the compression and hydrogen filling performance of the MHHC. Temperatures are measured using five thermocouples, placed inside the metal hydride bed longitudinally at distinct locations, and two thermocouples are set to measure the HTF inlet as well as outlet temperatures. Hydrogen mass flow rate in the hydrogen line is measured using a Coriolis flow meter (CFM). HTF flow rate is measured by a positive displacement flow rate meter (type: helix, make: ATN Instruments).

3.1 Demonstration of the coupling of reactors for continuous operation of the three-stage MHHC

The 3-stage MHHC are set up at NETRA as shown in Fig. 11. For the continuous operation of the three-stage MHHC, two MH reactors for each stage were arranged in such a way so that while one cylinder is absorbing hydrogen, the other cylinder is taken into service for desorption of hydrogen. Further, tubes, tube fittings, and valves were fitted for the gas circuit. For effective heat transfer during absorption (removal of heat) and desorption (supply of heat), the hot bath and the cold bath were utilised for recirculation of HTF (water) at constant temperature.

Coupling of reactors (Stage I to Stage II). The Stage 1 reactor was sensibly heated to 70 °C, leading to a pressure rise up to 55 bar. At this time, the Stage 2 reactor was cooled and maintained at a temperature of ~10 °C. 245 g of hydrogen was transferred from the Stage 1 reactor to the Stage 2 reactor, and consequently the pressure of the Stage 2 reactor bed rose to 25 bar. Temporal variation of bed temperature during hydrogen transfer from the Stage 1 to the Stage 2 reactor has been shown in Fig. 12.

Coupling of reactors (Stage II to Stage III). After absorption of hydrogen, the Stage 2 reactor was heated to raise the temperature up to 90 °C and the pressure also rose up to 100 bar. Then, HTF with the temperature ~5 °C was circulated through the Stage 3 reactor for cooling and maintaining its temperature at ~5 °C. Under this condition 275 g of hydrogen was transferred from Stage 2 to Stage 3. Temporal variation of bed temperature during hydrogen transfer from the Stage 1 to the Stage 3 reactor has been shown in Fig. 13. Then the Stage 3 reactor was sensibly heated to ~95 °C. Variation of hydrogen pressure during sensible heating of stage 3 reactor to cylinder have been shown in Fig. 14.

Storage of compressed hydrogen. After hydrogen was absorbed in the Stage 3 reactor bed, it was heated to raise the temperature up to 45 °C, leading to a reactor bed pressure of 160 bar. Compressed hydrogen was then transferred to refill an empty gas cylinder up to 60 bar in one cycle. Variation of hydrogen pressure during sensible heating of the stage 3 reactor has been shown in Fig. 15, and the temporal variation of bed temperature during hydrogen transfer from Stage 3 to the cylinder for storage of compressed hydrogen has been shown in Fig. 15.

Fig. 11. Site photograph of the setup of the 3-stage MHHC.

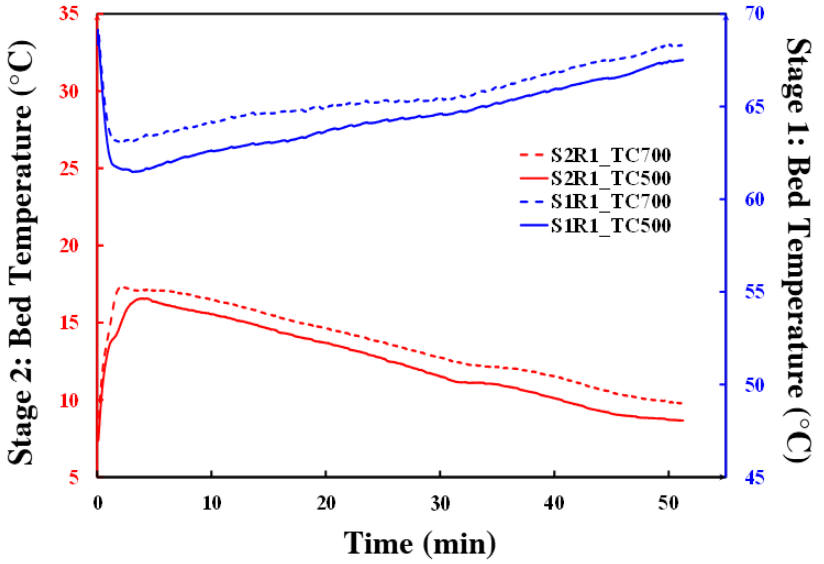

Fig. 12. Temporal variation of bed temperature during hydrogen transfer from stage 1 to stage 2 reactor.

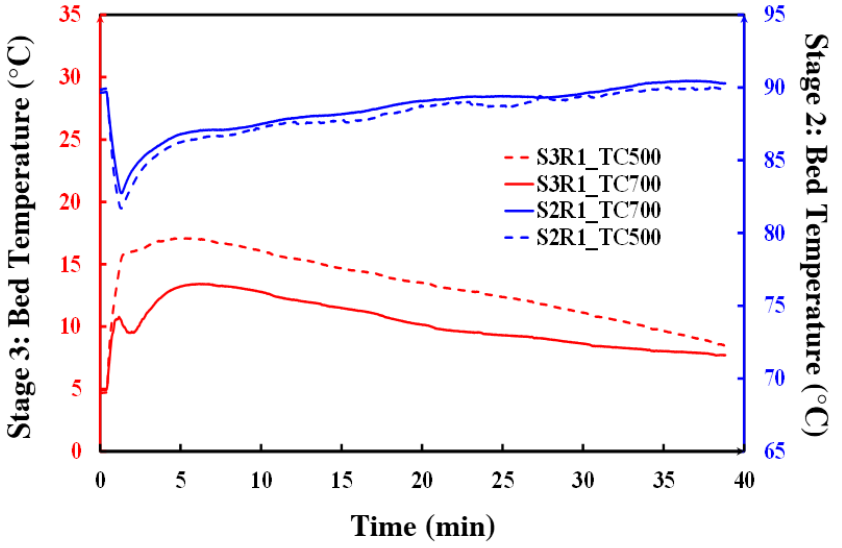

Fig. 13. Temporal variation of bed temperature during hydrogen transfer (coupled stage 2 and stage 3 reactors).

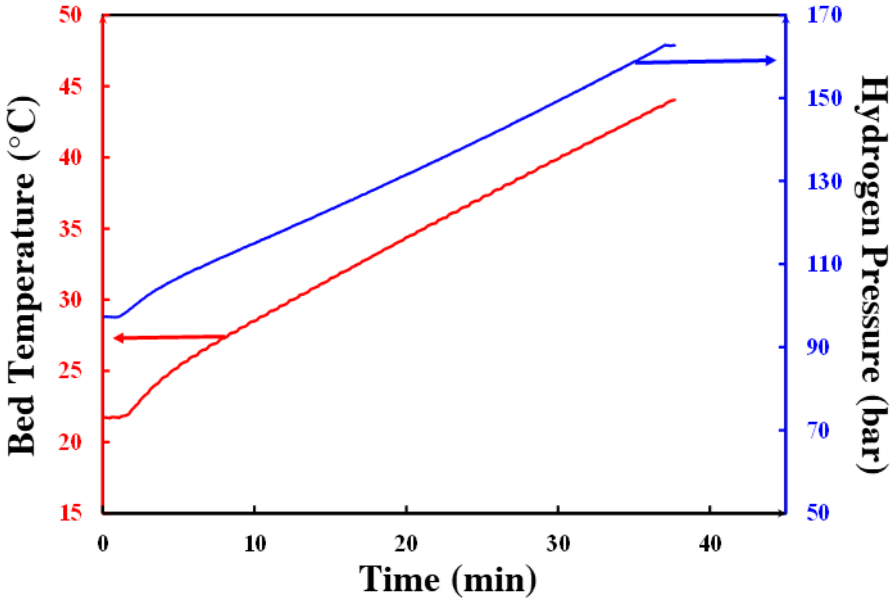

Fig. 14. Variation of hydrogen pressure during sensible heating of stage 3 reactor to cylinder.

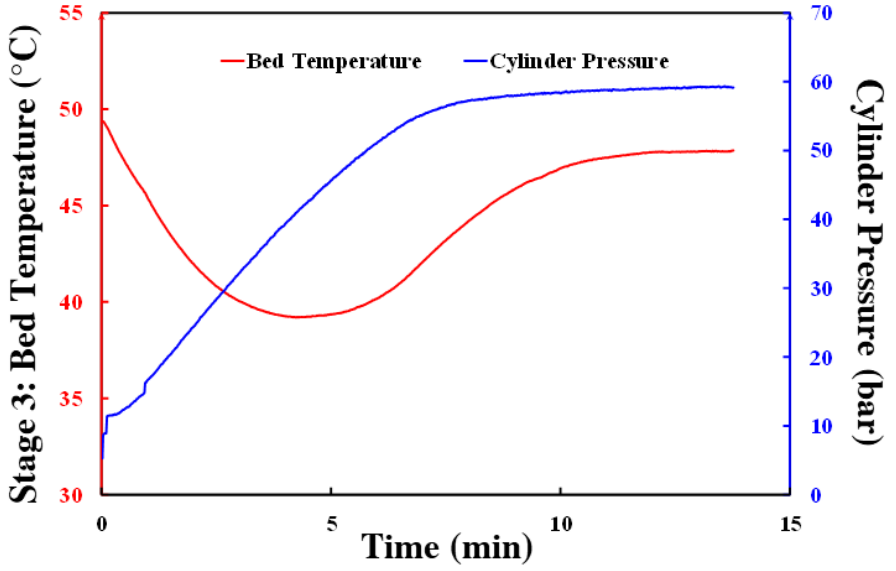

Fig. 15. Temporal variation of bed temperature during hydrogen transfer from stage 3 reactor to cylinder.

3.2 Thermal Performance Analysis

The heat flow schematic for the complete cycle consisting of absorption and desorption has been shown in Fig. 16 for reactor 1.

Thermal energy consumption. All three stages' reactors were sensibly cooled alternately after desorption to facilitate absorption efficiently. Heat flow during cooling, exothermic absorption, heating, and endothermic desorption was shown in Fig. 17. As shown in Eq. 6, the cumulative thermal input (Q_{total}) required for completion of a single compression cycle, including cooling, heat removal during absorption, and heating for desorption, includes sensible heat (Eq. 7) and reaction heat (Eq. 8), taking their absolute values.

$$Q_{total} = |Qsensible| + |Qreaction| \tag{6}$$

$$Q_{Sensible} = |Q1sensible| + |Q3sensible| + |Q5sensible| + |Q7sensible| + |Q9sensible| + |Q11sensible| \tag{7}$$

$$Q_{Reaction} = |Q2reaction| + |Q4reaction| + |Q6reaction| + |Q8reaction| + |Q10reaction| + |Q12reaction| \tag{8}$$

The mass of each reactor is 61 kg, and the mass of hydride material filling the reactor is taken to be 25 kg (maximum wt.). So, the total mass of each reactor system is 86 kg. The specific heat is approximated for each reactor system as 500 J/(kg.K) [4]. So, the total estimated sensible heat for cooling as well as heating, taking their modulus, is 20.64 MJ using Eq. 9. Here, ΔT_1, ΔT_2, and ΔT_3 represent the temperature differences between the desorption temperature (~90°C) and the optimum absorbing temperatures of ~15°C, ~10°C, and ~5°C for Stage I, Stage II and Stage III reactors, respectively.

$$Q_{sensible} = \sum_{i=0}^{n}(m_i \times c_i) \times \Delta T = 2mc\,(\Delta T_1 + \Delta T_2 + \Delta T_3) \tag{9}$$

Reaction heat is estimated from Eq. 10. Here, the enthalpy of absorption (ΔH_a) and the enthalpy of desorption (ΔH_d) are obtained from P-C-T [4]. Here, m_{H2} is the mass of hydrogen absorbed/ desorbed, and M_{H2} is the molar mass of hydrogen.

$$|Qreaction| = m_{H_2} \times \Delta H_a / M_{H_2} + m_{H_2} \times \Delta H_d / M_{H_2} \tag{10}$$

By measuring the mass of hydrogen absorbed/desorbed for Stage I, Stage II, and Stage III reactors, 307 g, 388 g, and 275.5 g, respectively, and corresponding enthalpy of formations for absorption/desorption are 27 kJ/kg, 27.5 kJ/kg/23.5 kJ/kg, and 23.8 kJ/kg and 18.3 kJ/kg, respectively, total reaction heat obtained was ~17.2 MJ. For compressing 275.5 g (3.1 Nm^3) of hydrogen, the required total thermal energy is about 36.2 MJ or 10.1 kWh, which is higher as compared to power consumed by a diaphragm compressor (i.e., 2.45 kWh/kg H_2) compressing hydrogen from 30 bar to 200 bar installed at NETRA [4]. Sourcing thermal energy from waste energy or solar energy will enhance the efficiency of the system. Utilizing the phase change material (PCM), the reaction heat released during absorption can be stored and then can be recycled for the hydrogen desorption processes, enhancing thermal efficiency [23].

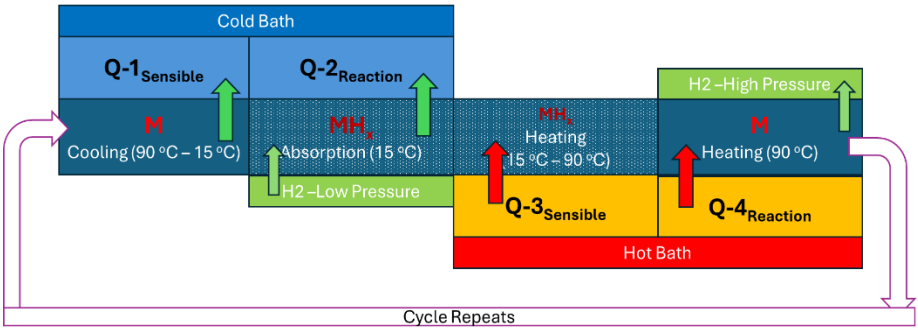

Fig. 16. Heat flow during absorption and desorption phases of reactor 1

3.3 Comparative Analysis of MHHC

Though electrochemical hydrogen compressors can perform with high efficiencies, reaching up to 80–95%, they are not taken in applications due to several limitations, such as response towards hydrogen impurities, limited hydrogen throughput, and higher cost implications. Further, mechanical compressors can provide higher efficiency and throughput, but their function is associated with high noise levels, high electrical power, and frequent maintenance work.

In contrast, the developed MHHC in this study exhibited a thermal efficiency of approximately 5%. Despite the lower thermal efficiency, MHHCs offer distinct advantages: they are inherently safer, simpler in design, have lower operational costs, and possess the added benefit of hydrogen purification during the absorption–desorption cycle.

The performance evaluation of the developed three-stage MHHC provides improved hydrogen compression as compared to the similar three-stage designs developed as listed in Table 9 [31, 32].

The hydrogen throughput of about 134 L/min was achieved by discharging over 200 g of hydrogen, filling the empty cylinder in 17 min during the test as described above. Based on this result, taking a total of 75 kg of alloy filling the reactor, the specific productivity of 107.2 L_{H_2}kg^{-1}h^{-1} was achieved as compared to the productivity of 67.2 L_{H_2}kg^{-1}h^{-1} achieved by the 6-stage MHHC developed by HYSTORE [33].

Table 9. Comparison of hydrogen compression pressures

MHHC/Yr	Stage I desorption pressure (bar)	Stage II desorption pressure (bar)	Stage III desorption pressure (bar)
Three Stage MHHC [32]/2018	3.4 (at 59 °C)	18.4 (at 80 °C)	115.4 (at 100 °C)
Three Stage MHHC [31]/2012	16 (at 100 °C)	36 (at 100 °C)	92 (at 100 °C)
Developed Three Stage MHHC/2025	55 (at 70 °C)	100 (at 90 °C)	160 (at 45 °C)

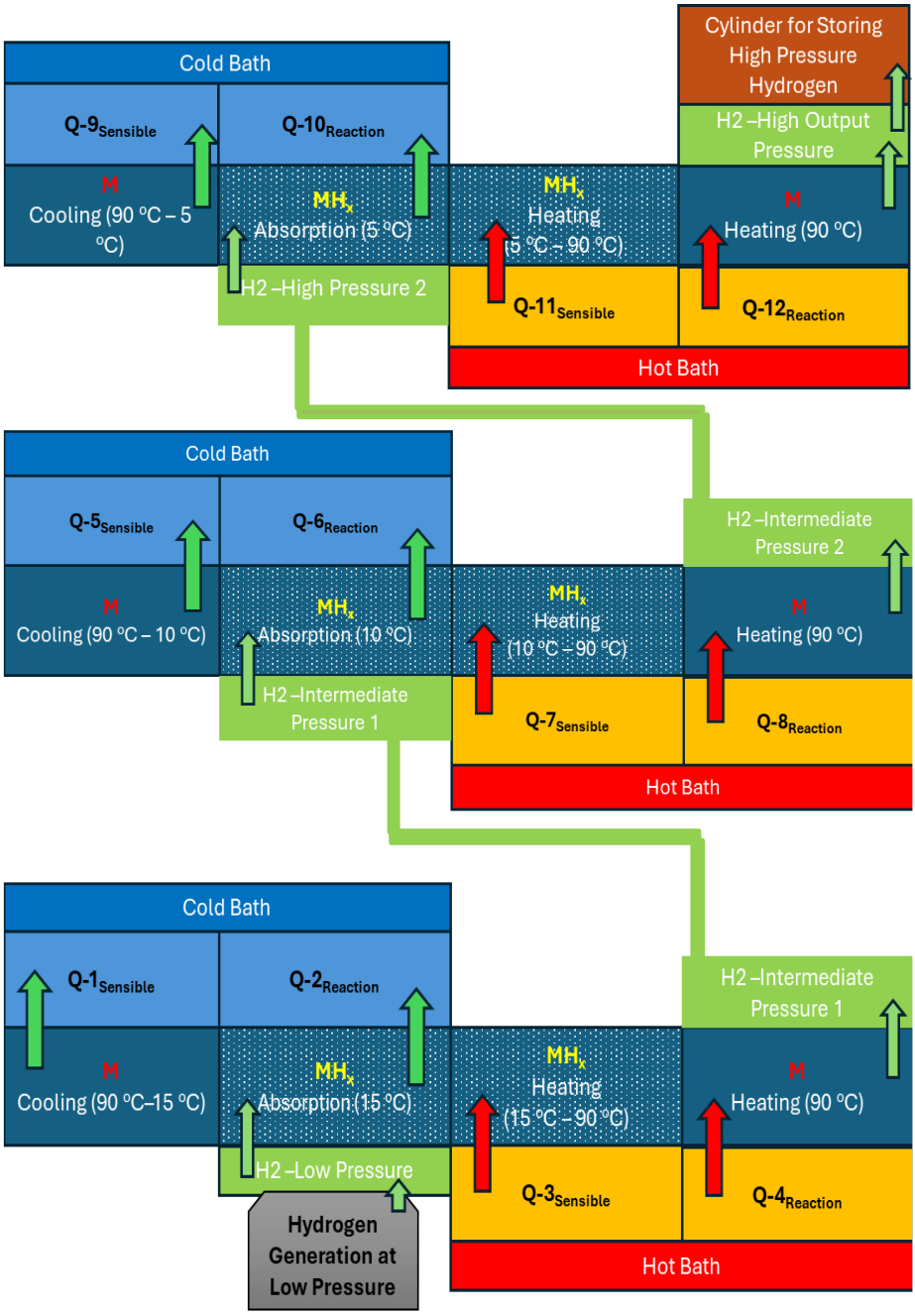

Fig. 17: Heat flow during one complete cycle of three-stage MHHC

4 Conclusion

The implementation of a hydrogen microgrid, incorporating solar-driven PEM/SOEC electrolysis and EDR-treated wastewater, demonstrates the technical viability of integrated renewable hydrogen systems for continuous power supply. The development and successful testing of a three-stage metal hydride hydrogen compressor (MHHC), utilizing $La_{0.8}Ce_{0.2}Ni_5$, $La_{0.5}Ce_{0.5}Ni_4Fe$, and $Ti_{0.8}Zr_{0.2}CrMn_{0.3}Fe_{0.6}Ni_{0.1}$ alloys for successive compression stages, achieved hydrogen output pressures exceeding 150 bar at operating temperatures below 45 °C. The system demonstrated a throughput of 134 L/min, compressing over 200 g of hydrogen in 17 minutes, thereby validating its operational efficiency and reliability under practical conditions.

The MHHC system offers distinct advantages over conventional diaphragm compressors, including lower thermal energy requirements, simplified operation, and reduced maintenance. Future work may focus on optimizing thermal design, increasing the number of stages to achieve higher pressures, and adopting next-generation hydride alloys with improved plateau pressures and absorption/desorption kinetics.

Acknowledgements.

M/s Spirare and M/s Ohmium for development and set up of PEM based electrolyser, hydrogen storage and fuel cell system, M/s Green Power International and M/s H2e for development and set up of HTSE system, M/s Central Salt & Marine Chemicals Research for development and set up of EDR system and M/s Fourth Partner Energy Ltd. for development and set up of 4 MWp Solar Unit at NETRA. The development of the 3-stage metal hydride-based hydrogen compressor was a part of collaborative project between IIT Guwahati and NTPC NETRA.

Disclosure of interests. The authors have no competing interests to declare that are relevant to the content of this article**.**

References

1. Yanez-Barnuevo, M. Microgrids and Energy Improvements in Rural Areas. Environmental and Energy Study Institute (EESI), 2023, Web: https://www.eesi.org/articles/view/microgrids-and-energy-improvements-in-rural-areas, accessed on 27.06.2025
2. IRENA. Green hydrogen cost reduction: scaling up Electrolysis to meet the 1.5°C climate goal. In Renew Energy Agency, Abu Dhabi 2020;2020:105.
3. Van, L.P., Chi, K. D. & Duc, T. N. Review of hydrogen technologies based microgrid: Energy management systems, challenges and future recommendations. International Journal of Hydrogen Energy 48 (2023) 14127-14148
4. Parida, A., Kumar, A., Muthukumar, P., Dalal, A & Kumar, S. Experimental study and performance evaluation of a large-scale multistage metal hydride-based hydrogen compressor. Applied Energy 390 (2025) 125798.
5. Sdanghi, G., Maranzana, G., Celzard, A. & Fierro, V. Review of the current technologies and performances of hydrogen compression for stationary and automotive applications. Renewable and sustainable energy reviews, volume 102, March 2019, Pages 15-170.

6. Melnik, D., Burger, I., Mitjel, J., Kab, j., Sarkezi-Selsky, P., Jahnke, T. & Knoi, T. Energy efficient cold start of a Polymer Electrolyte Membrane Fuel Cell coupled to a thermochemical metal hydride preheater. Applied Energy 359 (2024) 122585
7. Lototskyy, M.V., Yartys, V.A., Pollet, B.G. & Bowman Jr., R.C. Metal hydride hydrogen compressors: review. International Journal of Hydrogen Energy 39 (2014) 5818-5851
8. Tarasov, B.P., Bocharnikov, M.S., Yanenko, Y. B., Fursikov, P.V., Minko, K.B. & Lototskyy, M.V. Metal Hydride hydrogen compressors for energy storage systems: layout features and results for long-term tests. J.Phys.: Energy 2(2020)024005
9. Yartys, V.A., Lototskyy, M., Linkov, V., Grant, D., Stuart, A., Eriksen, J., Denys, R. & Bowman Jr., R.C. Metal hydride hydrogen compression: recent advances and future prospects. Appl. Phys. A (2016) 122:415
10. Chen, Y.H., Shen, C.C., Hsu, C.W. & Lee, S.L. Development of a metal hydride compressor with high-pressure hydrogen storage alloys. Materials Chemistry and Physics 314 (2024) 128917.
11. Lototskyy MV, Yartys VA, Pollet BG, Bowman RC. Metal hydride hydrogen compressors: A review. International Journal Hydrogen Energy 2014:39:5818-51.
12. Muthukumar P, Kumar A, Raju NN, Malleswararao, K, Rahman MM, A Critical Review on Design Aspects and Developmental Status of Metal Hydride Based Thermal Machines. Int J Hydrogen Energy 2018:43:17753-79.
13. Puszkiel, J., von Colbe, J.M.B., Jepsen, J., Mitrokhin, S.V., Movlaev, E., Verbetsky, V. & Klassen, T. Designing an AB2-type Alloy (tiZr-CrMnMo) for the Hybrid Hydrogen Storage Concept. Energies 2020, 13, 2751.
14. Karagiorgis, G., Christodoulou, C.N., von Storch, H., Tzamalis, G., Deligiannis, K., Hadjipetrou, D., et al. Design, development, construction and operation of a novel metal hydride compressor. Int J Hydrogen Energy 2017; 42:12364-74.
15. NTPC and Indian Army ink PPA for solar-hydrogen microgrid in Ladakh. RenewableWatch, Feb. 2025. Web. https://renewablewatch.in/2025/02/05/ntpc-and-indian-army-ink-ppa-for-solar-hydrogen-microgrid-in-ladakh/ accessed on 29.06.2025.
16. Chao, Y.M., & Liang, T.M. A feasibility study of industrial wastewater recovery using electrodialysis reversal. Desalination 221 (2008) 433-439.
17. Goodman, N.B., Taylor, R. J., Xie, Z., Gozukara, & Y., Clements, A. A feasibility study of municipal wastewater desalination using electrodialysis reversal to provide recycled water for horticultural irrigation. Desalination 317 (2013) 77-83.
18. Sedighi, M., Usefi, M.M.B., Ismail, A.F., & Ghasemi, M. Environmental sustainability and ions removal through electrodialysis desalination: Operating conditions and process parameters. Desalination 549 (2023) 116319.
19. Kunrath, C.C.N., Patrocinio, D.C., Rodrigues, M.A.S., Benvenuti, & T., Amado, F.D.R. Electrodialysis reversal as an alternative treatment for producing drinking water from brackish river water: A case study in the dry season, northeastern Brazil. Journal of Environmental Chemical Engineering 8 (2020) 103719.
20. R. Bailon, J. Rodriguez & A. Woocay (2021). Energy Efficiency Analysis of a PEM Electrolyzer and a PEM Hydrogen Fuel Cell. Derechos Reservados @2021, SOMIM ISSN 2448-5551.
21. Yoon, K.J., Lee, S., Park, S.Y. & Minh, N.Q. Advances in high-temperature solid oxide electrolysis technology for clean hydrogen and chemical production: materials, cells, stacks, systems and economics. Progress in Materials science 154 (2025) 101520.
22. Okonkwo, P.C., Ige, O.O., et.el. Platinum degradation mechanisms in proton exchange membrane fuel cell (PEMFC) system: A review. International Journal of Hydrogen Energy 46 (2021) 15850-15865.

23. Dong., X., Zhao, H., Li, H., Fucucci, G., Zheng, Q., Zhao, H. et al. A novel design of a metal hydride reactor integrated with phase change material for H2 storage. Appl Energy 2024; 367:123321.
24. Wang, D., Wang, Y., Wang, F., Zheng, S., Guan, S., Zheng, L., et al. Optimal design of disc mini-channel metal hydride reactor with high hydrogen storage efficiency. Appl Energy 2022:308.
25. Ye, Y., Zhu, H., Cheng, H., Miao, H., Ding, J. & Wang, W. Performance optimization of metal hydride hydrogen storage reactors based on PCM thermal management. Appl Energy 2023; 338:120923.
26.ASME. ASME Boiler and Pressure Vessel Code: Section II Part A. 2020.
27.ASME. ASME Boiler and Pressure Vessel Code: Section II Part D. 2011.
28.Yartys, V.A., Lototskyy, M., Linkov, V., Grant, D., Stuart, A., Eriksen, J., Denys, R. & Bowman Jr., R.C. Metal hydride hydrogen compression: recent advances and future prospects. Appl. Phys. A (2016) 122:415.
29.Chesalkin, A., Martaus, A., Averina, J.M. & men'shikov, V.V. La-Ni Based Alloy Modification by Ce and Fe for the next Hydrogen Storages in Low-Temperature Metal Hydrides. ISSN 1067-8212, Russian Journal of Non-Ferrous Metals, 2019, Vol. 60, No. 4, pp. 492-498. @Allerton Press Inc. 2019.
30.Li, Q., Peng, Z., Jiang, W., Quyang, L., Wang, H., Liu, J. & Zhu, M. Optimization of Ti-Zr-Cr-Fe alloys for 45 MOA metal hydride hydrogen compressors using orthogonal analysis. Journal of Alloys and Compounds 889 (2021) 161629Li, Q., Peng, Z., Jiang, W., Quyang, L., Wang, H., Liu, J. & Zhu, M. Optimization of Ti-Zr-Cr-Fe alloys for 45 MOA metal hydride hydrogen compressors using orthogonal analysis. Journal of Alloys and Compounds 889 (2021) 161629.
31.Muthukumar, P., Patel, K.S., Sachan, P. & Singhal, N. Computational study on metal hydride based three-stage hydrogen compressor. Int J Hydrogen Energy 2012; 37:3797-806.
32.Galvis, E.A.R., Leardini, F., Ares, J.R., Cuevas, F. & Fernandez, J.F. Simulation and design of a three-stage metal hydride hydrogen compressor based on experimental thermodynamic data. Int J Hydrogen Energy 2018; 43:6666-76.
33.Kelly, N.A. & Girdwood, R. Evaluation of a thermally driven metal-hydride-based hydrogen compressor. Int J Hydrogen Energy 2012; 37:10898-916.

Microgrid: A Blueprint for Decentralized Energy Systems

Shyam Manohar Gupta*, Abhinav Ashish, Ravi Kumar, Partha Mukherjee

Energy Storage Group, NTPC Energy Technology Research Alliance, NTPC Ltd., Greater Noida, Uttar Pradesh, India.
*smgupta@ntpc.co.in

Abstract. India's push toward renewable integration and decentralized energy has made Microgrids, Mini grids, and Distributed Energy Resources (DERs) vital for energy access and sustainability. The government's PM-Surya Ghar scheme and policies from bodies like MNRE, CEA, and CERC promote DER adoption, particularly in rural and remote regions. State-specific regulations in Uttar Pradesh, Gujarat, and Rajasthan also support microgrid growth through financial incentives, simplified approvals, and innovative frameworks like blockchain-based energy transactions. Case studies, including the NTPC NETRA Microgrid Project and community initiatives in West Bengal and Jharkhand, underscore the adaptability and social impact of microgrids. Despite challenges in financial viability and regulatory alignment, enhanced subsidies, community engagement, and R&D investments can drive further deployment.

Keywords: Microgrid, Battery Energy Storage System (BESS), Distributed Energy Resources (DERs), Smart Grid, Energy Policy.

1. Introduction

Microgrids, mini-grids, and Distributed Energy Resources (DERs) are key concepts in decentralized power generation and distribution, aimed at enhancing energy access, reliability, and sustainability. This decentralized model promotes renewable energy integration, local energy independence, and resilience against power disruptions. Together, these technologies are essential for modernizing energy systems and achieving sustainable and reliable electricity access for all.

The Indian government has recently introduced a national framework to promote DERs. One of the government's schemes, PM-Surya Ghar: Muft Bijli Yojana, aims to provide 300 units of free electricity per month to one crore households through rooftop solar installations. The scheme is implemented through a structured framework involving both national and state-level agencies [1]

India's energy sector has undergone a significant transformation, driven by ambitious targets for renewable energy integration and the need to provide reliable electricity access across rural and remote areas. Microgrids and mini grids, defined by capacities below and above 10 kW respectively, have emerged as vital components in bridging the energy access gap. This research paper assesses the current policies,

S. Shaswattam et al. (eds.), *NTPC Transactions on Energy Research (NTER 2025)*,
https://doi.org/10.2991/978-94-6463-849-3_12

institutional roles, and deployment of microgrids in India, emphasizing the role of the Ministry of New and Renewable Energy (MNRE), Central Electricity Authority (CEA), Central Electricity Regulatory Commission (CERC), state-specific policies, and the broader impact on sustainable development.

2. Indian Institutional and Policy Framework

2.1 Ministry of Power (MoP)

The Office Memorandums issued by the Ministry of Power (MoP) India for the National Smart Grid Mission (NSGM) highlight financial support initiatives for microgrids., covering up to 30% of project costs as grants. Key requirements include adhering to technical standards for grid integration and maintaining power quality. The mission promotes rooftop PV systems within microgrids and mandates real-time monitoring for improved reliability. Additionally, consumer engagement and staff training are prioritized to build community support and operational expertise. Microgrids are encouraged in islands, SEZs, and remote areas where grid expansion is challenging, with careful site selection essential to ensure environmental and project benefits [2].

2.2 Ministry of New and Renewable Energy (MNRE)

The MNRE is the primary body responsible for India's renewable energy policy and has pioneered initiatives supporting microgrids and mini grids. In 2016, MNRE issued a Draft National Mini and Microgrid Policy aimed at deploying 10,000 renewable energy-based micro and mini-grids, targeting a capacity of 500 MW over five years. The policy emphasized financial support, technical standards, and operational models (including "open market" and "mixed" approaches) to encourage private investment and state-level policy adaptation [3].

2.3 Central Electricity Authority (CEA)

The CEA of India has not issued a dedicated policy exclusively for microgrids. However, microgrids are addressed within broader frameworks and guidelines concerning distributed generation and renewable energy integration.

The National Electricity Plan (NEP) Volume I (2023) and Volume II (2024) by the Central Electricity Authority (CEA) address India's strategy for integrating microgrids and renewable energy sources into its power infrastructure.

Volume I emphasize the role of microgrids in rural electrification and distributed power generation, recognizing challenges like high initial costs, technical complexities in grid integration, and cybersecurity risks. It highlights the need for regulatory support and financial models to ensure microgrid viability [4].

Volume II focuses on the transmission system, addressing the technical and infrastructural demands of integrating microgrids with the national grid. Key challenges

include cybersecurity, transmission capacity needs, and regulatory alignment to facilitate microgrid operations [5].

Both volumes underscore the importance of technological advancements, such as hybrid substations and virtual power plants (VPPs), to enhance grid stability and resilience. The CEA emphasizes cybersecurity protocols, robust infrastructure, and streamlined regulations as critical to supporting decentralized energy solutions, especially for renewable energy integration.

The CEA Technical Standards for Connectivity of Distributed Generation Resources provides guidelines for safely integrating microgrids and other distributed generation resources into India's electricity grid. Key standards cover voltage, frequency, synchronization, and cybersecurity to ensure grid stability. These guidelines align with international benchmarks, notably the IEEE 1547 standard, to maintain consistency and uphold best practices in grid interconnection. Microgrids must have protection systems for fault detection and comply with power quality standards, including harmonics and voltage stability, as per IEEE 519-2014. Additionally, distributed generation resources require a Unique Registration Number and regular compliance checks. These standards are essential for maintaining reliable and secure grid operations while supporting the growth of decentralized energy sources like microgrids [6].

2.4 Central Electricity Regulatory Commission (CERC)

CERC's regulations support the integration of Distributed Energy Resources (DERs), including Renewable resources with storage, hybrid energy projects, into India's power system by establishing guidelines on grid connectivity, tariff determination, and market access. The Tariff Determination for Renewable Energy Regulations, 2020 ensures fair compensation, enhancing financial viability for microgrid projects. Grid Code and Connectivity Regulations outline standards for safe integration with the main grid. Power Market and Deviation Settlement Mechanisms enable DERs to participate in power markets and manage renewable variability. Renewable Energy Certificates (RECs) incentivize clean energy production, while ancillary services and storage guidelines further promote operational stability and flexibility for microgrids and Mini grids [7] [8].

2.5 State-Specific Policies

Some States of India have led the way in adapting central bodies framework into localized policies as follows:

Uttar Pradesh. introduced a mini-grid policy in 2016, offering a 30% subsidy to private players who operate under a Build, Own, Operate & Maintain (BOOM) model. The policy ensures power supply for a minimum of eight hours daily in underserved areas, contributing to job creation and local manufacturing [9].

Bihar and Odisha. included mini grids within broader renewable energy frameworks, offering incentives to developers and streamlining the approval process to encourage private sector involvement [10] [11].

Karnataka. The Karnataka Peer-to-Peer (P2P) Solar Energy Transaction Regulation enables secure, blockchain-based energy trading that aligns well with microgrid operations. By supporting local renewable integration, empowering participants as "prosumers," and providing real-time monitoring, this regulation promotes resilient, efficient energy exchanges within microgrids, enhancing community-based energy management and independence [12].

Rajasthan. The Rajasthan Electricity Regulatory Commission (RERC) Regulations and its amendments are designed to facilitate the integration of Distributed Energy Resources (DERs) into Rajasthan's power grid, with specific implications for the development and operation of microgrids and Mini grids. The RERC regulations support the deployment of DERs, by providing technical, financial, and operational guidelines. By simplifying approval processes, promoting net metering, enabling flexible tariff structures, and offering financial incentives, the regulations make it easier for microgrids to thrive in Rajasthan [13] [14] [15].

Gujarat. The Gujarat Electricity Regulatory Commission (GERC)'s Green Energy Open Access Regulations, 2024 support microgrids by enabling non-discriminatory grid access, allowing energy banking, and simplifying approvals for renewable projects. Flexible billing and net metering empower microgrid participants to produce and trade energy, while transparent transmission charges aid financial planning. Priority access for renewables and financial incentives encourage decentralized, sustainable energy growth. These regulations foster renewable-based microgrids, enhancing energy reliability and supporting Gujarat's goals for clean, resilient energy solutions [16].

These policies address unique state challenges and encourage local solutions, supporting sustainable energy development in diverse regions.

3. Microgrid Case Studies in India

Several case studies demonstrate the effectiveness of decentralized renewable systems in India.

- A significant project of NTPC Energy Technology Research Alliance (NETRA) involves the development of a large microgrid at NETRA's Greater Noida campus. This microgrid aims to enhance energy reliability and efficiency by integrating Distributed Energy Resources (DERs). The NETRA campus features interconnected microgrids with Distributed Energy Resources (DERs) based on diverse technologies, creating a robust and versatile energy ecosystem. These include a 4 MWp Solar PV system paired with a 1 MW/1 MWh Battery Energy Storage System (BESS), a 110 kW AC Microgrid, a 30 kW DC Microgrid, a 25 kW Fuel cell-based Hydrogen energy storage, a 400 kW Municipal Solid Waste (MSW) system, and cumulatively 296 kWp rooftop solar PV plants. Together, these systems demonstrate a range

of cutting-edge renewable energy solutions, fostering resilience and sustainability on campus [17].

- Sundarbans, West Bengal: Initiatives like WWF-India's "Sahasra Jyoti" project and community-driven microgrids on the Kumirmari and Satjelia islands exemplify localized, community-led renewable systems providing reliable energy where grid extensions are impractical. By incorporating community-based management and prepaid metering, these projects have proven successful in maintaining financial sustainability [18].
- Jharkhand's Jargatoli and Basua Villages: Implemented by Mlinda Sustainable Environment Pvt. Ltd., these villages utilize a solar-diesel hybrid microgrid system to supply consistent electricity to 80% of households. The model includes prepaid meters and subsidized appliances to promote energy-efficient usage, thus addressing power reliability and affordability challenges [19].

These case studies reflect the adaptability and scalability of microgrid systems when tailored to local conditions, with significant impacts on local livelihoods, health, and economic opportunities.

4. Challenges in Scaling Microgrids and Mini grids

Despite the potential of decentralized energy, several obstacles remain:

4.1 Financial Viability

The capital expenditure for Rooftop Solar PV capex is approximately Rs 4-5 Cr/MW (Exclusive of land & evacuation system); Wind turbine generators is Rs 6-7 Cr/MW; BESS: Rs2-3 Cr/MWhr; micro/Small hydro is Rs 4-5 Cr/MW (Excluding land); cost of expertise for integrating DER's and BESS for microgrid is 1 Cr per microgrid.

The High installation costs, especially for storage components like batteries, elevate the per-unit cost of microgrid electricity especially when they are compared with DG sets power output. DG sets have lower upfront cost with high running cost. However, the BESS with higher upfront cost gives clean energy and helps maintain autonomous off-grid systems too.

4.2 Challenges in Deployment

Installing, commissioning, and stabilizing large Microgrids come with technical challenges. Installation issues include grid integration, integrating and controlling DER's, control of flexible loads to design the EMS is a bespoke solution which varies with the variety of DER's i.e solar PV, wind turbine generator, MSW generators, micro/small hydro plants. Extensive study of the various characteristics and constraints of each of these resources is studied for setting priority of resources for supplying base load and ramp up/ramp down operation.

Not just the sizing and control but operation and maintenance of the microgrids involves advanced skillset and expertise which is not available in remote areas which are suitable candidates for benefitting from this technology.

4.3 Technical and Operational Issues

Many rural areas experience voltage instability and technical limitations, complicating integration with the central grid. Further, scaling up the size of microgrid complicates the system which requires advanced expertise for integration and troubleshooting.

4.4 Policy Gaps and Inconsistencies

The Draft National Mini/Microgrid Policy (2016) remains unfinalized, creating policy uncertainty. Additionally, varying state-level policies and incentive structures can complicate the regulatory landscape for developers looking to operate across multiple states. Each state must have exhaustive policy for promoting this technology which would help reduce our dependency on DG Sets and add resilience to the power system democratizing the energy market of India.

5. Recommendations for Policy Enhancement to Scale Up Microgrids in India

To accelerate India's microgrid and mini-grid deployment, the following policy recommendations are proposed:

5.1 Finalization of National Microgrid Policy and Standardized Regulations

The government should finalize and implement the MNRE's Draft National Mini and Microgrid Policy with a clear roadmap, financial assistance through monetary and fiscal policies, skill development of local people to operate and maintain these futuristic technologies to develop communities.

Standardizing state-level regulations will simplify approvals, making investment processes smoother. Additionally, establishing a single-window clearance system for microgrid developers will help reduce delays and encourage faster deployment.

5.2 Financial Support and Incentives

To enhance the financial viability of microgrids, the government should increase capital subsidies for Battery Energy Storage Systems (BESS), hybrid microgrids, and smart grid technologies. Providing zero-interest or low-interest loans will further encourage private sector participation, particularly in off-grid regions. A Viability Gap Funding (VGF) mechanism can help bridge financial gaps for large-scale microgrid projects.

VGF funding, subsidy by the government, low-cost financing for deploying rooftop solar PV assisted by BESS of sufficient size to substitute DG Sets in commercial buildings, residential complexes will bring sea change in carbon footprints of commercial and institutional places of India.

5.3 Community Engagement and Capacity Building

Promoting community ownership models can improve the sustainability of microgrid projects. The government should establish training centers to develop a skilled workforce for installation, operation, and maintenance. Providing subsidies or tax incentives for rural consumers adopting microgrid power can make electricity more affordable and encourage greater adoption.

5.4 Research & Development Investments and Smart Grid Integration

Investing in cost-effective energy storage solutions, advanced microgrid controllers, and AI-driven load forecasting will improve efficiency and scalability. The government should support pilot projects for blockchain-based energy transactions and real-time monitoring systems to enhance reliability and security. Developing predictive maintenance frameworks using AI and IoT can ensure long-term operational stability.

6. Conclusion

Microgrids and DERs are pivotal for India's transition to sustainable energy, addressing rural electrification and energy security. While India's policy framework, including PM-Surya Ghar and state-specific initiatives, provides a foundation for microgrid expansion, challenges like high costs, policy inconsistencies, and technical constraints remain. Standardized guidelines, increased subsidies for storage, and community-centric models are essential to overcome these hurdles. Energy is going to be the next UPI and microgrid technologies integrating DER's with storage will be foundation of the Peer-to-Peer energy trading without congesting the distribution/sub transmission networks. Microgrids will improve the energy reliability and add resilience to remote and rural power distribution networks. They will help in restoration of the local power distribution systems, in events of natural calamities, independent of the central power grid. Successful projects like the one installed at NETRA demonstrate microgrids' potential to foster resilience and economic growth. A dedicated policy for promoting Micro, Mini and smart grid initiatives with energy storage is recommended, offering special tariff-based incentives to encourage power delivery during off-solar hours. This approach can enhance commercial and technical viability, ensuring reliable energy supply even when renewable resources are unavailable. By addressing policy gaps and encouraging local participation, India can achieve a robust, decentralized energy system aligned with its renewable energy and sustainability goals.

References

1. PM Surya Ghar Muft Bijli Yojna https://www.india.gov.in/spotlight/pm-surya-ghar-muft-bijli-yojana
2. National Framework for Promoting Energy Storage Systems, 2023, Ministry of Power, Government of India
3. Draft National Mini and Microgrid Policy, 2016, Ministry of New and Renewable Energy, Government of India.
4. National Electricity Plan, Volum I Generation, March 2023, Central Electricity Authority, (CEA), Government of India
5. National Electricity Plan, Volum II Transmission, October 2024, Central Electricity Authority, (CEA), Government of India
6. Notification, Technical standards for connectivity of the Distribution Generation Resources Regulation, February 2019, Central Electricity Authority, (CEA), Government of India
7. Notification, June 2020, Central Electricity Regulatory Commission, Government of India
8. Statement of Reasons, July 2020, Central Electricity Regulatory Commission, Government of India
9. Uttar Pradesh Mini-Grid policy, 2016, UP New and Renewable Development Agency
10. Bihar Policy for Promotion of Bihar new and Renewable Energy Sources, 2017, Energy Department, Government of Bihar
11. Resolution, Odisha Renewable Energy Policy, 2022, Energy Department, Government of Odisha.
12. Notification, Draft KERC (Implementation of Peer-to-Peer Solar Energy Transaction through block-chain based platform) regulation 2024, Karnataka Electricity regulatory Commission.
13. Notification, Regulations for Grid Interactive Distributed Renewable Energy Generating Systems, April 2021, Rajasthan Electricity Regulatory Commission
14. First Amendment, Regulations for Grid Interactive Distributed Renewable Energy Generating Systems, Aug 2023, Rajasthan Electricity Regulatory Commission
15. Second Amendment, Regulations for Grid Interactive Distributed Renewable Energy Generating Systems, July 2024, Rajasthan Electricity Regulatory Commission
16. Notification, GERC (Terms and Conditions for Green Energy Open Access) Regulations, 2024, Gujarat Electricity Regulatory Commission (GERC)
17. Compendium 2017-2023, U.S. India Collaborative for Smart Distribution System with Storage (UI-ASSIST)
18. WWF-India & Schneider Electric. (2021). Sahasra Jyoti: Solar Microgrid Project.
19. Mlinda Sustainable Environment Pvt. Ltd. (2018). Village Electrification in Jharkhand: Jargatoli and Basua Case Study.
20. Centre for Science and Environment. (2022). Mini-Grids: A Just and Clean Energy Transition.

Steam-Enhanced Gasification of Municipal Solid Waste (MSW)/Refuse Derived Fuel (RDF)

Shanta Kumar*[1], Rajesh Deshpande [2], Yashwant Kumar Saini[1], Jitendra Patidar[1], Manish Sonker[1], Subrata Sarkar[1]

[1]Hydrogen, Biomass & Waste to Energy Group, NTPC Energy Technology Research Alliance, NTPC Ltd., Greater Noida, Uttar Pradesh, India.

[2]Thermotech System Ltd., Ahmedabad, Gujarat, India
*shantakumar@ntpc.co.in

Abstract. Steam-enhanced gasification of MSW/RDF is an innovative sustainable waste management technique to generate rich syngas for the generation of either electricity or hydrogen. Renewable energy generation through gasification is clean as well as affordable. It has the potential to facilitate the development of sustainable cities and communities. Auto-thermal, chemical looping gasification, plasma gasification, etc. are types of gasification classified based on variation of the environment of gasification. A demonstration plant, based on steam-enhanced gasification of MSW/RDF effectively gasifies 15 TPD MSW/RDF to produce syngas. Innovative solutions such as for syngas cleaning and refiring of tar collected in the gasifier contribute sustainable waste treatment for energy production. The innovative heat recovery mechanism for in-process applications improves the thermal efficiency of the system. It is analysed that separation of hydrogen from syngas is more efficient and economical as compared to generation of hydrogen through electrolysis using the electricity generated. Enriching an oxidising agent such as air with oxygen will further enhance the hydrogen generation capacity. Hydrogen generated through the thermochemical route, whereas hydrogen separated from syngas using separation technologies, is considered green hydrogen.

Keywords: Gasification, MSW/RDF, Waste to Energy, Hydrogen

1 Introduction

By 2030, energy demand in India is projected to rise by 35%. The energy imports bill of India, the third largest energy consumer globally, has already reached $185 billion in 2022 [1]. Moreover, energy consumption is the main contributor of 33.1 Gt CO_2 emission from energy production based on fossil fuels in 2018 [2].

Municipal solid waste (MSW) contains organic materials such as food waste, decayed vegetables, paper, cardboard, rotten fruits, slaughterhouse waste, etc. and inorganic materials such as electronic waste (e-waste), metals, batteries, construction and demolition debris, textiles, rubber, glass, plastics, ceramics, etc. [3-5]. Conventionally, wastes are dumped into non-engineered landfills or incinerated in the open, either way impacts the environment adversely [2]. For instance, 1805 PJ of energy lost through incinerators and 1409 PJ through landfills for waste disposal in the EU in 2012 [2, 6]. It necessitates the development of technologies and systems for

S. Shaswattam et al. (eds.), *NTPC Transactions on Energy Research (NTER 2025)*,
https://doi.org/10.2991/978-94-6463-849-3_13

sustainable waste management in urgency to tackle the global challenge of projected 6 million tonnes/day waste generation by 2025 [3, 7]. Subsequently, Waste to Energy (WtE), an important global concept to develop a sustainable waste management system, could be a source of affordable and clean energy, leading to the development of sustainable cities and communities, in turn generating wealth from waste. Thus, waste-to-energy technologies could be an instrument to achieve some of the United Nations' sustainable development goals [3, 8].

Either electricity or hydrogen can be generated after gasification of MSW/RDF (refuse derived fuel) and controlled treatment of syngas generated. In line with India's net-zero target, it is required to produce 5 MMTPA of green hydrogen by 2030 [1, 9]. For bolstering green hydrogen generation in India, the World Economic Forum, along with Bain & Company, delineated the strategies in their report titled "Green Hydrogen: Enabling Measures Roadmap for Adoption in India," claiming greenhouse emission reduction by 50 million metric tons [1]. With the expected humongous increase in demand for hydrogen for greening the steel industry and heavy-duty transportation sector, the National Institution for Transforming India (NITI Aayog) projected a quadruple increase in demand for green hydrogen, amounting to 29 million tonnes by 2050 [10]. When produced using renewable energy sources, hydrogen, being a clean fuel, has the potential to contribute to the decarbonisation of the thermal power plants and other industries in the energy sector [3, 11]. Globally, at present 96% of total hydrogen is generated using fossil fuels, which includes 30% from heavy oil and naphtha, 48% from natural gas, and 18% from coal. Hydrogen produced from these processes is not green, as these processes are associated with the emission of about 560 million tonnes CO_2 annually, which accounts for 1.7% of energy-related CO_2 generation globally [3, 12].

A demonstration plant of an MSW/RDF based steam-enhanced gasification plant has been set in Greater Noida by research wing of a power generating public sector enterprise. It was envisioned that hydrogen production would come from the syngas produced in the MSW/RDF gasifier. Moreover, the power block for the generation of electricity using syngas was planned for meeting the part requirement of renewable electricity for the green hydrogen microgrid that will also contribute to making research centre, a net-zero campus. In addition to air, the use of a mixture of air-steam gasification medium may enhance the percentage of hydrogen in the syngas.

2 Material & Methods

2.1 Waste

Suitable wastes for the generation of energy are mainly biomass wood wastes such as paper industry waste, municipal solid waste, packaging and plastics, sewage sludge, RDF, timber industrial wastes, etc. [3, 13, 14]. In general, MSW is comprised of several kinds of wastes, such as recyclable material, biodegradable waste, combustible materials, inert and electronic waste, hazardous toxic wastes, etc. [3]. The average higher heating value of MSW as found in the European Union is around 10 GJ/Mg. As per the Central Electricity Regulatory Commission, "municipal solid waste' implies residential and commercial wastes generated in a notified or municipal area in either solid or semi-solid form. Further, as per this definition, industrial hazardous wastes are not included in municipal solid waste, but treated biomedical wastes are taken. The components of MSW, such as plastic, pulp, wood, organic waste, and other chlorinated

materials, are considered combustible parts of MSW. As per the SWM Rules, 2016, the combustible part of MSW in the form of fluff or pellets, which is produced by processes including drying, shredding, dehydrating, and compacting solid waste is called RDF.

As shown in Fig. 1, the residual dry combustible fraction of the municipal solid wastes, such as textiles, rags, paper, jute, multi-layered packaging, leather, rubber, thermocol, non-recyclable plastic, other compound packaging, cell phones, melamine, coconut shells, etc., are different components of RDF taken one or all together. The station heat rate for power projects that use RDF and municipal solid waste (MSW) shall be 4200 kcal/kWh. The energy content of RDF depends upon its composition, which may vary as their origins vary [15-17]. It further depends on methodologies of sorting, separating, and processing waste material. Table 1 compares the energy content of MSW with respect to other potential biomasses. Here, daf is expanded as dry ash basis and db as dry basis.

For meeting the requirement of gasification, MSW is pretreated to achieve desired physical and chemical properties [18]. The pretreatment processes consisted of both mechanical (Fig. 2) and biological techniques, and they were executed in several stages: sorting, separating, size reduction, briquetting, etc.

2.2 Gasification

The thermochemical processes for waste to energy such as gasification, auto-thermal gasification, chemical looping gasification, plasma gasification method, etc. have several advantages, such as seventy to eighty percentage reduction of mass and an eighty to ninety percent reduction of volume of municipal solid wastes fed as feedstock. Further, bottom ash and slag produced as solid residue in thermochemical processes may be reused in construction-related activities like filler for concrete, road construction, asphalt or low-cost tiles, embankments, etc. [19].

The gasification process involves heating carbonaceous feed at a high temperature range such as 500 ^{o}C to 1200 ^{o}C keeping 0.1 MPa atmospheric pressure, and maintaining an oxygen-deficient environment. In such environment, partial combustion of the combustible component of municipal solid waste occurs, generating syngas rich in hydrogen and carbon monoxide [20]. With air as oxidant, a gasifier operating at atmospheric process produces a low-energy gas mix consisting of about 10% CO_2, 20% CO, 15% H_2 and 2% CH_4 (by volume) with an energy content in the approximate range of 5.2 to 6.0 MJ/m^3 [20]. The energy content of syngas enhances with oxygen as oxidant in the range of 12.9 to 13.8 MJ/m^3 [20]. Further, a stringent pre-treatment process is required for processing feedstock, making it a more energy intensive process [21].

2.3 Production of Syngas from MSW-RDF

A demonstration plant for producing syngas through steam-enhanced gasification of MSW/RDF with a capacity of utilizing 15 TPD MSW/RDF has been set up to generate energy (Fig. 3). The gasifier is designed to feed 565 kg/h of MSW/RDF to produce 1400 Nm^3/h syngas at gasifier output. The produced syngas is cleaned and conditioned and used as a fuel in an internal combustion (IC) engine to generate electricity. With designed feed rate, 130 kg/h ash is also produced as solid residue. About 200 L/h water is fed to water jacket which converts into steam through gasifier heat. This steam along with air are blown to gasifier as oxidiser.

Fig.1. Photograph of MSW-RDF received at site.

Fig.2. Photograph of shredded MSW.

Table 1. Characteristics of MSW and other biomass feedstocks [17]

Biomass/ Parameters	MSW	Grasses	Sugarcane Bagasse	Primary Sewage	Wood
C (%, daf)	27-55	46-51	45.3	43-53.3	50-55
H (%, daf)	3-9	6-7	6.1	6.5-7.2	5-6
N (%, daf)	0.4-1.8	0.4-1.0	0.2	3.8-5.3	0.1-0.2
O (%, daf)	22-44	41-46	46.8	32-46.6	39-44
S (%, daf)	0.04-.18	<0.02-.08	-	2.1	0-0.1
Volatile matter (% db)	41-71	75-83	NR	60-80	70-90
Ash (% db)	12-50	1.4-6.7	NR	16-25	0.1-8
Moisture content (% fresh wt.)	15-40	Not Reported (NR)	NR	90-96	5-20 (dried wood)
HHV (MJ/Kg)	2-14	18.3-20.6	16.7	18-29	19-22
Particle size (mm)	Average: 180-200	Not Applicable (N/A)	0.56-0.85	<5 (82% wt. <0.1)	NA

2.4 Process Description

The process of gasification of MSW/RDF and generation of electricity can be divided into six different sections: 1. Preparatory, 2. Gasification, 3. Gas Cleaning, 4. Engine, 5. Utility, and 6. Auxiliary sections.

Preparatory Section. Pre-treatment of MSW is defined as all intermediate process steps for modifying physical or chemical properties of an MSW/RDF as desired [18]. The intermediate process steps include sorting, separation, mechanical size reduction, and biological treatment [18]. The loose RDF with a size of around 200-250 mm is screened to remove oversize materials, stones, rocks, and heavy materials and passes over a magnetic plate to remove ferrous metals. Then, it is lifted using a Bobcat and loaded on a conveyor for shredding to resize it up to 30-50 mm using a 2 TPH capacity shredder. The shredded material is stored in a storage area of 80 square metres by using a storage conveyor (Fig. 2). Two briquetting machines with one tonne per hour (TPH) production capacity each are utilized for making approximately 100 mm long briquettes with 90 mm diameter after compressing the resized RDF hydraulically. Briquettes are stored manually in a storage area of 75 square metres. Each briquetting machine has its standalone cooling tower and water circulating pumps for internal cooling of its lubricating oil.

Gasification Section. Solid fuel (RDF briquettes) is converted to gaseous fuel (syngas) with the help of a gasifying medium that is a mixture of air and steam. The RDF gasifier is an updraft fixed-bed gasification system designed to process RDF briquettes at a feed rate of 15 tonnes per day (TPD).

Fig. 3. Photograph of the RDF gasification-based net 400 kWe X 24 hrs power generation plant.

As per the design of the updraft-type gasifier, the gasifying medium (air and steam mixture) is forced to pass through the fuel bed in the gasifier from the bottom, and the generated syngas exits out from the top. There are four distinct processes: (i) Combustion, (ii) reduction/gasification, (iii) pyrolysis, and (iv) drying of MSW/RDF occur in different zones of the gasifier with syngas as a final desirable product.

Water, carbon dioxide, and pyrolysis products occur in the combustion zone. Also, pyrolysis products are uncombusted but partially cracked. When these products of the combustion zone pass through the heated charcoal bed, the reduction reactions take place. Fuel pyrolysis is an intricate process. The composition of syngas varies according to temperature, pressure, residence time, and heat losses occurring in the gasifier. Based on experiments, a general trend can be expected based on variation in temperature and other control factors. At first, only water is driven off from RDF up to the temperature of 200 ºC. Then, phenolic compounds with left out water are given off between 200ºC to 280 ºC. Large quantities of tar are produced during actual pyrolysis taking place between 280 ºC to 500 ºC. During this temperature range of 500 ºC to 700 ºC, a small quantity of syngas is produced. Thus, the updraft gasifier is prone to produce tar compounds significantly. As the fuel has a moisture content of up to 10%, this moisture gets evaporated in the drying zone to make the fuel dry. The gasifier shell has two jackets, one above the other (Fig. 4). One (topside) for air preheating and another (bottom side) for steam generation. These jackets mainly prevent overheating of the gasifier shell and recycle the heat back to the gasifier in the form of preheated air and steam. The blower supplies adequate air to generate the desired quantity of gas. The air blower changes speed by sensing gasifier outlet pressure with the help of a variable frequency drive (VFD) to maintain the required air quantity in the gasifier. Air is passed through the top side jacket of the gasifier to preheat air before injecting it into the gasifier. The steam generated in the bottom side jacket of the gasifier is mixed with preheated air in the steam injector, and the mixture is introduced in the gasifier. The water level of the steam jacket is maintained by pumping make-up water.

Gas cleaning Section. Hot syngas exiting from the gasifier is cooled with the first gas cooler from 210°C to 85°C. As temperature goes down, the higher volatile compounds (if any) are condensed based on their condensation temperature. The temperature of syngas is maintained around 85°C by controlling the flow of cooling water. The gas then passes through the electrostatic precipitator (ESP), where tar and fine solids are separated. gas from the ESP is passed through the second gas cooler, where it gets cooled to around 45°C and the majority of volatiles and water vapour are removed. Subsequently, cooled syngas is passed through the scrubber.

The process of gasification has been shown in Fig. 5. Here, in the direct contact type, the scrubber, the entire syngas, is scrubbed with water and cleaned up to its maximum limit, and it is ensured that there should not be any unwanted particles and/or phenolic compounds in the gas. Then, the gas is passed through the gas chilling section in the chilled water cooler, where indirect cooling occurs and moisture as well as low-temperature volatiles, if any, get separated.

2.5 Innovative Features

- The gasifier shell has two jackets, one above the other, one for air preheating (topside) and the other for steam generation (bottom side). The main purpose for the arrangement of both jackets is to prevent overheating of the gasifier shell and recycle the heat back to the gasifier in the form of preheated air and steam.
- The required quantity of air by the gasifier to generate the desired quantity of gas is supplied by an air blower, which changes speed by sensing gasifier outlet pressure with the help of a variable frequency drive (VFD) to maintain the required air quantity in the gasifier. Air is passed through the top side jacket of the gasifier to preheat the air before injecting it into the gasifier. The steam generated in the bottom side jacket of the gasifier is mixed with preheated air in the steam injector and then introduced into the gasifier. The water level of the steam jacket is maintained with a pump.
- Water vapour, tar, phenolic compounds, etc., which are generated in the gasifier during the gasification process, need to be separated using the gas cleaning section. The separated liquids called tar and phenolic water (a mixture of water and phenolic compounds) are the liquid pollutants of this process, and both compounds have some calorific value. Therefore, tar and phenolic water are recycled back to the gasifier for re-firing. This recycling helps to utilize available heat value and to reduce effluent, making zero liquid discharge (ZLD) process. All equipment in the cleaning section has a separate bottom outlet for separation of condensed tar and/or phenolic water. This tar and phenolic water are transferred to respective underground tanks for further separation and reuse.

Fig.4. Photograph of the MSW/RDF Gasifier

- Collected tar from the cleaning section is passed through a heater to preheat. The preheated tar is injected into the combustion zone of the gasifier with the help of a gear pump. Phenolic water collected in the cleaning section is evaporated in a separate evaporator with the help of gasifier jacket steam. The generated phenolic water vapours are mixed with the preheated air in the steam injector. The air and phenolic water vapour mixture (as a gasifying medium) is injected to the gasifier.
- The gas cooler has two sections. The gas is cooled to 20°C in a gas cooler, which is used as a pre-cooler for scrubber outlet gas. The scrubber outlet gas is cooled by 20°C. This precooling helps to reduce the load on the chiller.

2.6 Waste to Energy

After gasification, electricity is generated by using any of the two possible routes. First, hydrogen is separated from syngas, and then electricity is generated using PEM-based fuel cells. Additionally, electricity is produced by combusting balanced carbon monoxide with the minimum required percentage of hydrogen in a gas engine. Moreover, separation of hydrogen and then electricity generation has also the advantage of gasifying MSW/RDF at the source and generating electricity at the place of need.

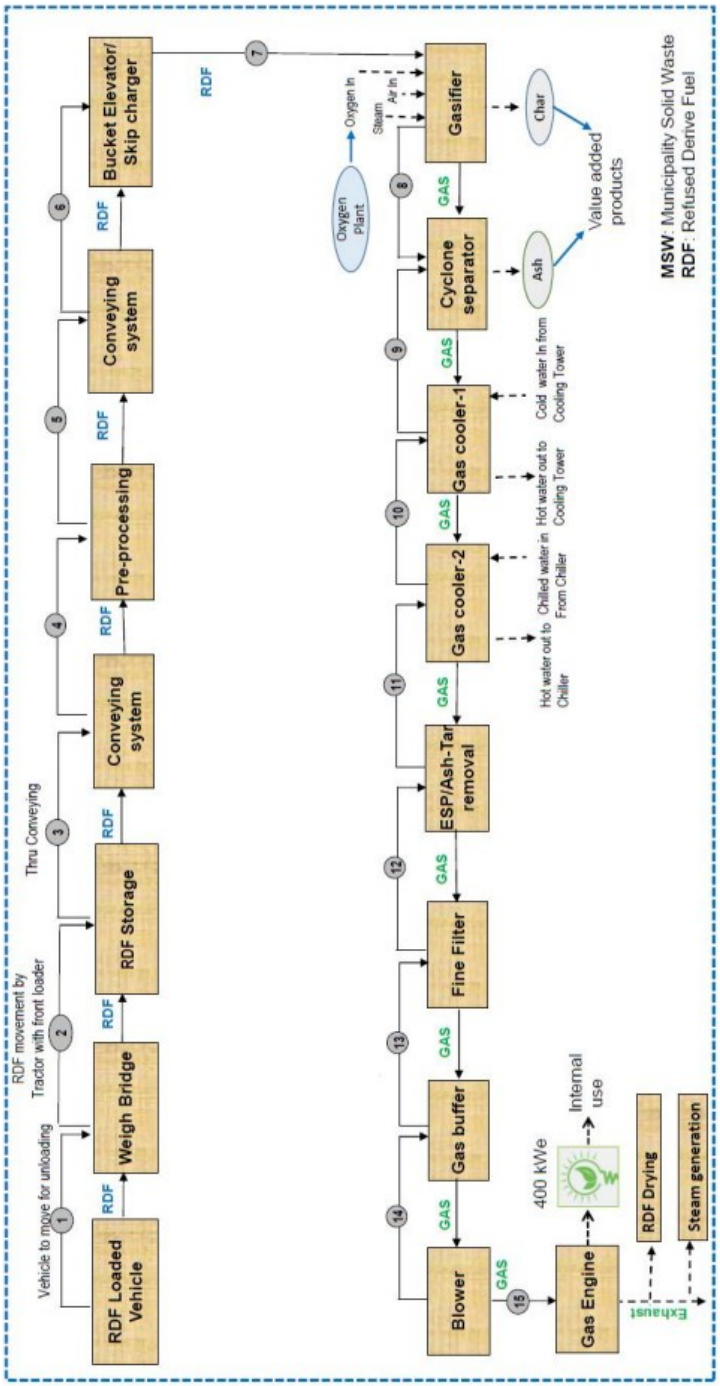

Fig. 5. MSW/RDF based Gasification Process Flow Sheet

Secondly, electricity can be generated directly by combusting total syngas produced in a gas-based internal combustion engine and feeding the power into the grid. Presently, the second path of electricity generation from the gasification of MSW/RDF has been demonstrated.

The power generation section of the demonstration plant consists of a gas engine, an alternator, an engine exhaust, and engine cooling equipment. Clean syngas is transferred into the gas holder with the help of the induced draft (ID) blower. Further, the gas holder acts as a buffer for the supply of gas to the engine. Clean syngas from the holder is combusted in the gas engine to generate the electricity. The ID blower changes speed with the help of VFD by sensing gas holder pressure and varying the gas flow as per requirement. Booster blowers controlled with VFDs supply from the gas holder to the engine in a controlled way, sensing pressure at the engine inlet. Electricity is generated with combustion of syngas in the engine and associated alternator. Two different cooling circuits called high-temperature (HT) cooling and low-temperature (LT) cooling are working independently to fulfil engine-cooling requirements. Part of the generated power is used to operate plant utilities, and the remaining power is exported into the grid.

3 Results and Discussion

3.1 Pre-Treatment of MSW/RDF Feed

The typical composition of briquettes (Fig. 6) consists of 71.64% carbon, 3.51% hydrogen, 2.4% moisture, 0.61% sulphur, 16.54% ash, 0.58% nitrogen, 7.12% oxygen, and 0.10% chlorine with a gross calorific value (GCV) of about 3158 kcal/kg as obtained from laboratory experiment with procedures conforming to IS 1350 Part 1 (proximate analysis), ASTMD 5865 (GCV), ASTMD 5373 (C,H&N), ASTM D 4239 (S) and apparatuses: CHNS Analyser (Vario Macro Cube), automatic bomb calorimeter (Arico Instruments IP-1), Sulfur Analyser (ELTRA CS-580A). For preventing any damages, the briquettes are fed into the gasifier using bucket lift. This ensures in maintaining distinct zones for several processes/reactions for efficient gasification producing quality syngas.

3.2 Operational Evaluation

Operational data of the steam-enhanced MSW/RDF gasification for a random day has been taken for evaluation. As shown in Fig. 7, the syngas generated from gasifier consists of 13.22% H_2, 55.25% N_2, 22.91% CO and 1.493% CH_4 and other gases, which has been evaluated using gas chromatograph (Make: Kshama, Model: 1310RJ). The hourly variation of feed to the gasifier and corresponding power generated, auxiliary power consumed, and net power exported have been shown in Fig. 8. Power has been exported as per demand based on NETRA Microgrid management system. As shown in table 2, 11.11 tonnes of MSW/RDF have been fed to produce 7088 kWh electricity. 1098 kWh electricity out of this generated electricity has been utilized as auxiliary power to run pumps, motors, fans, etc. Based on the energy content in the feedstock and total power generated, 20.56% efficiency has been achieved.

Exhaust Gas Management. To enhance environmental sustainability, exhaust gases from the engine are directed to the auxiliary section for scrubbing before final venting

to the atmosphere. As shown in the Fig. 9, the continuous emission monitoring system (Make: Bhoomi, model: B1700-RM-Flexi) monitors pollutants in the exhaust, enabling real-time control to maintain emissions within regulatory limits. It complies the requirement of ISO 17025:2005 standard with certified gas concentration CO2 17.75%, CO-770 ppm, NO-745 ppm and NMHC is 730 PPM.

Energy Recovery in Gas-Gas Heat Exchanger (GGX). During the process, syngas after wet scrubber with temperature 33 ^{o}C is cooled using chiller for separation of moisture by condensation and then the cleaned syngas is heated to room temperature 30 ^{o}C before blowing into the gas buffer for storage and further applications. For the purpose of energy recovery, as shown in figure, the incoming comparatively hot syngas and outgoing chilled gas are passes through GGX (Fig. 10). The power saved for cooling has been estimated using water droplets from GGX. 5 Kg of water has been collected from GGX. Estimation and consider double effect of cooling and heating, 161 kWh per day.

3.3 Ash Management

Wet Ash Collection. The ash exiting the bottom of the gasifier is wet because it passes through the water seal. As shown in Fig. 11, The wet ash cake is periodically removed by rotating the ash pot. Next, the ash is weighed and loaded into a mobile trolley, which transports it to temporary storage for disposal or use in various applications.

Ash Utilization. According to the preliminary chemical analysis report, the ash can be used as a fertilizer or vermicompost. The bottom ash obtained from the gasification process contains calcium (~218 ppm), potassium (~48 ppm), phosphorous (~4.39%), potash content (~13.90%), and other elements. The test has been carried on by Oatman Overseas Private Ltd. (an ISO: 9001:2015 & ISO:14001 certified laboratory).

Fig. 6. Photograph of the MSW Briquettes.

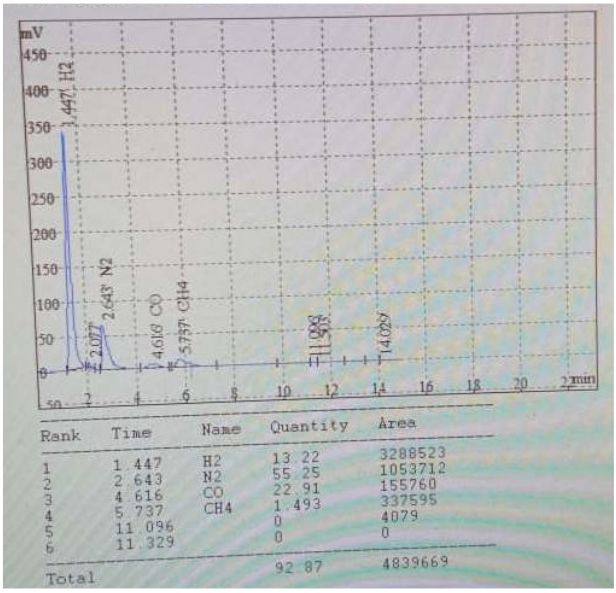

Rank	Time	Name	Quantity	Area
1	1.447	H2	13.22	3288523
2	2.643	N2	55.25	1053712
3	4.616	CO	22.91	155760
4	5.737	CH4	1.493	337595
5	11.096		0	4079
6	11.329		0	0
Total			92.87	4839669

Fig. 7. Syngas Composition

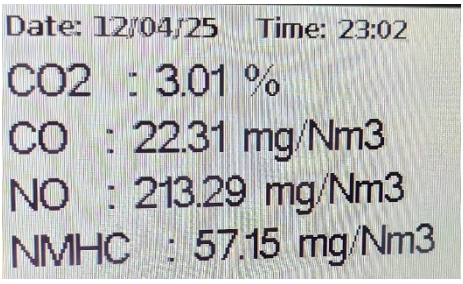

Fig. 8. Photograph of the display screen showing continuous emission monitoring system

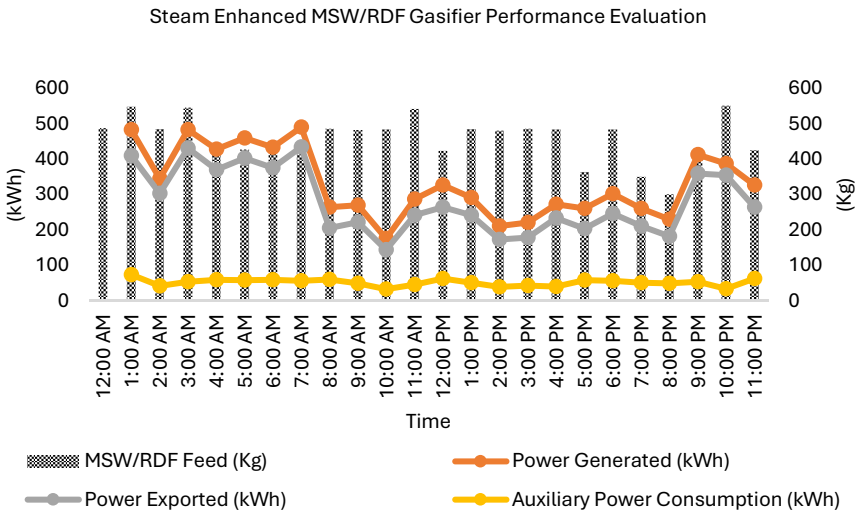

Fig. 9. Performance evaluation of steam enhanced MSW/RDF gasification plant for power generation

Fig. 10. Photograph of the gas-gas heat exchanger with chiller unit.

Table 2. Operational Parameters Evaluation

Plant Performance Indicators	Value
Total Feed in a Day (Kg)	11110
Average Hourly Feed (kg)	462.92
Total number of Bucket used	183
Average per bucket feed (kg/bucket)	60.71
Average Ash % in MSW/RDF	8
Ash% Range in MSW/RDF	7-9
Average Moisture % in MSW/RDF	6
Moisture% Range in MSW/RDF	5-8
Average GCV of MSW/RDF (kcal/kg)	2668.70
Total Energy Input (kcal)	29649257
Total Energy Input (kWh)	34481.76
Power Input (kW)	1436.74
Total Power Produced from gas engine (kWh)	7088
Total Power Exported NETRA grid (kWh)	5990
Auxiliary Power Consumption (kWh)	1098
%Efficiency of Power Conversion	20.56
%Efficiency of the System	17.37
Average AFR	2.27
AFR Range	2-2.5
Water Consumption (L)	7750
Water Consumption per Hour (L/h)	322.92

3.4 Chemical Processes Involved in Gasification

In the current design of the gasification plant, the syngas output has carbon monoxide (CO) between 16% and 18% by volume and hydrogen between 12% and 14% by volume. Further, nitrogen, the major constituent of the syngas, is between 55% and 60% by volume. The calorific value of syngas is determined by the percentage of constituent carbon monoxide, hydrogen, and inert gases in the syngas. composition is identified using online gas analyser (type: Semiconductor sensor, Make: Figaro engineering Inc. for gas sensor and Atmel Corporation for microcontroller).

The gasification process in the gasifier is accomplishes in four stages, which are drying of incoming feedstock, pyrolysis, oxidation (i.e., combustion), and reduction [22]. In the drying stage, moisture from MSW/RDF is evaporated, whereas dried MSW/RDF and water vapour are produced. Dried MSW/RDF undergoes devolatilization reactions during the pyrolysis stage, producing char as solid products, tar as liquid products, and condensable and non-condensable products (CO, CO_2, H_2, CH_4) as gases [23]. During the oxidation stage, partial oxidation reactions take place between oxygen with char, hydrogen, and methane, besides thermal cracking of heavy tar to lighter gases [23].

In the final stage, reduction reactions occur, producing carbon dioxide, hydrogen, and methane. These reactions are critical for the composition of flammable gases (i.e.,

CO, H_2, CH_4, etc.) and low heating value (LHV) [23]. Reactions occurring in the gasification process are listed in Table. 2. CO_2 formation is required for heat generation and hydrogen generation. The higher the hydrogen percentage, higher is the calorific value of the syngas, but it also generates CO_2 (inert for PG as fuel), which reduces calorific value.

Enrichment of oxygen present in air by 5% shall reduce the presence of inert nitrogen in the syngas, but the hydrogen production does not necessarily increase. In fact, the hydrogen production (in absolute terms) is a function of the heat available for endothermic reaction and the quantity of additional steam injection possible in the gasifier. Table 3 enlists the expected composition of the syngas.

It can be seen from the above data that nitrogen from air forms a maximum of 64% by weight of the syngas. Hydrogen, on the other hand, is 1% by weight, which corresponds to around 15 kg/h for the syngas generation of 1500 kg/h by design. It is possible to isolate this hydrogen through a series of cold separation processes for CO_2, hydrogen, and other gases. A three-column pressure swing adsorption process for low-pressure CO_2 separation has already been demonstrated by setting up a plant.

Combined with this process, molecular sieve-based membrane separation and recovery of hydrogen is possible. The potential for hydrogen recovery at 75% yield is 270 kg/day. Air may be enriched with oxygen to reduce nitrogen concentration. In case of higher concentration (>5%) of oxygen to handle, the basic design parameters & configuration of the existing gasifier reactor need to be changed.

There would be a corresponding change in the weight percentage of hydrogen generated from the syngas through oxygen enrichment as shown in table 4. It is expected that the hydrogen generation can be increased by up to 40% with 10% enrichment of oxygen in air. In other words, for the same 1500 kg/hr syngas generation, hydrogen generation capacity would be 21 kg H_2/hr and potential for hydrogen recovery at 75% yield is 378 kg H_2/day.

Comparison of Hydrogen Generation Options with Electrolysis and Gasification. As shown in table 5, the hydrogen production potential from the syngas generated from the gasifier directly is higher as compared to the hydrogen production potential via electrolysis of water using the same amount of electricity, which can be generated (400 kW) using the syngas generated in the gasifier (1500 kg/day) as a feed in the gas engine. Moreover, the electrolysis process includes capital-intensive equipment such as an engine, electrolyser, etc., whereas pressure swing adsorption (PSA) and molecular sieve can be used for separating hydrogen from syngas, which are comparatively less capital intensive.

Fig. 11. Photograph of the ash collection from gasifier.

Table 3: Reactions occurring during gasification process at 25 ºC [22]

Reaction	Reaction type	Reaction	ΔH (kJ/mol)
Carbon reaction			
CR1	Boudouard Reaction	$C + CO_2 \leftrightarrow 2CO$	+172
CR2	Water-gas or steam	$C + H_2O \leftrightarrow CO + H_2$	+131
CR3	Hydrogasification	$C + 2H_2O \leftrightarrow CO_2 + 2H_2$	-7.48
CR4		$C + 0.5O_2 \rightarrow CO$	-111
Oxidation reaction			
OR1		$C + O_2 \rightarrow CO_2$	-394
OR2		$CO + 0.5O_2 \rightarrow CO_2$	-284
OR3		$CH_4 + 2O_2 \leftrightarrow CO_2 + 2\ H_2O$	-803
OR4		$H_2 + 0.5O_2 \leftrightarrow H_2O$	-242
Shift reaction			
SR1	Water Gas Shift	$CO + H_2O \leftrightarrow CO_2 + H_2$	-41.2
Methanation reaction			
MR1		$2CO + 2H_2 \leftrightarrow CH_4 + CO_2$	-247
MR2		$CO + 3H_2 \leftrightarrow CH_4 + H_2O$	-206
MR3		$CO + 4H_2 \leftrightarrow CH_4 + 2H_2O$	-165
Steam-reforming reaction			
SRR1		$CH_4 + H_2O \leftrightarrow CO + 3H_2$	+206
SRR2		$CH_4 + 0.5O_2 \leftrightarrow CO + 2H_2$	-36

Table 4. Expected composition of syngas and effect of oxygen enrichment [24]

Syngas Composition	Composition with Ambient Air		Composition with O_2 Enrichment (by 5%)	Composition with O_2 Enrichment (by 10%)
	Vol%	Weight %	Vol%	Vol%
CO	16.3%	18.0%	18.8%	21.1%
H_2	13.2%	1.0%	15.2%	17.1%
CH_4	1.1%	0.7%	1.3%	1.4%
CO_2	7.2%	12.5%	8.3%	9.3%
N_2	58.4%	64.3%	52.0%	46.1%
O_2	0.1%	0.1%	0.1%	0.1%
Ar	0.6%	0.9%	0.7%	0.8%
SO_2	0.0%	0.0%	0.0%	0.0%
H_2O	3.0%	2.1%	3.5%	3.9%
VM	0.1%	0.3%	0.1%	0.1%

Table 5: Comparison of hydrogen generation options with electrolysis and gasification [24]

Hydrogen generation options	Capacity
Hydrogen generation potential by electrolysis	192 kg/day
Hydrogen generation potential (Without Oxygen enrichment)	270 kg/day (@75% recovery)
Hydrogen generation potential (With Oxygen enrichment)	378 kg/day (@75% recovery)

4. Conclusion

Gasification technology has been widely exploited for MSW/RDF conversion to syngas as a waste-to-energy technology, a way to sustainable management of municipal solid waste. Technical challenges, because of the uncertainty of the input feed compositions and thermoplastic wastes, make it difficult to control the output of the gasification process. The MSW/RDF-based gasification plant uses steam along with air as a gasifier medium to enhance the hydrogen percentage. Based on the experiment carried out for operating the plant, the following observations have been found:

i. The syngas generated from the gasifier typically consists of 13.22% H2, 55.25% N2, 22.91% CO, 1.493% CH4, and other gases.
ii. Gas exhaust from the gas engine to generate electricity complies with the requirements of the ISO 17025:2005 standard.

iii. Gas-gas heat exchanger (GGX), based on innovative energy recovery, saves 161 kWh per day, meeting the dual purpose of cooling and heating.
iv. The bottom ash obtained from the gasification process contains calcium (~218 ppm), potassium (~48 ppm), phosphorous (~4.39%), potash content (~13.90%), and other elements. The ash can be used as a fertilizer or vermicompost after validation of its nutritious effect on plants in the nursery of the experimental setup.
v. With the average daily feed of 11.11 tonnes of the MSW/RDF briquettes, 7088 kWh of electricity can be generated using the gas engine. Out of this electricity generated, 1098 kWh is utilized as auxiliary consumption, and the balance is exported for meeting the power requirement of the premises/campuses.

Further, the alternate uses of the syngas - either producing electricity using the gas engine and alternator or separating hydrogen using membrane/PSA technologies - have been analysed for identifying the efficient route of hydrogen production. Hydrogen can be separated by utilizing cold separation processes. The percentage of hydrogen also gets enhanced by the air-steam mix as a gasifier medium. Given the same input quantity of MSW/RDF briquettes, potential generation of hydrogen is around 30 to 50% more than equivalent generation via electrical energy and electrolysis routes. It further saves pure water consumption that is required to be split in electrolysis.

Acknowledgements. Ajay Kumar Sutrakar (DGM-NETRA) & Ajay Kuntal (Executive-NETRA) for project management and Thermotech System Ltd. for the design, development, installation and commissioning of the MSW/RDF based steam-enhanced gasification demonstration plant at NTPC-NETRA, Greater Noida.

Disclosure of Interests. The authors have no competing interests to declare that are relevant to the content of this article**.**

References

1. Theodore L., Buonicore, A.J., McKenna, J.D., Kugelman, I.J., Jeris, J.S., Santoleri, J.J, & McGowan, T.F.: Waste Management. Perry's Chemical Engineers Handbook, Section 25, McGraw-Hill Companies, Inc., (1999)
2. Carlos, L.: High Temperature air/steam gasification of biomass in updraft fixed bed type gasifier. Ph. D. thesis, Royal Institute of Technology, Energy Furnace and Technology, Stockholm, Sweden, (2005)
3. Chopra S. & Jain A. K.: A Review of Fixed Bed Gasification System for Biomass. Agricultural Engineering International, The CIGR E-journal 9, (2007)
4. Basu, P.: Biomass Gasification, Pyrolysis and Torrefaction: Practical Design and Theory. Book, Third Edition, Dalhousie University and Greenfield Research Incorporated, (2018)
5. Collins, L.: It is much cheaper to produce green hydrogen from waste than renewables. https://www.rechargenews.com/transition/its-much-cheaper-to-produce-green-hydrogen-from-waste-than-renewables/2-1-801160 last accessed on 2024/01/11
6. Gaining Momentum: Green hydrogen policies, plans and programmes. https://renewablewatch.in/2023/12/15/gaining-momentum-green-hydrogen-policies-plans-and-programmes/, last accessed on 2024/01/13
7. Selvi, V.A.: Best Out of Waste: Clean fuel prospects for India. https://renewablewatch.in/2023/12/17/best-out-of-waste-clean-fuel-prospects-for-india/, last accessed on 2024/01/13

8. Lui, J., Chen, W.H., Tsang, D. C.W. & You, S.: A critical review on the principles, applications, and challenges of waste-to-hydrogen technologies. Journal Renewable and Sustainable Energy Reviews, 134 (2020), 110365
9. Zhao, J., Xie, D., Wang, S., Zhang, R., Wu, Z., Meng, H., Chen, L., Wang, T. & Guo, Y.: Hydrogen-rich syngas produced from co-gasification of municipal solid waste and wheat straw in an oxygen-enriched air fluidized bed. International Journal of Hydrogen Energy 46 (2021) 18051-18063
10. Arena, U.: Process and technological aspects of municipal solid waste gasification. A Review, Waste Management 32 (2012) 625-639, ISSN 0956-053X
11. Wang, B., Gupta, R., Bei, L., Wan, Q., Sun, L.: A Review on gasification of municipal solid waste (MSW): production, tar formation, mineral transformation and industrial challenges. International Journal of Hydrogen Energy 48, 26676-26706 (2023)
12. Anand, S.: India Targets 5 MMTPA Green Hydrogen to Curb $185 Billion Energy Import Bill. https://energy.economictimes.indiatimes.com/news/renewable/india-targets-5-mmtpa-green-hydrogen-to-curb-185-billion-energy-import-bill/106682085?utm_source=Mailer&utm_medium=newsletter&utm_campaign=etenergy_news_2024-01-10&dt=2024-01-10&em=c2hhbnRhLmlpdGJAZ21haWwuY29t, last accessed on 2025/02/11
13. Gori, M., Pifferi, L. & Sirini, P.: Leaching behaviour of bottom ash from RDF high-temperature gasification plants. Waste Management 31 (2011) 1514-1521
14. Qi, J., Liu, J., Chen, G., Yao, J., Yan, B., Yi, W., Zao, H. & Xu, S.: Hydrogen production from municipal solid waste via chemical looping gasification using $CuFe_2O_4$ spinel as oxygen carrier: An Aspen Plus Modelling. Journal Energy Conversion and Management 294 (2023) 117562
15. Ghosh, S.K.: Sustainable SWM in developing countries focusing on faster growing economies, India and China. Precedia Environmental Sciences, 35 (2016), pp. 176-184, 10.1016/j.proenv.2016.07.073
16. Tian, H., Gao, J., Lu, L., Zhu, C. & Qiu, P.: Atmospheric pollution problems and control proposals associated with solid waste management in China: A review. Journal of Hazardous Materials 252-253, 142-154 (2013)
17. Saveyn, H., Eder, P., Ramsay, M., Thonier, G., Warren, K., Hestin, M.: Towards a better exploitation of the technical potential of waste-to-energy. JRC Sci Pol Rep 2018;1.
18. World Energy Council. World Energy Resources 2016. https://www.worldenergy.org/publications/entry/world-energy-resources-2016, last accessed on 2025/02/26
19. Nikolaidis, P. & Poullikkas, A.: A comparative overview of hydrogen production processes. Renewable and Sustainable Energy Reviews 67, 597–611 (2017)
20. Bisht, A.S. & Sharma, T.: Indian power sector decarbonization: Net-zero by 2050 or 2070. Energy for Sustainable Development 85 (2025) 101637
21. Hanson, E., Nwakile, C. & Hammed, V.O.: Carbon capture, utilization, and storage (CCUS) technologies: Evaluating the effectiveness of advanced CCUS solutions for reducing CO_2 emissions. Results in Surfaces and Interfaces 18, 100381(2025)
22. Saleh, A.R., Sudarmanta, B., Fansuri, H. & Muraza, O. production from municipal solid waste with a reduced tar yield by three-stages of air inlet to downdraft gasifier. Fuel 263 (2020) 116509
23. Stapf, D., Wexler, M., Ciceri, G. & Johansson, I. Pretreatment of municipal solid waste (MSW) for gasification (Biomass pretreatment for bioenergy –Case study 3). IEA Bioenergy, Technical Report, Feb 2019
24. Huang H., Wang X., Li C., Wang Y., Chen H. Examination of Oxygen-Enriched Gasification Process for Municipal Solid Wastes in South China. In: Qi H., Zhao B. (eds) Cleaner Combustion and Sustainable World. ISCC 2011. Springer, Berlin, Heidelberg, 2012.

Predictive Maintenance of Distributed Processing Unit (DPU) Failures in DCS and PLC Systems Using Artificial Neural Networks (ANN)

NitinTrivedi*

Carbon Capture & Utilization Group, NTPC Energy Technology Research Alliance, NTPC Ltd., Greater Noida, Uttar Pradesh, India.
nitintrivedi@ntpc.co.in

Abstract. In modern industrial automation, DCS (Distributed control System) and PLC (Programmable logic Controller) are widely used for controlling processes and ensuring the safe operation of complex systems. The Distributed Processing Unit (DPU), a very important component in both DCS and PLC architectures, is responsible for real-time data acquisition and control. However, due to its continuous operation in challenging environments, DPUs are susceptible to failures, leading to unplanned downtimes and substantial financial losses. This paper proposes a predictive maintenance framework using Artificial Neural Networks (ANN) to predict DPU failures by monitoring key operational parameters. The model got trained & validated using the "Application failure prediction " dataset from Kaggle, which includes sensor readings and other self-diagnostic parameters and failure logs that align well with the operational characteristics of DPUs. The ANN model demonstrated an accuracy of 92.8% on the validation dataset, providing a reliable solution for early failure prediction. By implementing this ANN-based predictive maintenance framework, industries can proactively predict and address DPU failures, reducing unplanned downtime and minimizing maintenance costs, thereby enhancing overall operational efficiency.

Keywords: DPU, DCS, PLC, Artificial Neural Networks, Predictive Maintenance, Failure Prediction, Kaggle, ANN

1 Introduction

1.1 Predictive maintenance

An AI-enabled maintenance strategy that utilizes real-time data, historical patterns, and machine learning models to forecast equipment failures before they occur**.** Before AI came into the picture, predictive maintenance was based on: Statistical trend analysis, Threshold-based alarms, Rule-based expert systems, Time-series pattern recognition and Feed-forward control logic**.** These methods relied on engineering rules, manual tuning, and fixed algorithms to predict or anticipate equipment issues. For instance, vibration

S. Shaswattam et al. (eds.), *NTPC Transactions on Energy Research (NTER 2025)*,
https://doi.org/10.2991/978-94-6463-849-3_14

analysis and thermography have long been used in rotating equipment health monitoring, without involving AI.

AI-Driven Predictive Maintenance (Modern Approach): Today, AI/ML techniques such as Artificial Neural Networks (ANN), Random Forests, Support Vector Machines (SVM), Long short term memory (LSTM) for time-series allow systems to learn from data and improve predictions dynamically, which adds accuracy, adaptability, and scalability over traditional methods.

While the term "predictive maintenance" may seem contemporary, its conceptual roots run deep into history. The philosophy emerged during World War II, when wartime aviation and military operations demanded unprecedented reliability from machinery. Engineers realized that by monitoring signs of wear and tear, they could proactively service critical components before catastrophic failures occurred. This laid the foundation for a proactive rather than reactive approach to system maintenance.

Interestingly, predictive intelligence in control systems predates the AI boom. In the context of thermal power plants, for instance, the three-element drum level control system—used to regulate water levels in boiler drums—employs a feed-forward control mechanism. This component anticipates load changes and adjusts feed-water flow pre-emptively, effectively exhibiting predictive behaviour. In essence, feed-forward control can be viewed as an early form of artificial intelligence, implemented through analogue control logic decades before the rise of neural networks.

With the evolution of control strategies and the introduction of Distributed Control Systems (DCS), the scope and capability of predictive logic expanded. What was once mechanical intuition encoded into control loops has now evolved into sophisticated ANN-based models, which can process massive amounts of real-time data, identify hidden patterns, and forecast failures with high precision. These models act as digital sentinels, tirelessly watching over assets, and ensuring timely human or automated responses.

1.2 In industrial automation, Distributed Processing Units (DPUs) are critical components in DCS (Distributed control System) and PLC (Programmable logic Controller), responsible for real-time data acquisition and control loop execution (see Fig. 1). However, due to continuous operation in harsh environments, DPUs are prone to failure, which can lead to unplanned downtimes and substantial financial losses.

Failure of active DPU leads to tripping of Unit/ halt of running processes. In a 660 MW power plant, for example, unplanned downtime can cost as much as INR 2.112 million (21.12 lakhs) per hour, considering the electricity generation rate of 660,000 kWh per hour at INR 3.20 per unit besides loss of DC charges and light up oil cost to bring back the unit on bar. the Total cost per unit tripping comes out INR 25 to 30 million (2.5 to 3 Cr). Additional risks include not only financial losses but also potential safety hazards and regulatory compliance issues.

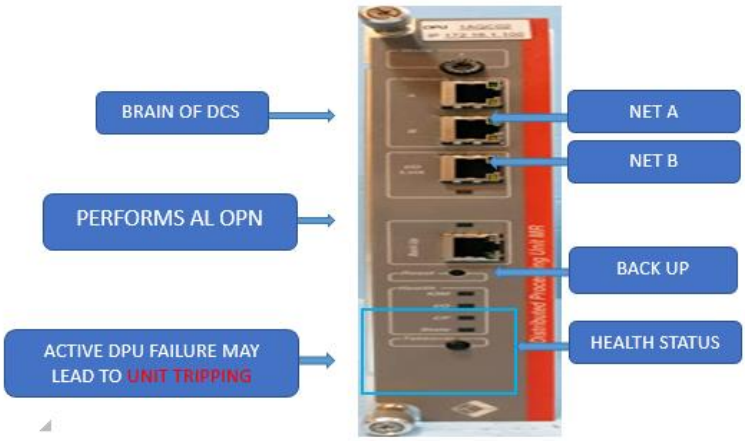

Fig. 1. DPU, MAX DNA DCS

Traditional maintenance methods, such as time-based preventive maintenance, often result in over-maintenance, where resources are wasted on fully functional systems, or corrective maintenance, which addresses failures only after they occur, causing costly unplanned downtimes. Current DPU monitoring tools only issue alarms once a threshold is crossed, providing no foresight into impending failures.

This paper proposes a predictive maintenance framework [1] based on Artificial Neural Networks (ANN) to overcome the limits of conventional methods. By analysing real-time operational data from DPUs, the ANN model can predict failures in advance, allowing for timely interventions and reducing both maintenance costs and downtime. ANN's ability to model complex non-linear relationships between input variables makes it particularly well-suited for predicting DPU failures, ensuring continuous operation in industrial systems.

2. Problem Definition and Scope

The failure of Distributed Processing Units (DPUs) in DCS (Distributed control System) and PLC (Programmable logic Controller) is a significant issue in industrial automation. DPUs are susceptible to various failure mechanisms, such as overheating, memory overload, and network errors. Overheating, particularly when operational temperatures exceed 85°C, degrades critical components, leading to performance issues or system crashes. Similarly, memory overload occurs when DPUs exceed their processing capacity, causing thread execution delays or complete system failures. Network errors, often caused by network-storms, introduce further instability, leading to packet loss and miscommunication between DPUs.

When a DPU fails, many systems rely on hot standby units to take over. However, this changeover process introduces inherent delays, which can destabilize the system further. Even successful transitions often result in temporary data loss or process interruptions, increasing the risk of a broader system shutdown.

Traditional maintenance methods, such as preventive maintenance, often result in over-maintenance, where DPUs are serviced unnecessarily, wasting resources and increasing downtime. In contrast, corrective maintenance, which only addresses failures after they occur, leads to unplanned downtimes that disrupt operations and increase financial losses.

This paper proposes an Artificial Neural Network (ANN)-based predictive maintenance framework that monitors key operational parameters, such as DPU temperature, memory usage, and network load, to predict failures before they occur. The model focuses on preventing thread execution errors, overheating, memory overload, and network-related failures, allowing for timely interventions and minimizing operational disruption.

2.1 STEPS OF PREDICTIVE ANALYSIS OF DPU FAILURE

Controller data is fetched through NTPC's PI server and exported into excel in an automated manner. The second step involves processing of excel data and applying AI-ANN algorithm. In the third step an audio alarm will appear in NTPC intranet PC in case of failure of any of the monitored DPUs.

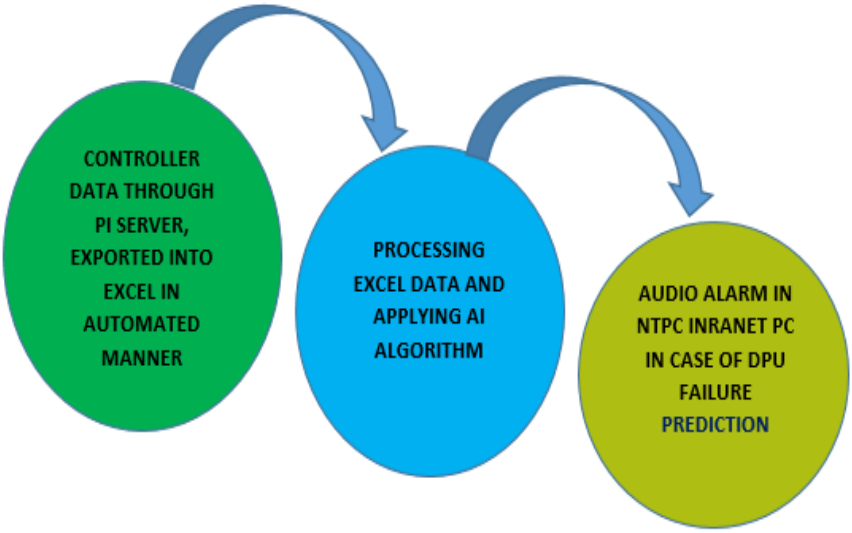

Fig. 2. Steps involved in predictive analysis of DPU failure.

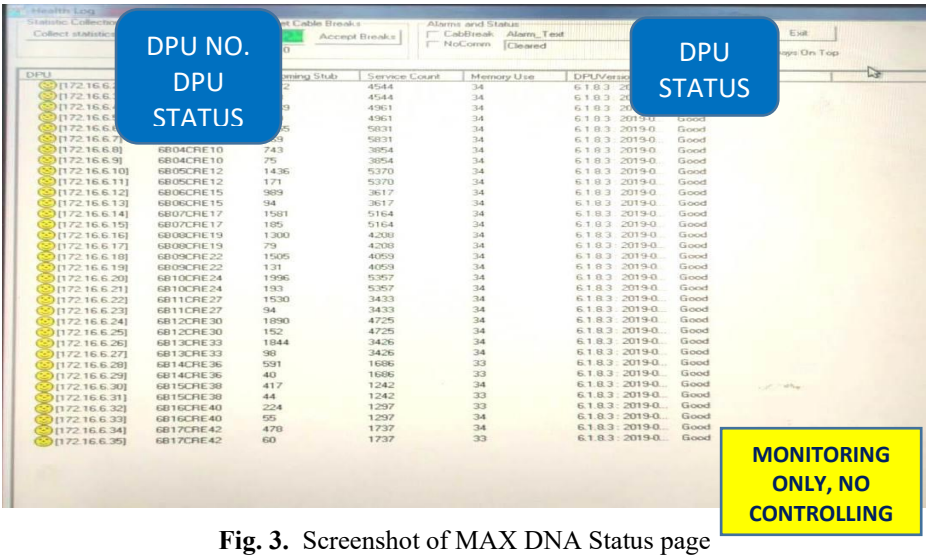

Fig. 3. Screenshot of MAX DNA Status page

2.2 DPU HEALTH MONITORING EXISTING TOOLS IN DCS

Limitation of existing tools / Health log. Several times DPU went into fatal error mode without indicating any specific reason, sometimes alarm comes after failure of DPU. In such cases a changeover to hot standby DPU will occur and even sometimes not. It has been observed that even after successful changeover, unit does not survive and trips due to inherent delays in changeover.

3. Why AI/ML (ANN) model for Prediction?

Developing an AI/ML-based model for DPU (Distributed Processing Unit) failure prediction offers several advantages over traditional methods. The nature of modern industrial systems, such as power plants, presents unique challenges—Big datasets, non-linear relationships and the need for real-time predictions—making AI/ML-based approaches particularly suitable. Below, we enumerate the reasons why AI/ML models, particularly those using algorithms like Artificial Neural Networks (ANN) or other deep learning methods [2], are more suitable than traditional statistical or rule-based models for DPU failure prediction.

3.1 Complexity of the Data

DPU Failure Scenarios. DPUs operate in environments that generate large amounts of sensor/diagnostic data, such as temperature, memory usage, DPU load, etc. These parameters interact in complex, non-linear ways, making it hard for traditional models to capture the associations between variables effectively.

Non-Linear Relationships. AI/ML models, especially neural networks, can capture non-linear relationships between inputs (e.g., DPU, memory, load) and outputs (e.g., failure or no failure). Traditional statistical methods like linear regression or rule-based

models assume linear relationships or predefined rules, which may not be adequate for real-world complexities.

3.2 Scalability and Adaptability

Scalability. Machine learning models can handle large datasets with thousands or even millions of records efficiently. This is particularly important in systems where DPUs generate massive amounts of data over time, and traditional models may struggle to process or make sense of such high-dimensional data.

Adaptive Learning. AI/ML models keep on learning from new data, improving their accuracy over time. This adaptability allows the models to adapt as system conditions change (e.g., aging hardware, changing workloads) without requiring constant manual updates or reconfigurations.

3.3 Real-Time Monitoring and Prediction

DPU failure can be influenced by rapidly changing conditions like temperature surges, sudden increases in network traffic. AI/ML models, especially deep learning models, could be trained to react to dynamic conditions in real-time, identifying potential failures early based on subtle trends and patterns in the data.

3.4 Multi-Variable Analysis and Interaction

High-Dimensional Data. In DPU systems, multiple sensor readings (e.g., temperature, memory usage, CPU usage) and other operational parameters are collected simultaneously. AI/ML models can analyse this high-dimensional data and understand interactions between these features. Traditional approaches often handle each variable separately, losing the context of how different factors interact to cause failures.

Feature Importance. AI/ML models can help identify the most important variables contributing to DPU failures. Techniques like Shapley Additive explanations or SHAP [2]in short, which is a feature importance analysis can provide insights into which factors are most influential, helping with both prediction and root cause analysis.

3.5 Predictive vs. Diagnostic Approaches

Proactive Failure Prediction. Traditional diagnostic models focus on identifying failures after they occur or based on predefined thresholds. AI/ML models, however, can predict failures proactively by recognizing patterns and anomalies in the data before they result in failure.

Threshold-Less Operation. Many traditional methods rely on preset thresholds to indicate failure conditions (e.g., DPU temperature>X degrees). However, failures often occur due to a combination of factors. AI/ML models can learn patterns that precede failure without relying on hardcoded thresholds.

3.6 Performance and Accuracy

Higher Accuracy. AI/ML models, particularly models for deep learning, often outperform traditional models in terms of prediction accuracy because they can observe complex patterns in the data that simpler models miss.

Learning from Historical Data. AI/ML models could be taught on large historical datasets to learn from past failures & successes, improving their ability to generalize to new situations. The above advantages coupled with availability of smart parameters in DCS itself pushed towards using ANNs for DPU failure prediction.

4 Variables available in DCS which can be considered as input Variables

On the analysis of various parameters already available in DCS, parameters pertaining to DPU temperature, memory and application/process and communication network related parameters found suitable for AI/ML(ANN) model. Further shortlisting done based on similarity to the variables used for training the algorithm.
Some of the parameters that were considered for the model are:

Physical Memory. This represents the total physical memory (RAM) installed in the DPU. It indicates the amount of memory available for running processes and executing control functions within the system. Low available memory may affect the DPU's performance and can cause delays or errors in data processing.
Thread Read. This refers to the operations where a thread is reading data from memory, sensors, or other system inputs. Monitoring the performance of thread read operations is essential to ensure that data is being processed in real time without unnecessary delays.
Thread Error. A network storm can lead to processing delays, packet loss, or miscommunication between nodes in the control system. This can result in Thread Errors due to timeouts, lost data packets, or errors in data transmission between DPUs, affecting the threads responsible for handling network communications.
Thread Execution. Thread Execution primarily measures the efficiency of how threads are performing their tasks; frequent execution failures or slowdowns might be caused by network errors that delay communication between DPUs. Threads responsible for reading or writing data over the network could be impacted by these issues.
Thread Idle. Thread Idle refers to the percentage of time that a thread is not doing any work and is in an idle state. High idle time might indicate that resources are being underutilized, whereas low idle time could suggest that the system is handling a large load or is near capacity.

5 Methodology for developing the model

5.1 Selection of Input Parameters

To effectively predict DPU failures, we considered key input parameters based on their relevance to DPU performance and reliability. Out of these 5 (mentioned above), 4 have been chosen as the final input variables which fit over trained model and are similar to

the variables used for training the algorithm. These variables have been identified as primary factors that influence DPU health. The table shows similarity.

Each of these variables plays a critical character in determining the health of the DPU. By monitoring them, we can effectively predict when a failure is likely to occur.

'Thread Idle' was **not included** as an input parameter due to reasons considered below.

Lack of Direct Correlation with DPU Failures.

a) Thread Idle represents the percentage of time a thread is not actively executing tasks.
b) A high idle percentage does not necessarily indicate an impending failure—it may just mean the system is not heavily loaded.
c) Unlike parameters such as Thread Execution or Thread Errors, idle time does not directly influence failure events.

Low Predictive Value in Failure Detection.

a) The ANN model requires input variables that show clear trends leading to failures.
b) Thread Errors, Memory Usage, and Network Load have direct effects on DPU failures, whereas 'Thread Idle' may not consistently contribute to failure patterns.

Table-1. Input

Memory GB		DPU Memory
Network_log10_mbps	(network	Thread execution.
error)		
Local_IO_log10_mbps		Thread read.
NFS_IO_log_mbps	(network	Thread error
storm)		

Table-2. Output

Failed Target	Same as ours-DPU

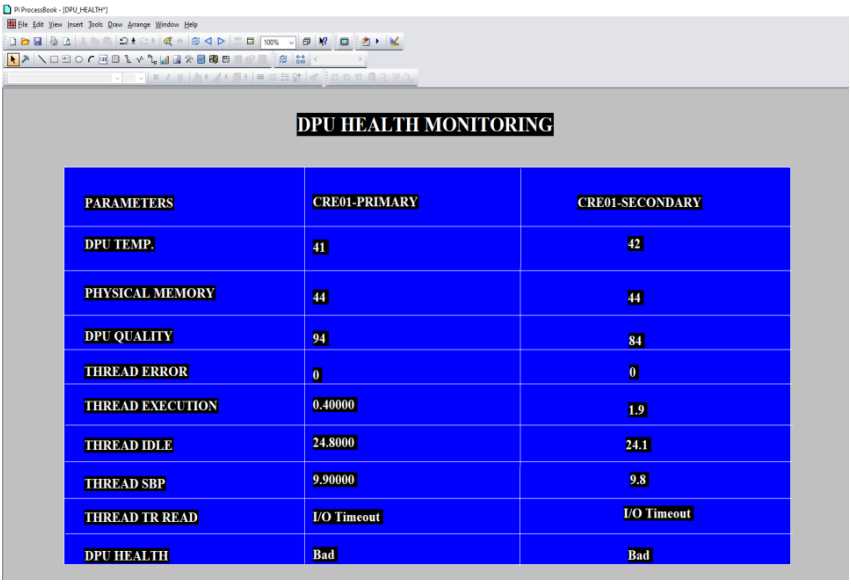

Fig. 4. Screenshot of parameters being fetched through PI

Possibility of False Alarms.

a) If 'Thread Idle' were included, the model might incorrectly classify normal low-load conditions as potential failures.
b) This could increase false positive rates, leading to unnecessary maintenance actions.

Redundancy with Other Selected Parameters: The impact of idle time is indirectly captured by parameters such as.

a) Thread Execution (which measures active processing time)
b) Memory Utilization (high memory usage indicates intensive processing, reducing idle time)

Since these parameters already provide failure-related insights, including 'Thread Idle' would not add significant new information**.** The input data can be fetched in safe and secure manner through PI server from anywhere through LAN.

5.2 Dataset Overview

The dataset utilized in this study is sourced from Kaggle (open access) [3], and it has been curated as part of two prominent research projects funded by the National Science Foundation (NSF), USA**:**

1. Computer System Failure Data Repository to Enable Data-Driven Dependability Research *(Project No. CNS-1513197 – Completed)*
2. Open Computer System Usage Repository and Analytics Engine *(Project No. CNS-2016704 – Ongoing)*

These projects are specifically designed to promote research in fault tolerance, failure prediction, and reliability modelling in large-scale computing systems—domains that closely align with the operational challenges faced in DPU-based industrial control systems. The Kaggle dataset comprises approximately 20,000 records of system operational parameters, including:

a) CPU load and memory usage
b) I/O throughput (read/write)
c) Network packet transfer rates
d) Process-level execution logs

In addition, the dataset includes over 1,600 labelled failure events**,** which makes it suitable for supervised learning models such as Artificial Neural Networks (ANN).

Relevance to MAX DNA DCS Environment. Although the dataset originates from general-purpose computing systems, its structure and variables exhibit strong parallels with the operational data available in MAX DNA Distributed Control Systems (DCS) used at NTPC:

a) Metrics such as CPU load**,** memory usage**,** and I/O network performance directly map to DPU diagnostics.
b) System logs detailing task execution and thread-level delays are analogous to thread errors**,** execution times, and network storm indicators used in DPU health monitoring.

Given that DPUs essentially operate on embedded or industrial-grade computing architecture, the failure patterns and bottlenecks recorded in the Kaggle dataset serve as a valid approximation for modelling predictive failure behaviour in NTPC's DCS setup.

Moreover, the dataset allows for robust pre-training of the ANN model before fine-tuning it with plant-specific live data acquired through NTPC's PI server. This approach significantly enhances model stability and predictive generalizability, especially when actual failure samples from plant DPUs are sparse or imbalanced.

5.3 Dataset Characteristics.

The dataset used for training the ANN model is sourced from Kaggle (Repository), National Science Foundation, U.S.A (NSF).This dataset includes structured failure records and system performance metrics, making it a suitable choice for pre-training the model. The dataset has already undergone some level of pre-processing.

Failure Labels: Each record is labelled as either "Normal" or "Failure," indicating the application's operational state at the time of data collection.

Parameters include system memory usage, network error, network storm, IO load, which influence system reliability. Corresponding equivalent parameters available in DCS were mapped (Table-1).

5.4 Pre-processing

Additional steps were taken to ensure compatibility with the ANN model:
Handling Missing Values. A check for missing sensor readings was performed. If any were found, mean imputation was applied to maintain data consistency.
Feature Scaling. Standard Scaler was applied to normalize input features, ensuring consistent input ranges, which improves the convergence of the ANN model.
These steps ensure that the Kaggle dataset is formatted correctly for training while acknowledging that it is not raw data collected
Outlier Detection and Removal. Outliers were identified using the Interquartile Range (IQR) method and removed to avoid skewed predictions.

Feature Scaling. All features were normalized using *Standard Scaler* [4] to ensure consistent input ranges, improving the convergence of the ANN model.

5.5 Dataset Splitting

Divide the dataset into two sets:

Training Set. 80% of the data used to train the model.
Validation Set. 20% of the data used to evaluate the model's performance after training.

5.6 Model Design

Choose a feedforward ANN architecture with two hidden layers. The first hidden layer could have a larger number of neurons, while the second hidden layer can have fewer neurons, depending on the complexity of the data.

5.7 Activation Functions selection Use the ReLU [5] (Rectified Linear Unit) activation function for the neurons in the hidden layers to allow for better learning of complex patterns.for the output layer, use the Sigmoid activation function [6] which is apt for binary task (e.g., predicting failure/no failure)

Justification for Activation Function Selection.

ReLU (Rectified Linear Unit) for Hidden Layers

In high dimensional data there is non-linear relationship in between input variables. To allow the model to learn complex patterns in high dimensional data ReLU has been used. A neural network with only linear activation function is equivalent to simple linear regression model and cannot learn complex relationship between input variables irrespective of number of layers incorporated in architecture of ANN.

Non-linearity enables an ANN model to approximate complex patterns, making it useful for Tasks like image recognition, speech processing or failure prediction.
The Rectified Linear Unit (ReLU**)** activation function is defined as:

$f(x) = \max(0, x)$

This means: If $x > 0$, ReLU returns x (linear region)

If $x \leq 0$, ReLU outputs 0 (introducing non-linearity)

This feature of ReLU activation function allows the network to learn complex representation.

In Industrial automation, DPU failures are caused by multiple interacting factors (Network overload, high memory usage etc). These interactive inputs cannot be modelled using simple linear function. ReLU enables ANN to learn these dependencies.

Vanishing Gradient Problem: If the activation function presses values into very small ranges (like sigmoid or tan h), the gradients of earlier layers become very small (close to zero). As the network gets deeper, these gradients shrink exponentially, making weight updates negligible, causing slow or stalled learning. This is called the vanishing gradient problem, and it prevents deep networks from learning effectively. "Glorot et al. (2011) demonstrated that using ReLU significantly mitigates the vanishing gradient problem, allowing deep networks to train efficiently compared to sigmoid and tanh activations."

Performance gains. "Empirical studies have shown that ReLU enables deep networks to converge up to 6 times faster than those using sigmoid activation (He et al., 2015)."

Sigmoid for Output Layer. Since the problem is binary classification (failure vs. no failure), the sigmoid function is a natural choice as it outputs values between 0 and 1, representing probabilities. Sigmoid enables the use of binary cross-entropy as the loss function, which is optimal for classification problems.

5.8 Compiling the Model

Define the loss function- binary cross entropy [7] for binary classification, optimizer – Adam [8] and evaluation metrics (e.g., accuracy, precision, recall).

5.9 Training the Model

ANN model is trained using the training dataset. Its performance monitored on the training set and techniques like cross-validation [3] used to ensure robust performance. Its advantage is it reduces overfitting risk and gives a better estimate of model performance

5.10 Model Evaluation

Evaluation of the model on the test dataset done to assess its performance using relevant metrics (e.g., accuracy, F1 score, ROC-AUC). Analysis of confusion matrices done to understand the quality of predictions.

5.11 Model Tuning

Model was further fine-tuned by adjusting hyper-parameters [3] (e.g., learning rate, batch size, number of epochs) and experimenting with different configurations for the hidden layers.

5.12 Deployment

Once the model achieves satisfactory performance, it is deployed for real-time monitoring and prediction of DPU failures.

5.13 Audio Alarm System for Real-Time Failure Alerts

As part of the deployment strategy for the ANN-based predictive maintenance model, an audio alarm system is implemented to immediately notify operators upon prediction of an imminent DPU failure. This component serves as a proactive alert mechanism, designed to ensure timely human intervention before the failure propagates or causes system-wide disruption.

Mechanism of Operation.

Trigger Condition. The audio alarm is triggered when the ANN model predicts a failure probability exceeding a predefined threshold (e.g., ≥ 0.7). This ensures that only high-confidence predictions lead to alerts, reducing false positives.

Integration with Intranet Systems. A lightweight monitoring script continuously evaluates the model's output in real time. When a failure is predicted, the script communicates with NTPC's intranet system to

a) Log the event with timestamp and DPU ID
b) Send an **audio-visual alert** to the designated operator terminals.

Alarm Characteristics.

a) **Sound File**: A standard .wav file with a distinctive tone (e.g., escalating beep or synthesized alarm) is played.
b) **Duration**: The audio alert continues for 15 seconds or until acknowledged manually.
c) **Repeat**: If the fault is not acknowledged or the predicted condition persists, the alarm re-triggers every 2 minutes.

User Interface. A pop-up window accompanies the alarm, displaying:

a) DPU Identifier (e.g., Unit-DPU-03)
b) Type of fault predicted (e.g., Memory Overload)
c) Failure probability (e.g., 0.86)
d) Timestamp

Benefits.

a) Enhances operator awareness and response time.
b) Provides a second line of defence after automated prediction.
c) Enables rapid diagnostics and preventive maintenance actions.
d) Reduces the risk of escalation due to unattended anomalies.

6 Coding Part

6.1 Importing libraries

Pandas: Used to load and manipulate CSV data.
Train_test_split. A function from sklearn [4] to split the dataset into training and validation sets.
Standard Scaler. A pre-processing tool that standardizes features by removing the mean and scaling to unit variance.

Sequential. A linear stack of layers from Keras[8] for building neural network models.
Dense: Fully connected neural network layer used to construct the architecture of the ANN.

6.2 Loading the dataset

pd.read_csv: Reads the **train_data.csv** file into a Data Frame. This is where we load the training data that contains features and the target variable (failed).

6.3 Preparing Features (X) and Target (Y)

X. The independent variables or features used for training the model. We drop job id (an identifier not relevant for prediction) and the failed column (since it's our target).

Y. The target variable we want to predict, which is the failed column (either 0 or 1).

6.4 Splitting Data into Training and Validation Sets

Train_test_split. This function splits the dataset into training (80%) and validation (20%) sets. The random_state ensures reproducibility, meaning you'll get the same split every time.
X_train, Y_train. The training data (features and target) used to train the model.
X val, Y_val: The validation data used to check how well the model performs on unseen data.

6.5 Feature Scaling

Standard Scaler. This normalizes the features for having a mean of 0 & a SD of 1(Standard Deviation). Neural networks perform better when the input data is scaled this way.
Fit transform. Calculates the scaling factors (mean & std. deviation) from the training data and applies the transformation [4].
Transform. Applies the same scaling to the validation data (without recalculating the mean/variance).

6.6 Building the ANN Model

Sequential. A model where layers are stacked sequentially.
Input_dim. The number of input features (i.e., the number of columns in X_trains), 4 in our case
Dense(64, activation='relu'). A fully connected layer with 64 neurons and ReLU (Rectified Linear Unit) activation.
Dense(32). second hidden layers with 32 neurons, respectively, using ReLU activation.
Dense (1, activation='sigmoid'). The output layer with 1 neuron and sigmoid activation (since we're doing binary classification, 0 or 1)

6.7 Compiling the Model

optimizer='adam'. The optimizer that adjusts the weights during training.
loss='binary_crossentropy': The loss function used for binary classification tasks. It measures how far off the model's predictions are from the actual target values.[3]

metrics=['accuracy']. Tracks accuracy as a metric during training to monitor model performance.

6.8 Training the Model

model.fit. The main function to train the model using the training data.
X_train_scaled and **y_train**: The scaled training data.
validation_data:The validation data (used to monitor model performance on unseen data).
epochs=20. The number of complete passes through the training data. Higher epochs mean the model gets more chances to learn but may also overfit if too high. Epochs restricted to 20 to avoid overfitting and as convergence was observed.
batch_size=32. The number of samples to process before updating the model's internal weights. Smaller batches lead to faster updates, but a higher batch size makes training smoother. [9]

6.9 Python Code for Real-Time Audio Alarm System

import section. Brings in Python libraries needed: pandas for data, time for delays, winsound to play audio, and date, time for timestamps.
Threshold. The alarm is triggered if the predicted failure probability is ≥ **0.7** (configurable).
Alarm sound settings: Beep sound plays at 1000 Hz for 15 seconds using winsound.Beep.
monitor_dpu_failures function. Continuously monitors the predictions from a CSV file. This simulates real-time output of the ANN model.
CSV structure. The prediction CSV must have: DPU_ID, Predicted Fault, Failure Probability. This simulates the model's real-time output.
Alarm logic. If a row has a failure probability above the threshold, it plays a sound, prints details to screen, and logs it to alarm_log.txt.

Polling interval. The system checks the prediction file every 5 minutes (300 seconds)**.** One can change check interval.
Error handling. If something goes wrong (e.g., file not found), the code waits and tries again.

7 ANN Model Architecture- explained

The ANN model used for predicting DPU failures consists of a feedforward neural network [3] with three layers: an input layer, two hidden layers, and an output layer.
Input Layer. The input layer consists of 04 neurons, each corresponding to one of the selected input variables.
First Hidden Layer. The first hidden layer contains 64 neurons and uses the Rectified Linear Unit (ReLU) activation function. ReLU helps introduce non-linearity into the model, which is crucial for modelling complex relationships between input variables.
Second Hidden Layer. The second hidden layer contains 32 neurons and also uses the ReLU activation function.
Reason for Selecting this model Architecture. A single-layer perceptron can only model linear relationships, while at least one hidden layer is required to capture non-linear dependencies in data. Two hidden layers strike a balance between complexity and generalization, avoiding under-fitting while not making the model excessively complex (which could lead to overfitting).
Empirical studies suggest that two hidden layers are often sufficient for most structured datasets in industrial applications. Reference. Hornik, K., Stinchcombe, M., & White, H. (1989). Multilayer feedforward networks are universal approximators. *Neural Networks, 2(5), 359-366.*

Why 64 and 32 Neurons in Hidden Layers? The number of neurons was chosen based on experiments with different configurations, ensuring a balance between learning capacity and computational efficiency. The first hidden layer has 64 neurons to capture broader feature interactions, while the second layer with 32 neurons refines the learned representations. The choice was validated using hyper-parameter tuning techniques called cross-validation. [10]

Output Layer. The o/p layer comprises of a single neuron with a sigmoid activation function. The output provides a probability score, indicating the likelihood of DPU failure.

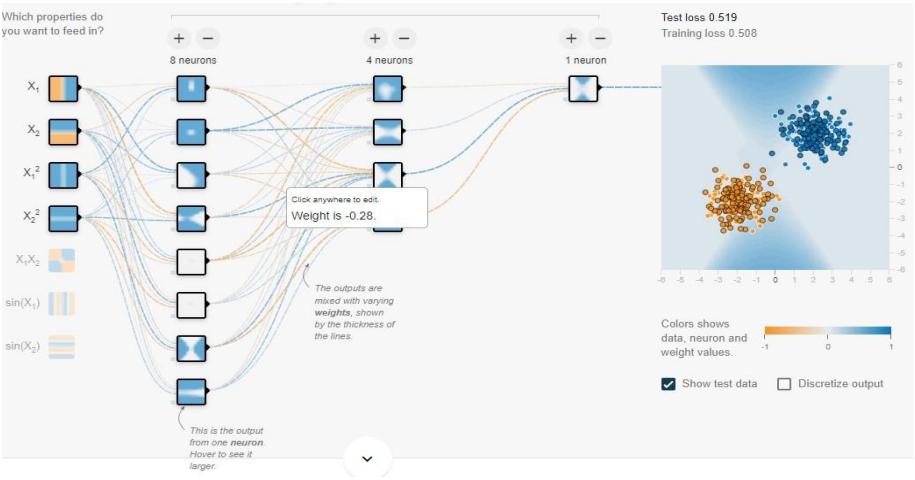

Fig. 5. Depictive Image for ANN model Architecture

7.1 Model Compilation

The ANN model was compiled using the Adam optimizer, which adjusts the learning rate during training to accelerate convergence. The function used for loss is **binary cross entropy**, which is suitable for binary classification tasks like failure prediction.

7.2 Working Mechanism

Forward Propagation. Data flows path is input layer → hidden layers → O/p layer, in O/p layer predictions are made. Each neuron applies an activation function [11] (e.g., ReLU, Sigmoid) to its input to decide whether to "fire" or pass the signal.
Loss Function. The network compares its predictions with the actual outcomes using a loss function (e.g., mean squared error for regression tasks, cross-entropy for classification tasks).
Backpropagation. This is the process by which the network adjusts the weights and biases based on the error. It calculates gradients of the loss function and updates the parameters using an algorithm for optimization like gradient descent.

7.3 Model Training and Validation

The dataset was split into two parts: 80% of the data was used for training the ANN model, while the remaining 20% was used for validation. The process for training involved feeding data in the form of mini batches into network and updating the model weights through backpropagation.

7.4 Training Setup

- **Batch Size**: 32
- **Epochs**: 20 (after cross-validation tests)
- **Learning Rate**: 0.001
- **Validation Split**: 0.2 (20% validation data)

The training process aimed for lessening the loss function by fine-tuning the model weights. Early ending was employed to prevent overfitting, monitoring the validation loss to terminate training if no improvement was observed.

8. Results

The ANN model achieved a high level of accuracy on the validation set, indicating its effectiveness in predicting DPU failures. The model demonstrated strong performance across various evaluation metrics, including accuracy, precision, recall, and F1-score. A confusion matrix is a table used to evaluate the performance of a classification algorithm [12]. It provides a detailed breakdown of the model's prediction results by comparing the predicted and actual classifications. The matrix typically consists of four key metrics, arranged in a 2x2 table for binary classification problems (Confusion Matrix Layout for Binary Classification [12])

True Negatives (TN). Model correctly predicted no failure.
False Positives (FP). Model incorrectly predicted a failure.
False Negatives (FN). Model incorrectly predicted no failure.
True Positives (TP). Model correctly predicted a failure.

Key Metrics Derived from the Confusion Matrix.
Accuracy. Proportion of correct predictions (TP + TN) out of total predictions.
Accuracy = (TP+TN) / (TP+TN+FP+FN)
Precision. Proportion of true positive predictions out of all positive predictions made by the model.
Precision = TP / (TP+FP)
Recall (Sensitivity or True Positive Rate). Proportion of actual positives that were correctly predicted.
Recall = TP / (TP + FN)
F1 score. Proportion of actual positives that were correctly predicted.
F1 = 2* (Precision*Recall) / (Precision + recall)

Performance Metrics (Achieved)
Accuracy. The overall accuracy of the model in predicting failures was 92.8%.
Precision. The model had a precision of 0.91, meaning that 91% of the time, when the model predicted a failure, the DPU actually failed.
Recall. The recall score was 0.89, indicating that 89% of actual failures were successfully predicted by the model.
F1-Score. The F1-score, which balances precision and recall, was 0.90, demonstrating the model's ability to handle imbalanced data effectively. ROC Curve (Receiver Operating Characteristic Curve)
Definition. The ROC curve is a graphical representation of a binary classifier's performance across different threshold settings. It plots the True Positive Rate (TPR) against the False Positive Rate (FPR).

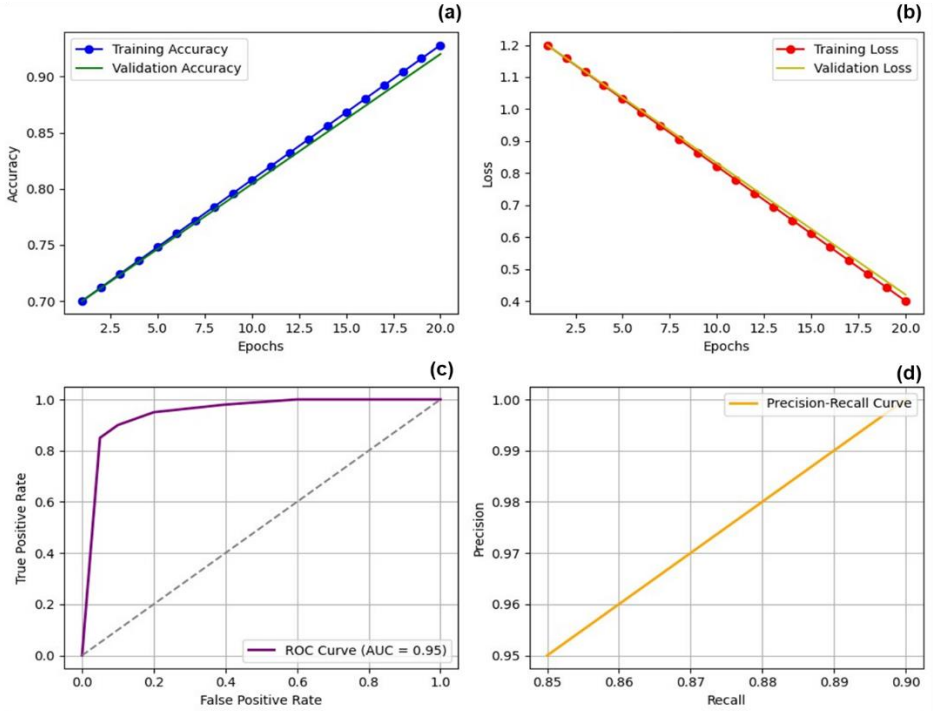

Fig 6. Plots showing **(a)** Training *vs* Validation Accuracy **(b)** Training *vs* Validation loss **(c)** ROC Curve **(d)** Precision Recall Curve.

Table 3. Confusion Matrix Layout for Binary Classification

	Predicted Positive	Predicted Negative
Actual Positive	True Positive (TP)	False Negative(FN)
Actual Negative	False Positive(FP)	True Negative(TN)

Axes.
X-axis. False Positive Rate (FPR) = FP / (FP + TN)
Y-axis. True Positive Rate (TPR) = TP / (TP + FN)

Precision-Recall Curve
Definition. The Precision-Recall curve is another way to evaluate the performance of a binary classifier, particularly in cases of imbalanced classes. It plots Precision against Recall (True Positive Rate).
Axes.
X-axis. Recall (also known as Sensitivity or TPR) = TP / (TP + FN)
Y-axis. Precision = TP / (TP + FP)

9. Discussion

The results demonstrate that the ANN model can effectively predict DPU failures by analysing operational parameters such DPU load, memory use, network error, and I/O error rates. This predictive proficiency allows for pre-emptive maintenance planning, reducing the likelihood of unplanned downtime. SHAP, or Shapley Additive explanations, which is a method for interpreting Artificial Neural Networks (ANNs) explains individual predictions by assigning each feature (or input variable) a "Shapley value," indicating its contribution to a specific prediction. Using SHAP in our algorithm we can uncover the exact reason as to why the ANN model predicts a DPU failure, which is valuable for proactive maintenance in DCS and PLC systems.

Key insights from the model include.
CPU and RAM (memory) Utilization. High CPU load and RAM utilization were major contributors to failure. This underscores the need for monitoring resource usage and Implementing periodic CPU and memory optimizations or load-balancing strategies might reduce strain on DPUs, potentially extending their operational lifespan.
I/O Error Rates: Signal errors were a less common, but highly indicative, factor in predicting DPU failures, suggesting that communication channels should be closely monitored for noise and signal degradation.

10. Conclusion

The implementation of Artificial Neural Networks for predicting DPU failures in DCS or PLC has demonstrated significant potential for improving the reliability of industrial control systems. By selecting input parameters such as DPU utilization, memory usage, I/O latency, operating and historical failure records, we are able to construct a model that can accurately predict impending DPU failures.
The ANN model trained on the Kaggle dataset produced consistent results in terms of predictive accuracy, showing that it can serve as a robust tool for early fault detection in real-world DCS or PLC environments. This proactive approach to predictive maintenance can minimize unexpected downtime, prevent potential operational hazards, and reduce the overall maintenance costs in critical industrial systems.
The key advantage of using ANN is its ability to learn complex non-linear relationships between the input parameters and DPU failures, which may not be as easily captured by traditional rule-based systems. In particular, the use of multiple hidden layers enhances

the model's ability to generalize over diverse failure scenarios. By continuously updating the model with new data, the ANN can evolve to adapt to changes in operational conditions, making it a versatile solution for dynamic industrial environments.

Future Scope. A potential enhancement to this model involves leveraging Recurrent Neural Networks (RNN) with Long Short-Term Memory (LSTM) units, which are designed to handle time-series data. Since DPU data often exhibits time-dependent trends—such as gradual temperature rises or periodic network loads—LSTM networks can effectively learn from these sequences, recognizing patterns that unfold over time. This improvement would allow the model to detect subtle, progressive changes leading to failures, further increasing its predictive accuracy and providing earlier warnings. Further with similar approach, different machine learning models can be developed to protect our digital assets, like Predictive maintenance of steam turbine- where the input variables will change and appropriate dataset is to be used.

References

1. Wang, S., Zhou, Y.: Machine Learning Approaches for Predictive Maintenance. IEEE Transactions on Industrial Informatics 16(5), 2020. and Rojas, M. D., Feldman, K.: Predictive Maintenance Strategies in Industrial Systems. Journal of Maintenance Engineering 25(3), 2019.
2. Kaggle Dataset: Available at: https://www.kaggle.com/datasets. & Lundberg, S. M., Lee, S. I.: A Unified Approach to Interpreting Model Predictions. In: Advances in Neural Information Processing Systems, pp. 1–12 (2017). Molnar, C.: Interpretable Machine Learning. https://christophm.github.io/interpretable-ml-book
3. Goodfellow, I., Bengio, Y., Courville, A.: Deep Learning, 2nd edn. MIT Press (2016). Chollet, F.: Deep Learning with Python, 1st edn. Manning Publications (2017).
4. Pedregosa, F., et al**.** Scikit-learn: Machine Learning in Python, J. Mach. Learn. Res., **12**, 2825–2830 (2011).
5. Original ReLU introduction**:** Nair, V., & Hinton, G. E. (2010). Rectified linear units improve restricted Boltzmann machines. Proceedings of the 27th International Conference on Machine Learning, 807–814.
6. Rumelhart et al. (1986)- Backpropagation with sigmoid activation Rumelhart, D. E., Hinton, G. E., & Williams, R. J. (1986). Learning representations by back-propagating errors. *Nature*, **323**(6088), 533–536. https://doi.org/10.1038/323533a0
7. Binary Cross-Entropy (BCE) **in** machine learning : Goodfellow, I., Bengio, Y., & Courville, ***A.*** *(2016).* Deep Learning. *MIT Press.*
8. Chollet, F. (2015). Keras: Deep learning library for Python. *GitHub repository*. Retrieved from https://github.com/keras-team/keras.
9. Keskar, N. S., Mudigere, D., Nocedal, J., Smelyanskiy, M., & Tang, P. T. P. (2017). On large-batch training for deep learning: Generalization gap and sharp minima. *arXiv preprint arXiv:1609.04836*.
10. He, K., Zhang, X., Ren, S., & Sun, J. (2015). Delving deep into rectifiers: Surpassing human-level performance on ImageNet classification. IEEE International Conference on Computer Vision (ICCV).

11. Hochreiter, S., Schmidhuber, J.: Long Short-Term Memory. Neural Computation 9(8), 1735–1780 (1997).
12. Fawcett, T. (2006). An introduction to ROC analysis. Pattern Recognition Letters*, 27(8*), 861-874.

From Waste to Resource: Elemental Characterization of Fly Ash Using EDXRF

Sunit Kumar Singh*, G. D. Vani, Pranay Sharma, Anil Kumar Das

EDXRF Lab, NTPC Energy Technology Research Alliance, NTPC Ltd., Greater Noida, India
sksingh27@ntpc.co.in

Abstract. Energy Dispersive X-ray Fluorescence Spectroscopy (EDXRF) is a powerful, non-destructive analytical technique employed to determine the elemental composition of various materials. It operates by bombarding a sample with high-energy X-rays, which causes the emission of secondary (fluorescent) X-rays unique to each element. These emitted X-rays generate an energy spectrum that serves as a distinct fingerprint, enabling the qualitative identification of elements present in the sample. Furthermore, the intensity of these characteristic X-rays is directly proportional to the elemental concentration, allowing for accurate quantitative analysis. This technique is particularly valuable in analyzing coal fly ash, where the elemental composition plays a crucial role in defining its properties, environmental behavior, and possible industrial applications. Fly ash composition affects the strength and durability of concrete when used as a partial substitute in Portland cement. In addition, elemental analysis can reveal the presence of economically significant components such as rare earth elements, opening opportunities for resource recovery and sustainable waste utilization. A detailed understanding of the elemental makeup also supports the development of innovative uses, including wastewater adsorbents and materials for carbon capture and storage.

Keywords: Energy Dispersive X-ray Fluorescence Spectroscopy (EDXRF), X-rays, elemental composition, Fly ash, Waste management.

1 Introduction

1.1 Energy Dispersive X-ray Fluorescence Spectroscopy (EDXRF)

Electromagnetic radiant energy propagates through space as waves that span a wide range of frequencies and wavelengths, collectively forming the electromagnetic spectrum (Figure 1A). Radiant energy waves with wavelengths ranging from 0.01 to 10 nm and frequencies between 3×10^{16} Hz and 3×10^{19} Hz are classified as X-rays [1].

X-ray fluorescence (XRF) spectroscopy is a non-destructive analytical technique widely used for determination of the elemental composition of materials. In this technique, the sample is irradiated with high-energy X-rays, which excite its constituent

S. Shaswattam et al. (eds.), *NTPC Transactions on Energy Research (NTER 2025)*,
https://doi.org/10.2991/978-94-6463-849-3_15

atoms and cause them to emit secondary (fluorescent) X-rays. These emitted X-rays have characteristic energies specific to the elements in the sample, enabling their identification and analysis (Figures 1A and 1B) [2]. The spectrometer separates the beam components with different energies. It measures the energy intensities inside narrow energy arrays. In EDXRF, the dispersion of beam components is performed directly within the detector. The associated electronics also play a key role in this process. This setup generates an energy-dependent signal for each absorbed X-ray photon.

Energy-dispersive detectors are typically based on semiconductor technology. The energy of each detected X-ray corresponds to the identity of the emitting element, while the intensity (i.e., the number of detected X-rays) is directly proportional to the concentration of that element. The processed signals are displayed as an energy spectrum, where X-ray counts are plotted against X-ray energy, typically measured in kiloelectron volts (keV). Each peak in the spectrum corresponds to a specific element in the sample, and the intensity of the peak indicates its relative abundance [3], [4].

1.2 Coal Fly Ash (CFA)

In power plants, CFA is a by-product of coal combustion. During the combustion process, the coal burns to produce energy. The mineral impurities in coal, such as clay, quartz, feldspar, and other silicate minerals, do not combust. These impurities are left behind as ash. This ash is then collected as CFA. The fine particles that rise with flue gases are called fly ash, which is typically collected using electrostatic precipitators or other filtration systems. The composition of CFA raises environmental concerns due to the presence of heavy metals and trace elements. These can pose risks if not properly managed, such as groundwater contamination or air pollution through dust [5], [6].

The composition of CFA varies based on the type of coal used, combustion conditions, and other influencing factors. Among the primary components of fly ash is silica and alumina. Silica (SiO_2) constitutes 20-60%, alumina (Al_2O_3) constitutes 15-30%, Iron oxide (Fe_2O_3) constitutes 5-15%, Calcium oxide (CaO) constitutes 1-30%, Magnesium oxide (MgO) constitutes 1-5%, Titanium dioxide (TiO_2) typically varies from 1% to 2%, and Sodium oxide (Na_2O) and Potassium oxide (K_2O) are typically in the range of 0.5% to 5%.

In addition to these major oxides, CFA can contain trace amounts of elements which include heavy metals such as arsenic (As), mercury (Hg), lead (Pb), chromium (Cr), and cadmium (Cd). Other than heavy metals, Rare earth elements (REEs) elements like cerium (Ce), neodymium (Nd), and yttrium (Y) are found in small quantities [5].

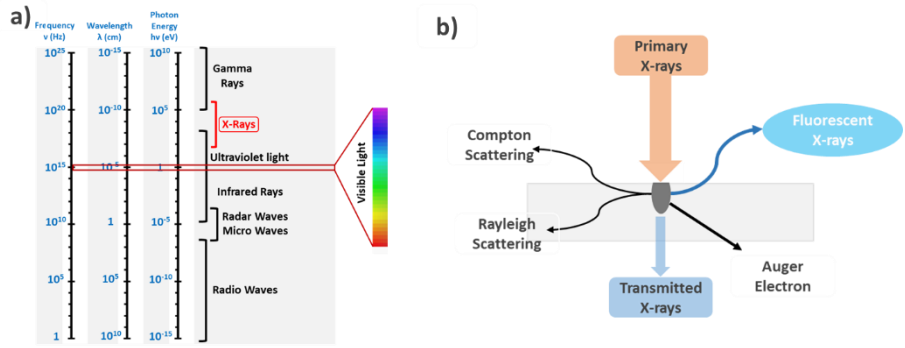

Fig. 1. a) Electromagnetic spectrum of light, b) X-rays interacting with a substance.

2 XRF Equipment in NETRA, NTPC Ltd.

The Xenemetrix EDXRF EX-6600, employed at NETRA, NTPC Ltd., is an EDXRF spectrometer specifically designed for elemental analysis of a wide range of materials (Figure 2) [7]. This X-ray fluorescence (XRF) system offers versatility in detecting elements from sodium (Na) to uranium (U), covering a broad concentration range—from trace levels in parts per million (ppm) up to 100%. It is equipped with a high-power X-ray tube, operating at up to 50 kV and 50 W, which generates the primary X-rays necessary for exciting atoms in a sample. Certain configurations feature a silver (Ag) anode for enhanced performance. The system employs Silicon Drift Detectors (SDD), known for their exceptional resolution, rapid data acquisition, and high count rate capability, enabling precise measurements even within complex sample matrices. Advanced calibration software supports both semi-quantitative and fully quantitative analysis, incorporating intuitive user interfaces and sophisticated correction algorithms to address challenges such as matrix effects and inter-element interferences. Additionally, the system enables multi-channel analysis, allowing the simultaneous detection and measurement of multiple elements, making it highly efficient for comprehensive elemental profiling.

Calibration and quantitative analysis are reinforced by the use of certified Standard Reference Materials (SRMs) supplied by the National Institute of Standards and Technology (NIST), including SRM 2691, SRM 2690, SRM 2689, and SRM 1633b. These SRMs, rigorously tested and accompanied by Certificates of Analysis detailing certified values, measurement methods, and traceability to the International System of Units (SI), ensure accuracy, precision, and traceability in scientific and industrial applications. Comparative analyses of elemental oxide concentrations in these SRMs against values obtained using the XRF system confirm strong alignment with NIST standards, underscoring the reliability and performance of the instrument. Table 1 shows wt% concentration of elements in their oxide forms as specified in certificate of analysis provides by NIST versus the concentration evaluated in NETRA for same SRM samples. The results are in congruence with the NIST standard values.

Table 1. Elemental Quantification Data (in wt% Concentration) comparing NIST SRM values with data generated in Laboratory for same standards using Xenematrix EDXRF.

Elements (in Oxide form)	SRM							
	2691		2690		2689		1633c	
	NIST (wt%)	NETRA (wt%)	NIST (wt%)	NETRA (wt%)	NIST (wt%)	NETRA (wt%)	NIST (wt%)	NETRA (wt%)
Na_2O	1.46 ± 0.06	1.37 ± 0.21	0.32 ± 0.02	0.34 ± 0.15	0.33 ± 0.01	0.38 ± 0.14	0.23 ± 0.01	0.23 ± 0.13
MgO	5.17 ± 0.13	4.23 ± 0.11	2.53 ± 0.08	2.28 ± 0.06	1.01 ± 0.08	0.93 ± 0.04	0.82 ± 0.08	0.90 ± 0.04
Al_2O_3	18.531 ± 0.73	18.15 ± 0.09	23.32 ± 0.52	23.11 ± 0.10	24.44 ± 0.39	24.17 ± 0.11	25.08 ± 1.15	25.93 ± 0.11
SiO_2	35.99 ± 0.25	36.06 ± 0.11	55.29 ± 0.36	56.29 ± 0.14	51.46 ± 0.17	50.86 ± 0.14	45.56 ± 1.12	49.07 ± 0.14
P_2O_5	1.16 ± 0.04	1.05 ± 0.02	1.19 ± 0.02	0.89 ± 0.02	0.22 ± 0.02	0.15 ± 0.01	0.43 ± 0.02	0.29 ± 0.01
SO_3	2.07 ± 0.12	2.14 ± 0.02	0.37 ±0.02	0.38 ± 0.00	Not Given	0.82 ± 0.01	0.27 ± 0.04	0.55 ± 0.01
K_2O	0.40 ± 0.01	0.43 ± 0.01	1.25 ± 0.04	1.23 ± 0.01	2.65 ± 0.04	2.87 ± 0.01	2.13 ± 0.07	2.09 ± 0.01
CaO	25.81 ± 0.44	27.18 ± 0.09	7.98 ± 0.18	8.119 ± 0.03	3.04 ± 0.08	3.16 ± 0.01	1.90 ± 0.05	1.87 ± 0.01
TiO_2	1.50 ± 0.03	1.52 ± 0.01	0.86 ± 0.01	0.91 ± 0.01	1.25 ± 0.16	1.31 ± 0.01	1.21 ± 0.05	1.24 ± 0.01
MnO	0.02 ± 0.01	0.07 ± 0.01	0.03 ± 0.01	0.04 ± 0.002	0.03 ± 0.01	0.03 ± 0.002	0.03 ± 0.004	0.03 ± 0.002
Fe_2O_3	6.32 ± 0.04	6.47 ± 0.02	5.10 ± 0.08	5.58 ± 0.02	13.32 ± 0.08	14.34 ± 0.05	15.00 ± 0.55	16.91 ± 0.06

Table 2. PT test results.

S. No.	PT Parameters	Observation 1	Observation 2	Avg. (X)	Total participants	Assigned Value ($X_{assigned}$)	σ (Standard Deviation)	Z score
1	Al_2O_3,%	28.73	28.78	28.76	13	28.39	1.47	0.24
2	CaO,%	1.52	1.54	1.53	13	1.48	0.20	0.24
3	Fe_2O_3,%	5.10	4.92	5.01	12	4.81	0.265	0.71
4	LoI,%	0.35	0.37	0.36	13	0.32	0.0564	0.67
5	MgO,%	0.84	0.87	0.86	13	0.78	0.0771	0.98
6	SiO_2,%	60.00	60.25	60.13	13	60.81	1.32	-0.49
7	SO_3,%	0.12	0.13	0.13	13	0.17	0.0058	-0.68

Fig. 2. Xenematrix EDXRF Model EX-6600.

Proficiency testing (PT) and Z-scores are crucial for validating analytical results, ensuring accuracy, and maintaining quality control in laboratory testing. A Z-score evaluates a laboratory's performance in a PT by measuring the deviation of its result from the assigned value, calculated as:

$$Z = \frac{X - X_{assigned}}{\sigma}$$

where X is the laboratory's result, $X_{assigned}$ is the assigned or consensus value, and σ is the standard deviation of PT results. In PT, a Z-score determines result acceptability: $|Z| \leq 2.0$ is satisfactory, indicating compliance with acceptable limits; $2.0 < |Z| \leq 3.0$ is questionable, requiring further review; and $|Z| > 3.0$ is unsatisfactory, necessitating immediate corrective action. The PT test on fly ash samples was conducted in collaboration with Global PT Provider Pvt. Ltd., New Delhi, and the results are presented in Table 2.

3 Sample analysis using EDXRF

The samples selected here for discussion are different variety of sample received from NTPC stations regularly for analysis of elemental composition of their ash after combustion. Sample are received in different categories such as coal (before combustion), CFA (from boiler of thermal power plant), Bottom Ash, Clinker, and other alternate boiler fuels. Alternated fuel includes biomass sourced from paddy, wheat straw, rice husk, pine needle and municipal solid waste. EDXRF spectra of these samples are shown in Figure 3. The spectra are collected in the range 0 to 10 keV. The elements (with their characteristics X-Ray wavelength energy) estimated in this range are Na (1.041 keV), Mg(1.254 keV), Fe(6.403 keV), Al(1.487 keV), Si(1.740 keV),

K(3.313 keV), P(2.015 keV), Ca(3.691 keV), Ti(4.510 keV), S(2.308 keV) and Mn(5.898 keV).[8]

Table 3 shows the detailed elemental quantification in oxide form for the above discussed samples. As can be seen from Table 3, Alumina content in the first four samples varied in the range 24-29 wt%, Iron varied in the range 4-8 wt% and Silica varied in the range 59-61.5 wt% which is not much variation. Overall, all other element showed minor variation. Torrified charcoal showed significant difference in quantities of these elements. Silica (11.95 wt%) and alumina (52.82 wt%) is found in lower values than coal with significant increase in alkaline metals Mg (4.98 wt%) and Ca (14.99 wt%). Biomass generally have variations in elemental composition compared to coal. Biomass is characterized by lower levels of alumina and more level of alkaline earth metals (Table 3). Calcium and magnesium are vital for plant growth and cellular functions. Calcium is essential for maintaining cell wall structure and stability, while magnesium serves as a central component of chlorophyll, the molecule responsible for photosynthesis. Plants actively absorb these minerals from the soil as they grow, leading to relatively high concentrations of Ca and Mg in plant tissues, and thus in biomass derived from these plants. As plant material transforms into coal, it undergoes intense heat, pressure, and chemical reactions that change its composition. This process, called coalification, drives off water and volatile organic compounds, and leads to a concentration of carbon while reducing some mineral content. Thus, elements like Ca and Mg can either volatilize, dissolve, or integrate into other mineral structures in coal, resulting in their relatively lower levels compared to raw biomass [9], [10]. The elemental composition of Municipal Solid Waste (MSW) ash varies depending on the type of waste processed, combustion conditions, and local waste management practices. However typically, the composition of MSW ash is closer to biomass than coal as can be observed in Table 3. Mill-rejected coal (Table 3) refers to coal that is considered unsuitable for combustion due to quality concerns. Excessive ash content lowers combustion efficiency and contributes to issues such as slagging, fouling, and increased maintenance. Slagging occurs when molten ash deposits accumulate on boiler surfaces, reducing heat transfer and raising energy consumption. Fouling happens when ash particles adhere to heat exchanger tubes, decreasing efficiency and causing blockages. High levels of SiO_2 and Al_2O_3 make ash highly refractory, meaning it melts at elevated temperatures and forms hard, sticky deposits. Iron oxide interacts with other minerals, such as calcium and sulfur, to create low-melting-point compounds that produce sticky ash, which readily adheres to boiler tubes. Elevated Fe_2O_3 content lowers the ash fusion temperature, further increasing the likelihood of slagging and fouling.

The calcium (Ca) and silicon (Si) content in fly ash play pivotal roles in determining its suitability for various applications. These elements influence the reactivity, strength, and durability of materials in which fly ash is used, particularly in construction and environmental applications. High-Ca fly ash (Class C fly ash) has a high lime content ($CaO \geq 20\%$) that enables it to exhibit self-cementing behavior when mixed with water, forming hydration products like calcium silicate hydrate (C-S-H) and calcium aluminate hydrate (C-A-H) [11]. This property makes it suitable for direct use as a binder in road bases, soil stabilization, and low-strength construction applications. Even, Low-Ca fly ash (Class F fly ash) can contribute to pozzolanic reactions when

mixed with lime or Portland cement, enhancing strength over time. A balanced combination of Si (for pozzolanic activity) and Ca (for early strength) is ideal. High-Ca fly ash accelerates early strength gain, while high-Si fly ash ensures long-term strength and durability. Calcium reacts with silica (SiO_2) and alumina (Al_2O_3) in the presence of water to form additional cementitious products [12, 13]. High-Ca fly ash is effective in neutralizing acidic environments, such as mine tailings or acidic wastewater, due to its alkaline nature. It is also used for immobilizing heavy metals in contaminated soils by forming stable calcium complexes. Even, Al compounds in fly ash adsorb and immobilize contaminants, making it effective in environmental applications [14]. High-Si fly ash is a preferred raw material for geopolymers, where silica reacts with an alkaline activator to form a three-dimensional aluminosilicate network, yielding materials with excellent mechanical and chemical properties [15,16].

Table 3. Elemental Analysis of samples using EDXRF received from NTPC Stations.

Oxides	*Na_2O*	*MgO*	*Al_2O_3*	*SiO_2*	*P_2O_5*	*SO_3*	*K_2O*	*CaO*	*TiO_2*	*MnO*	*Fe_2O_3*
Samples						**Wt%**					
Coal	0.21 ±0.09	0.94 ±0.04	28.25 ±0.11	59.39 ±0.15	0.20 ±0.01	0.44 ±0.01	1.09 ±0.01	1.19 ±0.01	1.94 ±0.02	0.031 ±0.001	5.59 ±0.02
Fly Ash	0.101 ±0.027	0.61 ±0.04	27.57 ±0.11	60.63 ±0.15	0.20 ±0.01	0.21 ±0.004	1.06 ±0.01	1.51 ±0.01	2.03 ±0.02	0.032 ±0.001	4.45 ±0.02
Bottom Ash	0.097 ±0.012	0.51 ±0.04	27.72 ±0.12	60.38 ±0.17	0.17 ±0.01	0.07 ±0.003	0.91 ±0.01	0.59 ±0.01	2.37 ±0.02	0.038 ±0.002	6.13 ±0.03
Clinker	0.118 ±0.012	0.70 ±0.04	24.03 ±0.11	61.19 ±0.16	0.32 ±0.01	0.05 ±0.003	1.32 ±0.01	1.06 ±0.01	1.80 ±0.02	0.037 ±0.001	7.99 ±0.03
Torrified Charcoal	1.694 ±0.687	4.98 ±0.14	11.95 ±0.07	52.82 ±0.13	1.25 ±0.03	0.97 ±0.01	4.02 ±0.03	14.99 ±0.06	0.63 ±0.01	0.039 ±0.002	5.46 ±0.03
Biomass Paddy	4.558 ±0.923	2.56 ±0.07	5.89 ±0.06	67.45 ±0.16	0.73 ±0.02	2.63 ±0.03	8.39 ±0.04	4.89 ±0.02	0.16 ±0.003	0.047 ±0.001	2.02 ±0.01
Biomass Wheat Straw	0.141 ±0.015	3.94 ±0.10	5.69 ±0.06	45.66 ±0.15	7.56 ±0.18	11.26 ±0.11	9.75 ±0.02	10.51 ±0.05	0.30 ±0.01	0.064 ±0.004	4.19 ±0.02
Biomass Rice Husk	0.229 ±0.049	1.05 ±0.03	6.52 ±0.06	80.03 ±0.16	0.82 ±0.02	0.37 ±0.01	2.91 ±0.02	2.89 ±0.02	0.31 ±0.004	0.039 ±0.001	4.46 ±0.02
Biomass Pine Needle	0.239 ±0.058	10.70 ±0.19	6.61 ±0.06	26.00 ±0.11	5.57 ±0.08	2.77 ±0.03	7.05 ±0.02	35.82 ±0.13	0.31 ±0.01	0.069 ±0.001	4.46 ±0.03
Municipal Solid Waste	1.296 ±0.159	6.46 ±0.19	12.94 ±0.08	42.65 ±2.36	2.36 ±1.38	1.38 ±0.02	2.98 ±0.02	22.36 ±0.08	1.09 ±0.01	0.048 ±0.002	5.58 ±0.03
Mill Rejected Coal	0.312 ±0.067	0.25 ±0.01	9.94 ±0.06	38.21 ±0.11	0.02 ±0.01	1.63 ±0.02	1.05 ±0.01	1.12 ±0.01	0.36 ±0.004	0.025 ±0.001	46.27 ±0.25

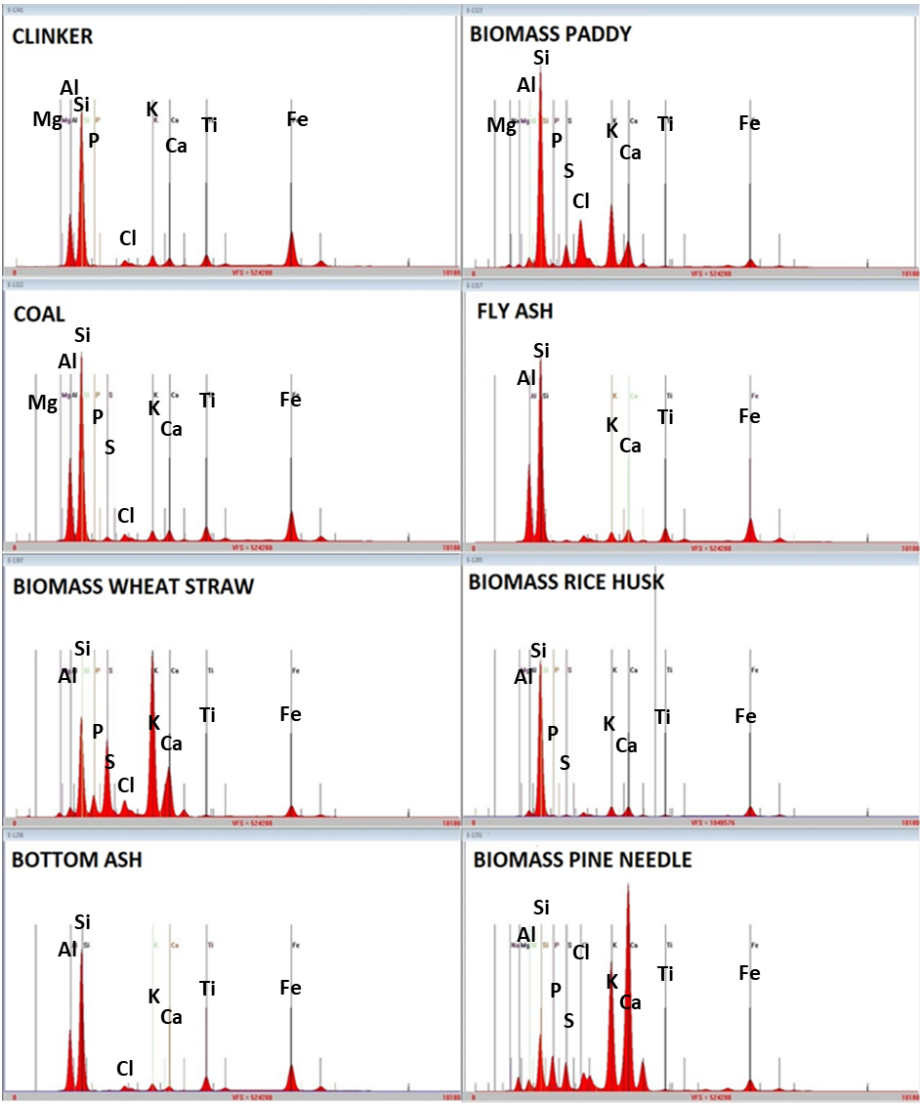

Fig. 3. EDXRF Spectra of different sample received from NTPC stations.

4 Conclusion

EDXRF is a powerful technique in elemental analysis, widely used for its non-destructive nature, rapid results, and ability to analyze a wide range of elements in various sample types. It can analyze solids, liquids, powders, and thin films. This versatility allows it to be used across different industries. Unlike some other analytical techniques, EDXRF requires minimal preparation. Samples can be analyzed as is, saving time and reducing the potential for contamination or loss of material. EDXRF can simultaneously detect multiple elements in a single measurement, making it highly efficient for routine analysis and quality control processes where speed is critical. It provides both qualitative (identifying which elements are present) and quantitative (determining their concentrations) results. This makes it useful for material characterization and quality assurance in manufacturing and production.

In NTPC, CFA is a byproduct generated during the combustion of coal. The large-scale production of CFA poses significant environmental and management challenges. Without proper control measures, fly ash particles can become airborne and pose significant health risks, such as respiratory problems and lung diseases. Significant research is being conducted to find sustainable ways to handle fly ash and convert it into valuable products. This requires regular monitoring of elemental composition of the ash where EDXRF has been pivotal in quality monitoring and control.

Acknowledgments

The authors gratefully acknowledge NETRA, NTPC Ltd. for providing the laboratory facilities essential for carrying out this work. Special thanks are extended to the Executive Director, NETRA, for the kind support and encouragement provided to the analytical laboratories.

Disclosure of Interests

The authors declare that they have no competing interests.

References

1. Attix, Frank H.: Introduction to Radiological Physics and Radiation Dosimetry. WILEY-VCH Verlag GmbH & Co. KGaA, (1986).
2. What is X-ray fluorescence (XRF), HORIBA. Available at: https://www.horiba.com/usa /scientific/technologies/energy-dispersive-x-ray-fluorescence-ed-xrf/what-is-x-ray-fluorescence-xrf/ (last accessed: 2024/10/08).
3. Penner-Hahn, J. E.: Handbook of X-ray Spectrometry, 2nd ed., Revised and Expanded Edited by René E. Van Grieken (University of Antwerp) and Andrzej A. Markowicz (Vienna, Austria). Marcel Dekker, Inc: New York and Basel (2002).
4. Newbury, D. E.: Standardless Quantitative Electron-Excited X-ray Microanalysis by Energy-Dispersive Spectrometry: What Is Its Proper Role? In Microscopy and Microanalysis (Vol. 4, Issue 6, pp. 585–597). Oxford University Press (OUP). (1998).

5. Mathapati, M., Amate, K., Durga Prasad, C., Jayavardhana, M. L., Hemanth Raju, T.: A review on fly ash utilization. In Materials Today: Proceedings (Vol. 50, pp. 1535–1540). Elsevier BV (2022).
6. Izquierdo, M., Querol, X.: Leaching behavior of elements from coal combustion fly ash: An overview. In International Journal of Coal Geology 94, 54–66 (2012).
7. Xenematrix NexT Series Operational Manual, EX-3600M/66000 XRF Spectrometers, D/N 0160805200101, Revision 5.0, Feb 2009.
8. Thompson, A., et al.: X-ray Data Booklet. Lawrence Berkeley National Laboratory, University of California. (2009) https://xdb.lbl.gov/, (last accessed: 2024/10/12).
9. Vassilev, S. V., Baxter, D., Andersen, L. K., Vassileva, C. G. An overview of the chemical composition of biomass. Fuel 89(5), 913–933 (2010).
10. Dai, S., Ren, D., Zhou, Y., Chou, C.-L., Wang, X., Zhao, L., Zhu, X.: Mineralogy and geochemistry of a superhigh-organic-sulfur coal, Yanshan Coalfield, Yunnan, China: Evidence for a volcanic ash component and influence by submarine exhalation. Chemical Geology 255(1–2), 182–194 (2008).
11. Chindaprasirt, P., Rattanasak, U.: Calcium wastes as an additive for a low calcium fly ash geopolymer. Scientific Reports, 13(1), 16351 (2023).
12. Yadav, V. K., Fulekar, M. H.: Advances in methods for recovery of ferrous, alumina, and silica nanoparticles from fly ash waste. Ceramics, 3(3), 384-420 (2020).
13. Kelechi, S. E., Adamu, M., Uche, O. A. U., Okokpujie, I. P., Ibrahim, Y. E., Obianyo, I. I.: A comprehensive review on coal fly ash and its application in the construction industry. Cogent Engineering, 9(1), 2114201 (2022).
14. Aughenbaugh, K. L., Stutzman, P., Juenger, M. C.: Assessment of the glassy phase reactivity in fly ashes used for geopolymer cements. Geopolymer Binder Systems, 1566, 11-20 (2013).
15. Peng, X., Tonglin, Z.: Comprehensive utilization of high alumina coal fly ash under the recyclable economy model. Ind. Chem, 4, 128 (2018).
16. Alterary, S. S., Marei, N. H.: Fly ash properties, characterization, and applications: A review. Journal of King Saud University – Science, 33, 6, 101536 (2021).

Harnessing Indian Coal Fly Ashes for Rare Earth Elements Recovery: A Review

Akanksha Aggarwal[1*], Raj K Tripathi[1], A Lakshman Kumar[2], Pranay Sharma[3], Anil Kumar Das[4]

[1] Analytical Lab, NTPC Energy Technology Research Alliance, NTPC Ltd., Greater Noida, Uttar Pradesh, India.

[2] Corrosion & Research Analysis Lab, NTPC Energy Technology Research Alliance, NTPC Ltd., Greater Noida, Uttar Pradesh, India.

[3] Coal Lab, NTPC Energy Technology Research Alliance, NTPC Ltd., Greater Noida, Uttar Pradesh, India.

[4] NDE, Imaging and Life Management Lab, NTPC Energy Technology Research Alliance, NTPC Ltd., Greater Noida, Uttar Pradesh, India.

akankshaaggarwal@ntpc.co.in

Abstract. Coal fly ash (CFA), produced in large quantities by thermal power plants in coal-dependent India, has emerged as a potential source for extracting Rare Earth Elements (REEs). Given the increasing demand for REEs in high-tech and green technologies, exploring alternative sources like CFA is vital. This review evaluates the composition and variability of REE content in fly ash from various Indian power plants. It examines extraction methods such as acid leaching, solvent extraction, and ion exchange, assessing their efficiency, feasibility, and associated environmental and economic implications. The necessity for innovative and sustainable sources of REEs is pressing. India produces approximately 140 million tons of CFA yearly, yet a substantial portion remains underutilized or is directed to landfills. The recovery of REEs from CFA represents a sustainable alternative that addresses the scarcity of essential materials and the environmental challenges of coal ash disposal. Emerging extraction methods, which are still primarily in the laboratory phase, offer significant promise for commercial applicability, highlighting the urgent need for effective strategies to recover valuable components. This review accentuates the significance of sustainable practices in recovering REEs, promoting a circular economy within India's energy sector.

Keywords: Thermal Power Plants, Coal Fly Ash, Utilization, Rare Earth Elements, Recovery.

1. Introduction

Coal plays a crucial role as a fuel source for electricity generation, accounting for more than 39 percent of global energy production [1, 2]. Beyond its use in generating electricity, coal is also important in metallurgical processes and cement production, as well as a precursor for activated carbon and various industrial chemicals. The

S. Shaswattam et al. (eds.), *NTPC Transactions on Energy Research (NTER 2025)*,
https://doi.org/10.2991/978-94-6463-849-3_16

traditional burning of coal produces significant amounts of coal ash, which can cause environmental and economic issues if not managed properly.

Coal ash mainly consists of three components: fly ash, bottom ash, and slag. While bottom ash and slag are usually removed from the furnace, fly ash is made up of finer particles that are carried away with flue gas during combustion. The mineral makeup of coal ash often contains various rare earth elements (REEs) in concentrations that can be much higher than in the original coal. Research has shown that fly ash may have REE levels that are eight to ten times greater than those found in source coal, with concentrations reported to reach up to 1.85% on an oxide basis.

Globally, copious amounts of coal ash are produced; for example, India produces approximately 140 million tons of coal fly ash (CFA) per annum from thermal power plants, with 78.14 % of it being effectively utilized [3]. Despite its potential as a resource, a significant quantity of CFA is commonly sent to landfills. The rising production of CFA emphasizes the need for recycling and repurposing, particularly for the extraction of REEs, which could provide a sustainable domestic supply of these essential materials. Simultaneously, the demand for REEs has experienced a notable increase, driven by their critical applications in emerging technologies. This juxtaposition presents an opportunity to explore CFA not just as a waste but as a resource for REE recovery.

1.1 Overview of Coal Fly Ashes

CFA is a lightweight material composed of fine particles produced from coal combusted in thermal power plants. India is one of the leading producers of CFA worldwide, with thermal power plants generating millions of tons each year. Currently, much of this fly ash is either landfilled or used for low-value applications like cement production, leading to environmental concerns and resource wastage.

CFA is composed predominantly of calcium oxide (CaO), alumina (Al_2O_3), iron oxide (Fe_2O_3), and silica (SiO_2), alongside traces of other metals, including REEs. The mineralogical composition differs depending on the origin of coal, combustion conditions, and the specific processing of the ash [4]. REEs are typically found in lower concentrations but can be recovered using specialized extraction techniques. Notably, CFA from certain thermal power plants in India can have REEs concentrations sufficient to make their recovery economically viable.

Indian coal, particularly from significant mining regions such as Chhattisgarh, Jharkhand, Madhya Pradesh, Odisha, West Bengal, and Telangana, contains a variety of trace elements, including valuable REEs such as lanthanum (La), cerium (Ce), and neodymium (Nd). The concentration of these elements in fly ash can be influenced by the coal seams' geological characteristics and the power plants' combustion efficiency [5].

1.1.1 Rare Earth Elements. REEs comprise a set of 17 chemical elements that majorly consist of lanthanides, along with scandium and yttrium [6]. Typically, classified into three main categories: light (LREE– Sc, La, Ce, Pr, Nd, and Sm), medium (MREE – Eu, Gd, Tb, Dy, and Y), and heavy (HREE– Ho, Er, Tm, Yb, and Lu) [7–9]. Based on market demand and significant applications across numerous sectors, REEs have been divided into three more categories: critical (Nd, Eu, Tb, Dy, Y, and Er), excessive (Ce, Ho, Tm, Yb, and Lu and uncritical (La, Pr, Sm, and Gd) [5, 9, 10]. These metals, characterized by their unique physical and chemical properties,

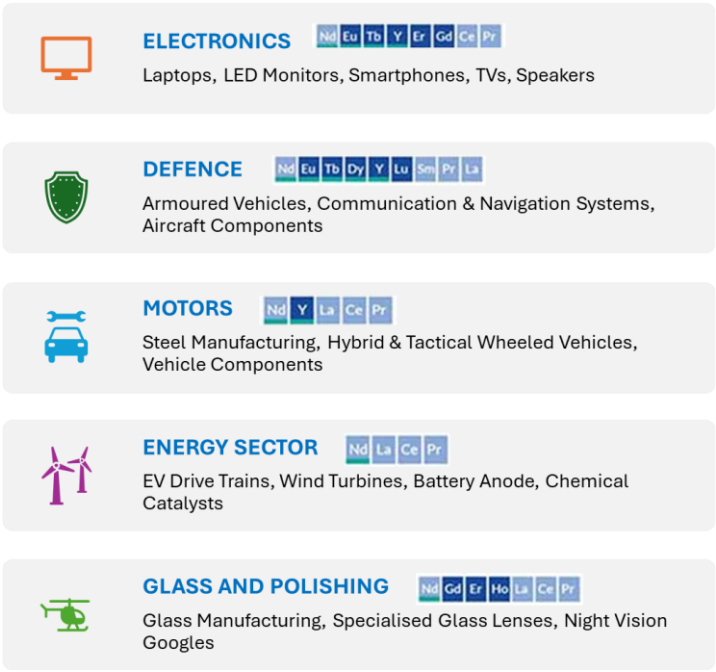

Fig. 1: Schematic representing the utilization of REEs for specific products

play a crucial part in several applications, including electronics, green or renewable energy technologies, and defense systems. In the Indian context, the usability of REEs is specified by the Ministry of Mines. The Ministry has declared REEs as critical minerals with a value chain in zero-emission vehicles, defense, and security technologies. These materials are vital for numerous applications across various industries, as represented in Fig. 1. They serve in the production of permanent magnets for electricity generators and motors, enhance catalysts and polishing agents,

and contribute to the development of batteries and electronics. These materials are also critical in defense technologies and play a key role in the wind energy sector, as well as in aviation and space exploration. Their diverse applications highlight their importance in driving innovation and efficiency across multiple fields. The worldwide need for REEs has increased significantly, fueled by technological progress and the shift toward sustainable energy options [11]. Currently, a considerable volume of CFA is disposed of in landfills, which contributes to both air and soil contamination, as well as the leaching of hazardous metals into groundwater sources. Figure 2 displays the overall generation, utilization, and accumulation of CFA between 1996 - 2019 in India [12]. Currently, the production of CFA in India is 142.07 million tons, while ~78% is being utilized. Thermal power plants like NTPC have been using CFA in the production of construction materials such as cement, bricks, and tiles. This helps reduce the environmental impact caused by fly ash disposal and offers a sustainable alternative to traditional building materials [4]. Fly ash is also being used in road construction, which enhances the durability and strength of roads while reducing the cost and environmental footprint. Utilizing CFA for the recovery of REEs can reduce these environmental risks

while simultaneously addressing the scarcity of these materials [13]. While some CFA is employed in construction (e.g., concrete and cement) and agriculture (as a soil amendment), the potential for improved resource recovery through REE extraction remains largely untapped. This paper aims to investigate the feasibility of CFA as a resource for the recovery of REEs in India, advocating for sustainable practices that can contribute to both environmental protection and resource recovery.

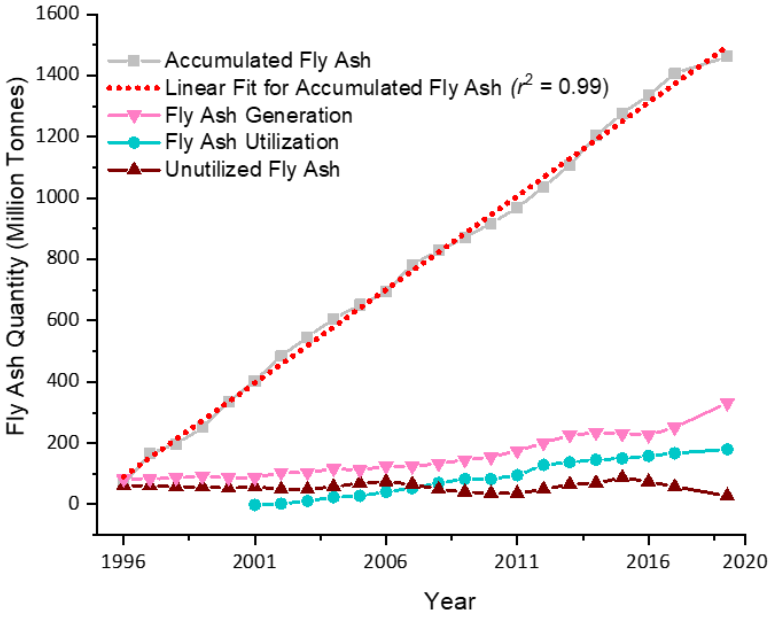

Fig. 2. Represents the overall utilization, generation, and accumulation of CFA from 1996 to 2019 in India [27]. Accumulated fly ash inclination with time (in years) shows a linear trend (r^2 = 0.99) which suggests that by 2030 the accumulated fly ash reaches around 2400 million tons.

2. REEs Recovery from Coal Fly Ash

The extraction of REEs from typical ores involves a complex, multi-stage process that demands significant financial investment, consumes a considerable amount of energy, produces large quantities of undesired tailings, and leads to negative environmental impacts. Moreover, since REEs are seldom found in substantial concentrations, standard mining techniques are often insufficient. Given the unique characteristics of REE-containing ores and their increasing demand, it has become essential to develop innovative methods for extracting REEs from both conventional and alternative sources [1].

Various techniques have been proposed for extracting REEs from minerals such as monazite, bastnäsite, and xenotime. These methods include gravity separation and flotation, among others. Additionally, techniques like supercritical extraction, solid-liquid extraction, electro-winning, precipitation, liquid-liquid extraction, and electro-

refining have been documented for concentrating REEs from relatively low-grade ores. More recent approaches include (1) microwave irradiation combined with the addition of powdered carbon, subsequently followed by physical separation processes, and (2) roasting in conjunction with pretreatment using an aqueous NaOH solution, among others. Traditional separation processes such as gravity separation, flotation, electrostatic techniques, and magnetic separation are generally employed to process industrial rare earth minerals, including monazite, bastnäsite, and xenotime. [1, 14].

Examination of the current and emerging technologies used for extracting REEs from Indian CFA, involving hydro- and pyro-metallurgy, is ongoing. Hydrometallurgical methods, such as acid leaching, solvent extraction, and precipitation, were extensively employed for extracting REEs from CFA. Acid leaching using sulfuric or hydrochloric acid has shown promising results for extracting REEs from ash matrices [15, 16]. High-temperature processing techniques, including smelting and calcination, offer alternative methods for concentrating and extracting REEs [16]. Technologies such as bioleaching and the use of ionic liquids (ILs) are gaining traction as more sustainable and efficient methods for REEs extraction [4]. Research is ongoing to develop greener methodologies that minimize waste and energy consumption. However, these methods typically require significant energy input, raising concerns about their sustainability.

3. Extraction Methodologies

The process of extracting REEs from CFA after characterization typically includes numerous steps:

1. Leaching: Various leaching agents, such as hydrochloric acid (HCl), sulfuric acid (H_2SO_4), or ammonium sulphate $(NH_4)_2SO_4$), are employed to solubilize REEs from CFA.
2. Purification and Separation: Methods such as ion-exchange, solvent extraction, and precipitation are being utilized to separate specific REEs from the leachate.
3. Recovery: Finally, REEs can be recovered in high purity through crystallization or other suitable processes.

Rao et al. (2022) established a two-phase solvent extraction method to recover REEs from sulphuric acid leachate attained in Indian CFA containing REEs with ~2160 mg/kg concentration. They discovered that using 12% (v/v) and 40% (v/v) concentrations of D2EHPA solvent allowed for the recovery of ~ 94% of HREE in the initial stages and ~ 86% of LREE in subsequent stages of the extraction process. Following this, the concentrated organic streams underwent treatment with a 6M HCl solution to remove REEs values. The resulting acidic liquors were then effectively neutralized using NaOH and treated further with oxalic acid dihydrate to precipitate LREE oxalate, which contained 17.5% LREE, along with HREE [1, 15].

CFA samples collected from various power plants across India were analyzed by Rao and colleagues [15, 16]. In their work REEs were extracted using different solvents i.e. water, buffer solution of ammonium acetate (at pH of 8.3 and 5), hydrochloric acid, a strong oxidizing combination of nitric acid and hydrogen peroxide, hydrofluoric and nitric acid combination, dissolution in strong basic sodium peroxide followed by dissolution in strong acidic HCl. All the above solvents were used to evaluate the type of REEs present in the fly ash samples. Apart from understanding the appropriate solvent for extraction of REEs, authors also optimized the leaching parameters like

rotating speed (varied b/w 100 - 700), acidic strength (varied b/n 0.5M to 3M), leaching period (0 - 12 h), solid content (varied b/w 10 - 40% solid by weight), and temperature (25 - 90 ºC) [16]. In addition, using X-ray techniques (XRD and XRF), authors reported that the chief elements in fly ash are silicon, aluminum, iron, and calcium. The mineral composition of fly ash includes Quartz (36-61%), Alumina (10-30%), Iron oxide (3 to 10% as magnetite and hematite), and killalaite mineral, along with gypsum (constituting 9–30% CaO). Quartz is the major mineral (36-61%) found in fly ash. Quartz structure lacks lattice sites to accommodate REEs, and this statement is further strengthened by established scientific agreement that quartz is deficient in REEs [15, 16]. The authors also concluded that ~ 55% of REEs were ion-exchangeable and that ~ 38% were linked to the Fe phase. However, the results reported by Pan et al. [17] exhibited notable discrepancies, which can be attributed to the differing sources and ranks of coal examined. Pan et al. [17] analyzed fly ash from low-volatile bituminous coal, while Rao et al. studied fly ash from lignite coal. Further, a comparison of these two studies reveals that leaching REEs from low-rank CFA (where REEs are 55% ion-exchangeable) is easier and economically viable than extracting REEs from bituminous CFA, which contains REEs in their alumina silicate phase (requires strong aggressive acids for their extraction) [16].

Ionic solvents, often known as ILs or room-temperature molten salts, belong to a category of solvents that remain in the liquid state at or around ambient temperature. Recently, ionic and deep-eutectic solvents (DESs) have gained significant attention as effective alternatives to traditional methods of metal recovery. Their unique properties and capabilities position them as promising options in the field of metal extraction. These systems operate as responsive agents in leaching and extraction procedures. Karan et al. used two varieties of DESs, i.e., choline chloride (ChCl) with lactic acid and ChCl with para-toluene sulphonic acid monohydrate (pTSA), to extract REEs from CFA [1, 4]. Further, the REEs in the extract were precipitated by using a cocktail of different chemicals and further diluted with DM water [1]. DES systems achieved a recovery of 85–95% of REEs from the CFA. Moreover, research has been conducted on rare earth oxides' dissolution processes from bauxite residue utilizing the IL betainium bis(trifluoromethyl sulfonyl)imide (HbetTf2N). The findings indicated that temperature and retention time are crucial factors, with elevated temperatures and prolonged retention times resulting in increased REEs extraction, reaching up to 70–85% [1].

Kumari et al. investigated geographically varied coal samples and found 0.5 to 1.5 kg/ton of REEs in a specific coal seam located in eastern India. To this end, systematic leaching experiments were conducted to extract REEs from Indian coal ash samples through hydrometallurgy. The highest dissolution of REEs from these samples was observed when HCl concentrations in the range of 2 to 6 M were used at higher temperatures. More than 90% of the REEs were recovered from the leachate through oxalate precipitation. The developed process holds significant promise for commercialization following feasibility assessments [18].

Mondal et al. utilized the HNO_3 acid-digestion method to dissolve various CFA samples from multiple power plants and fused the resulting material in a NaOH + $NaNO_3$ mixture at 600 °C, subsequently treating it with hydrothermal processes. The overall concentration of REEs was found to be between 300 and 500 mg/kg. The extraction of REEs from the matrix utilized XAD-7 resin that had been treated with N, N, N′, N′-tetrakis-2-ethyldiglycolamide (TEHDGA). The REEs that had been loaded were subsequently eluted using 0.01 M HNO_3 [1, 19].

Extraction through acid leaching has shown to be one of the most effective methods of extracting REEs from CFA. Research indicates that acid leaching can achieve recovery rates of approximately 70-90% for specific REEs like lanthanum and cerium. However, the concentration of acids used can pose environmental hazards, necessitating thorough management strategies post-extraction. With its selective separation capabilities, solvent extraction has demonstrated the potential to recover up to 80% of REEs from CFA. It operates on the principle of using organic solvents to extract specific REEs based on their chemical properties. While the process is highly efficient, challenges remain concerning the disposal of used solvents and the economic viability of the process when scaled for larger operations. Although the Ion Exchange method has lower recovery rates, generally in the range of 50-70%, it offers advantages in selectivity and the potential for the regeneration of ion-exchange materials. The ability to utilize fewer caustic chemicals makes it more environmentally friendly, which can be a significant factor in terms of sustainability.

Some of the extraction methods that have shown promise for retrieving REEs from CFA, particularly for industrial applications, are being worked upon in India, such as:

- Ionic Liquids: This method has shown promising results, and its research is currently underway in India [20]. The use of ILs like HbetTf2N has demonstrated high efficiency in extracting REEs due to their ability to be tailored for specific element affinities. However, the scalability and cost-effectiveness of this method for large-scale industrial applications are still under evaluation [21].
- Sequential Extraction Techniques: These techniques have proven to be effective in selectively extracting REEs from CFA. The multi-step process helps in reducing reagent consumption and process complexity, making it more environmentally friendly and cost-effective. Studies have shown that sequential extraction can achieve high recovery rates of REEs, but the method's efficiency can vary depending on the specific composition of the fly ash.
- Improved Ambient Temperature Extraction: This method, developed by the U.S. Department of Energy's National Energy Technology Laboratory, has shown high levels of extraction efficiency (ranging from 80-100%) using mild inorganic acids at ambient temperatures. This approach is particularly advantageous as it reduces energy costs and environmental impact [22]. While this method is promising, its application in India is still in the early stages, and further research is needed to optimize it for local CFA compositions.

Research in India has been increasingly focused on optimizing the extraction process of REEs from CFA. Various studies have acknowledged effective leaching methods and have developed optimized protocols for the separation and purification of these elements. However, challenges remain in improving the efficiency and economic viability of these processes to ensure commercial scalability.

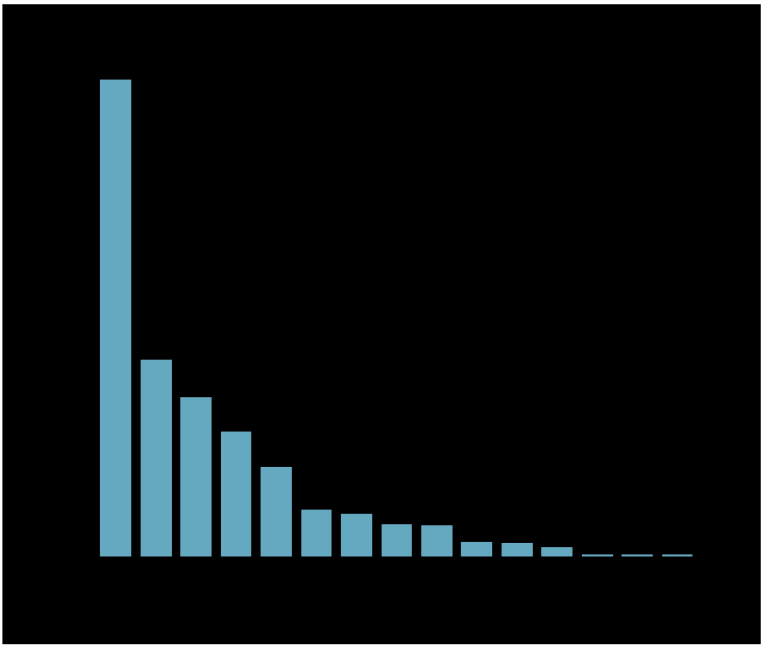

Fig. 3. Average proportion of individual REEs to total REEs (%) in CFA samples [5].

4. Characterization of REEs

A thorough analysis of the ash is conducted to quantify and identify the specific REEs present. Various analytical techniques, viz. Inductively Coupled Plasma-Mass Spectrometer (ICP-MS) [5, 23, 24], X-ray fluorescence (XRF) [25, 26], X-ray diffraction (XRD) [25], Neutron Activation Analysis (NAA) [27], Inductively Coupled Plasma-Optical Emission Spectrometer (ICP-OES) [19, 25, 28], Laser-Induced Breakdown Spectroscopy (LIBS) [29], and Microscopy techniques [25] have been used for REEs analysis in diverse matrices comprising of coal and CFA samples [5].

Gautam et al. (2021) and Sandeep et al. (2023) quantified rare earths in Indian CFA using ICP-MS. Results from chemical analysis indicate that Ce is the most abundant among the REEs, whereas Lu demonstrates the lowest concentration [5, 30]. Figure 3 presents the average proportion of each REEs to the total REEs (∑REE) concentrations (%). The contribution of Ce to the ∑REE ranges from 36% to 40%, with a mean value of 37.5%. Conversely, the contribution of Lu is notably minimal, ranging from 0.15% to 0.23%. Among the more significant REEs—including Eu, Nd, Dy, Tb, Y, and Er—neodymium reflects a significant contribution, ranging from 12% to 13.1%, followed by yttrium, which contributes between 9.9% and 10.8%, and dysprosium with a contribution of 2.3% to 3.2% within Indian CFA samples [5].

Rao et al. (2020) used various techniques (XRF, XRD, ICP-OES, Optical microscopy, and SEM-EDX) for the characterization of the fly ash samples. The authors reported a feasible concentration of ∑REE (~ 2100 mg/kg), out of which 20% are HREE. Optical microscopy demonstrated that the LREE are found as Zircon and Monazite minerals [25].

Mondal et al. analyzed elements (major and trace) by ICP-OES and observed that all the samples had analogous element distribution with ∑REE ranging from 300-500 mg/kg. The major elements present were Al, Si, Ca, Fe, and Mg [19] while in the case of Maity et al., the ∑REE ranged from 51-66 mg/kg, with Pr having the highest concentration [28].

Table 1 shows comparative data of the average concentrations of REE in Indian CFA published by various authors [5, 19, 25, 27, 28, 30, 31]. The present work compared these data using the criteria outlined by the authors [10, 23], which include the outlook coefficient (C_{out}), ∑REE, uncritical percentage (U_p), critical percentage (C_p), and excessive percentage (E_p). The formulas used for these calculations are provided below [10, 23]:

$$C_{out} = \sum CREE / \sum EREE \tag{1}$$

$$C_P = \frac{\sum CREE}{\sum REE} \times 100 \tag{2}$$

$$\mathrm{U_P} = \frac{\sum \mathrm{UREE}}{\sum \mathrm{REE}} \times 100 \tag{3}$$

$$\mathrm{E_P} = \frac{\sum \mathrm{EREE}}{\sum \mathrm{REE}} \times 100 \tag{4}$$

As the name implies, critical minerals are in extreme demand. Therefore, the parameters C_p and C_{out} are particularly important, as they determine the economic viability of extracting the given samples. Authors [32, 33] described that a C_p value above 30% and a C_{out} value greater than 1 are considered favourable [32, 33]. However, as indicated in Equation 1, C_{out} is influenced by both C_p and E_p. A C_{out} value of less than 1 can still indicate the sample's utility as a viable secondary source for REEs, highlighting its potential for further evaluation and application. Therefore, all major parameters mentioned in eq. (1-4) must be analyzed to assess the economic potential of the source effectively.

Table 1: Data Comparison of Average Concentration of REEs in Indian CFA published by several authors

Element	Chand et al. (2024)	Banerjee et al. (2024)	Sandeep et al. (2023)	Maity et al. (2022)	Pooja et al. (2021)	Rao et al. 2020)	Mondal et al. (2019)	Average (ppm)
La	120.0	91.6	57.1	1.0	123.1	253.0	62.4	101.2
Ce	208.0	166.9	136.9	BDL**	265.6	580.0	137.4	249.1
Pr	29.0	19.9	13.3	54.0	36.9	85.0	20.2	36.9
Nd	68.2	71.2	45.7	BDL	166.9	508.0	45.9	151.0
Sm	20.3	13.3	12.5	BDL	33.4	95.0	5.9	30.1
Eu	4.3	2.9	2.1	0.1	7.9	23.0	2.3	6.1
Gd	9.9	16.1	9.6	BDL	30.3	96.0	5.7	27.9
Tb	2.5	2.1	1.5	BDL	3.3	8.0	1.2	3.1
Dy	14.0	11.2	9.5	BDL	22.4	61.0	4.9	20.5
Y	NA*	59.6	36.4	0.8	123.6	300.0	34.5	92.5
Ho	2.5	2.2	1.7	0.5	1.5	1.0	0.9	1.5
Er	5.1	6.0	4.6	BDL	9.6	28.0	0.9	9.0
Tm	2.5	0.9	0.6	BDL	1.2	1.0	0.6	1.1
Yb	8.9	5.2	4.6	0.2	9.3	20.0	3.8	7.4
Lu	1.4	0.8	0.7	0.6	1.1	1.0	1.4	1.0
∑REE	496.6	469.8	336.7	57.2	836.2	2060.0	328.0	654.9
LREE (%)	89.7	77.3	78.8	96.1	74.9	73.8	82.9	81.9
MREE (%)	6.2	19.5	17.6	1.6	22.4	23.7	14.8	15.1
HREE (%)	4.1	3.2	3.6	2.3	2.7	2.5	2.3	3.0
CREE (ppm)	94.1	152.9	99.8	0.9	333.8	928.0	89.7	242.7
UREE (ppm)	179.2	140.9	92.5	55.0	223.7	529.0	94.2	187.8
EREE (ppm)	223.3	176.0	144.5	1.3	278.7	603.0	144.1	224.4
C_{out}	0.4	0.9	0.7	0.7	1.2	1.5	0.6	0.9
C_p	18.9	32.5	29.6	1.6	39.9	45.0	27.3	27.9
U_p	36.1	30.0	27.5	96.1	26.8	25.7	28.7	38.7
E_p	45.0	37.5	42.9	2.3	33.3	29.3	43.9	33.5

*NA – Not Available; **BDL- Below Determination Limit

5. Environmental and Economic Implications

5.1 Environmental Considerations

Recovering REEs from CFA can significantly mitigate the environmental impacts associated with ash disposal. By converting waste into value-added products, the process can contribute to reduced landfill use. However, potential ecological risks associated with leaching agents and chemical processes must be carefully managed to prevent secondary pollution [31]. Recycling waste aligns with the principles of sustainable development and the circular economy. Apart from waste reduction and environmental pollution mitigation, fly ash utilization could be beneficial in the reduction of the carbon footprint associated with mining and processing virgin materials [18]. Thus, extracting REEs from fly ash provides an alternative source of these critical materials, thereby increasing the efficacy of resource utilization.

5.2 Economic Viability

The economic aspects of REEs recovery from CFA hinge upon factors such as the concentration of the elements within the ash, the cost of extraction processes, and market prices for REEs. Given the fluctuating nature of REE prices globally and the competitive landscape of extraction, robust economic models need to be established to assess the viability of large-scale operations. While initial extraction costs may be high, the growing demand for REEs can potentially make this process economically viable. Investment in research and development, coupled with supportive government policies, can further enhance the viability of REEs recovery from CFA. Thus, there is a need for an assessment of the cost-effectiveness of rare earth extraction from CFA compared to traditional mining methods [31, 32].

With only 6.9 million metric tons of reserves, India is ranked fifth in the world for REEs. Figure 4 lists the major nations and their global reservoirs of REEs as of 2023 (in 1,000 metric tons of rare earth oxides) [34]. An estimated 11.93 Mt of monazite with 55%–65% rare earth oxides can be found in beach sand in India [11]. Although India holds 35% of the world's coastal sand mineral resources, it relies entirely on imports for its REEs. India's supply chain is more vulnerable because of its heavy reliance on imports of REEs from China. As observed from Table 1, the $C_{out} > 1$ accounts for the viability of Indian CFA as a promising alternative for REE resources and harnessing CFA for REEs recovery.

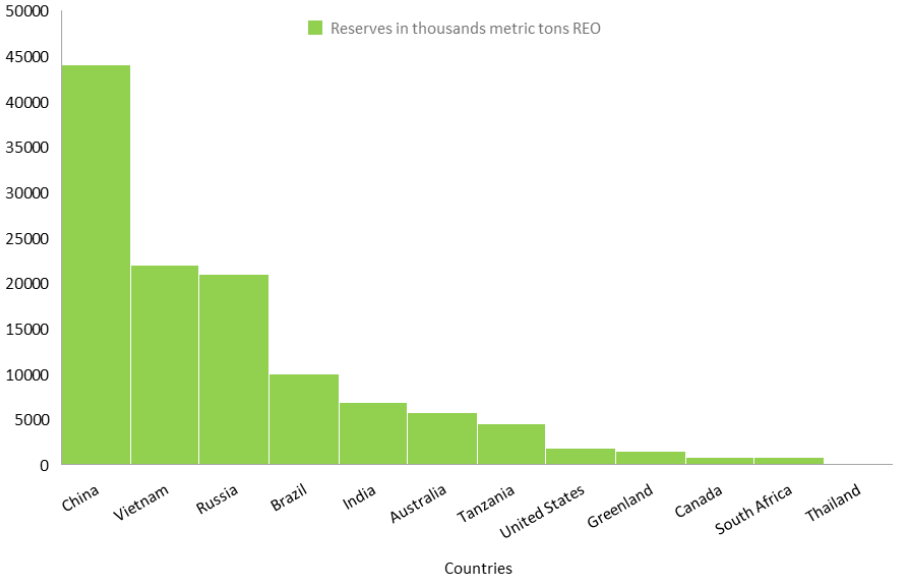

Fig. 4: REEs reserves worldwide (in thousand metric tons rare earth oxides) [34]

6. Conclusion and Recommendations

CFA represents a significant and underutilized resource in India, offering a dual solution to waste management and resource scarcity, particularly in recovering REEs. This paper highlights the considerable potential of CFA in the recovery of REE, advocating for sustainable practices that support both environmental conservation and resource recovery. By adopting innovative extraction techniques and sustainable practices, India can transition from a conventional coal economy to a more circular and resource-efficient model. A concerted effort is needed to explore future research directions, challenges, and opportunities to escalate the REEs' extraction efficiency from CFA. Collaborative research initiatives should optimize extraction processes, minimize environmental impacts, and explore economic models that incentivize recycling efforts. Cooperative efforts between academia, industry, and government are critical to unlocking CFA's potential and addressing energy and environmental challenges in the country.

Acknowledgments. The authors are thankful to Shri S. Shaswattam, ED-NETRA, for their continuous support and guidance towards the exploration of modern condition monitoring techniques for the sustainable development of the Power sector. The authors are thankful to Smt. Kiran Diwakar for her extreme lab support in conducting the present study.

Disclosure of Interests. The authors hereby declare that there are no competing interests relevant to the content of this article.

References

1. Dodbiba, G., & Fujita, T.: Trends in Extraction of Rare Earth Elements from Coal Ashes: A Review. Recycling, 8 (1), 17 (2023)
2. Dai, S., Finkelman, R.B.: Coal as a promising source of critical elements: Progress and future prospects. Int. J. Coal Geol., 186, 155–164 (2018)
3. Central Electricity Authority. Report On Fly Ash Generation at Coal/Lignite Based Thermal Power Stations and it's Utilization in the Country for the 1st half of the Year 2022–2023 (April 2022 to September 2022), https://cea.nic.in/wp-content/uploads/tcd/2023/05/Half_Yearly_Ash_Report_2022_23.pdf, last accessed on 2024/10/25
4. Karan, K. K., Masto, R. E., Agarwalla, H., Bari, S., Kumar, M., Gopinathan, P., Hazra, B., Saha, S., & Maity, S.: Separation of coal combustion residue for critical element extraction and other bulk uses. Environmental Science Advances, 3(1), 109–118 (2023)
5. Sandeep, P., Maity, S., Mishra, S., Chaudhary, D. K., Dusane, C., Pillai, A. S., & Kumar, A. V.: Estimation of rare earth elements in Indian coal fly ashes for recovery feasibility as a secondary source. Journal of Hazardous Materials Advances, 10, 100257 (2023)
6. Yuksekdag, A., Kose-Mutlu, B., Kaya, B., Kumral, M., Wiesner, M. R., Koyuncu, I.: Comprehensive characterization of secondary sources originating from Turkey in terms of rare earth elements and scandium. Science of The Total Environment, 777, 146033 (2021)
7. Dai, S., Zhou, Y., Ren, D., Wang, X., Li, D., & Zhao, L.: Geochemistry and mineralogy of the Late Permian coals from the Songzo Coalfield, Chongqing, southwestern China. Science in China Series D Earth Sciences, 50(5), 678–688 (2007)
8. Palozzi, J., Bailey, J. G., Tran, Q. A., Stanger, R.: A characterization of rare earth elements in coal ash generated during the utilization of Australian coals. International Journal of Coal Preparation and Utilization, 43, 2106–2135 (2023)
9. Wang, Z., Dai, S., Zou, J., French, D., Graham, I. T., Rare earth elements and yttrium in coal ash from the Luzhou power plant in Sichuan, Southwest China: Concentration, characterization and optimized extraction. Int J Coal Geol, 203, 1–14 (2019)
10. Seredin, V.: A new method for primary evaluation of the outlook for rare earth element ores. Geology of Ore Deposits, 52(5), 428–433 (2010)
11. Report of the Committee on Identification of Critical Minerals. (2023). In Ministry of Mines, https://mines.gov.in/admin/storage/app/uploads/649d4212cceb01688027666.pdf, last accessed on 2024/10/25Banerjee, R., Chakladar, S., Chattopadhyay, S. K., & Chakravarty, S.: A comparative study on the association and extractability of rare earth elements from laboratory ash, bottom ash, fly ash: A perspective on Indian coals. Minerals Engineering, 213, 108745 (2024)
12. Coal ash in India: A Compendium of Disasters, Environmental and Health risks. (2020). Health Energy Initiative, https://unesdoc.org/ark:/48223/pf0000139578, last accessed on 2024/10/25
13. Liu, P., Zhao, S., Xie, N., Yang, L., Wang, Q., Wen, Y., Chen, H., & Tang, Y.: Green Approach for Rare Earth Element (REE) Recovery from Coal Fly Ash. Environmental Science & Technology, 57, 5414−5423 (2023)
14. Jordens, A., Cheng, P. Y., & Waters, E. K.: A review of the beneficiation of rare earth element bearing minerals. Minerals Engineering, 41, 97-114 (2013)
15. K, A. R., Karan, R., J, M. B., G, R. D., & T, S.: Development of process scheme for recovery of rare earths from leachate of coal flyash. Cleaner Chemical Engineering, 4, 100078 (2022)
16. Thomas, B. S., Dimitriadis, P., Kundu, C., Vuppaladadiyam, S. S. V., Raman, R. S., & Bhattacharya, S.: Extraction and Separation of Rare Earth Elements from coal and coal fly ash: A review on fundamental understanding and on-going engineering advancements. Journal of Environmental Chemical Engineering, 12(3), 112769 (2024)

17. Pan, J., Nie, T., Hassas, B. V., Rezaee, M., Wen, Z., & Zhou, C.: Recovery of rare earth elements from coal fly ash by integrated physical separation and acid leaching. Chemosphere, 248, 126112 (2020)
18. Kumari, A., Jha, M., Chakravarty, S., & Pathak, D.: Indian Coal Ash: A Potential Alternative Resource for Rare Earth Metals (REMs). In the minerals, metals & materials series, 265–273 (2020)
19. Mondal, S., Ghar, A., Satpati, A., Sinharoy, P., Singh, D., Sharma, J., Sreenivas, T., & Kain, V.: Recovery of rare earth elements from coal fly ash using TEHDGA impregnated resin. Hydrometallurgy, 185, 93–101 (2019)
20. India Science, Technology & Innovation - ISTI Portal, https://www.indiascienceandtechnology.gov.in/research/extraction-and-separation-rare-earth-elements-coal-fly-ash-using-ionic-liquids-multifunctional, last accessed on 2025/02/19
21. Wang, K., Adidharma, H., Radosz, M., Wan, P., Xu, X., Russell, C., Tian, H., Fan, M., & Yu, J.: Recovery of rare earth elements with ionic liquids. Green Chem., 19, 4469-4493 (2017)
22. TECHBRIEF_Improved REE Extraction, https://netl.doe.gov/sites/default/files/2020-11/TECHBRIEF20-004_20N-12_Improved%20REE%20Extraction.pdf, last accessed on 2025/02/19
23. Blissett, R., Smalley, N., & Rowson, N.: An investigation into six coal fly ashes from the United Kingdom and Poland to evaluate rare earth element content. Fuel, 119, 236–239 (2013)
24. Lin, R., Howard, B. H., Roth, E. A., Bank, T. L., Granite, E. J., & Soong, Y.: Enrichment of rare earth elements from coal and coal by-products by physical separations. Fuel, 200, 506–520 (2017)
25. K, A. R., Md, S., RamaDevi, G., Thakurta, S. G., & T, S.: On the characterization and leaching of rare earths from a coal fly ash of Indian origin. Separation Science and Technology, 56(3), 541–557 (2020)
26. Nakayama, K., & Nakamura, T.: X-ray Fluorescence Analysis of Rare Earth Elements in Rocks Using Low Dilution Glass Beads. Analytical Sciences, 21(7), 815–822 (2005)
27. Chand, M., Bagchi, S., & Khan, B. H.: Assessing rare earth elements in Indian coal ash using Westcott formalism in NAA and leaching studies. RSC Advances, 14(35), 25820–25829 (2024)
28. Maity, S., Choudhary, A. K. S., Kumar, S., & Gupta, P. K.: Partitioning of Rare Earth Elements (REEs) from Coal-to-Coal Fly Ash in Different Thermal Power Stations (TPSs) of India. Journal of the Geological Society of India, 98(4), 460–466 (2022)
29. Phuoc, T., Wang, P., & Mcintyre, D.: Detection of rare earth elements in Powder River Basin sub-bituminous coal ash using laser-induced breakdown spectroscopy (LIBS). Fuel, 163, 129–132 (2015)
30. Gautam, P., Sharma, P., & Satyakam, R.: Determination of rare earth elements in NTPC coal fly ash through ICPMS Technique. NETRA Journal, 26, 55-59 (2019)
31. Banerjee, R., Chakladar, S., Chattopadhyay, S. K., & Chakravarty, S.: A comparative study on the association and extractability of rare earth elements from laboratory ash, bottom ash, fly ash: A perspective on Indian coals. Minerals Engineering, 213, 108745 (2024)
32. Seredin, V., & Dai, S.: Coal deposits as potential alternative sources for lanthanides and yttrium. International Journal of Coal Geology, 94, 67–93 (2012)
33. Franus, W., Wiatros-Motyka, M. M., & Wdowin, M.: Coal fly ash as a resource for rare earth elements. Environmental Science and Pollution Research, 22(12), 9464–9474(2015)
34. Statista 2024, https://www.statista.com/statistics/277268/rare-earth-reserves-by-country/, last accessed on 2024/10/25

Geospatial Mapping of Chlorine in NTPC-Linked Coalmines

Aarti Sharma, Gaurav Richhariya*, Pranay Sharma, Anil Kumar Das

Coal Lab, NTPC Energy Technology Research Alliance,
NTPC Ltd., Greater Noida, Uttar Pradesh, India

*Corresponding author: grichhariya01@ntpc.co.in

Abstract. Chlorine (Cl) is a trace element present in coal which undergoes complex changes when coal is combusted in boiler. Chlorine may combine with iron and sulphur in slag deposits in areas of the boiler where reducing conditions occur to form compounds that can corrode the wall tubes. In the present study, chlorine content mapping of major NTPC linked coal mines has been done using Trace Elemental Instruments (TEI) chlorine analyzer "Explorer-X". While most of the Indian coal mines exhibit low chlorine levels between 10 and 60 ppm, the Ragavpuram coal deposit stands out with a significantly higher concentration of 146 ppm.

Keywords: Chlorine mapping, iron, sulphur, alkali metals, slag, NTPC linked coal mines

1 Introduction

Thermal power plants have been the backbone of electricity generation for decades while they remain essential for meeting global energy demands, their environmental impact necessitates ongoing technological innovation. Thermal power plants while crucial for electricity generation, pose environmental and operational challenges due to contamination and corrosion [1,2]. These issues arise from various sources including fuel combustion, water use, and the materials involved in plant construction and operation. Chlorine is a significant contributor to high/low temperature corrosion in coal- fired power plants [3]. The chlorine content of coal is influenced by various geological factors, including its proximity to marine environments [4]. Additionally, the migration of groundwater contributes to elevated chlorine levels in coal [5]. Chlorine may be incorporated into the plant material that initially formed the coal [6]. Some plant matter or its residues may assimilate chlorine from the environment, embedding it within the resulting coal formation. Human interventions such as industrial pollution or saline water discharge can potentially introduce chlorine compounds into coal deposits. Nevertheless, these anthropogenic sources are typically less prevalent than naturally occurring chlorine origins. Upon combustion, chlorine combines with hydrogen to form hydrogen chloride gas which is highly corrosive. At high temperatures, chlorine also reacts directly with metals sodium and potassium to form low melting metal chlorides [7]. These metal chlorides can evaporate or form deposits on equipment surfaces leading to chlorine-induced hot corrosion [8]. The presence of sulphur and iron along with chlorine aggravates corrosion by forming a molten corrosive layer on boiler tubes [9]. Iron pyrite decomposes in furnace (from FeS_2 to FeS). Decomposition product is low melting leading to slagging on water wall tubes as shown in Fig.1.

S. Shaswattam et al. (eds.), *NTPC Transactions on Energy Research (NTER 2025)*,
https://doi.org/10.2991/978-94-6463-849-3_17

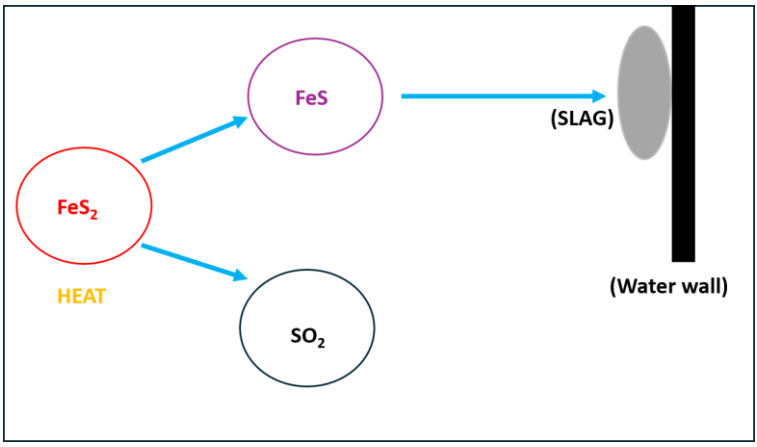

Fig. 1. Water wall slag formation.

A coarse pyrite particle (FeS_2) undergoes thermal decomposition in the flame to iron sulphide (FeS). The molten iron sulphide, accelerated by high velocity gases from the coal pipe or burner, impacts the waterwall with sufficient force to adhere and form slag. At high temperature chlorine leads to the formation of $FeCl_2$ and $FeCl_3$, which can evaporate and redeposit, causing the metal to oxidize and degrade [10]. The process typically occurs in superheater and reheater tubes where temperatures are high. In cooler parts of the flue gas system, chlorine may combine with water vapor to form hydrochloric acid (HCl) leading to acid corrosion of ducts, filters and chimneys. Further, the Gross Calorific Value (GCV), Ash, Moisture and Volatile Matter (VM) varies over a wide range in a coal matrix. Hence the chlorine content was assessed over GCV, ash and VM [11]. Researchers have made effort to study the chlorine content in foreign coals [12-13]. The American, Australian and African coal has high chlorine content 0.02-0.6% [14]. Considering the detrimental effect of chlorine on the power plant equipment, the present study aims at estimation of chlorine content of the various coal mines linked to NTPC.

2 Geological Formations of the Coalfields

Central Coalfields Limited (CCL) primarily operates in Jharkhand and Bihar, while Eastern Coalfields Limited (ECL) covers West Bengal and Jharkhand. Bharat Coking Coal Limited (BCCL) specializes in high-grade coking coal extraction from the Jharia Coalfield, whereas Northern Coalfields Limited (NCL) operates in the Singrauli Coalfield, spanning Madhya Pradesh and Uttar Pradesh. Mahanadi Coalfields Limited

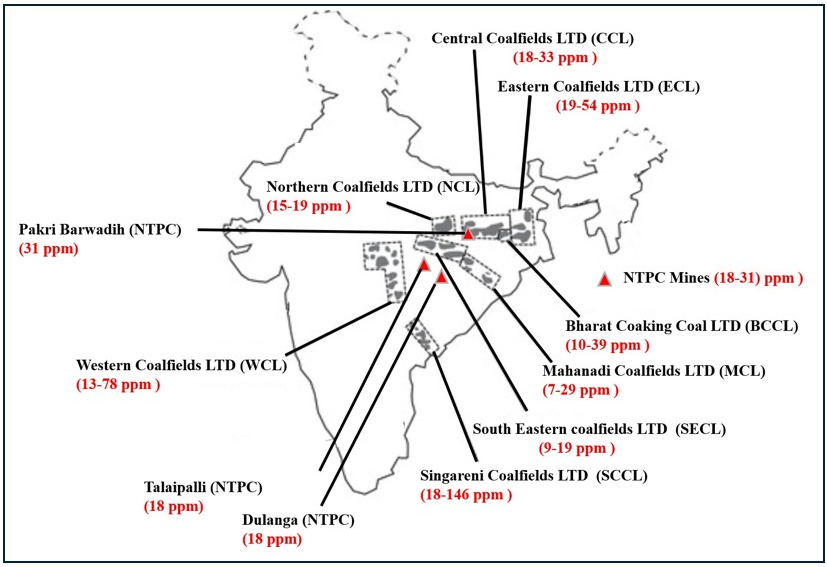

Fig. 2. Chlorine mapping of Indian Coal

(MCL), located in Odisha, lies within the Gondwana sedimentary formation. South Eastern Coalfields Limited (SECL) has its operations concentrated in Chhattisgarh and Madhya Pradesh, while Singareni Collieries Company Limited (SCCL) operates in Telangana. Western Coalfields Limited (WCL) primarily manages coal mines in Maharashtra, with some extending into Madhya Pradesh.

The coal deposits of NTPC, CCL, ECL, BCCL, NCL, MCL, SECL, SCCL, and WCL are part of the Lower Permian Barakar and Raniganj Formations, which belong to the Gondwana Supergroup. The geographical distribution of these coalfields (along with chlorine) is illustrated in Fig. 2.

3 Coal sample acquisition from mines and sidings

The coal samples for this study were collected from various mines and adjacent railway sidings used for shipment. Specifically, samples were obtained from Pakri BNDG NTPC, Tallaipalli KCHP, and Dulanga sidings, corresponding to the Pakri Barwadih, Tallaipalli, and Dulanga coal mines, respectively.

For Eastern Coalfields Limited (ECL), samples were collected from the PSBP, PMCS, CCSJ, SSAP, MCSP, NMCL, PSCE, POCP, and PMCS sidings. Similarly, for Central Coalfields Limited (CCL), primary sidings analysed included PLCP, DCSK, SLSP, BSDC, BLCC, BCBM, CPCS, and CHRI. In Bharat Coking Coal Limited (BCCL) mines, major sidings used for chlorine analysis were KLSK, KKBK, AKKK, TCSB, CCSR, BCSR, NUGP, DRGM, TPST, and POCP.

The sample sources for Northern Coalfields Limited (NCL), included Aryan IPAT, Amelia THDC, Nighai, Dudichua, and Nighai WW. In Mahanadi Coalfields Limited (MCL), samples were obtained from sidings at Kulda MCLK, Basundhara MFSJ, Garjanbahal MFSJ/MCLK/K/MCLF, IB Valley BOMB, Lajkura LOCM, Lakhanpur BOCM/BOCB, Jagannath SBCT/ACTR, Lingaraj, Hingula, Bharatpur, Siarmal MFSJ, Samleshwari LOCM, and Talcher KT.

For Southeastern Coalfields Limited (SECL), sidings analysed for chlorine content included Gevra GPCK, New Kusmunda NKCR, Dipka SCDG, Kusmunda KMKA, Baroud BOMK, Chhal SLCC, Manikpur MCK, and Old Kusmunda OKSR. In Western Coalfields Limited (WCL), chlorine analysis was conducted on samples from Pouni-II GGPP, Penganga GGS, Gourideep PRPI, Gokul UMSG, Umrer UMSG, Dhuptalla MBCB, Ballarpur MBCB, Kolar WANI, Bellora GGS, Sasti MBCB, Mungoli GSG, Makardhokra-I UMSG, Makardhokra-III UMSG, Neeljay GGS, Ukni WANI, and Dumrikhurd.

For Singareni Collieries Company Limited (SCCL), coal samples for analysis were collected from JVR CHP JVRB, GDK GXSG, RCHP RUSG, GDK CHP GOSG, as well as sidings at Ramakrishna, Singareni, Godavari, Jalagam, Ragavapuram, Deoragaram, and BPA CHP.

4 Method

In the present study, chlorine measurement in coal has been done using TEI make chlorine analyser, model "Xplorer-X". The instrument is based on standard ASTM D -6721. The same standard has been used for chlorine assessment globally [15]. Sample containing halides is introduced into the furnace using introduction module "Solid Module for solids and petrochemical products with a final boiling point > 420 °C". The schematic of Xplorer- X is presented as Fig. 3.

The sample containing chlorides is oxidized at high temperature (1000°C). After conditioning the gas stream so produced by removing water and any other interference compounds in the sulfuric acid scrubber, the dried and clean gases are led into a temperature-controlled titration cell where the chloride ions react with the silver ions. The amount of charge (the integral of the regeneration current over the measuring time) used to generate the lost silver ions, is directly related to the chlorine (Cl) content of the sample.

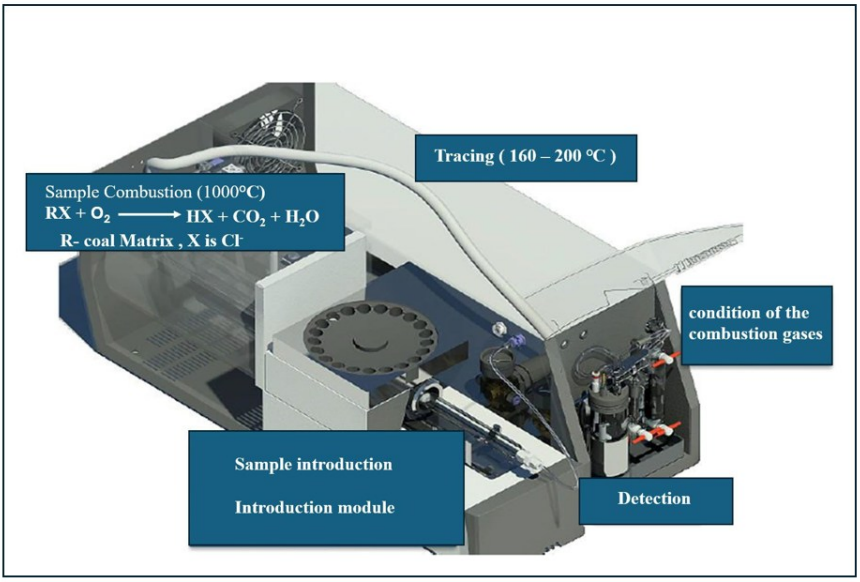

Fig. 3. TEI "Xplorer -X along with its components (Courtesy of Trace Element Instruments)

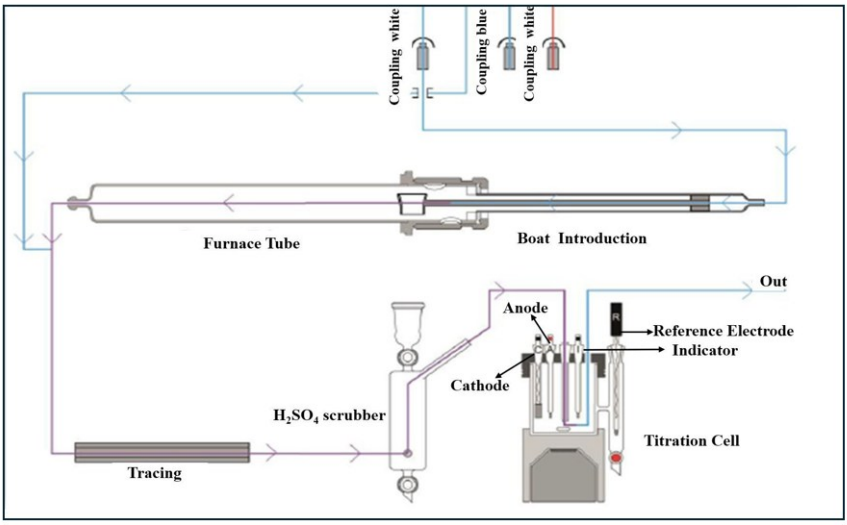

Fig. 4. Flow path - This diagram shows flow path of chlorine containing sample from boat introduction up to detection by coulometric cell (by courtesy of Trace Element Instruments)

5 Test Procedures

The test procedure of the coal samples for the trace of chlorine is presented as Fig. 4. A sample quantity of 10-20 mg is introduced through boat into furnace tube. The sample is subjected to oxidation at high temperature around (1000°C). The reaction among the products of combustion leads to formation of HCl gas which is conditioned through sulphuric acid scrubber. Furthermore, the conditioned sample is detected through micro coulometry.

6 Results

The chlorine concentration of NTPC, ECL, CCL & BCCL mines lies in the range of 10-50 ppm. There is not much significant variation in the coal chlorine content of NTPC, ECL, CCL & BCCL mines as coal formation belongs to Gondwana era with Barakar and Raniganj as the major coal bearing formation. The chlorine content of NTPC, ECL, CCL & BCCL mines presented as Fig. 5.

The chlorine content of SECL, SCCL & SECL is presented as Fig. 6. It lies in the typical range of 10-60 ppm except for Raghavpuram coal mine. The higher chlorine content of Raghavpuram mines is associated to its presence in the vicinity of coastal area.

The chlorine concentration of WCL & MCL mines typically ranges from 10 to 60 ppm, Fig. 7. Coal from these mines shows minimal variation in coal chlorine, as they originate from the Gondwana era, primarily within the Barakar and Raniganj coal-bearing formations. However, there were slight variations of Makardhokra-I UMSG (78 ppm) and Makardhokra-III UMSG (72 ppm) which could be attributed due to the heterogeneity of organic matter at the time of deposition.

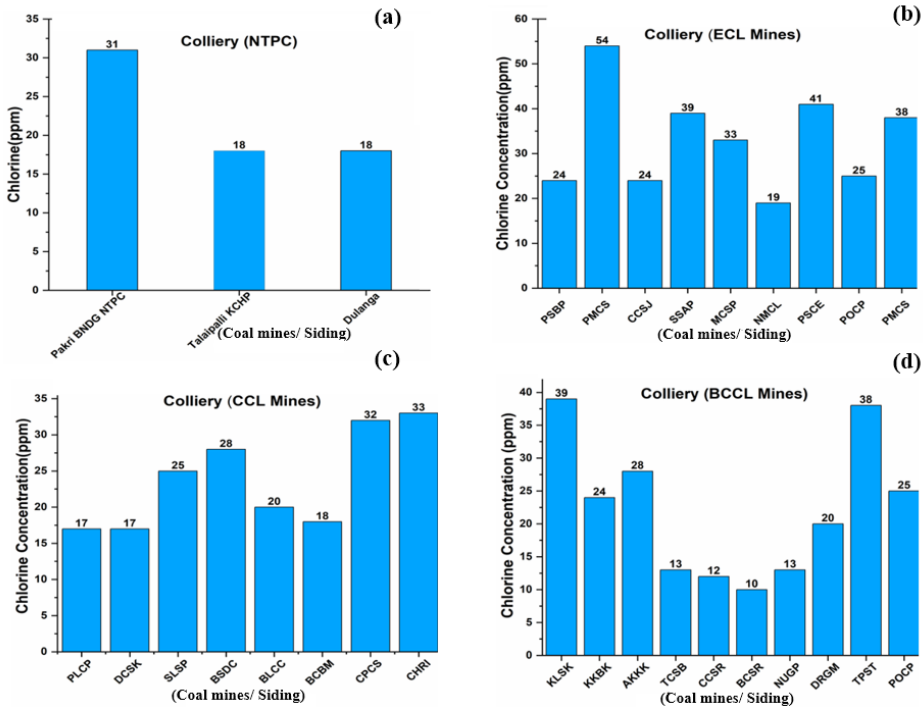

Fig. 5. Chlorine content of NTPC(a), ECL(b), CCL(C) & BCCL(d) mines

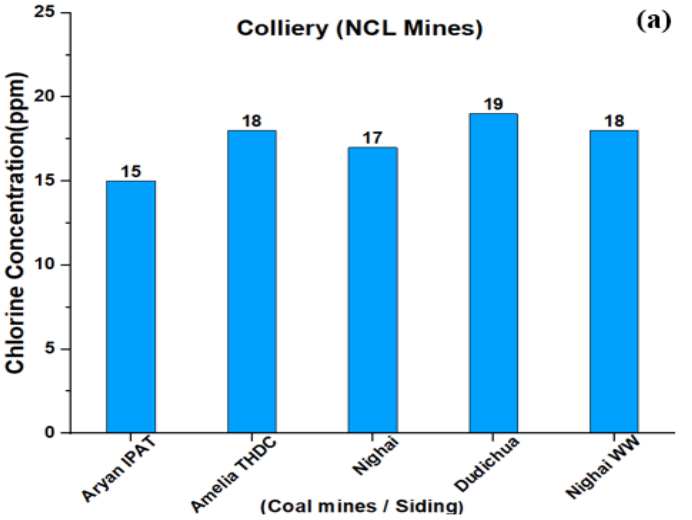
(a)
Colliery (NCL Mines)
Chlorine Concentration(ppm)
25
20
15
10
5
0
15
18
17
19
18
Aryan IPAT
Amelia THDC
Nighai
Dudichua
Nighai WW
(Coal mines / Siding)

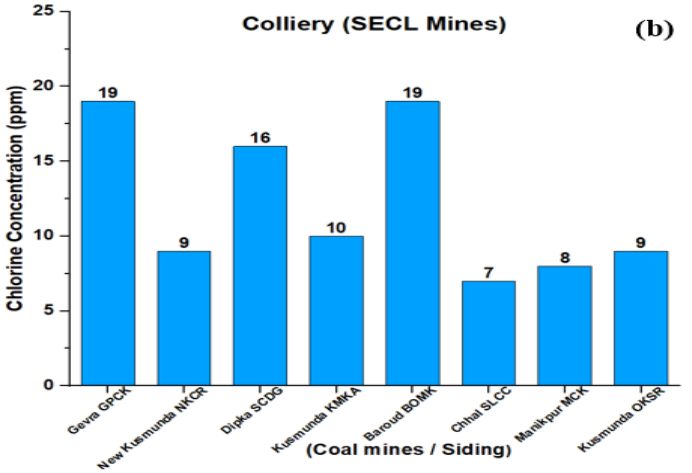
(b)
Colliery (SECL Mines)
Chlorine Concentration (ppm)
25
20
15
10
5
0
19
9
16
10
19
7
8
9
Gevra GPCK
New Kusmunda NKCR
Dipka SCDG
Kusmunda KMKA
Baroud BOMK
Chhal SLCC
Manikpur MCK
Kusmunda OKSR
(Coal mines / Siding)

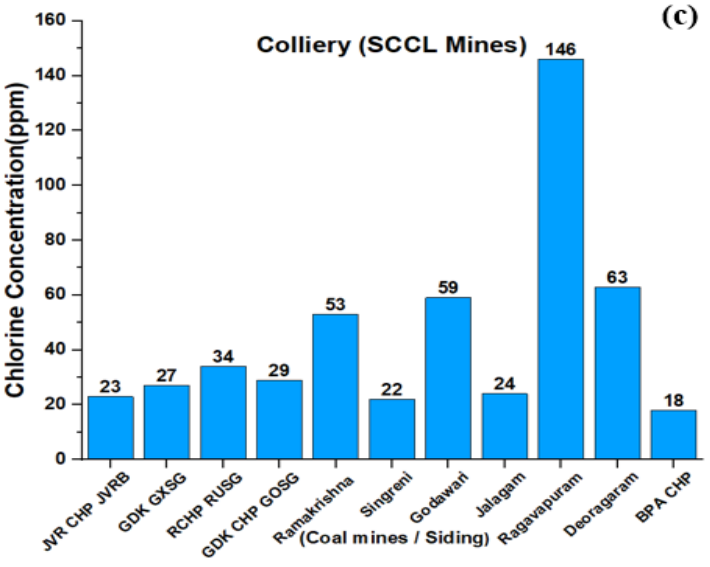
(c)
Colliery (SCCL Mines)
Chlorine Concentration(ppm)
160
140
120
100
80
60
40
20
0
23
27
34
29
53
22
59
24
146
63
18
JVR CHP JVRB
GDK GXSG
RCHP RUSG
GDK CHP GOSG
Ramakrishna
Singreni
Godavari
Jalagam
Ragavapuram
Deoragaram
BPA CHP
(Coal mines / Siding)

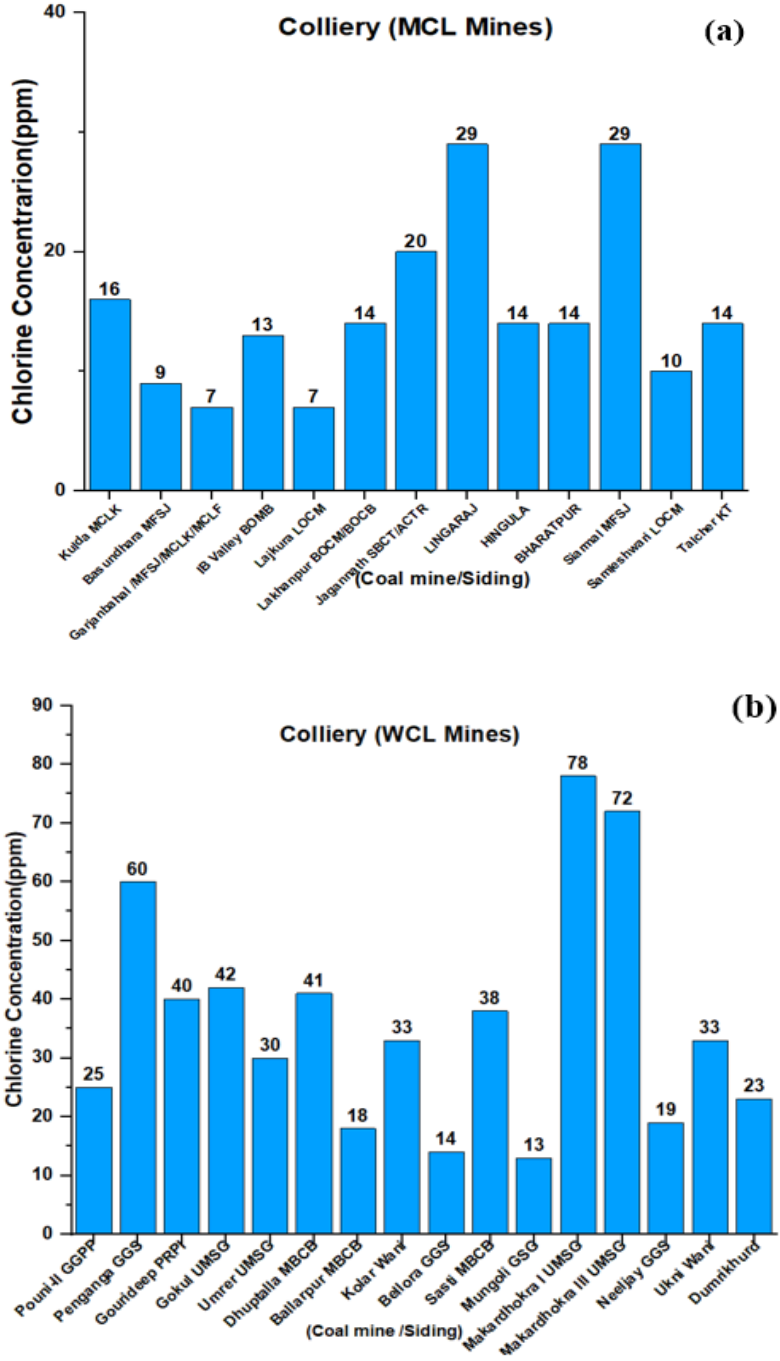

Fig. 7. Chlorine content of MCL(a) & WCL mines(b)

7 Conclusions

Indian coal typically contains chlorine levels ranging from 10 to 60 ppm, with few exceptions. The primary coal-bearing formations, Barakar and Raniganj, are found across all coalfields within the Gondwana subgroup. NTPC-owned coal mines have chlorine concentrations between 18 and 31 ppm. Most Indian coal mines, including those operated by ECL, CCL, BCCL, NCL, SECL, and MCL, generally feature chlorine content below 50 ppm, with the exception of SCCL and WCL mines. Notable locations with slightly higher chlorine levels include SCCL sidings such as Godavari (59 ppm) and Deoragram (63 ppm), as well as WCL sidings like Penganga GGS (60 ppm) and Makardhokra (72–73 ppm). The Rhagavpuram siding of WCL, situated near the coastal region, exhibits a significantly higher chlorine level of 146 ppm. In general, Indian coal mines are characterized by relatively low chlorine content.

Acknowledgments. The authors express their sincere gratitude to Executive Director (Mr.Shaswattam) NTPC Energy Technology & Research Alliance (NETRA) for providing the necessary facilities and support to carry out this research work. Special thanks are due to the laboratory and technical staff for their assistance in the experimental setup, CO_2 handling, and materials characterization. The authors also acknowledge valuable discussions and guidance from colleagues in the field of carbon capture and utilization.

Disclosure of Interests. The authors declare that they have no competing interests relevant to the content of this article.

References

1. Xu M, Xue S, Hu F, et al Failure case study on reheater pipes in a subcritical unit served for a thermal power plant. Case Stud Therm Eng 59:104550. (2024) https://doi.org/10.1016/j.csite.2024.104550

2. Sun Q, Fang T, Chen J, Da C Characteristics of chlorine releasing from coal-fired power plant. Atmosphere (Basel) 12(2021):. https://doi.org/10.3390/atmos12121550

3. Miltner A, Beckmann G, Friedl A Preventing the chlorine-induced high temperature corrosion in power boilers without loss of electrical efficiency in steam cycles. Appl Therm Eng 26:2005–2011(2006). https://doi.org/10.1016/j.applthermaleng.2006.01.006

4. Yudovich YE, Ketris MP Chlorine in coal: A review. Int J Coal Geol 67:127–144(2006). https://doi.org/10.1016/j.coal.2005.09.004

5. Mazurek I, Skawińska A, Sajdak M Analysis of chlorine forms in hard coal and the impact of leaching conditions on chlorine removal. J Energy Inst 94:337–351(2021). https://doi.org/10.1016/j.joei.2020.10.002

6. Svensson T, Löfgren A, Saetre P, et al Chlorine Distribution in Soil and Vegetation in Boreal Habitats along a Moisture Gradient from Upland Forest to Lake Margin Wetlands. Environ Sci Technol 57:11067–11074(2023). https://doi.org/10.1021/acs.est.2c09571

7. Zhai W, Yang B, Zhang S, et al Study on High Temperature Chlorination Corrosion of Metallic Materials on the Waste incineration boilers. IOP Conf Ser Earth Environ Sci 450(2020):. https://doi.org/10.1088/1755-1315/450/1/012006

8. Spiegel M, Zahs A, Grabke HJ Fundamental aspects of chlorine induced corrosion in power plants. Mater High Temp 20:153–159(2003). https://doi.org/10.3184/096034003782749080

9. Hernas A, Imosa M, Formanek B, Cizner J High-temperature chlorine-sulfur corrosion of heat-resisting steels. J Mater Process Technol 157–158:348–353(2004). https://doi.org/10.1016/j.jmatprotec.2004.09.054

10. Li P, Du M Effect of chloride ion content on pitting corrosion of dispersion-strengthened-high-strength steel. Corros Commun 7:23–34(2022). https://doi.org/10.1016/j.corcom.2022.03.005

11. V. Saravanan, K. Subbiramani, T.M. Rao, Gross Calorific Value of Indian Coals and its Correlation with Ash Content, Power Res. - A J. CPRI. 14 71–75(2023). https://doi.org/10.33686/pwj.v19i1.1124.

12. Chen, Han Lin, and Mark Pagano. "The removal of chlorine from Illinois coal by high temperature leaching." Fuel processing technology 13.3: 261-269(1986).

13. Spears, D. A. "A review of chlorine and bromine in some United Kingdom coals." International Journal of Coal Geology 64.3-4: 257- 265(2005).

14. Mazurek, I., Skawińska, A., & Sajdak, M.. Analysis of chlorine forms in hard coal and the impact of leaching conditions on chlorine removal. Journal of the Energy Institute, *94*, 337–351(2020). https://doi.org/10.1016/j.joei.2020.10.002

15. Luppens BJA, Janke LG, Mccord JD, et al (2007) Performance Audit of the U . S . Geological Survey , Energy Resource Program Inorganic Geochemistry Laboratory U . S . Geological Survey(2007)